Measurement of the Structure Function Ratio F_2^{He}/F_2^D and a Comparison with Existing Data and Theoretical Models on Nuclear Effects in Deep Inelastic Scattering

Michele Arneodo

A dissertation presented to
the Faculty of Princeton University
in candidacy for the degree of
Doctor of Philosophy

Recommended for acceptance
by the Department of Physics
January 1992

Abstract

The ^{4}He to D structure function ratio was measured in deep inelastic muon-nucleus scattering at an incident muon momentum of 200 GeV. The kinematic range $0.0035 < x < 0.65$ and $0.5 < Q^2 < 90$ GeV^2 was covered, where x is the Bjorken scaling variable and $-Q^2$ the mass of the virtual photon squared. The experiment was carried out by the New Muon Collaboration (NMC) at CERN, the European Laboratory for Particle Physics.

At small x the ratio is significantly smaller than unity; the size of the depletion grows with decreasing x and amounts to 7% at $x = 0.0035$. At intermediate x, $x \approx 0.1$, the ratio shows some enhancement above unity (by about 1%). The results do not depend significantly on Q^2.

An extensive review of the experimental and theoretical status in the field of nuclear effects in deep inelastic scattering is given. The present results, as well as those for the ratios of the carbon and calcium to deuterium structure functions, also measured by the NMC, are compared with the available theoretical predictions.

To Alice

Contents

List of Figures

List of Tables

Acknowledgements

This thesis covers research work that I carried out at CERN and at INFN in Torino during the period 1985-1991, as a member of the New Muon Collaboration (NMC). Working in the NMC has been a very fruitful and rewarding experience for me: I am grateful to my NMC colleagues not only for the help I received from them in the various phases of my work, but also for the pleasant atmosphere they managed to create within the collaboration. This is even more true for the colleagues of my group in Torino.

In particular I would like to express here my gratitude to Maria Itala Ferrero who introduced me to the world of high energy physics and to CERN. Her encouragement and support have been instrumental in bringing this thesis to its completion.

Cristiana Peroni has followed my work since I came back to Europe in 1985. In the early phases of the experiment we shared a number of tasks, from the testing and setting up of the beam hodoscopes to the development of the beam hodoscopes reconstruction software. Later, when I started the data analysis, she offered constant guidance and support. Her comments to the manuscript have greatly contributed to the clarity of the presentation.

Dietmar Nowotny and Christoph Scholz carried out parallel analyses on the He/D and on the C/D, Ca/D data; with them I shared the joy – and pain – of writing the paper about our results. Work with them has been a pleasure and has started a durable friendship.

For the theoretical review of this thesis I befitted from conversations and/or correspondence with several people. In particular I would like to thank B. Badelek, V. Barone, S. Barshay, M. Ericson, S. Liuti, N.N. Nikolaev, G. Piller, E. Predazzi, M.I. Strikman and W. Zhu.

Preliminary versions of the thesis, or parts thereof, were critically read and commented by B. Badelek, M. Botje, G. van Middelkoop, N.N. Nikolaev, D. Nowotny, Ch. Scholz and Y. Tzamouranis. To all of them I express my gratitude.

The Beam Hodoscopes were designed and built in Torino. The competent and enthusiastic contributions of G. Dughera and G. Giraudo, from the INFN mechanical workshop, and of P.P. Trapani from the electronics workshop were essential to carry out the project within the tight schedule.

My gratitude also goes to Liz Cumiskey, the joyful and efficient NMC secretary at CERN and to Yolande Camp, who handled the thousands of tapes that we wrote over these years.

Last, but not least, I would like to thank Pierre A. Piroué for accepting to be my thesis advisor and for his valuable comments to the manuscript.

Introduction

Particle and nuclear physics have been considered for a long time as distinct disciplines with little overlap. The reason for this is that the energies involved in particle physics are much larger than those at which nuclear phenomena are relevant. In the past decade several experimental results have however shown that this is not always the case. In particular, Deep Inelastic Scattering (DIS) of charged leptons on different targets has proven that quarks and gluons are sensitive to the nuclear environment in which they are embedded: notably their momentum distribution in a nucleon – measured by the so-called structure functions – depends rather dramatically on whether the nucleon is free or bound in a nucleus.

The interactions between quarks and gluons are believed to be described by Quantum-Chromo Dynamics (QCD). QCD has been successful in describing a number of short distance phenomena, at scales $\ll 1$ fm; unfortunately, at the moment, it appears very difficult to derive from this theory quantitative predictions for processes involving larger distances, such as those typical of nuclear physics. In this respect the study of the nuclear effects in deep inelastic scattering is very interesting as it may shed some light on the large distance behavior of quarks and gluons.

The New Muon Collaboration (NMC) at CERN (the European Laboratory for Particle Physics situated near Geneva, Switzerland) is carrying out a program covering a wide range of physics topics in deep inelastic muon scattering. Special emphasis has been given to accurate measurements of nuclear effects.

We report here on the NMC results for the ratio of the ^{4}He and D structure functions; these results extend to very small values of the Bjorken scaling variable x and cover a wide range in Q^2, the four momentum squared transferred from the muon to the target. This kinematic region was so far unexplored.

This thesis is organized as follows:

- In chapter one we give a detailed and updated account of the current experimental and theoretical situation in the field of nuclear effects in deep inelastic scattering.
- In chapter two we describe the experimental apparatus used by NMC.
- In chapter three we summarize the software chain through which the data were processed.
- In chapter four we describe the final physics analysis: the data selection criteria, the kinematic cuts, the corrections used to extract the results are presented, as well as the results themselves.

- In chapter five we compare the He/D ratio with the results, also produced by NMC, on the ratios of the carbon and calcium to deuterium structure functions. The three NMC ratios are used together to study the A dependence of nuclear effects at small values of the Bjorken variable x. The NMC results are then compared with those of previous experiments. Our results and those of an earlier experiment carried out at the Stanford Linear Accelerator Center (SLAC) are combined to evaluate the fraction of the nucleon momentum carried by quarks in bound and in free nucleons. Finally the NMC ratios are compared with the available theoretical models.

The thesis is completed by a few appendices:

- Appendix A presents the analysis and the results of the beam momentum calibration runs: by means of a dedicated spectrometer an accuracy of a few tenths of a per cent was achieved in the calibration of the incident muon momentum.
- Appendix B describes in detail the hardware, the track reconstruction software and the on-line monitoring and checking programs of the beam hodoscopes, a set of scintillation counters which detect the incoming beam muons and measure their trajectory.
- Appendix C contains a critical discussion of the input parameters for the so-called radiative corrections. These corrections are needed to extract the single photon exchange contribution from the measured yields.
- Appendix D expands on some technical aspects of the calculation of the fraction of the nucleon momentum carried by quarks in bound and in free nucleons.
- Finally appendix E gives the composition of the New Muon Collaboration.

The research work described in this thesis was mainly carried out at CERN and at the Istituto Nazionale di Fisica Nucleare (INFN) in Turin, Italy. Such work involved a large number of people (cf. appendix E); the areas in which the author contributed most are the following:

- Design, construction and setting up of the beam hodoscopes, of which he was responsible during data taking (cf. appendix B).
- Development of part of the beam hodoscope track reconstruction software and of the on-line monitoring and checking tasks (cf. appendix B).
- Tuning of the software production chain for the data presented here (tuning is discussed section 3.6.2).
- Analysis of the He/D data and extraction of the results, presented in chapter four. This involved also work on the radiative corrections program (cf. appendix C).
- Analysis of the beam calibration runs, presented in appendix A.
- The author was responsible for data taking during the 1986 period in which the data discussed here were collected, as well as during three other data taking periods in 1987, 1988 and 1989.

Chapter 1

Nuclear Effects in Deep Inelastic Scattering

"There's no use trying," [Alice] said: "One can't believe impossible things."
"I daresay you haven't had much practice, said the Queen." [1]

Introduction

Charged lepton deep inelastic scattering off nucleons has been for a long time a powerful tool to investigate the structure of matter.

In the late 1960's "scaling" of the nucleon structure functions was discovered by the pioneering SLAC experiments. Scaling was interpreted as evidence that nucleons contain pointlike constituents – later identified with quarks. About ten years later "scaling violations" were detected, again by deep inelastic scattering experiments, showing that quarks interact as predicted by the theory of strong interactions, Quantum Chromo-Dynamics.

Nuclear effects in deep inelastic scattering were thought to be largely negligible, essentially because the energies involved in deep inelastic scattering are much larger than those typical of nuclear processes. The nucleus was viewed as a collection of quasi-free nucleons and quarks were believed to be insensitive to the nuclear environment. This picture was however proven wrong by a comparison of the iron and deuterium structure functions, produced by the European Muon Collaboration at CERN in 1982. Since then considerable effort has been spent both at the experimental and the theoretical level in order to shed light on the phenomenon. In spite of this, a quantitative and detailed understanding of the physical mechanisms behind these effects is not yet available.

Section one of this chapter gives a brief introduction to deep inelastic scattering, mainly intended to define the basic quantities and concepts; a more detailed presentation of the subject can be found elsewhere (see e.g. [2]). Section 1.2 summarizes the experimental situation of nuclear effects in deep inelastic scattering. Finally a detailed survey of the theoretical ideas proposed to explain such effects is given in section 1.3.

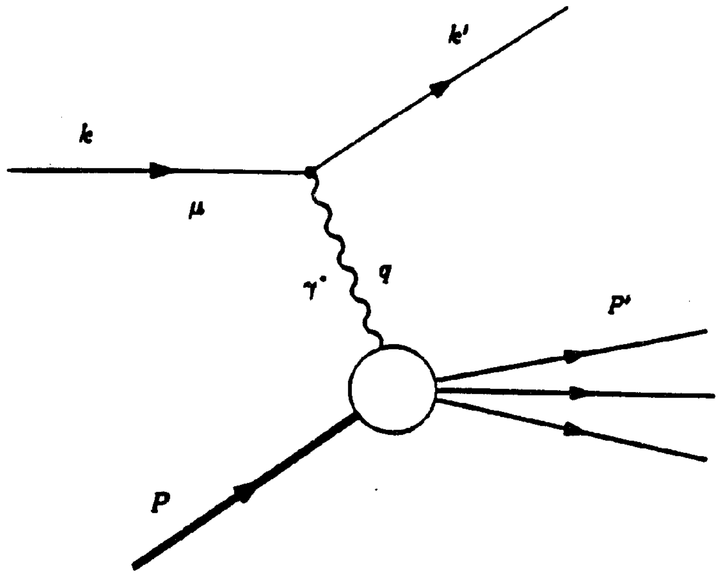

Figure 1.1: Deep inelastic muon-nucleon scattering

1.1 Deep Inelastic Scattering (DIS)

1.1.1 Generalities of Charged Lepton Deep Inelastic Scattering

We are interested in the process $\mu + N \rightarrow \mu + X$, where a charged lepton (in this case a muon) scatters inelastically off a nucleon; the final state contains the scattered lepton and the debris of the nucleon. We consider the case in which the target nucleon is at rest and we assume that only the incoming and outgoing lepton momenta are measured. The Feynman graph for the process is shown in fig. 1.1, under the assumption that only one virtual photon is exchanged.

If E and E' are the energies of the incident and scattered lepton, k, k' their four momenta, and ϑ is the lepton scattering angle, the following kinematic variables can be introduced (we neglect the lepton mass):

- $q = k - k'$, the four momentum of the virtual photon,
- $Q^2 = -q^2 = -(k - k')^2 \simeq 4EE' \sin^2 \vartheta/2$, with q^2 the square of the four momentum transferred from the lepton to the target nucleon,
- $\nu = P \cdot q/M = E - E'$, the virtual photon energy,
- $W^2 = (P + q)^2 = M^2 - Q^2 + 2M\nu$, the total invariant mass squared of the target nucleon-virtual photon system,
- $x = Q^2/(2P \cdot q) = Q^2/(2M\nu)$, the Bjorken scaling variable,
- $y = P \cdot q/(P \cdot k) = \nu/E$,

where P is the four momentum of the target nucleon and the final expressions for Q^2, ν, W^2, x and y are valid in the laboratory frame, where the target nucleon is at rest. The mass M is conventionally taken to be that of the proton.

Using the known rules of Feynman diagrams and adopting the standard formalism of Bjorken and Drell [3], the basic amplitude for the process of fig. 1.1 can be written as

$$A \sim [j_\alpha \frac{1}{q^2} J^\alpha], \qquad (1.1)$$

where $j_\alpha = \overline{u}_{lepton}(k')\gamma_\alpha u_{lepton}(k)$ is the leptonic current and J_α is the a priori unknown current at the hadronic vertex.

Including all the appropriate phase space and flux factors and taking the modulus squared of the amplitude 1.1, we can write the differential cross section

$$\frac{d^2\sigma}{d\Omega dE'} = \frac{1}{2}\frac{\alpha^2}{MQ^4}\frac{E}{E'}L_{\mu\nu}W^{\mu\nu}, \qquad (1.2)$$

where α is the fine structure constant and Ω is the solid angle. The leptonic tensor $L_{\mu\nu}$ has the form:

$$L_{\mu\nu} = \frac{1}{2}\sum_{initial\ spins}\ \sum_{final\ spins} [\overline{u}_{lepton}\gamma_\mu u_{lepton}]^*[\overline{u}_{lepton}\gamma_\nu u_{lepton}] \qquad (1.3)$$

(we average over the initial state spins and sum over the final state ones). The hadronic tensor $W_{\mu\nu}$ is more complicated and corresponds to transitions of the target nucleon N to all possible final states X:

$$W_{\mu\nu} = \frac{1}{2}\sum_{in.\ spins}\sum_{X} < X|J_\mu(0)|N >^* < X|J_\nu(0)|N > (2\pi)^3\delta^4(p_X - p - q),$$

with p_X the four momentum of state X; the four dimensional δ function imposes energy and momentum conservation.

A general expression for the hadronic tensor can be found upon assuming parity and current conservation. After imposing the further requirement of symmetry ($L_{\mu\nu}$ is symmetric and hence only the symmetric part of $W_{\mu\nu}$ contributes to the cross sections), the tensor $W_{\mu\nu}$ turns out to be a function of q_μ, q_ν, P_μ, P_ν (and combinations thereof) and includes two unknown scalar functions, $W_1(\nu, Q^2)$ and $W_2(\nu, Q^2)$.

The final expression for the cross section reads:

$$\frac{d^2\sigma}{d\Omega dE'} = \frac{4\alpha^2 E'^2}{Q^4}\left(2W_1 \sin^2\frac{\vartheta}{2} + W_2\cos^2\frac{\vartheta}{2}\right). \qquad (1.4)$$

The structure functions $W_1(\nu, Q^2)$ and $W_2(\nu, Q^2)$ contain information about the inner structure of the target nucleon; they can be related to the photo-absorption cross sections σ_T and σ_L for transverse (i.e. with helicity $\pm$ 1) and longitudinal photons (helicity 0):

$$\begin{aligned} W_1 &= \frac{K}{4\pi^2\alpha}\sigma_T & (1.5)\\ W_2 &= \frac{K}{4\pi^2\alpha}(\sigma_T+\sigma_L)\frac{Q^2}{Q^2+\nu^2}, & (1.6)\end{aligned}$$

where K is the incident photon flux. For virtual photons there is some arbitrariness in the definition of the photon flux: Gilman's convention [4] is to take $K=\sqrt{\nu^2+Q^2}$; alternatively one can have (Hand's convention [5]) $K=\nu-Q^2/(2M)$. Both reduce to $K=\nu$ for real photons (Q^2=0).

The longitudinal to transverse virtual photon cross section ratio

$$R=\frac{\sigma_L}{\sigma_T}=\frac{W_2(\nu,Q^2)}{W_1(\nu,Q^2)}\left(1+\frac{\nu^2}{Q^2}\right)-1 \tag{1.7}$$

is an important quantity, being related (see below) to the spin of the nucleon's constituents.

In terms of σ_L and σ_T the cross section 1.4 becomes

$$\frac{d^2\sigma}{d\Omega dE'}=\Gamma(\sigma_T+\epsilon\sigma_L),$$

where

$$\epsilon=\left(1+2\frac{Q^2+\nu^2}{Q^2}\tan^2\frac{\vartheta}{2}\right)^{-1}, \tag{1.8}$$

and

$$\Gamma=\frac{K\alpha}{2\pi^2Q^2}\frac{E'}{E}\frac{1}{1-\epsilon}.$$

It is customary to define

$$\begin{aligned} F_1 &= MW_1\\ F_2 &= \nu W_2\end{aligned}$$

and rewrite 1.4 in terms of x and Q^2:

$$\frac{d^2\sigma}{dxdQ^2}=\frac{4\pi\alpha^2}{Q^4}\left[\left(1-y-\frac{Mxy}{2E}\right)\frac{F_2(x,Q^2)}{x}+y^2F_1(x,Q^2)\right]. \tag{1.9}$$

Often R is used instead of F_1, in which case we have:

$$\frac{d^2\sigma}{dxdQ^2}=\frac{4\pi\alpha^2}{Q^4}\frac{F_2(x,Q^2)}{x}\left[1-y-\frac{xyM}{2E}+\frac{y^2}{2}\frac{1+4M^2x^2/Q^2}{1+R(x,Q^2)}\right]. \tag{1.10}$$

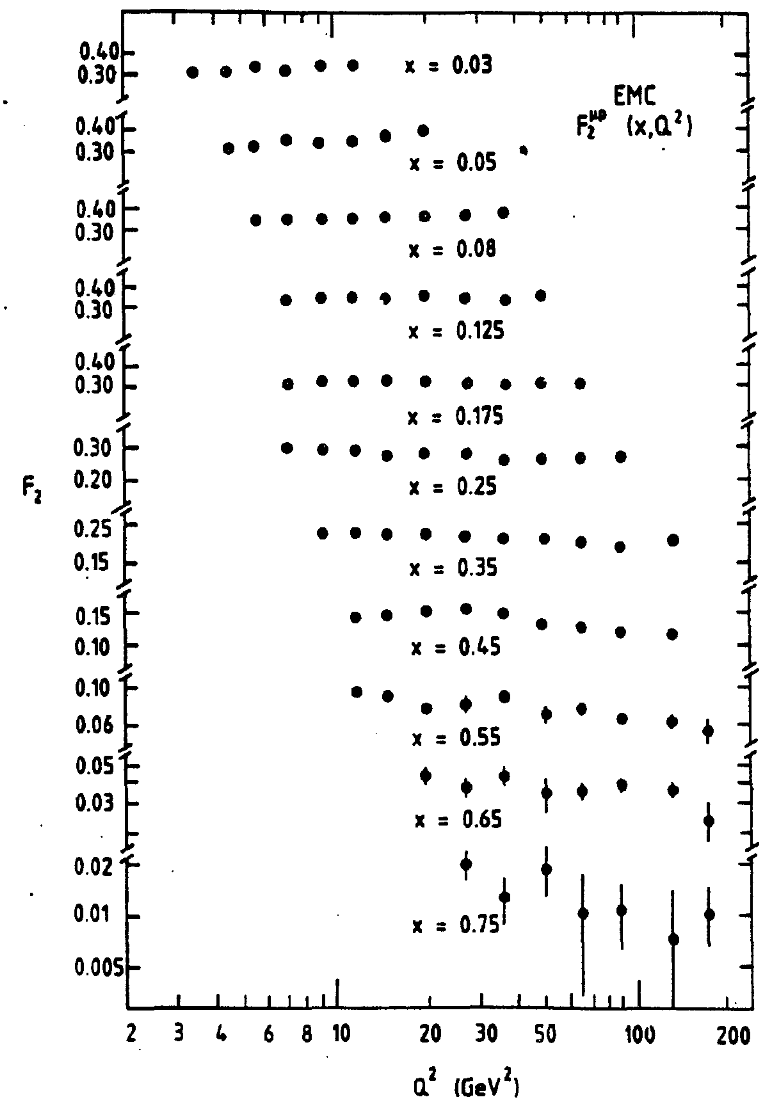

Figure 1.2: The proton structure function F_2^p as a function of Q^2 for different x bins (from [8])

1.1.2 Scaling and the Quark-Parton Model

The first measurements of the structure functions F_1 and F_2 were made with electron beams at SLAC [6] and DESY [7] at the end of the 60's; they were followed by extensive and detailed investigations both with electron and muon beams. Figure 1.2 shows the results of a recent high statistics measurement of the proton structure function $F_2^p(x, Q^2)$ [8].

It is clear from fig. 1.2 that F_2 is to first approximation independent of Q^2. In general both structure functions F_1 and F_2 appear to depend mainly on x; moreover they tend to a finite value even when both Q^2 and ν are large, as long as the ratio Q^2/ν is kept constant, the so-called "Bjorken limit" [9]. This scaling behavior was unexpected and strongly contrasts with the properties of elastic form factors, which instead rapidly vanish with increasing Q^2.

Scaling can be interpreted as a sign of the fact that the virtual photon is absorbed, inside the nucleon, by pointlike, electrically charged objects, first named partons by Feynman [10] and later identified with quarks.

Let us indeed assume that the observed cross section arises from the incoherent sum of the cross sections for elastic scattering of the lepton off pointlike, spin 1/2, charged objects. We will show that the resulting expressions for F_1 and F_2 are functions of x only. We will work in a frame where the momentum of the nucleon is very large, so that during the time of the photon-parton interaction, parton-parton interactions may be neglected because of the relativistic time dilation. Of all possible infinite momentum frames the Breit frame is often used, in which the virtual photon has zero energy and the parton exactly reverses its momentum in the collision. The cross section for elastic scattering off one parton has the same form as the electron-muon one (cf. e.g. [2]):

$$\frac{d^2\sigma}{d\Omega dE'} = \frac{4\alpha^2 E'^2}{Q^4}\left(\frac{e_i}{e}\right)^2\left(\frac{Q^2}{2m_i^2}\sin^2\frac{\vartheta}{2} + \cos^2\frac{\vartheta}{2}\right)\delta\left(\nu - \frac{Q^2}{2m_i}\right),$$

in which m_i is now the parton mass, e_i its charge and e the unit charge; the δ function imposes the kinematics of elastic scattering, $Q^2 = 2m_i\nu$. By comparing with expression 1.4 one finds that in this case the two structure functions read:

$$\begin{aligned} W_{1\,i}^{elastic} &= e_i^2\frac{Q^2}{4m_i^2\nu}\delta\left(1 - \frac{Q^2}{2m_i\nu}\right) \\ W_{2\,i}^{elastic} &= e_i^2\delta\left(1 - \frac{Q^2}{2m_i\nu}\right). \end{aligned}$$

The nucleon structure functions W_1 and W_2 can then be computed by summing $W_{1\,i}^{elastic}$ and $W_{2\,i}^{elastic}$ over all partons under the assumption that the probability to find a parton with a fraction ξ of the nucleon four momentum is $f(\xi)d\xi$:

$$W_1(\nu, Q^2) = \sum_i W_{1\,i}^{elastic} = \sum_i e_i^2\int_0^1 d\xi f(\xi)\frac{Q^2}{4\xi^2M^2\nu}\delta\left(1 - \frac{Q^2}{2M\xi\nu}\right),$$

where we set $m_i = \xi M$ (cf. [2] for a discussion of this seemingly unnatural assumption). Upon integration we obtain:

$$F_1 = MW_1(\nu, Q^2) = \frac{1}{2}f(\xi)\sum_i e_i^2, \tag{1.11}$$

with $\xi = Q^2/2M\nu$. Similarly:

$$F_2 = \nu W_2(\nu, Q^2) = \xi f(\xi) \sum_i e_i^2. \tag{1.12}$$

We thus have that F_1 and F_2 are indeed functions of $\xi = x = Q^2/2M\nu$ only, and that x can be viewed as the fraction of the nucleon's momentum carried by an individual parton.

From expressions 1.11 and 1.12 the Callan-Gross relation can be derived [11]:

$$F_2(x) = 2xF_1(x). \tag{1.13}$$

Finally we remark that formula 1.7 reads now:

$$R = \frac{4M^2x^2}{Q^2}, \tag{1.14}$$

which tends to zero in the Bjorken limit.

As we anticipated R depends strongly on the spin of the partons. We assumed spin 1/2 partons, but the calculation that we outlined above may easily be repeated for spin 0 partons. The cross section on a single parton then is the Mott one,

$$\frac{d\sigma}{d\Omega dE'} = \frac{\alpha^2 \cos^2 \frac{\vartheta}{2}}{4E^2 \sin^4 \frac{\vartheta}{2}} \left(\frac{e_i}{e}\right)^2 \delta\left(\nu - \frac{Q^2}{2m_i}\right).$$

Comparison with formula 1.4 shows that $W_1^{elastic}$ is in this case zero, which in turn implies (cf. expression 1.5) $\sigma_T = 0$ and $R = \infty$.

Partons as Quarks

The identification of partons with the spin-1/2, fractional charge quarks first suggested by Gell-Mann and Zweig is now an accepted fact. In fact one normally refers to the Quark-Parton Model (QPM), in which nucleons are described as composed of *valence* quarks, which define the charge and spin of the nucleon. In the proton there are two quarks of "flavor" u and one of flavor d. In the neutron there are two d quarks and one u quark. The electric charge of u quarks is $(2/3)e$, that of d quarks is $-(1/3)e$. The QPM, in its generally accepted formulation, goes beyond this and assumes that quarks interact via the exchange of spin-1 massless particles, the gluons (see next section), which can convert into quark-anti-quark pairs, generally referred to as *sea* quarks.

The consistency of the neutrino DIS results with those obtained in charged lepton DIS was instrumental in establishing the correctness of the QPM picture. The neutrino DIS cross sections can be formulated in terms of three structure functions: F_1^ν, F_2^ν and F_3^ν, the latter arising as a consequence of the parity non-conserving nature of weak interactions. These structure functions can also be expressed in the QPM as linear combinations of parton distributions, which turn out to be the same as those obtained with electrons and muons. In other words electrons (or muons) and neutrinos scatter off the same pointlike objects in the nucleon.

Neutrino scattering results allow a measurement of the number of valence quarks (the Gross-Llewellyn-Smith sum rule) and of the difference between u and d valence quarks in

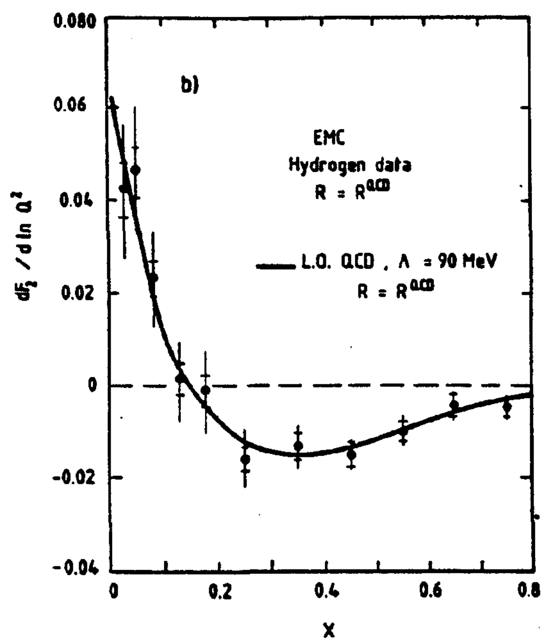

Figure 1.3: The logarithmic slope $dF_2^p/d\ln Q^2$ as a function of x. The solid curve is a QCD fit to the data (from [8])

the proton (the Adler sum rule). Charged lepton scattering allows a measurement of the difference of the u and d quark charges squared (the Gottfried sum rule). The values found for these quantities were originally in excellent agreement with the QPM expectations (although within large error bars), a fact which gave further credibility to the QPM. Discrepancies that were later found are not regarded as disproving the QPM picture. As an example a recent high precision measurement of the Gottfried sum rule by NMC [12] has yielded a result in disagreement with the QPM prediction. The discrepancy is not interpreted necessarily as contradicting the generally accepted values of the quark charges, nor as a severe failure of the identification of partons with quarks. The result is rather taken as an indication that some of the approximations made in deriving the QPM result (e.g. isospin symmetry, flavor symmetry of the sea) may be incorrect, or that a small admixture of extra objects (e.g. spin-1 diquarks) may be present in the nucleon, in addition to quarks and gluons.

Finally we remark that the value measured for R is close to zero: this is consistent with the spin 1/2 assignment for quarks.

1.1.3 Scaling Violations and QCD

Close examination of fig. 1.2 shows that F_2 does have a weak dependence on Q^2. Structure functions rise with increasing Q^2 for $x < 0.2$ and then start decreasing, as fig. 1.3 demonstrates in more detail. This dependence is often referred to as scaling violations.

As we mentioned above, partons interact among themselves and their behavior is described by Quantum Chromo-Dynamics (QCD), a non-abelian gauge theory. According to QCD each quark flavor may carry one of three possible "color" charges; quarks interact by exchanging spin-1 massless, electrically neutral particles called gluons, which are themselves colored.

In analogy with Quantum Electro-Dynamics (QED), quarks may radiate gluons and gluons may convert into quark anti-quark pairs. Unlike what happens in QED however, gluons, being colored, may directly interact with each other.

The QCD coupling constant has the following form:

$$\alpha_s(Q^2) = \frac{12\pi}{(33-2N_f)\ln(Q^2/\Lambda^2)}, \tag{1.15}$$

where N_f is the number of quark flavors and Λ is a mass scale parameter, the only free parameter in the theory that has to be determined from experiment. It is evident that the value of α_s tends to zero when Q^2 tends to infinity. This remarkable property of the theory is known as asymptotic freedom and, for large Q^2, justifies a posteriori the quark-parton model treatment of the previous subsection, where quarks were presented as essentially free. Asymptotic freedom is also the basis for the application of perturbative methods to large Q^2 phenomena (perturbative QCD). Non-perturbative approaches, although actively investigated, imply formidable computational problems and are – to date – of scarce predictive power.

Perturbative QCD is unable to compute the hadronic tensor $W_{\mu\nu}$ and therefore to predict the shape of the structure functions at fixed Q^2. It can however make predictions about the rate of change (the evolution) of the structure functions with Q^2, as long as Q^2 is large enough, so that α_s is sufficiently small and perturbative calculations are possible. The evolution of structure functions may be investigated by studying the evolution of their moments $M_n^{(j)}$

$$M_n^{(1)} = \int_0^1 dx x^{n-1} F_1(x,Q^2), \tag{1.16}$$

$$M_n^{(2)} = \int_0^1 dx x^{n-2} F_2(x,Q^2), \tag{1.17}$$

or, more easily, by using the Altarelli-Parisi evolution equations:

$$\frac{dq_i(x,t)}{dt} = \frac{\alpha_s(Q^2)}{2\pi}\int_x^1 \frac{dx'}{x'}\left[\sum_i q_i(x',t)P_{qq}(x/x') + G(x',t)P_{qG}(x/x')\right] \tag{1.18}$$

$$\frac{dG_i(x,t)}{dt} = \frac{\alpha_s(Q^2)}{2\pi}\int_x^1 \frac{dx'}{x'}\left[\sum_i q_i(x',t)P_{Gq}(x/x') + G(x',t)P_{GG}(x/x')\right], \tag{1.19}$$

where

- the sums are over all quarks and anti-quarks;
- $t = \ln(Q^2/\mu^2)$ (μ^2 is a scale unspecified in perturbative QCD, see below);
- x' is the momentum fraction carried by the parton;
- $q_i(x',Q^2)$ is the distribution function of quarks of flavor i (we called it f in the preceding subsection);
- $G(x',Q^2)$ is the gluon distribution function;

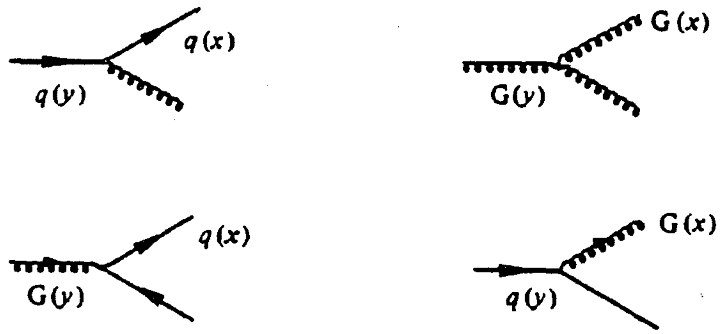

Figure 1.4: Graphical representation of the splitting functions (from [2])

- $P_{qq}(x/x')$, $P_{qG}(x/x')$ and $P_{GG}(x/x')$ are the quark-quark, quark-gluon and gluon-gluon splitting functions. $P_{ab}(x/x')$ measures the probability for finding a parton (we mean quarks and gluons, now) of type a with momentum fraction x "inside" (i.e. radiated from) a parton of type b and momentum fraction x'. The splitting functions are represented graphically in fig. 1.4.

In all QCD formulae seen above (notably in 1.15 and 1.18-1.19) Q^2 always appears scaled either by Λ^2 or μ^2. The magnitude of Λ controls the rate at which the QCD coupling constant runs as a function of Q^2; Λ is found to be $\approx$ 200 MeV. The scale μ can be regarded as the low-momentum cutoff for gluon radiation; in other words, for $Q^2 = \mu^2$ the nucleon appears simply as made up of three valence quarks. It can be argued that $\mu^2 \sim 1/\lambda^2$, where λ is the quark confinement size.

Some general properties of the quark and gluon behavior in the nucleon can be deduced from the Altarelli-Parisi equations:

1. The fraction of momentum carried by the valence quarks decreases as Q^2 increases. Momentum conservation implies that the momentum fraction carried by sea quarks and gluons increases with Q^2. Note that the fraction of the nucleon's momentum carried by gluons is substantial even at moderate Q^2: at Q^2=15 GeV^2 the total quark momentum fraction is 0.465 ± 0.023 [13].

2. All distributions become centered around smaller and smaller x values with increasing Q^2.

1.2 Phenomenology of Nuclear Effects in Deep Inelastic Scattering

The corrections to be applied to the deep inelastic lepton-nucleon cross section measured on a bound nucleon, as opposed to a free or quasi-free one, were for a long time believed to be either small and calculable or confined to specific kinematic regions. Grossly speaking this was justified on the basis of the fact that energy transfers in deep inelastic events are generally several orders of magnitude larger than the typical nuclear binding energy of 8 MeV/nucleon. Because of this, deep inelastic neutrino experiments or charged lepton ones at high Q^2, requiring high luminosities to compensate for the small cross section, were carried out on nuclear targets rather than on hydrogen or deuterium.

It was in one of these experiments, done by the European Muon Collaboration (EMC), that, in 1982, the nucleon structure function F_2 measured on iron was observed to differ from the one measured on deuterium [14]. For the first time it was the same experiment to carry out the measurements on the two targets, so that at least some of the systematic errors could cancel in the ratio. The deviation of the ratio from unity was thus left to be interpreted as a real physics effect: what came to be known as the EMC effect.

Before we begin a detailed discussion of the experimental evidence and of the theoretical models on the EMC effect, we briefly present the only two nuclear effects which were expected to play a role in deep inelastic scattering and were known prior to the EMC discovery: Fermi motion and shadowing.

1.2.1 Fermi Motion

The nucleons are not stationary in the nucleus, but move with an average momentum k_F.

The structure function F_2, as we have seen, is proportional in the QPM to the momentum distribution of the quarks inside the nucleus weighted by the square of their charges. This is only true for a free nucleon, i.e. for a hydrogen target. For a nuclear target the x variable is experimentally determined in the approximation that the nucleon is stationary. This is however not the case and the structure function measured on nuclear targets is in fact the convolution of the bare nucleon structure function with the momentum distribution function of the nucleon in the nucleus $f_N(z)$:

$$F_2^A(x) = \int_x^A dz f_N(z) F_2^N(x/z), \tag{1.20}$$

where z is the fraction of the nucleus momentum carried by the nucleon multiplied by A.

The effect of Fermi motion on the structure function ratio F_2^A/F_2^D has been calculated by several authors [15]-[19] for various nuclei. Some of the results available at the time of the EMC discovery are shown in fig. 1.5 for F_2^{Fe}/F_2^D. In this figure the solid line is from [15], the dashed line from [16], the dotted one from [17]; the dash-dotted line and triple-dot-dashed line are variants of the calculation [15] and indicate the sensitivity to different model assumptions. Much of the uncertainty follows from the poorly understood high momentum tail of the Fermi distribution.

A detailed discussion of Fermi motion and its interplay with the EMC effect can be found in [19].

1.2.2 Shadowing

In the low x region ($x < 0.1$), at small Q^2 (< 1 GeV^2), nuclear effects had long been known to be present and had been actively studied in the 1970's mainly by low energy electron experiments.

The cross section (per nucleon) for interactions between real photons and nuclei decreases with increasing atomic number (cf. [20, 21] and references therein). This effect is known as "shadowing" because of the analogy with the nuclear shadowing of the hadronic cross sections.

As we shall discuss at length below (section 1.3.2) this can be understood by assuming that the photon fluctuates from its pointlike, "bare photon" state into a superposition of vector mesons like the ρ, the ω or the ϕ (Vector Meson Dominance, VMD).

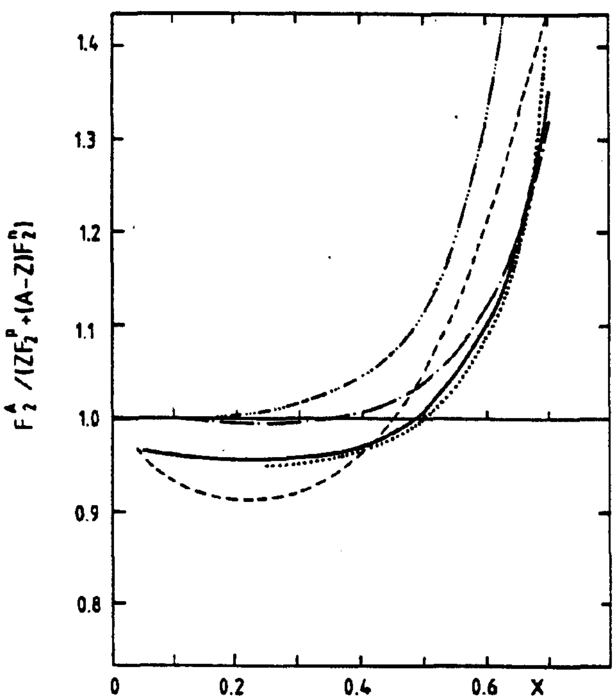

Figure 1.5: Theoretical predictions for the effects of Fermi motion on the structure function ratio F_2^{Fe}/F_2^D. For an explanation of the various curves see text

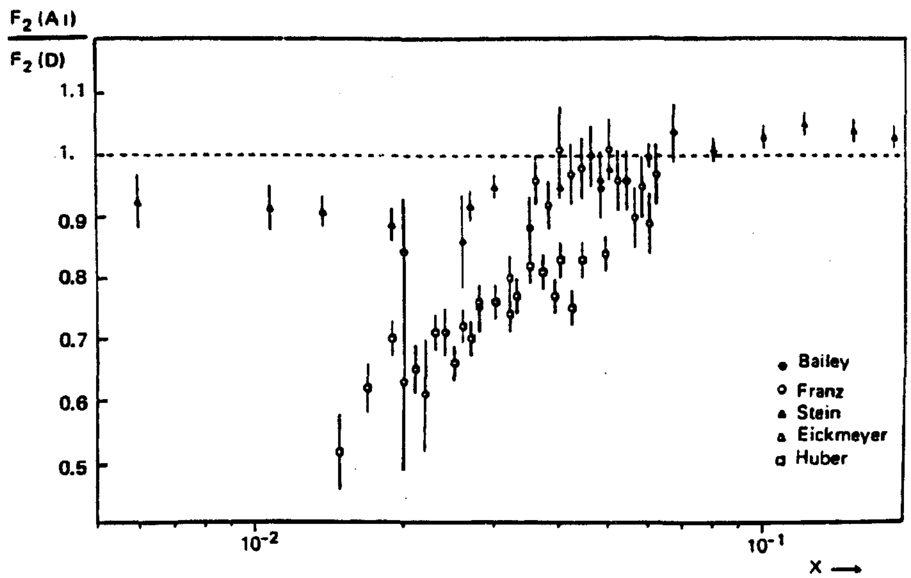

Figure 1.6: Shadowing in aluminum, as measured by different low energy lepto-production experiments: Bailey [22], Franz [23], Stein [24], Eickmeyer [25], Huber [26]

A similar but smaller effect had been observed, before the discovery of the EMC effect, for virtual photons in charged lepto-production at small values of Q^2 [22]-[26] (cf. table 1.1 for a summary of the main parameters of the quoted experiments). Figure 1.6 shows some of the data on shadowing in aluminum. The fact that the cross section ratio σ^{Al}/σ^D is lower than unity at small x is ascribed to shadowing of the virtual photon in aluminum nuclei. These early experiments were carried out with low energy electron or muon beams (< 20 GeV) and covered the small Q^2 region only, typically with $Q^2 < 2$ GeV^2. Based on vector meson dominance arguments there was a widespread prejudice that shadowing should disappear at larger Q^2.

A clear decrease of shadowing with increasing Q^2 – although not as fast as expected – was indeed observed [27] at the Fermi National Accelerator Laboratory (FNAL) near Chicago, using a 209 GeV beam, by the only high energy experiment which investigated shadowing before the discovery of the EMC effect. Figure 1.7 shows the results of this experiment in terms of the effective number of nucleons A_{eff} seen by the incident photon:

$$\frac{A_{eff}}{A} = \frac{\sigma(A)}{Z\sigma_p + (A-Z)\sigma_n} = A^{\epsilon}, \tag{1.21}$$

where σ_p and σ_n are the photo-absorption cross sections for the proton and the neutron, respectively, and $\sigma(A)$ is the observed nuclear cross section. The results are however somewhat misleading because they are integrated over x. Since large x events are mostly at large Q^2, the observed Q^2 dependence should in fact be partly ascribed to an x dependence of the signal.

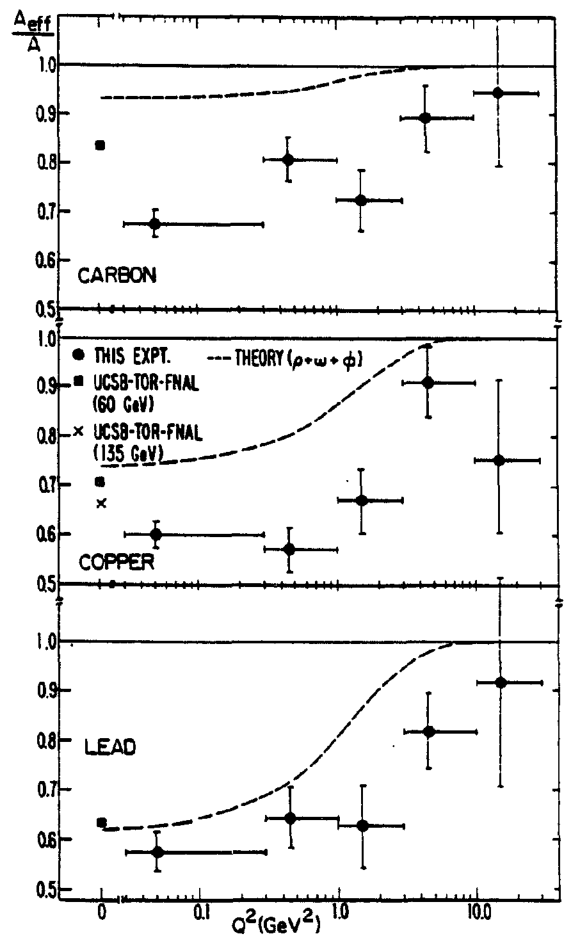

Figure 1.7: The ratio A_{eff}/A as a function of Q^2 for C, Cu and Pb as measured by the FNAL muon experiment [27]. Some real photo-production results [21] are also shown (from [27])

Lab.-experiment	beam type	beam energy [GeV]	target	x or ν range	Q^2 range [GeV^2]	ref.
FNAL	γ	4-18	C,Cu,Pb	$4 < \nu < 18$ GeV	0	[20]
FNAL	γ	20-185	C,Cu,Pb	$20 < \nu < 185$ GeV	0	[21]
Daresbury	e	5	H,D,Be,C,Al Co,Nb,Ta,U	$2.2 < \nu < 3.8$ GeV	0.066-0.25	[22]
DESY	e	7	H,D,Be,Al,Si	$0.3 < \nu < 6.5$ GeV	0.08-1	[23]
DESY	e	3.08-7	H,C,Al	$\nu < 6.2$ GeV	0.075-1	[26]
Cornell	e		H,D,C,Al Cu,Ta	$2.0 < \nu < 8.5$ GeV	0.1	[25]
SLAC-E61	e	13-20	H,D,Be,Al Cu,Au	$0.02 < x < 0.2$	0.4-1.6	[24]
SLAC-E87	e	9-20	D,Fe	$0.25 < x < 0.9$	3-20	[30]
SLAC-E49B	e	4.5-20	D,Al	$0.075 < x < 0.86$	2-20	[31]
SLAC-139	e	8-24.5	D,He,Be,C,Al Ca,Fe,Ag,Au	$0.09 < x < 0.9$	2-15	[35]
SLAC-E140	e	4-20	D,Fe,Au	$0.2 < x < 0.5$	1-5	[43]
FNAL	μ	209	C,Cu,Pb	$40 < \nu < 6.2$ GeV	0.01-30	[27]
CERN-EMC NA2	μ	120-280	D,Fe	$0.05 < x < 0.65$	9-170	[14, 29]
CERN-BCDMS	μ	280	D,N D,Fe	$0.08 < x < 0.7$ $0.2 < x < 0.7$	26-200 46-200	[36]
CERN-BCDMS	μ	280	D,Fe	$0.07 < x < 0.65$	14-200	[37]
CERN-EMC NA2$'$	μ	100-280	D,C,Cu,Sn	$0.03 < x < 0.6$	4-40	[38, 39]
CERN-EMC NA28	μ	280	D,C,Ca	$0.003 < x < 0.1$	0.3-3.2	[40]
FNAL-E665	μ	490	D,Xe	$5 \times 10^{-5} < x < 0.25$	0.01-60	[41, 42]
CERN-WA25,WA59	$\nu,\bar{\nu}$	15-160	D,Ne	$0.01 < x < 0.6$	0.05-30	[56, 57]
FNAL-E772	p	800	D,Xe	$0.03 < x < 0.3$	16-81	[61]

Table 1.1: Main parameters of some of the quoted experiments on shadowing and the EMC effect

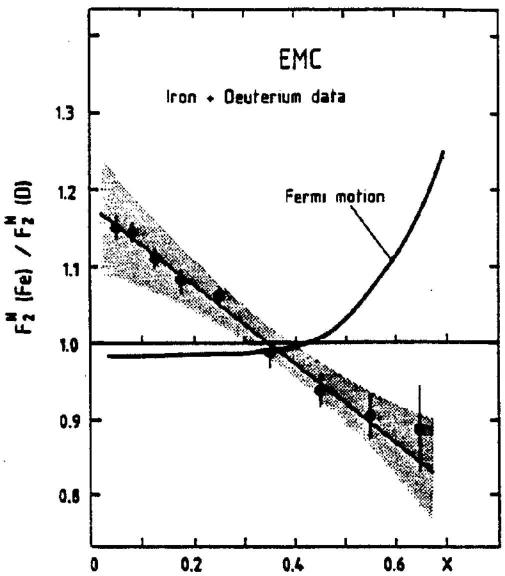

Figure 1.8: The ratio F_2^{Fe}/F_2^D as originally measured by EMC [14]. The shaded area indicates the size of the systematic errors. An additional ±7% normalization uncertainty is not included in the errors. The behavior expected from Fermi motion is also shown (from [14])

1.2.3 Experimental Review

The EMC NA2 experiment which discovered that the bound to free nucleon structure function ratio is not what is expected from Fermi motion had been designed to measure absolute structure functions and their Q^2 evolution. The measurement of the iron to deuterium structure function ratio was not included in its experimental program: it was only as a check of the Fermi motion corrections to be applied to the data that such ratio was initially evaluated.

The result, together with the expected behavior from Fermi motion effects, is shown in fig. 1.8; the theoretical expectations and the data are in clear disagreement. We will comment on this figure more in detail below; we only mention here that the iron and the deuterium data had been collected with different beam energies, intensities, target arrangements and triggers. This is the cause of the rather large systematic errors. Much of the effort of the experiments that followed the EMC results was spent in reducing these errors and extending the kinematic range covered.

A few months after the publication of the EMC ratio, similar results were obtained at SLAC [30, 31]. They were obtained from the reanalysis of empty-target data from two experiments carried out in the first half of the 1970's to measure the hydrogen and deuterium structure functions. Since the liquid hydrogen and deuterium had been contained in aluminum and iron vessels, the empty target data – originally taken for background studies only – made it possible to measure the aluminum and iron cross sections and compare them with the deuterium one.

The EMC data were mostly at large Q^2, while the SLAC ones covered a region of much smaller Q^2. In spite of the different kinematic conditions, the results were in good agreement in the region of overlap in x. This stimulated the experimental community to further investigate the phenomenon.

Between 1983 and 1985 three experiments were carried out in order to study the EMC effect in different kinematic ranges:

- The E139 experiment at SLAC [35], which used electrons up to 20 GeV and covered the small Q^2 region (< 15 GeV^2). Cross sections were measured on nine different target materials, from deuterium to gold.
- The NA4 experiment at CERN [36, 37] (BCDMS collaboration), which used 280 GeV muons and covered the very large Q^2 region, from 14 up to 200 GeV^2. Measurements were carried out on deuterium, nitrogen and iron targets.
- A new experiment by the EMC, NA2′ [38, 39], with deuterium, carbon, copper and tin targets, using muon beams with energies from 100 to 280 GeV. The intermediate Q^2 region was covered, $4 < Q^2 < 40$ GeV^2.

These experiments were designed with the goal of minimizing the systematic errors in the measurement of cross section ratios: the data on the different materials were taken very close in time, exchanging the targets frequently, or even with all target materials in the beam simultaneously. The experimental conditions under which the data were collected were in all cases kept as similar as possible.

The results of SLAC E139 and BCDMS agreed with the original EMC NA2 ones for x larger than 0.3. There was however some confusion concerning the low x region. Here the EMC NA2 ratios were much higher than the SLAC E139 ones. The BCDMS data were in between and could not solve the issue (see right part of fig. 1.13, below).

It was speculated that the differences might originate from a Q^2 dependence of the ratio in the low x region or from a dependence of $R = \sigma_L/\sigma_T$ on A. In the latter case, as discussed below, cross section ratios (as measured by SLAC E139) and structure function ratios (as measured by EMC NA2 and BCDMS) would not be equal.

The EMC NA2′ data clarified the problem (fig. 1.14, below). The structure function ratios at low x were indeed shown to be much lower than those initially measured by NA2 and the ratio appeared to become smaller than unity for $x < 0.1$.

The agreement with SLAC E139 was at this point satisfactory. This was of deeper relevance than the clarification of an experimental dispute. It confirmed that there was no significant Q^2 dependence in the EMC effect, since the average Q^2 of the EMC NA2′ data was much larger than that of the SLAC E139 ones. Furthermore, the fact that the ratio was lower than unity at small x indicated that shadowing persisted at high values of Q^2.

That shadowing does not depend significantly on Q^2 was confirmed by the EMC NA28 experiment [40], also using 280 GeV muons but covering the very low x (down to 3×10^{-3}) and Q^2 region (between 0.3 and 3 GeV^2). The experiment had been conceived before the discovery of the EMC effect, and was intended to carry out a systematic investigation of shadowing.

The combination of these data with the EMC NA2′ and the SLAC E139 ones at higher x provided finally a consistent experimental picture of nuclear effects in DIS, in which shadowing and the EMC effect join smoothly in the region of $x \approx 0.2$ and there is little dependence on Q^2.

About at the same time another SLAC electron experiment, E140 [43], measured the difference of $R = \sigma_L/\sigma_T$ in e-D, e-Fe, and e-Au scattering. The results were consistent with no dependence of R on A, lending experimental support to the identification of cross section and structure function ratios.

Means other than the deep inelastic scattering of electrons or muons have been used to investigate the effects of the nuclear environment on the nucleon structure functions:

- Experiments with neutrino beams are able to discriminate between sea and valence quarks, and are therefore potentially very interesting. Unfortunately such experiments are affected by large uncertainties and so far no single experiment could by itself confirm the effect. Just to mention one problem, while several hundred thousand events after cuts are not uncommon for a charged lepton scattering experiment, the largest number of events accumulated by a neutrino experiment is about 40,000.
- Drell-Yan experiments are sensitive to the anti-quark distribution in the nucleon. In one of them shadowing effects similar to those seen in DIS have been observed.

We shall now examine the available experimental results in more detail, following an approximately chronological order. For a summary of the main parameters of the experiments described, see table 1.1.

The Early Results: EMC NA2 and the SLAC Reanalysis

The ratio of the iron to the deuterium structure function was originally evaluated by the EMC (NA2) [14] as a direct check of the procedure used to correct for Fermi motion the structure functions obtained from heavy targets. The results were thus expected to resemble the curves shown in fig. 1.5.

For iron, the F_2 data obtained with beam energies of 120, 200, 250 and 280 GeV [28] were used. For deuterium, data at 280 GeV only were available [29]. Note that the Fe and D measurements were taken under different experimental conditions and at different times.

The iron data were corrected for the non-isoscalarity of $^{56}_{26}$Fe; neither of the data-sets was corrected for Fermi motion. Only data points with a total systematic error of less than 15% were used for the ratio.

The kinematic region covered is limited by the extent of the deuterium data. The x range extends from $x = 0.05$ to $x = 0.65$. The Q^2 range is different for each x value and varies from 9 to 27 GeV^2 for $x = 0.05$, from 11.5 to 90 GeV^2 for $x = 0.25$ and from 36 to 170 GeV^2 for x=0.65.

The results are presented in fig. 1.8 as a function of x, together with the behavior expected from Fermi motion calculations. The disagreement between experiment and theoretical expectations is quite striking. No significant Q^2 dependence was observed.

The EMC measurement was subsequently confirmed by a reanalysis of data taken ten years earlier by the SLAC experiments E87 [30] and E49B [31], a remarkable example of archaeology in high energy physics. The experiments had been designed to extract the proton and the neutron structure functions; their results had been initially published in 1973 for E49B [32] and in 1974 for E87 [33]. The data had been collected using electron beams with energies ranging between between 9 and 20 GeV for E87, 4.5 and 20 GeV for E49B.

After the EMC discovery the deuterium events were compared with those originating in the deuterium vessel walls, made of steel in the case of E87 and of aluminum in that of E49B. The kinematic range covered is $0.25 < x < 0.9$, $3 < Q^2 < 20$ GeV^2 for E87 and $0.075 < x < 0.86$, $2 < Q^2 < 20$ GeV^2 for E49B. The resulting cross section ratios are shown in fig. 1.9 (full symbols), together with the EMC data and the photo-production results [20]. The results of the SLAC experiment E61 [24] (labelled "SLAC") on shadowing are also shown; this experiment

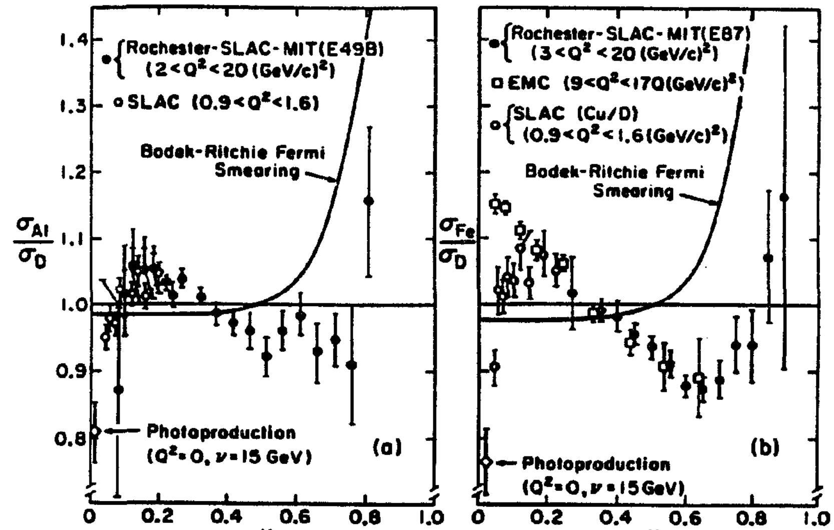

Figure 1.9: (a) The ratio σ^{Al}/σ^{D} from SLAC E49B (full symbols); (b) the ratio σ^{Fe}/σ^{D} from SLAC E87 (full symbols). For an explanation of the other symbols, see text (from [31])

was carried out in the 1970's with electrons up to 20 GeV and covered the range 0.1 GeV^2 < Q^2 < 1.8 GeV^2 (targets: H, D, Al, Be, Cu, Au),

The EMC result was also confirmed indirectly by the BFP collaboration [34], which found their F_2 extracted from muon-iron data to agree, apart from a 5% normalization shift, with the EMC iron results [28].

The Second Generation of Experiments: SLAC E139, BCDMS and EMC NA2′

The first experiment specifically designed to study the EMC effect was SLAC E139 [35], which took data in the range $0.09 < x < 0.9$ and 2 GeV^2 < Q^2 < 15 GeV^2 on deuterium and He, Be, C, Al, Ca, Fe, Ag, Au targets. Electron beams with energies ranging from 8 to 24.5 GeV were used in conjunction with the SLAC 8 GeV spectrometer. The experimental set-up did not allow simultaneous measurements with several targets, but the deuterium and the heavy targets were frequently exchanged in order to minimize systematic errors.

The cross section ratios σ^A/σ^D found by this experiment are presented in fig. 1.10. The figure also shows the original EMC NA2 results [14], those of the SLAC E49B [31] and E87 [30] experiments (labelled "Bodek *et al.*"), just described, as well as those of two experiments on shadowing: SLAC E61 [24] (labelled "Stein *et al.*"), mentioned above, and the FNAL muon experiment [27] also already quoted before (labelled "Goodman *et al.*").

While the original EMC NA2 results are again confirmed for $x > 0.3$, the two data-sets rather clearly disagree at lower values of x, the EMC points being systematically higher – by up to 15% – than the SLAC ones.

In the E139 results Fermi smearing is apparent at large values of x. These are in fact the only data in which the Fermi motion behavior is clearly visible.

Figure 1.11 shows the A dependence of the EMC effect as measured by SLAC E139: at fixed x a weak dependence of the cross section ratio is observed; it can be parametrized as $\sigma^A/\sigma^D = cA^\alpha$.

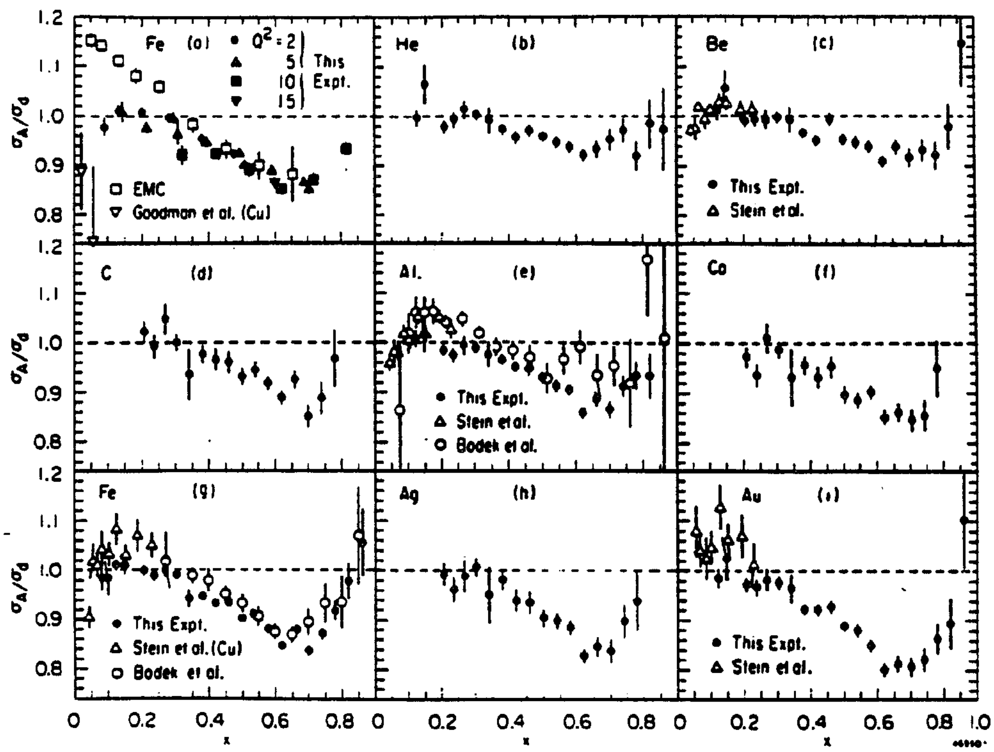

Figure 1.10: The ratios σ^A/σ^D from SLAC E139 (from [35]). For an explanation of the symbols see text

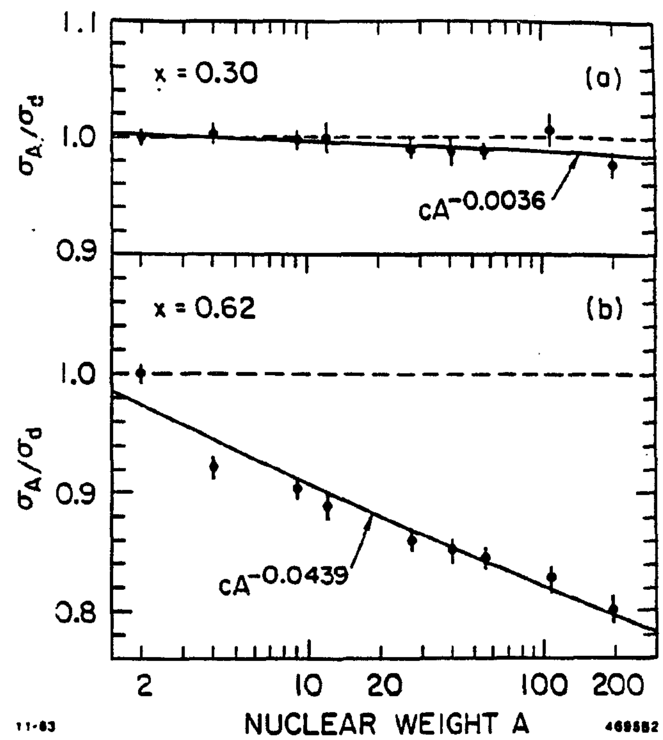

Figure 1.11: The ratios σ^A/σ^D from SLAC E139 as a function of A at fixed x (from [35])

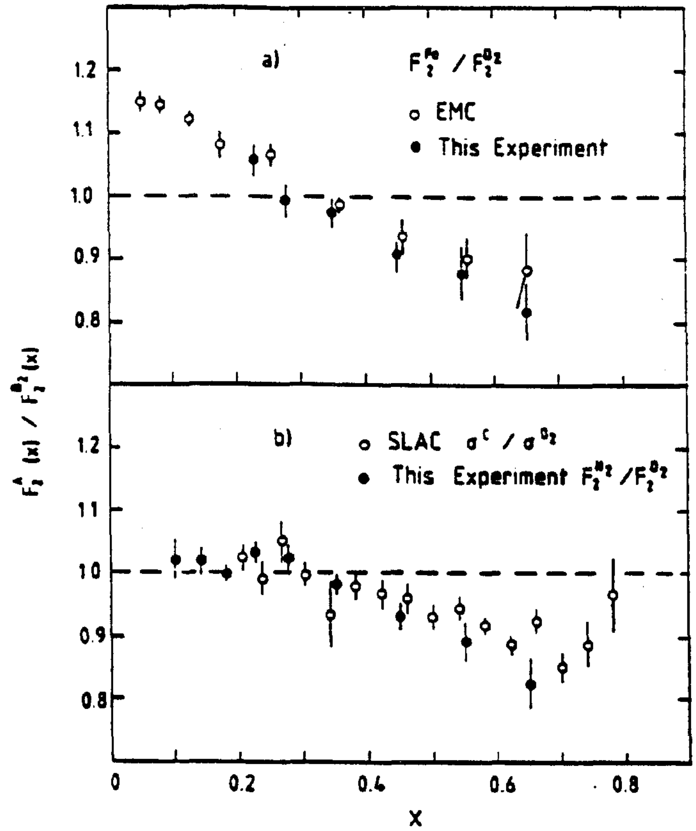

Figure 1.12: The ratios F_2^{Fe}/F_2^D and F_2^N/F_2^D measured by BCDMS (from [36])

At CERN the EMC results were later confirmed by the BCDMS collaboration (experiment NA4), which used a 280 GeV muon beam, the same as that of EMC. The apparatus consisted of an instrumented iron toroid with large acceptance for high Q^2 events. Data were taken with two target materials simultaneously in the beam, thus minimizing systematic errors from uncertainties on the energy calibration of incoming and scattered muons, on the detector efficiencies and on the beam flux measurements.

Two sets of measurements were carried out. In the first one [36] the target pairs simultaneously in the beam were Fe/D and Fe/N. The ratios of the nitrogen and iron to the deuterium structure functions were measured in the range $0.08 < x < 0.7$ and $0.2 < x < 0.7$, respectively. The Q^2 range covered is 26 to 200 GeV^2 for the F_2^N/F_2^D data and 46 to 200 GeV^2 for the F_2^{Fe}/F_2^D ones. The results are shown in fig. 1.12 together with the original EMC NA2 ones [14] for F_2^{Fe}/F_2^D and those, just presented, from SLAC E139 [35] for σ^C/σ^D.

The same collaboration later published a high statistics study of F_2^{Fe}/F_2^D over a wider x and Q^2 region [37]. The range covered was $0.07 < x < 0.65$ and $14 < Q^2 < 200$ GeV^2. The results are shown in fig. 1.13 and are compared with the earlier BCDMS ones [36] (open circles) and with those of the EMC NA2 [14], SLAC E139 [35] (labelled "Arnold *et al.*") and SLAC E61 [24] experiments (labelled "Stein *et al.*").

The BCDMS results were explicitely obtained as ratios of structure functions: the measured yields were first converted to cross sections, after correcting for acceptance, detector efficiencies

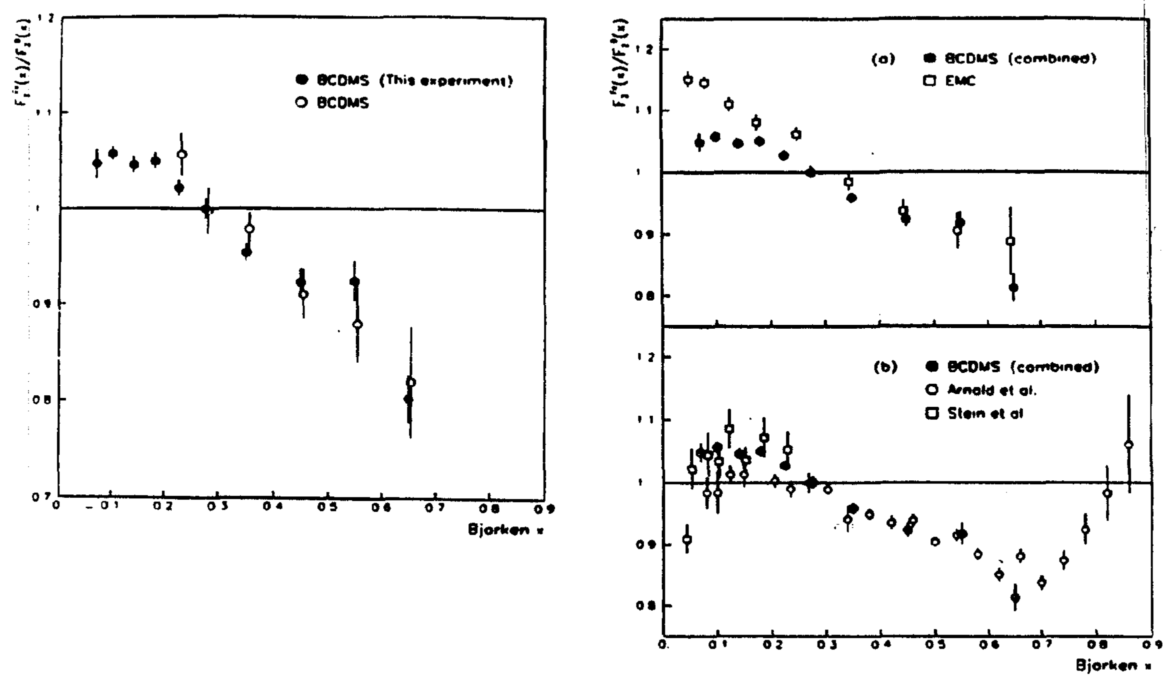

Figure 1.13: The ratio F_2^{Fe}/F_2^D measured by the BCDMS collaboration. The original EMC results [14] (labelled "EMC") are also shown, as well as those from SLAC E139 [35] (labelled "Arnold *et al.*") and SLAC E61 [24] (labelled "Stein *et al.*") (from [37])

etc., and then to structure functions.

The BCDMS data agree with the EMC NA2 and SLAC E139 ones at large x. For $x < 0.2$ they indicate a ratio lower than that originally measured by EMC but still above the E139 points, thus leaving open the question of the behavior of the EMC effect at small x. No Q^2 dependence is visible over the measured range.

The EMC collaboration itself engaged in 1984 and 1985 in two series of new measurements within the NA2′ experiment.

For the first measurement [38], data were taken on deuterium, carbon, copper and tin targets. The geometry of the targets was similar and they were frequently interchanged under the same beam and spectrometer conditions. Spectrometer acceptance corrections were the same for all targets and thus canceled in the ratio. Also, the effects of time dependent inefficiencies in the spectrometer and in the beam intensity monitoring apparatus could to a large extent cancel out.

The results are shown in fig. 1.14 with full circles. Data were taken at different beam energies, ranging from 100 to 280 GeV. The kinematic range covered is $0.03 < x < 0.6$ and $4 < Q^2 < 40$ GeV^2.

For the second measurement [39], data were taken with deuterium and copper targets simultaneously in the beam. Both targets were therefore exposed to the same beam flux and the ratios were thus free of normalization uncertainties due to the beam flux measurement. Acceptance corrections were instead different for each target, since the acceptance varied as a function of the target position. The kinematic range is similar to that covered by [38]. The results are shown in fig. 1.14 with open circles.

The EMC NA2′ data agree with the previous high Q^2 results (the original EMC NA2 one [14], and the BCDMS ones [36, 37]), at large x. The new results indicate however a turning over of the ratio at low x, similar to that observed by the lower energy experiment SLAC E61, mentioned above, thus providing the first clear evidence that shadowing persists also at considerable values of Q^2. This was largely unexpected because shadowing was believed – according to VMD – to disappear quickly for $Q^2 > 1$ GeV^2.

The Shadowing Region: the EMC NA28 and the E665 Results

A rather clear confirmation of the fact that shadowing depends only weakly – if at all – on Q^2 came from another EMC experiment: NA28.

In this experiment a special low angle trigger system was used, which was capable of selecting events where the muon was scattered at very small angles, down to 2 mrad. The beam energy was 280 GeV. Data were taken with deuterium, carbon and calcium targets. Structure functions were extracted for each target individually and then ratios were taken.

The ratios of the carbon and calcium to deuterium structure functions were measured in the range $0.003 < x < 0.1$ and $0.3 < Q^2 < 3.2$ GeV^2 [40].

The results are presented in fig. 1.15 as a function of x in different Q^2 bins. No Q^2 dependence is visible in the data. The same results, integrated over Q^2, are shown in fig. 1.16; statistical and systematic errors are summed in quadrature in this figure.

The large systematic errors are a consequence of the uncertainty in the trigger efficiency and of fact that the targets were not simultaneously in the beam, nor at the same position: both the uncertainty on the flux and that on the acceptance had thus to be taken into account.

The figure also shows the results of other lepto-production experiments discussed before: EMC NA2′ [38] (labelled "Ashman"), BCDMS [36, 37] (labelled "Bari" and "Benvenuti"),

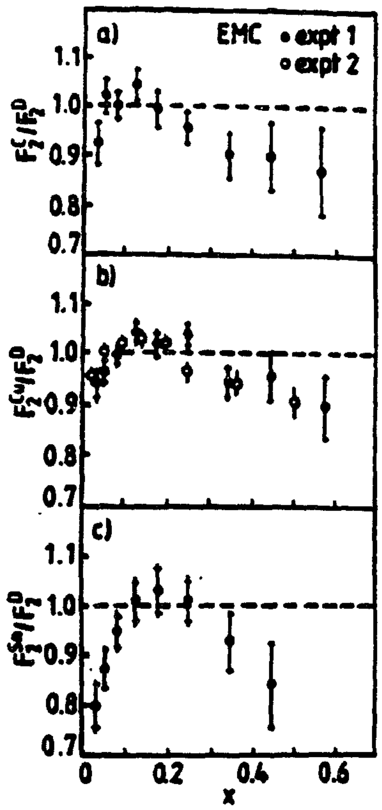

Figure 1.14: The ratios σ^C/σ^D, σ^{Cu}/σ^D and σ^{Sn}/σ^D measured by the EMC NA2′ experiment (full symbols from [38], open symbols from [39])

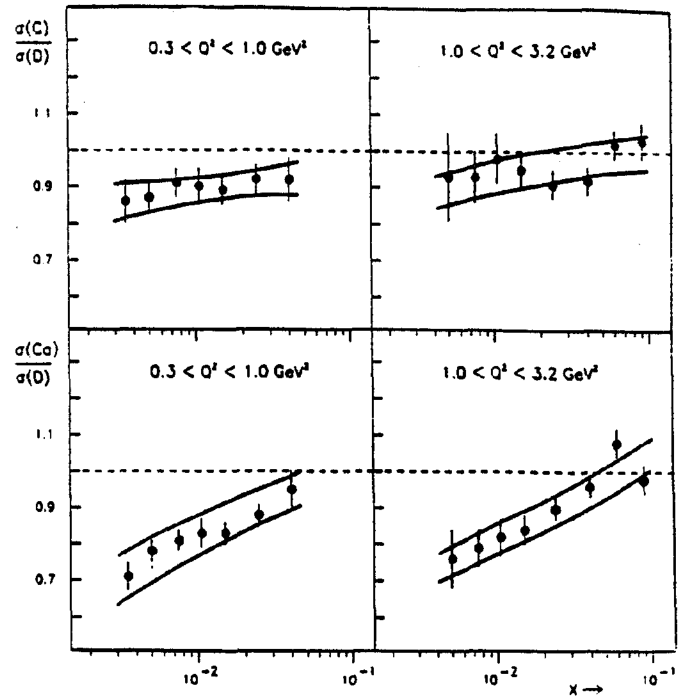

Figure 1.15: Results of the EMC NA28 experiment for σ^C/σ^D and σ^{Ca}/σ^D. The bars give the statistical errors and the solid lines indicate the size of the systematic errors. A $\pm 7\%$ normalization uncertainty is not included (from [40])

SLAC E61 (labelled "Stein") and the FNAL muon experiment [27] (labelled "Goodman"). For the latter the x values of the points were computed by dividing the published Q^2 values by $2M\nu$ using $\nu = 150$ GeV, an average value in the acceptance region of the experiment ($110 < \nu < 200$ GeV for $Q^2 < 3$ GeV^2 and $40 < \nu < 200$ GeV for $Q^2 > 3$ GeV^2). The points on the vertical axis are ratios from the real photo-production experiment quoted above [21], where the energy of the photon beam was 60 GeV.

Recently preliminary results from the muon scattering experiment E665 at the FNAL tevatron on the ratio of xenon ($A = 131$) to deuterium cross sections were presented [41]. The beam energy was in this case 490 GeV; the data cover the range $0.001 < x < 0.25$ and $0.1 < Q^2 < 20$ GeV^2. The results are shown in fig. 1.17 as a function of x and Q^2. No significant Q^2 dependence is visible in these data either and the observed x dependence agrees with that measured by NA28.

Figure 1.18 shows the results of a different analysis of the E665 data [42], in which the x and Q^2 range were extended to lower values: $5 \times 10^{-5} < x < 0.2$ and $0.01 < Q^2 < 60$ GeV^2. Radiative events in which the muon radiates a photon and elastic μ-e scattering events were rejected by using the information of an electromagnetic calorimeter. The remarkable feature of these data is that the ratio of the xenon to the deuterium cross section appears to saturate for x values lower than $\approx 10^{-3}$.

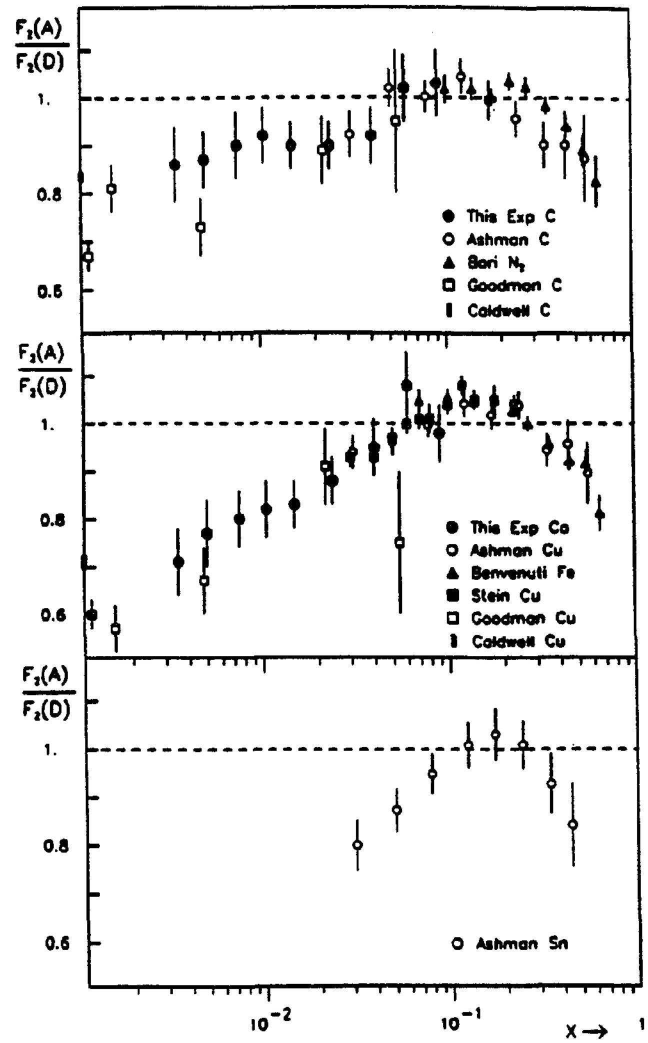

Figure 1.16: The EMC NA28 results of fig. 1.15 integrated over Q^2, together with a compilation of other lepto-production and photo-production experiments. Statistical and systematic errors (where available) are added in quadrature. The $\pm 7\%$ normalization uncertainty of the EMC NA28 data is not included. See text for an explanation of the symbols (from [40])

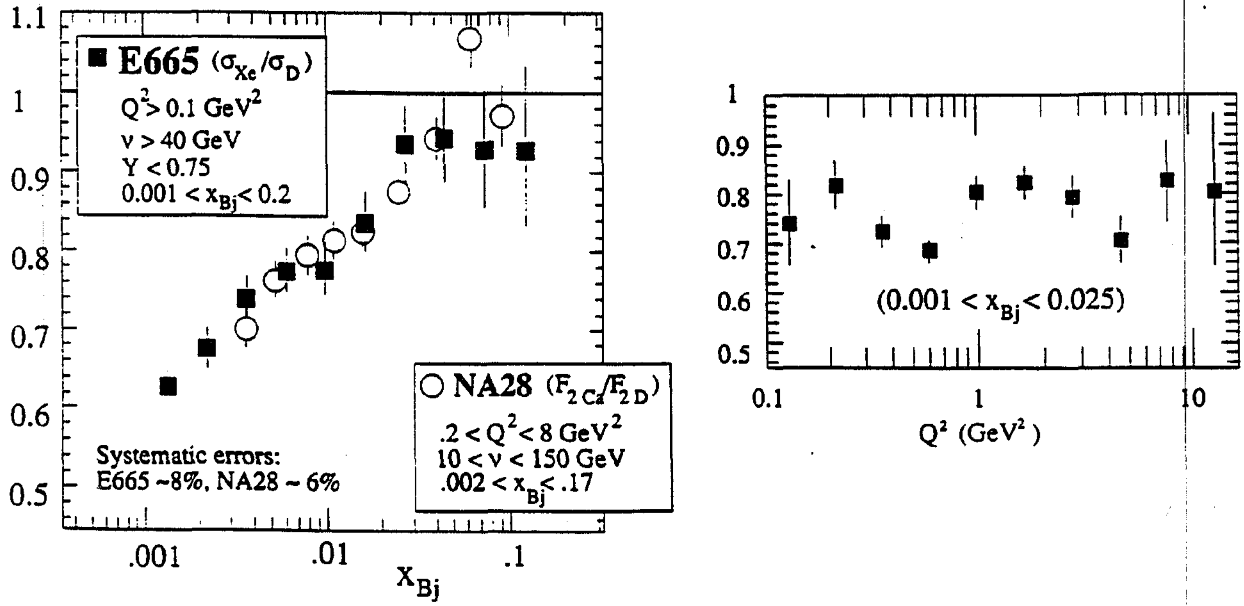

Figure 1.17: Preliminary results for the Xe to D cross section ratio from the FNAL experiment E665 [41] as a function of x and Q^2. The NA28 results [40] are also shown (from [41])

Nuclear Effects on $R = \sigma_L/\sigma_T$

We have mentioned that some experiments have measured cross section ratios rather than structure function ratios. The two ratios are the same as long as $R = \sigma_L/\sigma_T$ is the same for different target materials. This can be seen by rewriting relation 1.10 for a nuclear target A and for D, and then taking the ratio.

The SLAC experiment E140 published in 1988 results of a measurement of R on deuterium, iron and gold targets in the kinematic range $0.2 < x < 0.5$ and $1 < Q^2 < 5$ GeV^2 [43, 44], using the SLAC electron beam with energies between 4 and 20 GeV. While providing the first clear evidence of a fall-off of R with increasing Q^2 [45]-[47], the results demostrate that $R^A - R^D$ is consistent with zero; the average value of $R^A - R^D$, for A=Fe and Au is $< R^A - R^D >=$ 0.001 ± 0.018 (statistical) ± 0.016 (systematic). Figure 1.19 shows $R^A - R^D$ as a function of x.

Nuclear effects seem therefore to affect the structure functions F_2 and F_1 in the same way and to cancel in R, at least in the kinematic range covered by E140.

Present Status of the x Dependence

Figure 1.20 presents a compilation of results on the EMC effect covering a wide x and Q^2 range. Data from the SLAC experiment E140 [43], designed to investigate the A dependence of $R = \sigma_L/\sigma_T$ and just discussed, are also included as well as the results of a reanalysis of the E139 data for Fe/D using an improved radiative corrections procedure (the ratio is now higher by about 1% with respect to that presented in fig. 1.10 for $x < 0.25$). The results of the E139 reanalysis were also published in [43].

Figures 1.16, 1.18 and 1.20 summarize the experimental status of the x dependence of

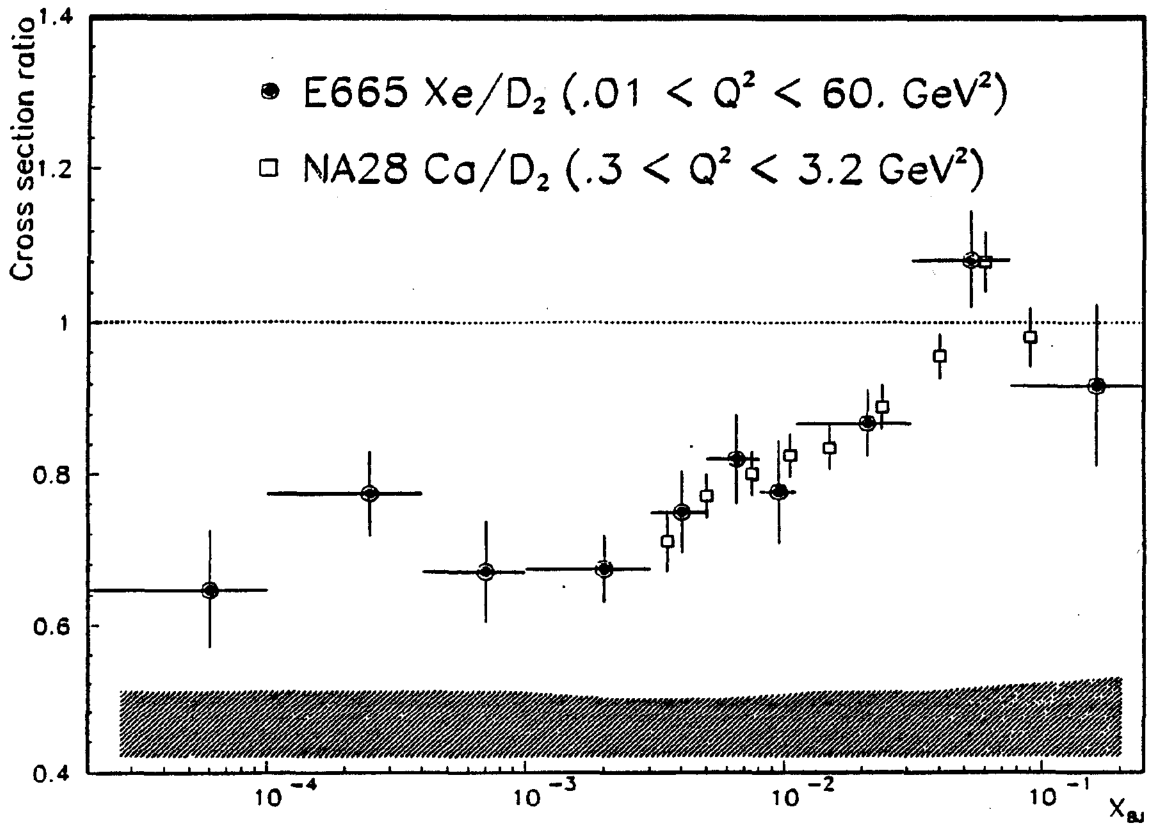

Figure 1.18: Preliminary results for the Xe to D cross section ratio from the FNAL experiment E665 [42] as a function of x. The shaded band indicates the size of the systematic errors. The NA28 results [40] are also shown (from [41])

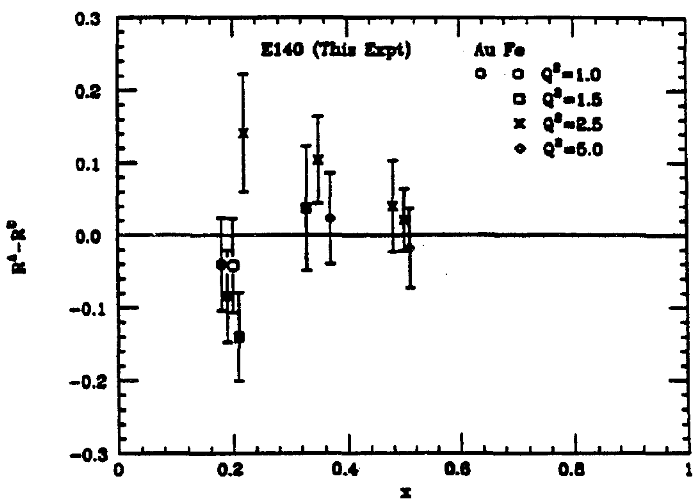

Figure 1.19: Results of the SLAC E140 experiment on $R^{Fe} - R^{D}$ and $R^{Au} - R^{D}$ [43] (from [44])

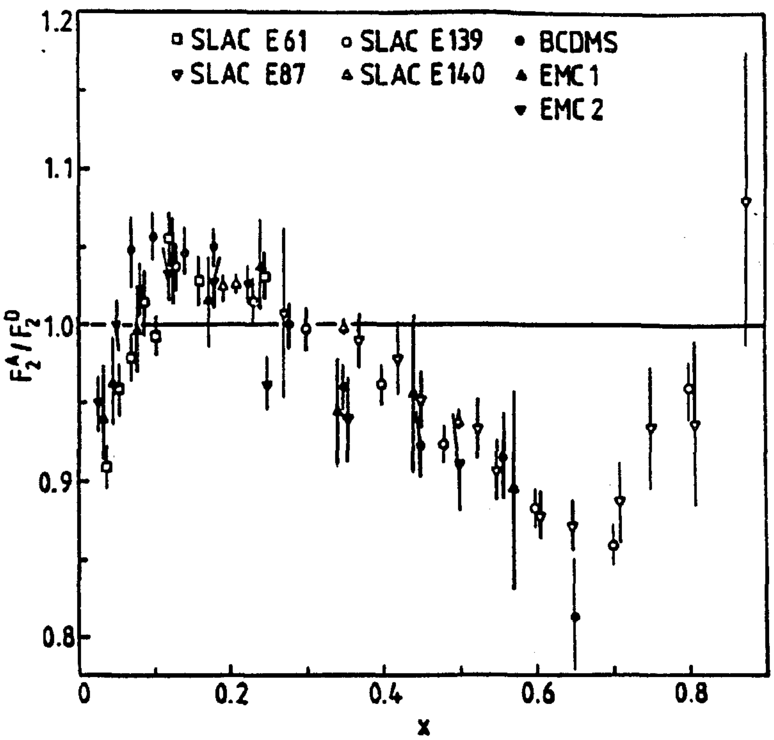

Figure 1.20: Compilation of results on the x dependence of the EMC effect for Fe and Cu: SLAC E61 [24], SLAC E87 [30], SLAC E139 [35], SLAC E140 [43], BCDMS [37], EMC NA2' [38] (labelled "EMC1") and [39] (labelled "EMC2")

nuclear effects in DIS before the NMC results.

The situation can be described as follows:

1. For $x < 0.1$ the ratio shows a significant depletion with respect to unity, regardless of Q^2. The size of the depletion increases with A. For $x < 10^{-3}$ saturation effects have possibly been observed.

2. The ratio becomes positive at $x \approx 0.05$-0.1. The x value at which the crossing occurs appears to be weakly A dependent, shifting from about $x = 0.05$ for carbon to $x = 0.1$ for tin.

3. For $0.1 < x < 0.3$ the effect is substantially reduced as compared with the original EMC NA2 data (but consistent with them within the quoted systematic errors). In this region the data indicate a few per cent enhancement of F_2^A with respect to F_2^D (sometimes referred to as "anti-shadowing"). The accuracy of the data does not permit to establish if there is an A dependence of the ratio in this region.

4. The structure function ratio decreases linearly for x between 0.3 (where it becomes again smaller than one) and 0.6. The dip around $x = 0.6$ becomes more pronounced as A increases (with approximately a $\ln A$ dependence). The position of the dip is however independent of A.

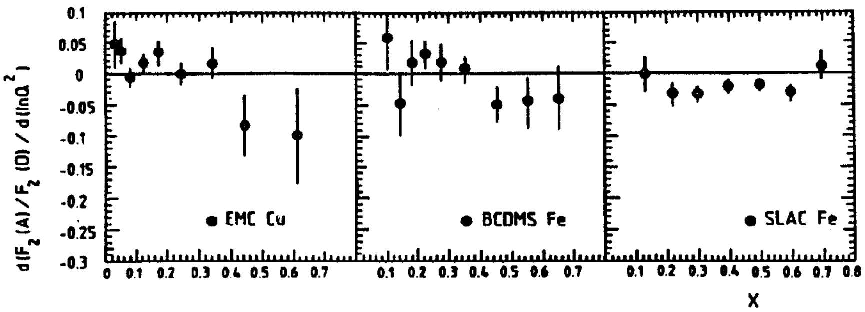

Figure 1.21: The logarithmic slopes $d(F_2^A/F_2^D)/d(\ln Q^2)$ from: EMC Cu/D [39], BCDMS Fe/D [37] and SLAC E139 Fe/D [35]

5. For $x > 0.6$ the ratio rises again, as expected from Fermi motion effects.

Present Status of the Q^2 Dependence

Figure 1.21 shows the slopes $b = d(F_2^A/F_2^D)/d(\ln Q^2)$ extracted from different experiments: EMC NA2′ [39] (on Cu and D), BCDMS [37] and SLAC E139 [35]. Only statistical errors were used to determine the slopes.

Both the EMC NA2′ and the BCDMS data are consistent with no Q^2 dependence; taken together, however, they show a similar trend with the slopes being positive for $x < 0.4$ and then turning to negative values. The SLAC E139 data give negative slopes $d(F_2^A/F_2^D)/d(\ln Q^2) \approx -0.02$ over a wider x range, from about $x = 0.2$ to $x = 0.6$.

The slopes b were not extracted from the BCDMS and SLAC data by the respective collaborations but appeared later as the result of the analysis of a member of the EMC collaboration [39].

At smaller x no indication of Q^2 dependence is present; see also figures 1.15 and 1.17.

Direct Measurements of the Gluon Distributions in Nuclei: J/ψ Production

An entirely different way to investigate nuclear effects in deep inelastic scattering of charged leptons is to probe the gluon distribution of different targets directly. This can be done by studying the inelastic production of charmed states.

Inelastic charm-anti-charm production is assumed to proceed according to the photon-gluon fusion mechanism [48] (fig. 1.22) in which the virtual photon couples to a gluon in the target via a charmed quark. The charm production cross section is therefore directly proportional to the gluon density in the nucleon.

The total cross section for inclusive J/ψ photo-production (extrapolated to Q^2=0) was measured by the EMC in hydrogen, deuterium and iron targets [49]. The ratio of iron to hydrogen and deuterium cross sections was found to be larger than unity, indicating an enhancement of the iron gluon distribution by 1.44 ± 0.12 (stat.) $\pm$ 0.20 (syst.) with respect to the H and D ones.

The experiment E691 [50], carried out at the FNAL photon beam, however produced results in contradiction with those of EMC and rather indicating a depletion of the photo-production cross section on iron compared to that on a free nucleon.

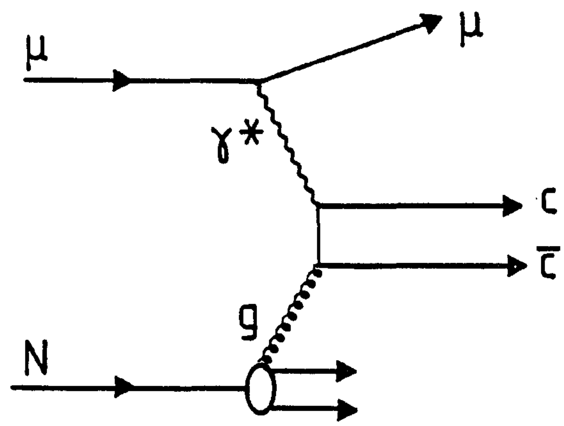

Figure 1.22: The photon-gluon fusion mechanism

The discrepancy between the two results – unresolved so far – shows that the method, although interesting, is not free of significant systematic uncertainties. One of the major difficulties in its application lies in the separation of the inelastically produced J/ψ's from those produced coherently off the whole nucleus or off a single nucleon.

Neutrino Scattering Results

Deep inelastic neutrino scattering is in principle an ideal tool to investigate the EMC effect as it may allow the behavior of the sea and valence quarks to be separated experimentally. The statistical significance of neutrino experiments is however poor and no individual experiment [51]-[56] could so far, by itself, confirm the effect.

In fig. 1.23 we show the results of a recent high statistics experiment carried out at the CERN bubble chamber BEBC by the WA25 and WA59 collaborations [56]. It represents the state of the art in the measurement of nuclear effects in neutrino DIS interactions. The ratios of the neon ($A = 20$) to deuterium cross sections are shown as a function of x and y for the neutrino, the anti-neutrino and the combined data samples. The results of the SLAC electron experiment E139 [35] for σ^{Al}/σ^{D} are also shown.

The following observations can be made on these data:

1. The ratio of the x distributions for $0.2 < x < 0.6$ is similar to that measured in charged lepton DIS.

2. The ratio of the y distributions measures the difference in the sea quark distribution relative to the valence one, averaged over x. The data indicate that the shape of the sea quark distribution is the same for Ne and D; they suggest however that the normalization of the distribution is smaller in Ne than in D by about 10-15% ± 5-10%.

3. For $Q^2 > 1$ GeV^2 no Q^2 dependence is visible in the measured ratios.

4. Finally, the total neutrino cross sections on neon and on deuterium turn out to be the same at the 4% level. This indicates that, within 4%, the integral gluon momentum

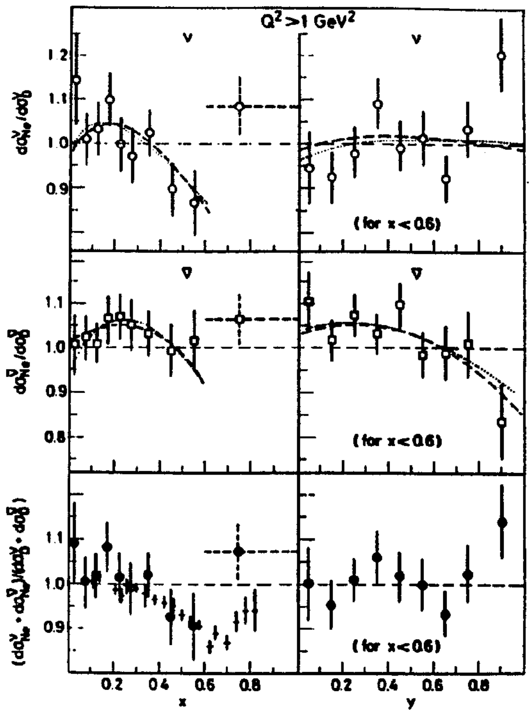

Figure 1.23: The ratios of the neon to deuterium cross sections as a function of x and y for the neutrino, the anti-neutrino and the combined data samples. The SLAC E139 electron results [35] for σ^{Al}/σ^{D} are also shown as crosses (from [56])

fraction, as well as the integral quark momentum fraction, is the same in neon and deuterium.

The same experiment also investigated shadowing effects in neutrino and anti-neutrino interactions on neon and deuterium [57].

Similarly to virtual photons, $W^{\pm}$ bosons may fluctuate into a virtual hadron system composed of vector and axial-vector mesons. Partial Conservation of Axial Current (PCAC) [58] also predicts a pion contribution to the propagator of the weak current; this contribution is important for $Q^2 < 0.2$ GeV^2. For larger values of Q^2, the vector (ρ) and axial-vector (a_1) contributions become dominant.

Figure 1.24 presents the measured ratio of the neon to deuterium cross sections for $x < 0.2$ as a function of Q^2 for the neutrino, the anti-neutrino and the combined data samples. Figure 1.25 shows the x dependence of the ratio for the combined neutrino and anti-neutrino data in different Q^2 bins. The full curves represent the predictions derived from PCAC. It is clear that the cross section in neon is indeed depleted relative to that in deuterium at low Q^2. This is the first evidence of shadowing in neutrino interactions.

Recently a new method to investigate nuclear effects in neutrino interactions was proposed [59]. High energy neutrino interactions in a heavy liquid bubble chamber can be clas-

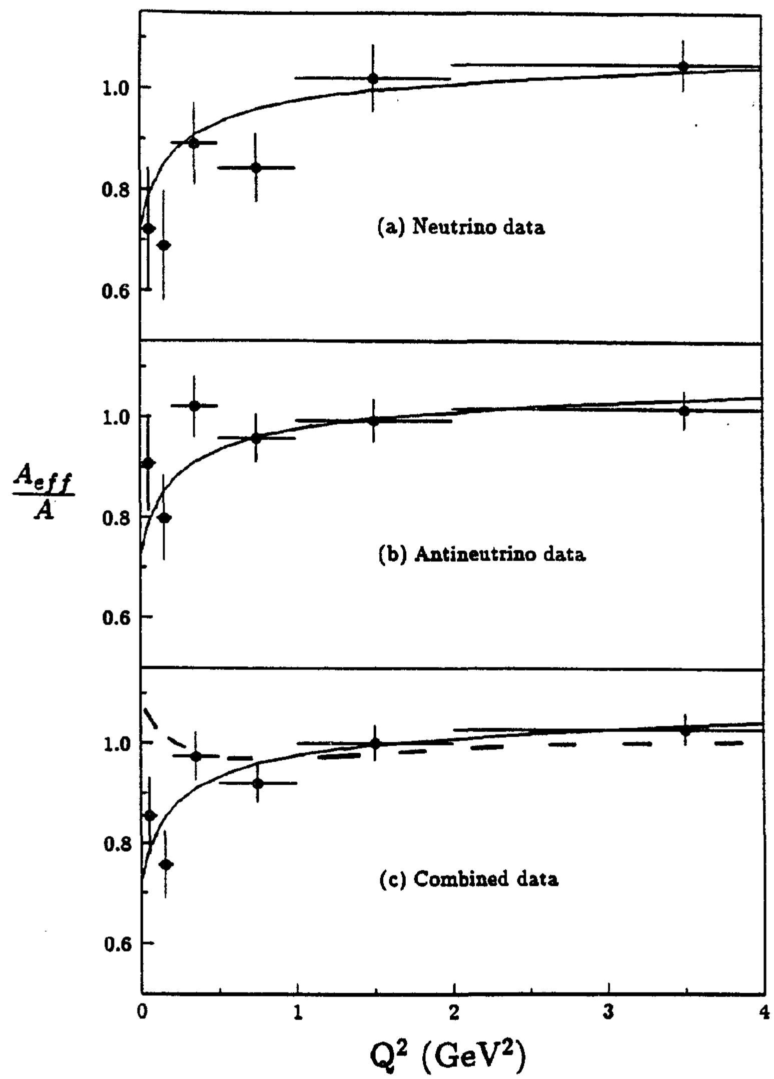

Figure 1.24: The Ne to D cross section ratios for $x < 0.2$ as a function of Q^2 for the neutrino, the anti-neutrino and the combined data samples. The full curves represent the PCAC predictions (from [57])

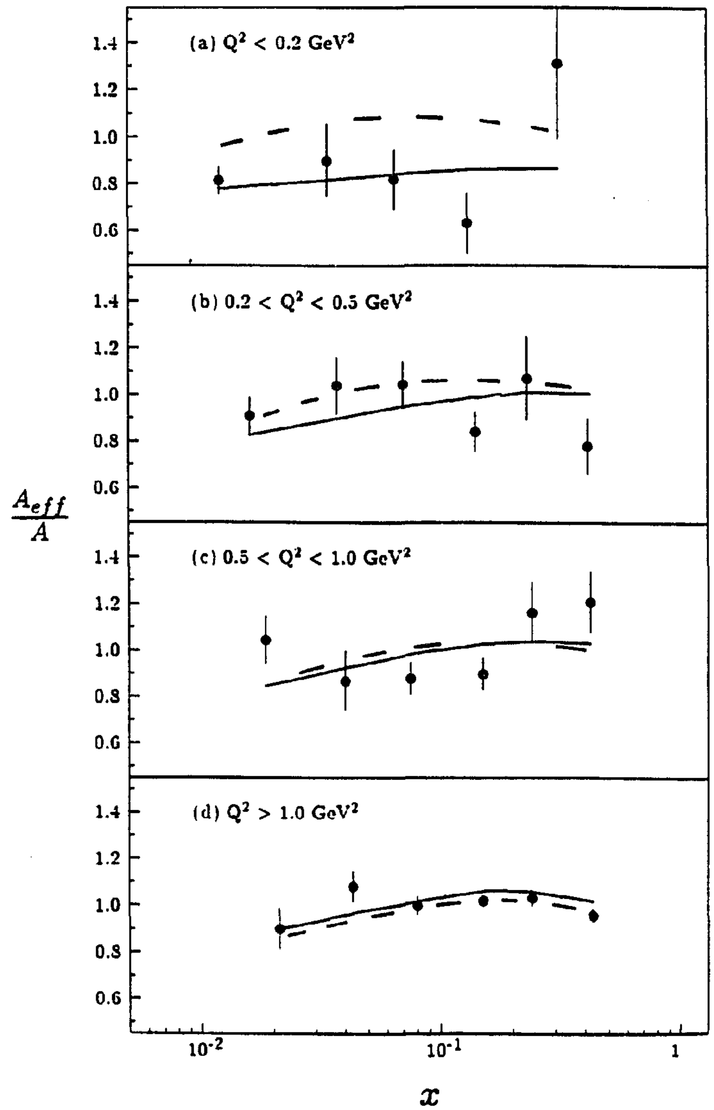

Figure 1.25: The x dependence of the Ne to D cross section ratio for the combined neutrino and anti-neutrino data in different Q^2 bins. The full curves represent the PCAC predictions (from [57])

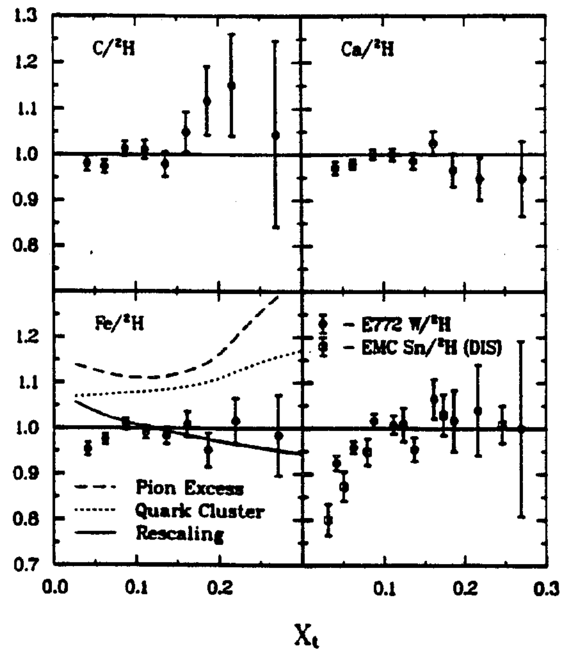

Figure 1.26: Results of the Drell-Yan FNAL E772 experiment [61]

sified by the presence or absence of dark tracks at the interaction vertex. Dark tracks are presumed to be mostly due to slow protons emerging from the target nucleus and may indicate an interaction with a deeply bound nucleon, rather than with a loosely bound one on the surface of the nucleus. Quark distributions can be extracted from the two sets of data and the results compared; those with dark tracks show an enhanced nuclear effect. The method is however not uncontested and there are claims that the effects seen are not correlated to nuclear phenomena and that they may be detected with hydrogen and deuterium targets as well [60].

Nuclear Effects in Drell-Yan Dimuon Production

Continuum dimuon production in high-energy proton-nucleus collisions provides an independent measurement of the modification of the quark distribution in nuclei. For fractional longitudinal momentum $x_F > 0.2$, the dominating mechanism in proton induced Drell-Yan production is the quark-anti-quark annihilation process $q_{proton} + \bar{q}_{target} \rightarrow \mu^+\mu^-$. The dimuon yield is thus proportional to the anti-quark content of the target nucleon.

The FNAL experiment E772 observed a depletion of the dimuon yield in calcium, iron and tungsten targets with respect to deuterium for $0.03 < x < 0.3$ and $Q^2 > 16$ GeV^2 [61]. Figure 1.26 shows the results; the W/D data are compared with the EMC NA2′ ones for Sn/D [38]. The size of the depletion observed is smaller but not inconsistent with the DIS results. Remarkably, no enhancement is visible in the $x \approx 0.1$-0.2 region.

1.3 Theoretical Review

"All models of the EMC effect are wrong, including mine." [62]

As we mentioned several times, the discovery of the EMC effect came as a surprise to both the particle and nuclear physics communities: it was generally thought that the only relevant nuclear effects in DIS could be Fermi motion, at large x, and shadowing at very small x and Q^2. Moreover the nucleon constituents were believed to be largely insensitive to the nuclear environment surrounding them.

It is fair to mention two exceptions, probably the only *pre*-dictions of the EMC effect. In 1975 Nikolaev and Zakharov [177], addressing the problem of shadowing within a parton model framework, explicitely predicted anti-shadowing for $x \approx 0.05$-0.1 and stated – in contradiction with a widespread prejudice – that both shadowing and anti-shadowing should not vary with Q^2. About in the same years, Krzywicki [126], in an attempt to explain some features of inclusive, high p_t pion spectra in proton-tungsten collisions, argued that when the nucleus is probed at very small distances it resembles more closely a single bag of partons than a collection of quasi-free nucleons. Among the consequences of this picture the author mentions "an anomalous nuclear enhancement in the cross section for the deep inelastic lepton scattering at small values of the Bjorken variable".

It was however only after the presentation of the EMC results on the iron to deuterium structure function ratio that the theoretical community seriously begun to study nuclear effects in DIS. In fact intense theoretical effort has been invested since then and several hundred papers have been produced. Originally the interest focused on the intermediate x region, $0.2 < x < 0.6$, where data were available. It gradually shifted to the region of smaller x, especially after the publication of the EMC NA2′ [38] and NA28 [40] results.

In what follows we will attempt to give a survey of the theoretical ideas proposed. We will split the discussion into two parts, examining first the models relevant to the EMC effect in the historical sense of the term, i.e. approximately to the region[1] $0.2 < x < 0.6$, and then those dealing more specifically with shadowing. Although there is some arbitrariness in this distinction, it reflects to a certain extent a difference in the physics on which the models are based.

Several reviews of the theoretical situation exist in the literature. We quote here the ones by Berger and Coester [63], Frankfurt and Strikman [64, 65], Barone and Predazzi [66]. A recent summary of the theoretical situation on shadowing can be found in [65] and [67].

The models of the EMC effect essentially try to explain the apparent softening of the quark distribution in bound nucleons with respect to free ones. They can be broadly classified into two cathegories:

1. "Conventional nuclear physics" models, describing the effect of the nuclear potential on the nucleons by means of a reduced effective nucleon mass, which implies (since $x = Q^2/(2M\nu)$) a shift of x to higher values and thus a softening of the valence distribution. In these models the mass shift is often accompanied by an increased density of virtual pions associated with the nuclear force.

2. Models which require an increase of the quark confinement size in nuclear matter. Because of the uncertainty principle this translates into a reduction of the average quark

[1] This nomenclature is not universally accepted and sometimes the term "EMC effect" is used to label all nuclear effects in DIS.

momentum. In some cases a simple increase of the nucleon radius is assumed. In others quark deconfinement is invoked, with the disappearance of the nucleon degrees of freedom in the nucleus in favor of multi-quark clusters or even quark-gluon plasma.

In the shadowing region the observed depletion of the nuclear to nucleon structure function ratio is generally explained by two types of models:

1. Vector Meson Dominance models in which the virtual photon is seen as fluctuating from a bare photon state to a superposition of vector mesons. These vector mesons interact hadronically with the nucleus and are absorbed mainly by the nucleons on the surface of the nucleus. The inner nucleons are thus "shadowed" by the surface ones and the measured cross section per nucleon is reduced with respect to the free nucleon one.

2. Partonic models in which – at least in their original formulation – shadowing is ascribed to the fact that in the Breit frame low x partons, because of the uncertainty principle, spread over a large longitudinal distance. Partons of different nucleons may thus overlap in space and fuse, thereby reducing the density of low momentum partons and increasing that of higher momentum ones.

In spite of the theoretical efforts made to understand the physics behind the EMC effect and shadowing there is as yet no unique and generally accepted model of these phenomena. Even worse, the models available are in general of modest predictive power and appear difficult to falsify: most often they just offer a description rather than an explanation of the experimental findings. To the high energy physicist spoiled by the successes of the Standard Model this may appear as an awkward situation; it reflects the difficulty of treating a problem which involves many degrees of freedom and in addition is of non-perturbative nature.

Before turning to a more detailed discussion of the models, one more remark is in order. It is generally assumed that, the deuteron being very weakly bound, F_2^D represents the structure function of an ideal isoscalar nucleon and that $F_2^D = 1/2(F_2^p + F_2^n)$. This assumption, uncontested for some time after the discovery of the EMC effect, appears now as not so well founded. Effects of a few per cent may be expected both at low x and in the dip region, around $x \approx 0.6$ [68, 69, 120, 208].

1.3.1 Models of the EMC Effect

The EMC effect indicates that in the region $0.2 < x < 0.6$ the valence quark distribution in bound nucleons is depleted with respect to that in a free nucleon. Several mechanisms have been proposed to produce such softening.

Models based on "conventional" nuclear physics invoke an excess of virtual pions in the nucleus, associated with the nuclear force. The virtual photon can therefore scatter not only on a quark in a nucleon, but also on a quark (or anti-quark) in a pion. Pions can carry a fraction of the nucleon momentum up to $x = M_\pi/M$. An enhancement of the cross section in the region $x < M_\pi/M$ is thus expected, reflecting the increase in the density of quarks and anti-quarks due to the pion's constituents. The momentum carried by the pions is lost by the nucleons, and thus by their quarks, which are then on the average slower than if there were no pions. This reduction in the quark momentum may lead to the measured EMC effect pattern.

Attempts have been made to compute the momentum fraction transferred to the pions. This can be done by expressing the effect of the nuclear medium in terms of the attractive potential in which the nucleons move: in a nucleus the total energy of a nucleon is reduced with respect to the free particle case because of the (negative) contribution of the potential energy. This can be viewed as a reduction of the effective mass of the nucleon, which in turn implies a shift of $x = Q^2/(2M\nu)$ to higher values ("x rescaling"). A given virtual photon thus probes the quark distribution in a bound nucleon at larger x than in a free one.

Alternatively, the valence distribution can be made softer by assuming that the quark confinement region increases in size. Because of the uncertainty principle this determines a reduction of the average quark momentum. In terms of QCD a change in the confinement size means a change of the scale μ^2 appearing in the Altarelli-Parisi equations 1.18-1.19; so the effective value of Q^2 for a bound nucleon is different from – in fact smaller than – that in a free nucleon. This is referred to as "Q^2 rescaling". Within this framework the QCD evolution in a bound nucleon "starts earlier"; consequently the amount of sea generated by QCD radiative processes per nucleon is larger in a nucleus than in a free nucleon. In some models the nucleonic structure tends to disappear at large Q^2, with quarks and gluons (or a fraction thereof) no longer confined to specific nucleons but rather spreading over the whole nuclear volume, which becomes some sort of a "color conductor". A similar viewpoint is shared by cluster models, in which quarks are conjectured to move quasi-freely inside enlarged bags, consisting of 6, 9, 12 or more valence quark clusters. It is worth mentioning that both nucleon swelling and multi-quark clusters are not new concepts, but have actually long been advocated by some nuclear physicists.

All these mechanisms give a fair description of the data in the region $0.2 < x < 0.6$, leaving to models of shadowing the task of accounting for the very small x region and ascribing to Fermi motion the rise of the structure function ratio at large x. The very high x region ($x > 1$), not covered by the present data, has also been the subject of considerable theoretical effort, notably in the framework of partial deconfinement and cluster models, where it is possible for a quark to carry a fractional momentum larger than unity.

We now proceed to the description of the individual classes of models; the reader not interested in the theoretical details of the EMC effect should turn to section 1.3.2, page 60.

Nuclear Binding, Pions and x Rescaling

Shortly after the publication of the EMC results [14] Llewellyn Smith [70] and Ericson and Thomas [71] showed that the gross features of the data could be explained by an enhancement of the pion field in nuclei, associated with the nucleon-nucleon interaction. This point of view was later expanded upon by other authors [72, 74]. The basic point of this approach is thus that if deuterium is made up of protons and neutrons only, iron also contains pions.

The structure function of a bound nucleon can be then written as the sum of two terms:

$$F_2^A(x,Q^2) = \int_{y\geq x} dy f_N(y) F_2^N(x/y,Q^2) + \int_{y\geq x} dy f_\pi(y) F_2^\pi(x/y,Q^2). \tag{1.22}$$

The first integral is the convolution of the free nucleon structure function F_2^N with the nucleon distribution function in the nucleus f_N. Similarly, the second term is the convolution of the pion structure function F_2^π with the pion distribution function in the nucleus f_π. The assumption is made that the structure functions $F_2^{N,\pi}$ of nucleons and pions are unaffected by the nuclear medium.

In the deep inelastic scattering on a pion at rest in a stationary nucleus x is bounded from above: $x < M_\pi/M \approx 0.15$. We therefore expect that if there are more pions in bound than in free nucleons, their direct contribution (the second integral in equation 1.22) is important at

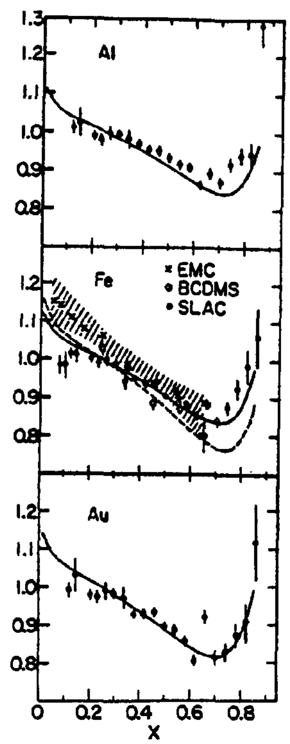

Figure 1.27: Predictions of the pion model [74] compared with the EMC NA2 [14], SLAC E139 [35] and BCDMS [36] results (from [74])

x smaller than ≈ 0.15. Such a model implicitely leads to an enhanced anti-quark distribution in nuclei, because of the the pion's valence anti-quark.

Furthermore, since these pions carry a fraction of the nucleus momentum, the nucleons are on the average slower than if there were no pions. Let η be the fraction of the nucleus momentum per nucleon carried by pions; then nucleons carry only a fraction $\overline{z} = 1 - \eta$. For a free nucleon – or in the absence of pions – this fraction would be unity.

The model successfully describes the experimental data in the range $0.1 < x < 0.8$. As an example the number of extra pions per nucleon needed to reproduce the EMC effect in aluminum is about 0.09; they carry approximately 5% of the nucleus momentum. These numbers turn out to be proportional to the nuclear density and rise to 0.11 and 6%, respectively, in gold. Figure 1.27 shows the predictions for the Al, Fe and Au to D structure function ratios compared with the original effect measured by EMC NA2 [14] and with the SLAC E139 [35] and BCDMS [36] results. The model is however less successful in describing the Drell-Yan data [61], since it predicts a strong enhancement of the anti-quark distribution – and thus of the cross section ratio – which is not observed in the data (cf. fig. 1.26; the theoretical curves in that figure are based on the calculations of [75]).

A straightforward extension of the model considers not only pions but also Δ's [76, 77]: the nucleus is then viewed as a set of nucleons, pions and Δ's. The structure function F_2 of a Δ baryon is expected to be shifted towards lower x values with respect to the nucleon one [78].

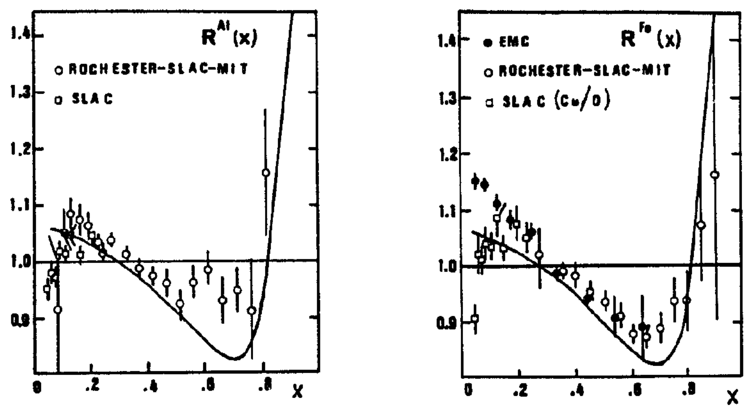

Figure 1.28: Predictions of the model [77] compared with the EMC NA2 [14] and SLAC E49B [31] results (from [77])

If the Δ's were the only non-nucleon component in the nucleus, a fraction of 10-15% such baryons per nucleon would be necessary to reproduce the observed EMC effect in iron for $x > 0.2$ [76]. Such a fraction is somewhat larger than allowed by current nuclear physics estimates [72]. If the nucleus is instead assumed to contain both pions and Δ's (beyond nucleons), then the effect measured in iron can be reproduced assuming a 4% and 12% admixture of Δ's and pions, respectively. Figure 1.28 shows the predictions of the model for Al and Fe.

While in the approaches outlined above $\bar{z}$ and the average number of pions in the nucleus are chosen so as to obtain the best agreement with the experimental results, Akulinichev *et al.* [79, 80] attempted to derive them in a nuclear physics framework. A similar approach was proposed by Birbrair *et al.* [81]. These authors express the effect of the nuclear medium in terms of the attractive potential V in which nucleons move. The nucleon energy in this case reads:

$$E_N = M + V + \frac{p^2}{2M}, \tag{1.23}$$

where p is the three momentum of the nucleon. The effect of the potential V (< 0) can be subsumed into an effective nucleon mass, lower than the free nucleon one, thus causing a shift in the scaling variable $x = Q^2/(2M\nu)$ towards higher values ("x rescaling"); the same conclusion can be reached from a relativistic extension of the Landau theory of quantum liquids [82]. The bound nucleon structure function F_2^A can be then approximated as:

$$F_2^A(x, Q^2) = F_2^D(\frac{x}{\bar{z}}, Q^2). \tag{1.24}$$

The rescaling parameter $\bar{z}$ is a function of V:

$$\bar{z} = 1 + V/M = 1 + \bar{\epsilon}/M, \tag{1.25}$$

where we have introduced the average one-nucleon separation energy $\bar{\epsilon}$. We recall that the separation energy is the energy necessary to "ionize" a nucleus and make it emit a nucleon.

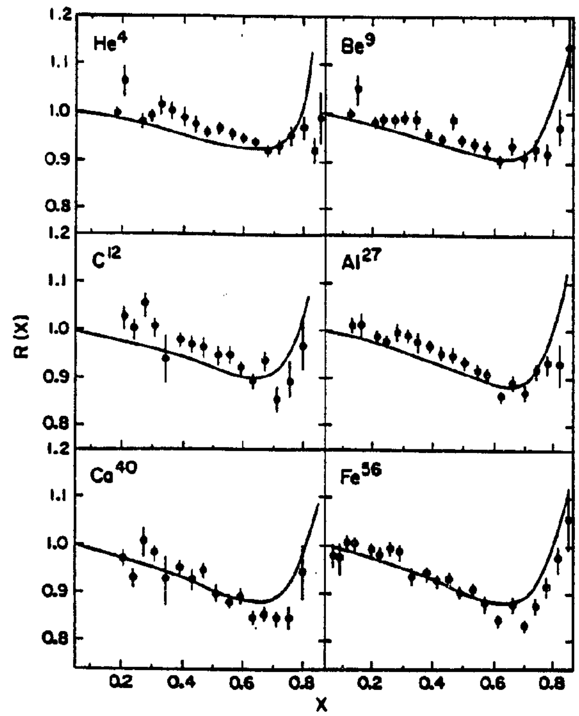

Figure 1.29: Predictions of the x rescaling model [79] compared with the SLAC E139 results [35] (from [80])

For example, given two nuclei both with Z protons and with N and $N-1$ neutrons, respectively, their masses are related by the following relationship:

$$M(Z,N) = M(Z,N-1) + M_{neutron} - \epsilon_{neutron}. \tag{1.26}$$

In terms of the binding energies of the two nuclei in question, equation 1.26 can be rewritten as

$$\epsilon_{neutron} = B(Z,N) - B(Z,N-1). \tag{1.27}$$

In equation 1.25 $\bar{z}$ is again the fraction of the nucleus momentum carried on the average by the individual nucleon. For iron $\bar{\epsilon}_{Fe} = -39$ MeV and $\bar{z}_{Fe} = 0.96$. Figure 1.29 compares the predictions of this model to the SLAC E139 results [35].

The present approach has been criticized for two reasons.

1. Frankfurt and Strikman [83] pointed out that the treatment of Akulinichev *et al.* uses an incorrect normalization of the relativistic spectral function and leads to an overestimate of the nuclear binding contribution to the EMC effect by up to a factor of three. A similar case was made by Jung and Miller [84]. Analogous criticisms apply to other relativistic treatments of the nucleus, like the one of Morley and Schmidt [85]. There are approaches at variance with that of Frankfurt and Strikman, e.g. the one proposed by Molinari and Vagradov [86]; these authors make however no explicit prediction for the EMC effect.

2. Li, Liu and Brown [87] showed that the separation energies used by Akulinichev *et al.* are too large (in absolute value) as they do not include an appropriate treatment of density-dependent interactions. In a Hartree-Fock description of the nucleus, they find for iron $\bar{\epsilon}_{Fe} = -26$ MeV and $\bar{z}_{Fe} = 0.972$; this further reduces the role of binding in explaining the EMC effect by an extra factor of two[2].

Using both the relativistic treatment à la Frankfurt and Strikman and the separation energies of Li, Liu and Brown, it is found that nuclear binding may account by up to about 20% only of the observed effect.

The model was later revived by Ciofi degli Atti and Liuti [90, 91] who showed that nucleon-nucleon correlations induced by realistic interactions strongly increase the average value of the removal energy, thereby making x rescaling a viable explanation of the EMC effect again. Figure 1.30 shows the result of this calculation compared with the data of SLAC E139 [35] (crosses), EMC NA2′ [38] (diamonds) and BCDMS [37] (squares); fig. 1.31 compares the predictions for ^{4}He with the data of SLAC E139 [35] (crosses) and with preliminary results from NMC based on the same data as those presented in this thesis [92] (diamonds). We remark that in these predictions the enhancement at small x has completely disappeared.

Similar conclusions were reached by Antonov *et al.* [93] in the framework of the coherent density fluctuation model [94], in which nucleon-nucleon correlations and binding effects are taken into account.

The discussion on the contribution of nuclear binding to the EMC effect is however not yet settled. Dieperink and Miller [95] studied the problem using realistic nuclear forces [96]. They also find that – at least for infinite nuclear matter – there are large deviations from the mean field picture due to nucleon-nucleon correlations, leading to increased nuclear separation energies. Their conclusion however is that nuclear binding can account for only a fraction ($\approx$ 70%) of the effect measured in large nuclei. The convolution formalism itself has been critically examined by several authors [97]-[99]. It is fair to say that there is still little consensus on the details of its implementation.

Finally we mention that Preparata and Ratcliffe [100] have given a justification of the nucleon mass shift and of the enhancement in the pion density in nuclei resorting to a rather unconventional description of nuclear forces [101]. In their theory the nucleus is seen as a fermionic superfluid where, inside domains of size $\approx$ 4.5 fm, nucleons and Δ's oscillate into each other, in phase with a condensed pion field.

Q^2 Rescaling Models

The starting point of the Q^2 rescaling model, formulated by Close, Roberts, Ross and Jaffe [102]-[104] is the observation that

$$F_2^A(x, Q^2) \approx F_2^D(x, \xi Q^2), \tag{1.28}$$

where $\xi > 1$. This suggests that the effective value of Q^2 may not be the same for a nucleus and for a nucleon.

We recall from section 1.1.3 that in QCD Q^2 always appears scaled by either Λ^2 or μ^2. At $Q^2 \approx \mu^2$ gluon radiation can be neglected and the nucleon appears as made up of the three

[2] These points in turn raised some critical discussion, see e.g. [88] and, more recently, [89].

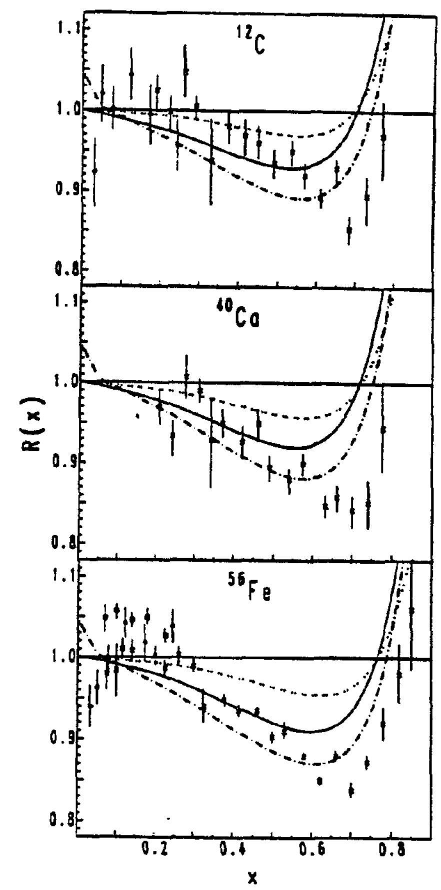

Figure 1.30: Predictions of the model of Ciofi degli Atti and Liuti (continuous curves) [90] for C, Ca and Fe; for an explanation of the symbols for the experimental points see text (from [90])

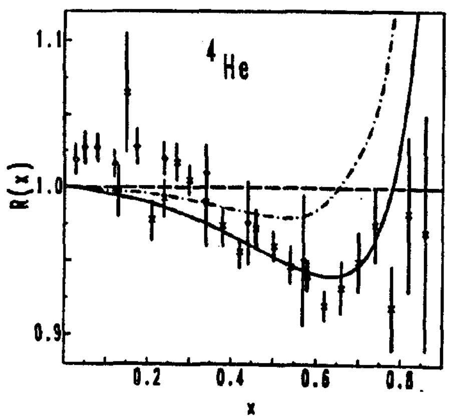

Figure 1.31: Predictions of the model of Ciofi degli Atti and Liuti (continuous curve) [90] for ^{4}He; for an explanation of the symbols for the experimental points see text (from [91])

valence quarks only; the quantity $\lambda \sim 1/\mu$ can then be taken as an estimate of the valence quark confinement size. One can suppose that the quark confinement size in a nucleus, λ_A, is larger than that in a free nucleon, λ_N. This idea was first proposed by Jaffe [105]; its relevance to the EMC effect becomes obvious if the uncertainty principle is considered, since a larger confinement region implies a softer momentum distribution for the quarks. The scales μ_A^2 and μ_N^2 are then also different, and $\mu_A^2 \sim \mu_N^2 \lambda_N/\lambda_A$. The effective value of Q^2 for bound nucleons is thus smaller than that for free nucleons: Q^2 needs to be rescaled up in order to obtain the quark distributions in a free nucleon from those in a bound one.

From the arguments just exposed it is clear that the rescaling factor ξ must be a function of μ_N/μ_A; the actual form can be derived by using the structure function moments M_n defined in formula 1.17. One can start at $Q^2 = \mu^2$, where the valence picture is a good approximation. So for $Q^2 = \mu_N^2$ in a nucleon and $Q^2 = \mu_A^2$ in a nucleus, the quark distributions are equal and so are the moments: $M_n^N(\mu_N^2) = M_n^A(\mu_A^2)$. If Q^2 changes, the moments of the nucleon structure functions evolve according to the QCD prediction:

$$\frac{M_n^N(Q^2)}{M_n^N(\mu_N^2)} = \left[\frac{\alpha_s(Q^2)}{\alpha_s(\mu_N^2)}\right]^{d_n}, \tag{1.29}$$

where d_n is the QCD anomalous dimension. For bound nucleons a similar relation must hold:

$$\frac{M_n^A(Q^2)}{M_n^A(\mu_A^2)} = \left[\frac{\alpha_s(Q^2)}{\alpha_s(\mu_A^2)}\right]^{d_n}, \tag{1.30}$$

hence, using $M_n^N(\mu_N^2) = M_n^A(\mu_A^2)$,

$$\frac{M_n^A(Q^2)}{M_n^N(Q^2)} = \left[\frac{\alpha_s(\mu_N^2)}{\alpha_s(\mu_A^2)}\right]^{d_n}. \tag{1.31}$$

The rescaling parameter ξ is now defined by the relationship $M_n^A(Q^2) = M_n^N(\xi(Q^2)Q^2)$; to leading order in α_s one finds that ξ varies with Q^2 but, rather remarkably, is independent of n:

$$\xi(Q^2) = \left(\frac{\mu_N^2}{\mu_A^2}\right)^{\alpha_s(\mu_A^2)/\alpha_s(Q^2)}. \tag{1.32}$$

At $Q^2 \approx 20$ GeV^2 the Fe/D data indicate a value of the rescaling parameter $\xi \approx 2$. This translates into $\lambda_{Fe} \approx 1.15\lambda_N$: the quark confinement radius for iron thus appears to be 15% larger than for a free nucleon. For helium the prediction is $\lambda_{He} = 1.079\lambda_N$ and $\xi(Q^2 = 20$ GeV$^2) = 1.43$.

So far the model provides no "explanation" for the observed change of scale, only a framework for discussing it. The physics of the change in the confinement radius may lie in nucleon overlap, which makes it more likely for quarks to leak outside the confinement radius of the free nucleon; in this case the effect is controlled by the nuclear density and by the nucleus surface to volume ratio. The nucleon-nucleon overlap probabilities can be estimated using the nuclear density and the nucleon-nucleon correlation function. Figure 1.32 compares the SLAC E139 results [35] with the model predictions thus obtained. In the range of applicability of the model ($0.2 < x < 0.8$) the agreement with the data is good.

The Q^2 dependence of the EMC effect in the Q^2 rescaling model was discussed by Bickerstaff and Miller [106]. Except at large x, where Fermi motion dominates, very little variation of the structure function ratio is predicted even over a wide Q^2 range. This is a consequence of the fact that the difference between the bound and free nucleon structure functions is small and their evolution slow. The Q^2 dependence predicted by this model is similar to that expected within the framework of nuclear binding and pion models. Figure 1.33 shows the predictions for F_2^{Fe}/F_2^D.

The QCD based Q^2 rescaling model just described and the conventional nuclear physics approach of the x rescaling model discussed before, although rather different in their starting points, can be formally connected [107, 108]. The average nucleon separation energy $\bar{\epsilon}$ and the Fermi momentum k_F can be related to the QCD anomalous dimensions d_n and to the increase of the confinement size. The fact that the nucleon, in the x rescaling model, carries only a fraction $\bar{z} = 1 + \bar{\epsilon}/M$ of the nucleus momentum can be expressed in terms of the structure functions moments as

$$M_{n=2}^A = \bar{z} M_{n=2}^N. \tag{1.33}$$

By comparing this relation with equation 1.31, one obtains:

$$\bar{\epsilon} = M\left[\left(\frac{\alpha_N}{\alpha_A}\right)^{d_2} - 1\right]. \tag{1.34}$$

Proceeding to the higher order moments one finds for $n = 3$:

$$k_F^2 = 5M^2\left[\left(\frac{\alpha_N}{\alpha_A}\right)^{d_3} - \left(\frac{\alpha_N}{\alpha_A}\right)^{2d_2}\right], \tag{1.35}$$

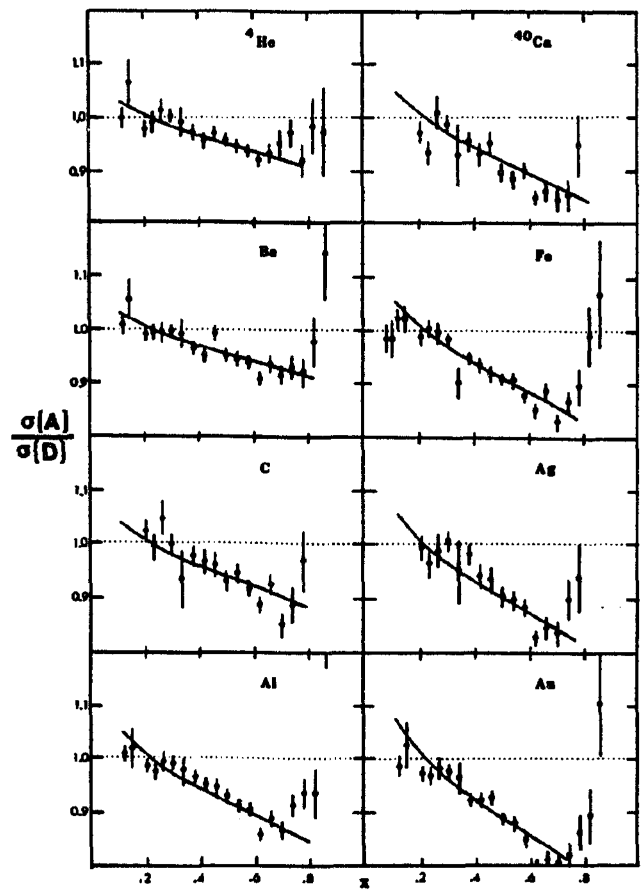

Figure 1.32: Predictions of the Q^2 rescaling model compared with the SLAC E139 results [35] (from [104])

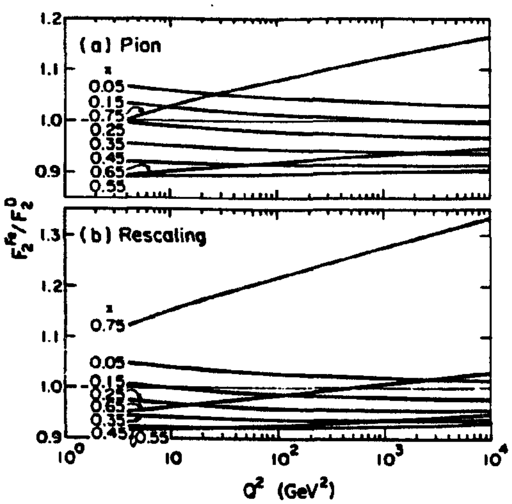

Figure 1.33: Predictions of the Q^2 rescaling and pion models as a function of Q^2 (from [106])

where a Fermi gas distribution has been assumed for the nucleons in the nucleus. Equation 1.35 relates the Fermi momentum k_F to the confinement size and the parameters of QCD. Using $n = 4$ yields new relations for $\bar{\epsilon}$ and k_F which are consistent with those given above.

This connection between Q^2 and x rescaling is interesting as it allows to express nuclear physics quantities in the language of QCD. The physical basis for this remains however unclear [109]. Dunne and Thomas [110] in fact argued that x and Q^2 rescaling, instead of being two different facets of the same physical process, should rather be viewed as complementary explanations of the EMC effect[3]. While x rescaling is still seen as a consequence of nuclear binding, Q^2 rescaling is assumed to take into account the fact that the structure function F_2^N in equation 1.22 is that of a nucleon off the mass shell: the dependence of F_2 on the invariant mass of the target nucleon is given by

$$\frac{M_n^A(Q^2)}{M_n^N(Q^2)} = \left[\frac{\alpha_s(P_N^2)}{\alpha_s(P_A^2)}\right]^{d_n}, \tag{1.36}$$

which is the same as equation 1.31 except that μ_A^2 and μ_N^2 have been replaced by the invariant masses of the struck nucleons in the two targets, respectively. The change of scale is thus a change of the mass and not of the confinement scale as in the original Q^2 rescaling model. Figure 1.34 shows the ratio of the ^{4}He to D structure functions calculated in this model, for different Q^2 values and with a effective nucleon mass of 919 MeV. The results without Q^2 rescaling are also shown (dashed curves).

An alternative approach to Q^2 rescaling is the one of Fredriksson [111] who described the nucleon as being mostly in a bound quark-diquark state, with the diquark $(ud)_0$ a small, spin zero, tightly bound quark pair. Fredriksson suggested that the diquark may be somewhat bigger in a bound than in a free nucleon as a consequence of the perturbing forces exerted by

[3]This approach was however criticised by Frankfurt and Strikman [83] on the grounds of an incorrect normalisation of the relativistic spectral function.

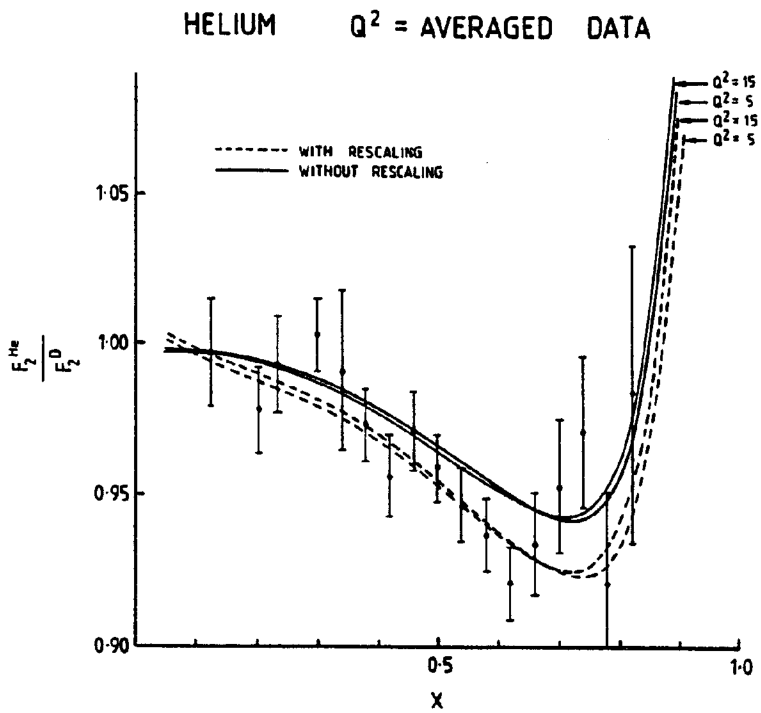

Figure 1.34: The ratio of the ^4He to D structure functions calculated in the model of Dunne and Thomas (continuous curves) [110]. The experimental points are from the SLAC E139 experiment [35] (from [110])

the quarks of the nearby nucleons. The effect of a swelling diquark on the structure functions is included by scaling Q^2 with the diquark mean square radius. The structure function of a bound nucleon thus reads

$$F_2^A(x, Q^2) \approx F_2^D(x, kQ^2), \tag{1.37}$$

where now $k = < r_d^2 >_A \, / < r_d^2 >_D$, with $< r_d^2 >$ the diquark radius squared. This is a consequence of the fact that the diquark form factor is expected to scale with $< r^2 > Q^2$. The Q^2 rescaling parameter is therefore different from the one proposed by Close, Roberts, Ross and Jaffe and, to first approximation, is simply given by the ratio squared of the bound to free nucleon confinement radii. The agreement of the model with the data is acceptable between $x = 0.2$ and $x = 0.6$. For iron $k \approx 1.2$-2, corresponding to an increase of the diquark radius of 10-45%. A critical discussion of this model compared with the one of [102]-[104] is presented in [112].

Nucleon Swelling

That a small change of the nucleon radius, regardless of its origin, can lead to the EMC effect has also been shown by Hendry, Lichtenberg and Predazzi [113]. This assumption was later combined with that of a reduced effective mass of bound nucleons with respect to free ones (a concept common to x rescaling models) [114]. The resulting predictions are in reasonable agreement with the SLAC E139 data [35] for $x > 0.2$. It is found that the nucleon radius is about 5 to 10% larger in iron than in deuterium; the effective mass is taken to be 5% smaller than the free nucleon one. Interestingly, in a later paper [116] the authors remarked that also at small x the behavior of the nuclear to free nucleon structure function ratio (shadowing, see next section) can be ascribed to nucleon swelling. Figure 1.35 shows a comparison of the model predictions with the EMC NA2′ results.

The concept of nucleon swelling is older than the discovery of the EMC effect. A 30% increase in the nucleon size in Fe was for instance advocated [117, 118] to account for quasi-elastic electron scattering data which revealed a softer charge form factor in bound nucleons than in free ones. Already at that stage nucleon swelling was related to a rescaling of the nucleon mass; this connection is automatic in the MIT bag model [119].

Frankfurt and Strikman [64, 120] also argued in favor of nucleon swelling in nuclei in order to describe the EMC effect for $x > 0.3$. They suggest that such deformation of nucleons may be analogous to the ones occurring in the atoms of a gas interacting via Van der Waals forces, where the interaction potential has the form

$$V \sim \frac{< r_i >^2 < r_j >^2}{R_{i,j}^6}; \tag{1.38}$$

here $< r_i >^2$ is the mean quadratic radius of the i-th atom and $R_{i,j}$ is the distance between atoms i and j. In order to have stable binding one finds that the mean quadratic radius of an atom in a medium must be larger than that of a free atom.

In QCD a hadron can be described as a superposition of quark-gluon configurations of different sizes. For example at small x and Q^2 large effective size configurations dominate; in the nuclear physics language this corresponds to saying that the pion cloud of the nucleon extends to large distances. At larger x (> 0.3) and Q^2 (> 1 GeV^2), configurations with only the

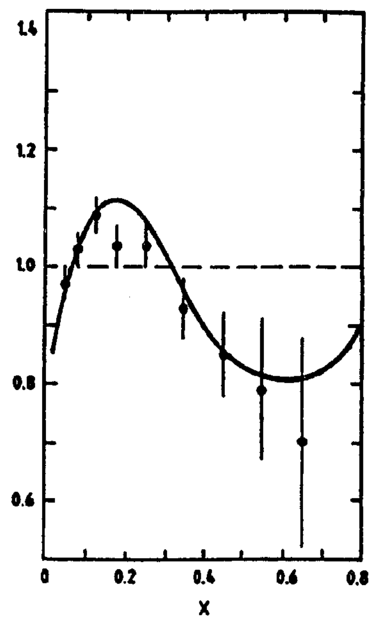

Figure 1.35: Predictions of the model [116] compared with a preliminary version of the EMC NA2′ data on Cu/D [115] (from [116])

three valence quarks dominate, with no pion clouds, sea quarks or gluons. Their size should be smaller; based on the analogy with the gas of neutral atoms presented above, the interaction of a bound nucleon in such a configuration with other nucleons should be weaker than that of larger size configurations (this property is often referred to as "color transparency"). Furthermore, based on energy considerations, these small size ("point-like"), high momentum configurations are suppressed in bound nucleons with respect to free ones. The suppression turns out to be related to the average kinetic energy of a nucleon in a nucleus and to the average binding energy per nucleon. The corresponding increase in the nucleon radius is about 1-2%, much smaller than that expected in other models.

Deconfinement and Color Conductivity

Q^2 rescaling is a natural byproduct of the color conductivity model [121]-[123]. The basic idea of this approach is that when a nucleus is observed with high resolution, i.e. at large Q^2, the nucleonic structure becomes unimportant: quarks and gluons are no longer confined to specific nucleons but rather spread over the whole nuclear volume. At large Q^2 the nucleus thus turns into a medium in which colored objects can travel freely, a "color conductor". In practice the effective nucleon radius, i.e. the quark and gluon confinement size, is taken to increase with Q^2 until full color conductivity sets in; the basic point of the Q^2 rescaling model [102]-[104], namely the variation of the confinement radius with Q^2, is thus recovered. With the explicit further assumption that the running coupling constant α_s is independent of A, one indeed finds again eq. 1.32 for the rescaling parameter ξ. The possibility that the QCD scale parameter Λ (and thus α_s) is a function of A is also explored. Instead of eq. 1.32 in this case one finds simply

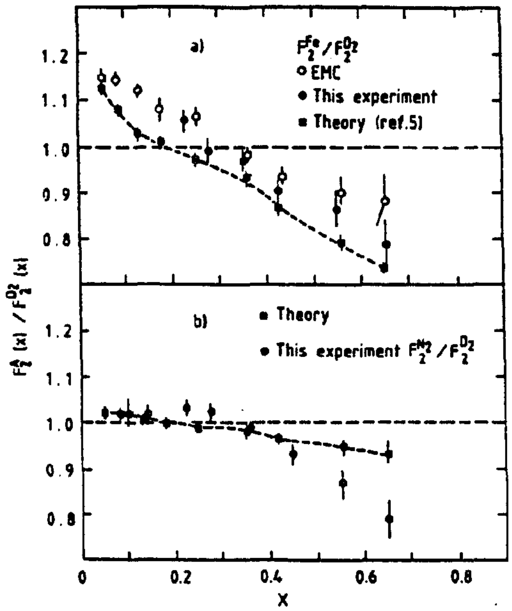

Figure 1.36: Predictions of the color conductivity model compared with the EMC NA2 data [14] and the BCDMS ones [36], labelled "This experiment" (from [124])

$\xi = (R_A/R_D)^2$ (with R_A, R_D the radius of nucleus A and of deuterium, respectively), the same as in the diquark model of Fredriksson [111]; the corresponding variation of the effective value of Λ is $\Lambda(A_1) = \Lambda(A_2)(R_{A_2}/R_{A_1})$. Figure 1.36 shows the predictions of the model together with the original EMC NA2 data on Fe/D [14] and the N/D data of BCDMS [36] (labelled "This experiment").

A slightly different viewpoint on deconfinement was expressed by Gupta *et al.* [125]. In their model the influence of the nuclear medium on the parton distributions consists in a changing the phase space volume open to quarks and gluons. In the infinite momentum frame the quarks in the nucleus have a minimum transverse momentum p_t^{min} given by the inverse of the nuclear radius:

$$p_t^{min} = \beta A^{-1/3},$$

where $\beta \approx 100$-200 MeV. Thus the cutoff in p_t decreases with increasing A and the phase space available to quarks increases. The scale parameter μ in the Altarelli-Parisi equations 1.18-1.19 is set in this model equal to p_t^{min}. This in turn means that the *effective* value of Λ_{QCD} extracted from data on nuclear targets, λ_A, is also a function of A:

$$\lambda_A = \Lambda A^{-1/3}.$$

A comparison of this model with the data is shown in fig. 1.37.

Deconfinement has been also approached in a thermodynamical framework, in which a fraction of deconfined partons is treated as a non-interacting Fermi gas at temperature T.

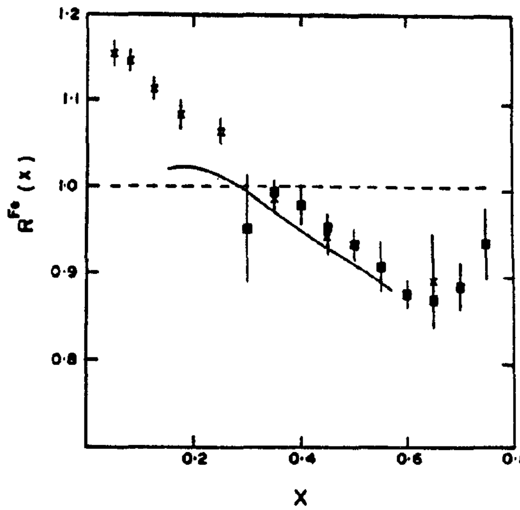

Figure 1.37: Predictions of the deconfinement model of Gupta *et al.* [125] for Al and Fe compared with the EMC NA2 data [14] (crosses) and the SLAC E87 ones [30] (from [125])

Krzywicki and Furmansky [127], developing the ideas presented in [126] (one of the only two partial *pre*-dictions of the EMC effect, together with that of Nikolaev and Zakharov [177]), regarded the whole nucleus as a dilute gas of quarks and gluons. The model is of course somewhat extreme, but reproduces the trend of the data, at least qualitatively, if $T = 30$ MeV. If only a few nucleons are instead assumed to "deconfine", with their constituents released into the full nuclear volume [128, 129], the agreement with the data improves (cf. fig. 1.38). The temperature of the deconfined parton is again found to be in the range 25-45 MeV and the average number of deconfined nucleons per nucleon is about 0.10-0.17.

The interpretation of structure functions in thermodynamical terms is not new. Angelini and Pazzi [130], before the discovery of the EMC effect, treated the valence quarks as a non-interacting, relativistic Boltzmann gas. They found that the measured structure functions could be well reproduced for $x > 0.1$ if the temperature was assumed to be about 50 MeV. In this framework the EMC effect can be understood in terms of a different quark gas temperature in bound and free nucleons [131]. For iron and deuterium the temperature difference is found to be $\Delta T = 3 \pm 1$ MeV. Furthermore the effective nucleon volume, i.e. the volume occupied by the quark gas, turns out to be 30% larger in Fe than in D, somewhat higher than many of the estimates for nucleon swelling given above.

Cluster Models

A variation on the themes of deconfinement and nucleon swelling is that of clusters. Several authors conjectured that a fraction of the valence quarks in the nucleus move quasi-freely inside enlarged bags, consisting of 6, 9 or more quark clusters. The possibility that clusters might explain the EMC effect was first mentioned by Jaffe [105] in the MIT bag framework.

Pirner and collaborators [132]-[134] proposed one such model before the discovery of the EMC effect in order to explain deep inelastic data from ^{3}He in the region $1 < Q^2 < 4$ GeV^2 [135]. In their approach, two nucleons are assumed to start forming a six-quark cluster when they are a distance $2R$ apart, where R is an effective nucleon radius; similarly, if a third nucleon is less

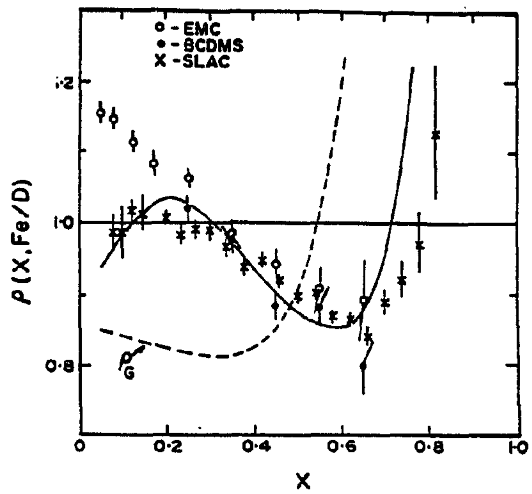

Figure 1.38: Predictions of the deconfinement model of Gupta *et al.* [128] compared with the EMC NA2 [14], SLAC E139 [35] and BCDMS [36] data (from [128])

than $2R$ from either of these two nucleons then we have a 9-quark cluster etc. The probability to have a cluster of a given size can then be calculated assuming realistic nucleon-nucleon potentials or by resorting to Monte Carlo simulations [136].

The momentum distribution of quarks in an i-quark cluster, $n_i(x)$ ($i = 6, 9, ...$), is taken to be

$$xn_i(x) \sim x^{1/2}[1 - x/(i/3)]^{2(i-1)-1},$$

based on counting rules [137, 138].

The experimental results on ^{3}He [135] are well described with an effective nucleon radius of 0.5 fm, leading to a 10-20% probability of non-nucleonic quark structures in the nucleus. The success of the quark-cluster model in explaining the ^{3}He data depends on the fact that a quark in a 6 or 9-quark bag has the possibility of carrying the whole momentum of two or three nucleons, thus providing high momentum components not present in a conventional picture based on 3-quark systems only.

Using similar arguments, Carlson and Havens [139] showed that the EMC effect in Fe can be described by assuming that nucleons are, with a 30% probability, subsumed into 6-quark or larger clusters. A similar discusion of 6-quark clusters has been proposed by Chemtob and Peshanski [140].

Faissner, Kim and Reithler [141]-[143] concentrated on the role of 12-quark clusters, i.e. α particles, which are known to be very stable systems. Their stability is a consequence of the large binding energy and can be easily understood in the QCD framework. We can picture a nucleon as made up of three quarks connected by color strings. Let us assume that the three quarks sit at the vertices of an equilateral triangle. While it is difficult to form a stable system out of two or three of these triangles, it is easy if four are considered, as they form a regular tetrahedron. The quarks thus loose their assignment to individual nucleons: the three differently colored quarks at each corner of the tetrahedron may be combined into a white

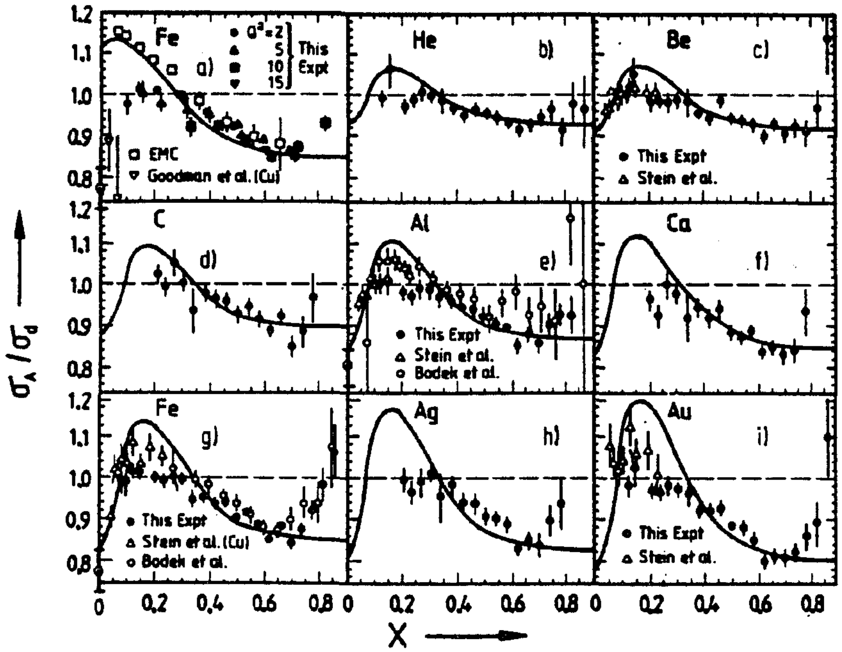

Figure 1.39: Predictions of the α-cluster model [143] compared with the compilation of experimental results of fig. 1.10 (from [143])

nucleon just as well as those belonging to the original triangles. The α particle is therefore not-just a 4-nucleon compound, but also a system of 12 valence quarks which form a singlet in spin, isospin and color.

In order to evaluate the structure functions of an α-cluster, a model is adopted in which the incoming lepton scatters off a pointlike "constituent" quark with an effective mass $m_q(Q^2)$. The motion of the constituent quark inside the cluster is described in terms of a distribution function f_q and the deep inelastic scattering cross section is obtained as the convolution of the lepton-quark cross section folded with the quark distribution f_q; each quark is taken to give an incoherent contribution.

The EMC effect data can be described by assuming that the Fermi momentum of the quarks inside the clusters is lower than inside the nucleon and that there is a fraction g_{cl} of α clusters in the nucleus. A lower Fermi momentum simply means that the size of the cluster is larger than the nucleon one. The EMC data can be reproduced in the region $0.2 < x < 0.6$ with a clustering probability $g_{cl} \approx 10\%$, with an effective quark mass $m_q = 150$ MeV and with a cluster radius equal to that of the α particle. The Fermi momentum of the quarks inside a free nucleon is set to 300 MeV and the explicit form of the distribution function f_q is found assuming a harmonic oscillator potential for the quarks inside the cluster.

In this framework the A dependence of the EMC effect has a geometrical origin: clusters are more likely to form well inside the nucleus rather than on its surface, where the number of neighbors is smaller. Figure 1.39 show the results thus obtained. Similar arguments on the geometrical origin of the A dependence of the EMC effect in a multi-quark cluster model were proposed by Daté *et al.* [144].

The relevance of α clusters was also discussed by Kondratyuk and Smatikov [145] who

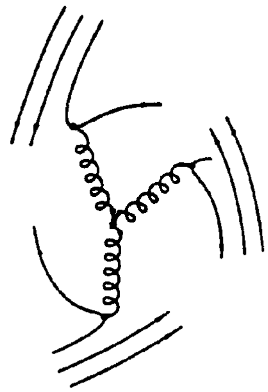

Figure 1.40: The dynamical mechanism proposed by Barshay [148] (from [148])

found that a 15-20% admixture of 12-quark clusters in the nucleus may explain not only the EMC effect data but also the behavior of the ^{4}He form factor at large Q^2. The momentum distribution of the quarks in the cluster is taken to be exponentially falling, $\sim x \exp(-ax)$, with $a \approx$ 8-10; this form is based on the assumption that the quarks inside a cluster behave like a Fermi gas.

A similar fraction of α clusters is also found in another model calculation by Clark *et al.* [146]. The authors remark however that the experimental results can be reproduced just as well with any two-component cluster model.

A dynamical mechanism that can lead to three and four nucleon clusters was proposed by Barshay [147, 148] and is depicted in fig. 1.40. When three nucleons are very close to each other, a valence quark from each nucleon may be exchanged to each neighbor with the emission of a hard gluon. The three gluons interact and the resulting repulsive force tends to give to the system an equilateral triangle configuration. The emission of these gluons softens the momentum distribution of the valence quarks and this leads to the EMC effect.

Quantitatively this idea is implemented by removing a fraction δ of the valence quarks contributing to the nuclear structure function with the same distribution as in a free nucleon. This fraction is assumed to move in a larger bag with a gaussian distribution of the type $Cx^{1/2}\exp(-Bx^2)$, where the normalization C is chosen in such a way as to keep the number of valence quarks constant and the parameter B reflects the spatial extent of this motion, about 1.3 fm. The structure function of a bound nucleon thus reads:

$$F_2^A(x) = \frac{5}{18}[xV(x)(1-\delta(A)) + Cx^{1/2}e^{-Bx^2} + xS(x)], \tag{1.39}$$

where $V(x)$ and $S(x)$ are the valence and sea quark distributions in a free nucleon. The A dependence of δ is taken to be the same as determined in [144], with the nucleons on the surface of the nucleus excluded from the three-nucleon correlation.

The mechanism can be thought to work also for sea quarks and anti-quarks, thus leading to a description of the shadowing region as well. In this case the distribution of the sea quarks involved in the three-body correlation is assumed to be of the type $Cx^{\beta}\exp(-B'x^2)$. The parameters B, B', β and the overall normalization factor δ can be estimated only approximately.

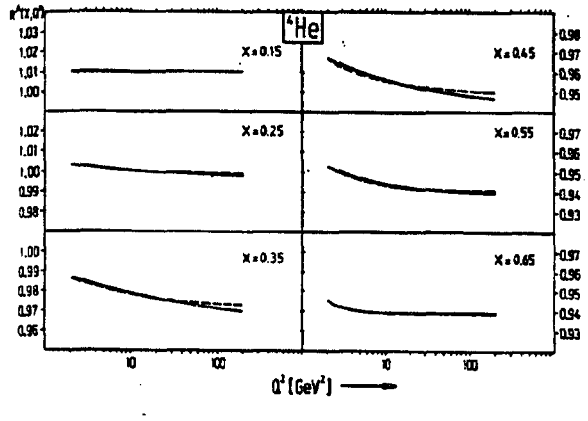

Figure 1.41: Predictions of the model by Barshay [148] for the Q^2 dependence of the ratio F_2^{He}/F_2^D (from [148])

What is done then is to fix them with a fit to the data, which renders the predictive power of the model rather modest, especially at small x.

With increasing Q^2, the valence quarks involved in the correlation will undergo an additional softening as a consequence of QCD evolution. This leads, for $x > 0.25$ to a further decrease of the structure function ratio. Quantitative predictions of the Q^2 dependence are based on the fits above and on the prejudice that the three nucleon correlation is essentially a higher twist effect. Figure 1.41 shows the results for ^{4}He.

Hoodboy and Jaffe [149] offered another view of the formation of quark clusters, which they also describe in terms of quark exchange between nucleons. The calculation is carried out for $A = 3$ nuclei only, for which reliable wave functions are available; a nuclear wave function completely anti-symmetrized in the nuclear coordinates as well as in the quark coordinates is used. Quark exchanges between two nucleons at the time are considered only. The resulting structure function ratio for an $A = 3$ isoscalar target is shown in fig. 1.42 for two different effective nucleon radii b and two different nuclear wave functions. The predictions of the Q^2 rescaling model [102] are also shown.

Lassila and Sukhatme [150] proposed a quark-cluster model in which the contribution of 6-quark clusters only is included. The valence and sea quark distributions in a cluster with N valence quarks are taken to have the forms:

$$\begin{aligned} V_N(x) &\sim x^{1/2}(1-x)^{b_N} \\ S_N(x) &\sim (1-x)^{a_N}. \end{aligned}$$

The exponent b_N is set to $b_N = 2N - 3$ (corresponding again to the simplest application of the dimensional counting rules [137, 138]); this gives $b_6 = 9$. The value found for $N = 2$, agrees with the measured pion structure functions. The sea distribution exponent is taken for a 6-quark cluster to be $a_6 = 11$; the results do not however depend strongly on this choice. Figure 1.43 shows the structure function ratio thus found (curve "A"); if one takes $b_6 = 10$

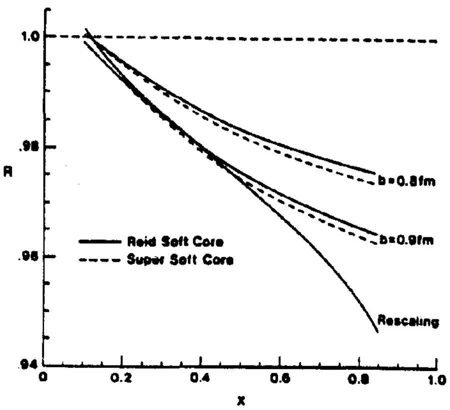

Figure 1.42: Predictions of the model of Hoodboy and Jaffe [149] for an $A = 3$ isoscalar target. For an explanation of the symbols, see text (from [149])

the curve labelled "B" is obtained. Finally curve "C" corresponds to $a_6 = 13$. The model predictions do not show any enhancement for $x \approx 0.1$-0.2; the authors claim however that the inclusion of 9-quark clusters causes the ratio to become larger than unity in this region. The predictions are compared with the EMC NA2$'$ data [38] on carbon, copper and tin, and with the EMC NA2 [14], BCDMS [36] and SLAC E87 [30] results for iron.

The same authors also made explicit predictions for the ratios of the gluon distributions in bound and free nucleons [151]. Figure 1.44 shows the results, together with the ratios expected for valence and sea. It is worth remarking that this model overlaps to some extent with the parton recombination approach used to describe the shadowing region and discussed below. Actually, like other parton recombination models, it can reproduce [152] the shadowing signal seen by the Drell-Yan experiment E772 [61]. This fact is at variance with the conclusions contained in [61], based on the calculations of [75].

Dias de Deus *et al.* [153] combined quark-clusters and Q^2 rescaling, introducing the scale factor $R_i^2 \sim 1/\mu_i^2$ which measures the mean free path of the quarks in the i-cluster; here μ_i^2 is the QCD scale parameter appropriate for the cluster: at $Q^2 \approx \mu_i^2$ the cluster can be viewed as made up by i valence quarks only. For larger values of Q^2 sea quarks, anti-quarks and gluons are generated. Equation 1.32 can now be written in the following form:

$$\frac{Q_i^2}{Q_j^2} = \left(\frac{\mu_i^2}{\mu_j^2}\right)^{\alpha_s(\mu_j^2)/\alpha_s(Q_j^2)} , \tag{1.40}$$

where Q_i^2 and Q_j^2 are the Q^2 values for which the same "amount" of QCD evolution has occurred in the i and j clusters. Denoting with p the average number of nucleons per cluster, the relationship between R_i and A is determined according to the ansatz

$$p = \frac{1 + \exp(-a)}{1 + \exp(-aA^{1/3})} \tag{1.41}$$

(where a is a constant), while for the dependence of R_i on p, the simple relation $R_i = R_1 p^{1/3}$ is used, with R_1 the confinement scale in deuterium. A fit to the EMC NA2 data [14] yields

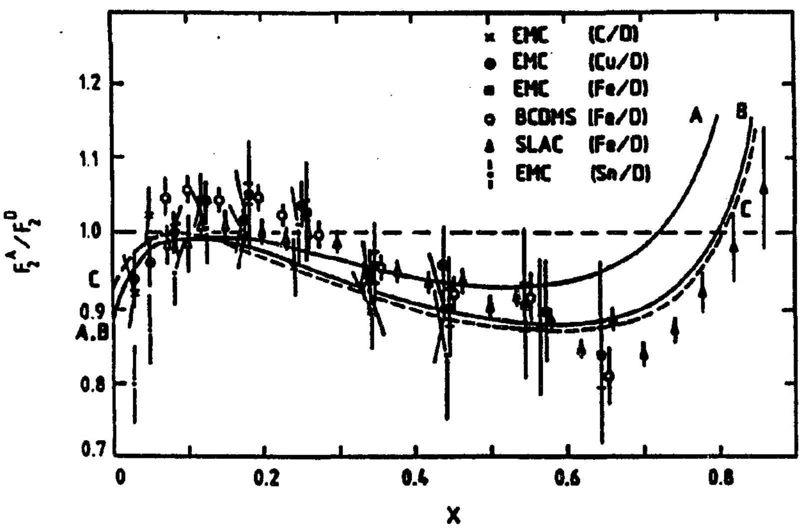

Figure 1.43: Predictions of the cluster model of Lassila and Sukhatme [150] compared with a compilation of experimental results. For an explanation of the symbols, see text (from [150])

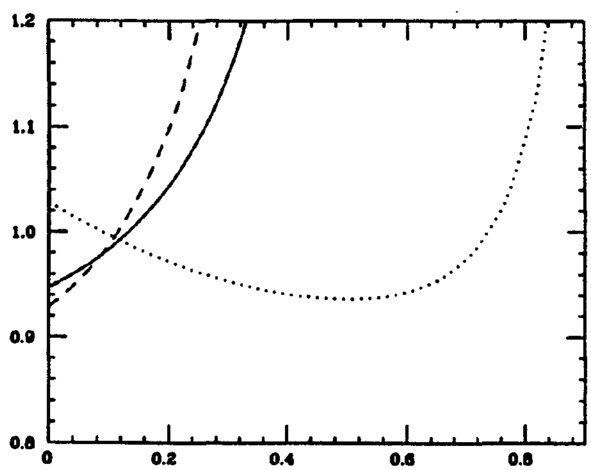

Figure 1.44: Predictions of the cluster model of Lassila and Sukhatme [150] for the ratio of glue (solid line), sea (dashed line) and valence (dotted line) in Ca and D (from [151])

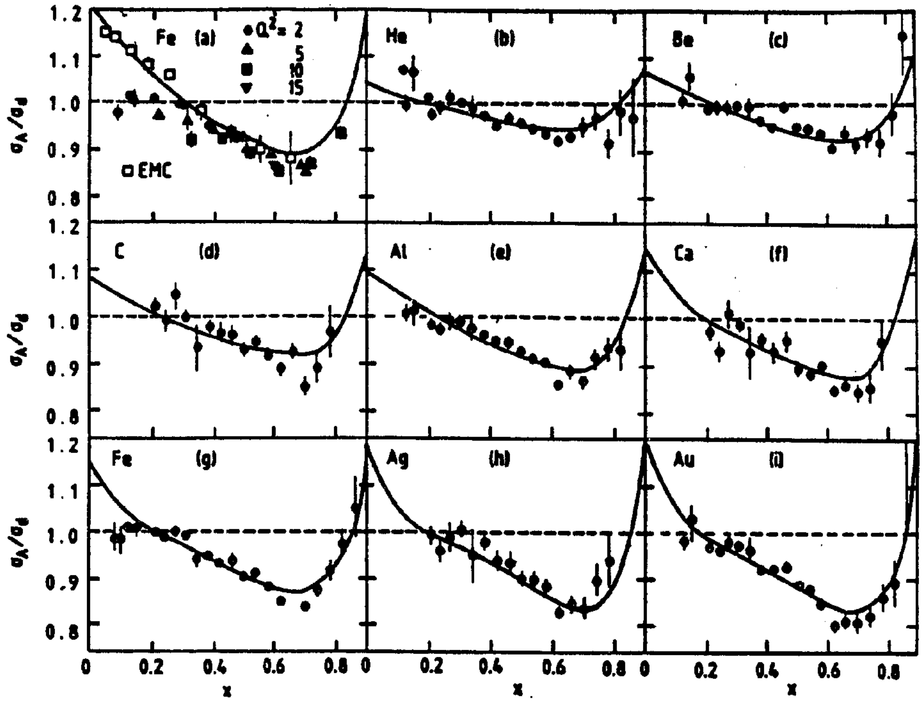

Figure 1.45: Predictions of the model of Dias de Deus *et al.* [154] compared with the experimental results of EMC NA2 [14] (open symbols) and those of SLAC E139 [35] (full symbols) (from [154])

$p = 1.05$ for iron. In a later paper [154] the same authors repeated the fit using the SLAC E139 results [35]. The ansatz 1.41 is replaced here by the simpler one $p = A^\lambda$, where λ is a free parameter. The fit gives $\lambda = 0.012$, which reproduces the value for $p(Fe)$ previously found. Figure 1.45 shows the results.

In closing this discussion of the cluster models we recall that they offer (together with all models predicting partial deconfinement) a natural framework to study nuclear structure functions for x values larger than unity, the so-called cumulative region (for a discussion see for instance [19], [134] and [155]-[157]): the cross section ratios in the $1 < x < 2$ region are affected by the existence of 6-quark clusters, in which a quark can carry up to twice the momentum of an individual nucleon. Similarly 9-quark clusters dominate the region $2 < x < 3$. Unfortunately no reliable experimental data exist for $x > 1$.

1.3.2 Models of Shadowing

The total hadron-nucleus cross section σ_{hA} is known to be smaller than A times the total hadron-nucleon cross section σ_{hN}:

$$\sigma_{hA} < A\sigma_{hN}.$$

Loosely speaking this is ascribed to the fact that the nucleons on the surface of the nucleus project their "shadow", in an optical analogy, onto the inner ones, which are thus not exposed

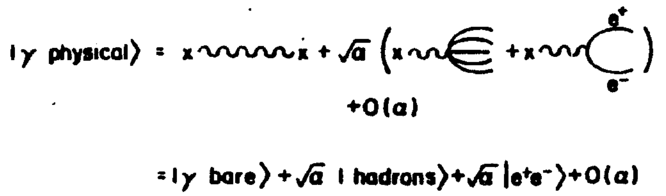

Figure 1.46: The perturbation expansion of the physical photon state (from [159])

to the full hadron beam intensity. If the hadron-nucleus cross section is large, then for large A the effective number of nucleons participating in the inelastic interactions is reduced to the number of surface nucleons, $\approx A^{2/3}$.

A theoretical framework describing the interaction of hadrons with nuclei is the Glauber multiple scattering model [158]. The basic assumption of the Glauber treatment is that the amplitude for the interaction of a high energy hadron with a nucleus can be built up from the scattering amplitudes off the individual nucleons. The phase shift experienced by the projectile is in fact simply taken to be the sum of the phase shifts that it would experience by interacting with each of the nucleons in isolation. The motion of the nucleons is neglected and their positions are taken as fixed. Furthermore the assumption is made that the target nucleons do not overlap significantly and that the incident hadron scatters mainly through small angles. In this framework the process in which the incoming hadron interacts with a nucleon and successively reinteracts with a second one turns out to have an amplitude opposite in phase (when the incoming hadron energy is large and the hadronic scattering amplitude is mainly imaginary) to that of the single scattering process, in which the hadron interacts with a single nucleon only. The cross section *per nucleon* is thus smaller in the rescattering case, giving rise to shadowing. For a nucleus with A nucleons also triple, quadruple, ..., A-fold interactions must be taken into account. The successive terms in this multiple scattering series decrease however in size; they also alternate in sign, so that while the double scattering amplitude is negative, the triple scattering one is positive etc.; this feature leads to the familiar diffraction-like pattern of hadron-nucleus cross sections.

High energy, photon-induced reactions bear a remarkable resemblance to purely hadronic reactions, apart from a scale factor $\simeq \alpha$ in the cross section, where α is the electromagnetic coupling constant. This finds a simple interpretation in terms of the hadron structure of the photon [159]-[161]. The physical photon can be viewed (fig. 1.46) as fluctuating between a bare photon state, a set of electromagnetic states (e.g. e^+e^- pairs) and a superposition of hadronic states with the same quantum numbers as the photon ($J^{PC} = 1^{--}$), namely vector mesons; the probability for the photon to convert to a hadron is about α. This is the basis of the Vector Meson Dominance (VMD) model. It is clear then that the photon-nucleus cross section must exhibit some of the characteristics of the hadron-nucleus interaction. Photon interactions should thus also be shadowed in nuclei, as first predicted by Stodolsky [162]. This is indeed observed [161]; the size of the effect increases with the photon energy and with the nucleon mass number A.

The VMD arguments sketched for the real photon case apply to virtual photons as well. The experimental evidence for shadowing of virtual photons was for a long time neither overwhelming nor consistent (fig. 1.6). Some effect was seen at low Q^2, but considerably less than that found in the photo-production experiments. Shadowing appeared to decrease rapidly as Q^2 increased. The situation became clearer with the EMC NA2′ [38, 39] and the EMC NA28 results [40] in which shadowing was unmistakably present in the small x region. In contrast to the earlier data, the effect was present also at values of Q^2 significantly larger than 1 GeV^2.

Originally only the lowest mass vector states (ρ, ω, ϕ) were considered in VMD models; it is clear now that heavier ones are also necessary in order to reproduce the experimental results. This approach, known as Generalized Vector Meson Dominance (GVMD), is able to give a reasonable description of the data up to $x \approx 0.1$. At least three different formulations of GVMD exist (Schildknecht *et al.* [165]-[170], Piller *et al.* [171]-[173] and Shaw *et al.* [174]-[176]), differing in the details of the implementation of the ideas just outlined, but all reproducing the EMC data.

While the framework in which the shadowing of photons was initially predicted and interpreded was the VMD one, a partonic approach, pioneered by Nikolaev and Zakharov [177], is also available. Shadowing is in this case ascribed to a depletion of partons in the small x region. In the Breit frame, low x partons spread over a large longitudinal distance because of the uncertainty principle; small momentum partons belonging to different nucleons may thus occupy the same region of space, they may interact and fuse. This leads to a decrease of the number density of low x partons with respect to the free nucleon case and – because of momentum conservation – to an increase in the density of higher momentum ones ("anti-shadowing"). Shadowing and anti-shadowing are not expected to vary appreciably with Q^2. The predictions of anti-shadowing and of the Q^2 scaling of shadowing and anti-shadowing are peculiar of partonic approaches.

The discussion of Nikolaev and Zakharov predates QCD. The mechanism they proposed has been investigated more recently in a perturbative QCD framework. Perturbative QCD does not predict the shape of parton distributions, even less so nuclear ones, but rather their Q^2 evolution. This evolution has been studied in detail by Müller and Qiu [178] and Qiu [179]; their analysis confirms the pre-QCD results of Nikolaev and Zakharov, finding only a weak Q^2 dependence for shadowing.

Some semi-quantitative attempts to describe the x shape of shadowing have also been made in this framework, with special emphasis on trying to predict the A dependence of the point where shadowing sets on (Berger and Qiu [180], Close and Roberts [181]). Models of this kind, based on phenomenological parametrizations of the x dependence of shadowing supplemented by QCD arguments, are now able to give an accurate description of the available data (Zhu *et al.* [184]-[190]).

Partonic models have also been formulated differently. In the laboratory system, where the target nucleus is at rest, the interaction of the virtual photon with the target is described in the language of hadron-hadron diffractive scattering by means of pomeron exchange (Castorina and Donnachie [193, 194], Brodsky and Lu [198]). The photon interacts then with a pomeron emitted from a nucleon rather than with the nucleon itself. If the pomeron is taken as a superposition of gluons, the photon may interact with the gluons via photon-gluon fusion processes. Alternatively, the photon may be seen to dissociate into a $q\bar{q}$ pair, with the pomeron interacting with the quarks in the pair. It is clear that if the $q\bar{q}$ pair is looked upon as a meson, we may recover the vector meson dominance picture discussed above. GVMD and partonic approaches have actually blended in a unitary picture in the recent papers of Frankfurt and Strikman [202, 206] and Nikolaev and Zakharov [207, 208]. These authors classify the $q\bar{q}$ pairs according to their transverse size: only the pairs of large transverse dimensions interact with hadronic cross section and give rise to shadowing. Nuclear matter is instead more transparent to small size pairs and the interaction cross section of such pairs with the nucleus is just proportional to the number of nucleons in the nucleus.

We turn now to a description of the available models, classifying them according to their approach being VMD-like or partonic. As we just mentioned, the distinction is somewhat artificial and the two types of treatment may have much in common. The reader not concerned with the theoretical details may want to proceed directly to chapter 2.

(Generalized) Vector Meson Dominance Models

Let $q_\mu = (\nu, \vec{k})$ be the four-momentum of the photon and M_V be the mass of the hadronic fluctuation; then the energy of the fluctuation will be:

$$E_V = \sqrt{M_V^2 + k^2},$$

to be compared with the original energy of the photon:

$$\nu = \sqrt{-Q^2 + k^2},$$

where, as usual, $Q^2 = -q^2$ and $k^2 = \nu^2 + Q^2$. The energy difference $\Delta E = E_V - \nu$ between the two states, for large values of ν, is

$$\Delta E = E_V - \nu \approx \frac{Q^2 + M_V^2}{2\nu}. \tag{1.42}$$

The hadronic fluctuation will then extend over a distance (the "coherence length")

$$d(M_V^2, Q^2) = \Delta t \approx \frac{1}{\Delta E} \approx \frac{2\nu}{Q^2 + M_V^2} = \frac{1}{Mx}\frac{1}{1 + M_V^2/Q^2} \tag{1.43}$$

and will have a mean free path $l(M_V^2) = 1/[\sigma_V(M_V^2)n_0]$, where n_0 is the nucleon density and $\sigma_V(M_V^2)$ is the cross section for interactions of the hadronic system of mass M_V with the nucleon. Necessary conditions for shadowing are that $d(M_V^2, Q^2) > l(M_V^2)$ and $R_A > l(M_V^2)$, with R_A the nuclear radius. Shadowing due to a fluctuation of mass M_V will thus disappear, at fixed ν, with increasing Q^2 because of the decrease of $d(M_V^2, Q^2)$. Conversely, at fixed Q^2, shadowing will decrease with increasing x. For $Q^2 = 0$ we recover the real photon case and we see that the length over which the hadronic fluctuation travels is directly proportional to ν. Shadowing of real photons will thus be a growing function of the photon energy.

The assertion that the hadronic fluctuations of the photon are solely constituted by the vector mesons ρ^0, ω and ϕ defines the VMD model in its simplest form [162]-[164]. The less restrictive assumption that higher mass resonances are also involved leads to the Generalized Vector Meson Dominance (GVMD) model.

In both VMD and GVMD the transverse virtual photon-nucleon cross section reads:

$$\sigma_{\gamma N} = \sum_i \frac{M_{V_i}^4}{(Q^2 + M_{V_i}^2)^2} \left(\frac{e}{f_i}\right)^2 \sigma_{V_i} \tag{1.44}$$

where the sum is over the vector mesons V_1, V_2, ..., V_N, the ratio (e/f_i) is the vector meson-photon coupling and σ_{V_i} is the total V_i-N cross section. The quantity

$$\frac{M_{V_i}^4}{(Q^2+M_{V_i}^2)^2}=\frac{1}{(1+Q^2/M_{V_i}^2)^2}$$

is the vector meson propagator squared. The only difference between VMD and GVMD is in the number of vector meson states V_i over which the sum is extended.

In the cross section 1.44 the possibility of interference between different vector states belonging (in the VMD sense) to the photon is excluded: such (G)VMD models are known as *diagonal* ones. *Off-diagonal* models include instead interference terms; the cross section in this case is:

$$\sigma_{\gamma N}=\sum_i\sum_j\frac{M_{V_i}^2}{Q^2+M_{V_i}^2}\frac{e}{f_i}\frac{M_{V_j}^2}{Q^2+M_{V_j}^2}\frac{e}{f_j}\sigma_{V_iV_j}, \tag{1.45}$$

where now $\sigma_{V_iV_j}$ is the total cross section for the process $V_iN\to V_jN$.

It is clear from relations 1.43-1.45 that the inclusion of higher mass resonances makes shadowing less lensitive to variations of Q^2; the inclusion of the off-diagonal transitions also may affect the Q^2 dependence of shadowing. The dependence of σ_V or $\sigma_{V_iV_j}$ on the mass of the vector mesons gives a further degree of freedom. Finally, the sums in 1.44 and 1.45 can be extended to an infinite series of vector states; in this case the equal spacing ansatz $M_{V_i}^2=M_0^2(1+i\lambda)$ is often taken for the spectrum of the vector states. Alternatively the sums can be turned into integrals. Formula 1.44 then becomes

$$\sigma_{\gamma N}=\int_{M_{thr}^2}^{\infty}dM_V^2D(M_V^2)\frac{M_V^4}{(Q^2+M_V^2)^2}\left(\frac{e}{f(M_V^2)}\right)^2\sigma(M_V^2), \tag{1.46}$$

where the lower limit of integration is generally set to twice the pion mass squared: $M_{thr}=2m_\pi$ and where we have introduced the density of vector states per unit mass squared interval: $D(M_V^2)=dN/dM_V^2$. The function D and the coupling (e/f) may be related to the cross section for e^+e^- annihilations into hadrons [159]:

$$\sigma_{e^+e^-}=16\pi^3\alpha^2\left[\frac{D(M_V^2)}{f^2(M_V^2)}\right]. \tag{1.47}$$

Using this relation and the ratio

$$R_{e^+e^-}(M_V^2)=\frac{\sigma(e^+e^-\to hadrons)}{\sigma(e^+e^-\to\mu^+\mu^-)} \tag{1.48}$$

with $\sigma(e^+e^-\to\mu^+\mu^-)=4\pi\alpha^2/(3M_V^2)$, one can rewrite the integral 1.46 as

$$\sigma_{\gamma N}=\frac{\alpha}{3\pi}\int_{M_{thr}^2}^{\infty}dM_V^2R_{e^+e^-}(M_V^2)\frac{M_V^2}{(Q^2+M_V^2)^2}\sigma(M_V^2). \tag{1.49}$$

Since $R_{e^+e^-}\sim const.$, in order for the integral in 1.49 to converge and for $\sigma_{\gamma N}$ to have the usual "scaling" behavior $\sigma_{\gamma N}\sim 1/Q^2$, the cross section $\sigma(M_V^2)$ must vary as $1/M_V^2$. This is somewhat non intuitive; off-diagonal models allow the more natural assumption $\sigma(M_V^2)\sim const.$

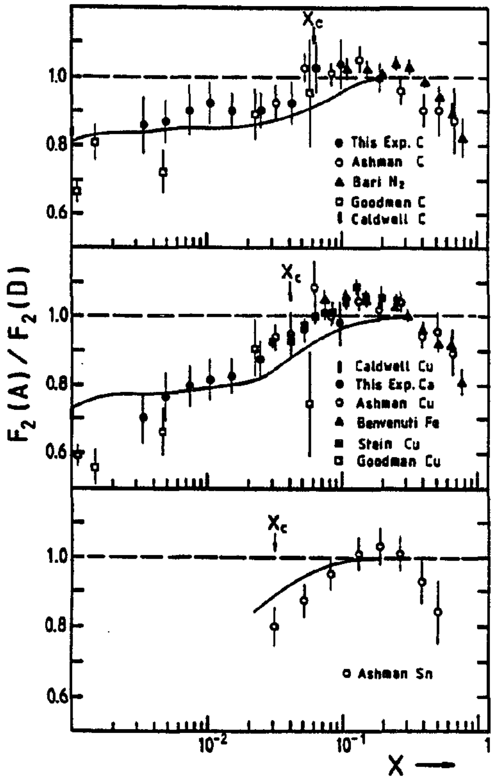

Figure 1.47: Predictions of the model of Schildknecht [165] compared with the experimental results of fig. 1.16 (from [169])

Only GVMD models are flexible enough to reproduce the experimental data both for $\sigma_{\gamma N}$ and $\sigma_{\gamma A}$ (notably their Q^2 dependence). We will now review the available formulations of GVMD limiting our discussion to those proposed or revived after the experimental situation was clarified by the quoted EMC results [38]-[40]. These models may have some relevance for the NMC data discussed in the present work.

One of the longest lived models is the effectively diagonal one of Schildknecht, originally proposed in 1973 [165]-[170]. In this model the sum over the ρ, ω and ϕ contributions is complemented by the integration over a higher mass continuum; the size of the continuum contribution is normalized at $Q^2 = 0$ to be 22% of the cross section, so as to guarantee the correct normalization of the total photo-production cross section. The cross section $\sigma(M_V^2)$ is assumed to vary as $\sigma(M_V) \sim 1/M_V^2$. This behavior is an effective one and in [167, 168] it is shown to be a consequence of the interference between different vector mesons in a full off-diagonal model in which $\sigma(M_V) \sim$ *const.* – as expected from the fact that strong interaction cross sections do not depend much on the mass of the particle. Figure 1.47 shows a comparison of the model predictions with the compilation of data already presented in fig. 1.16. Predictions of the A and Q^2 dependence of this shadowing model in specific x and Q^2 bins can be found in [170].

A similar formulation is the one of Piller, Takayanagi and Weise [171]-[173]. The calculation

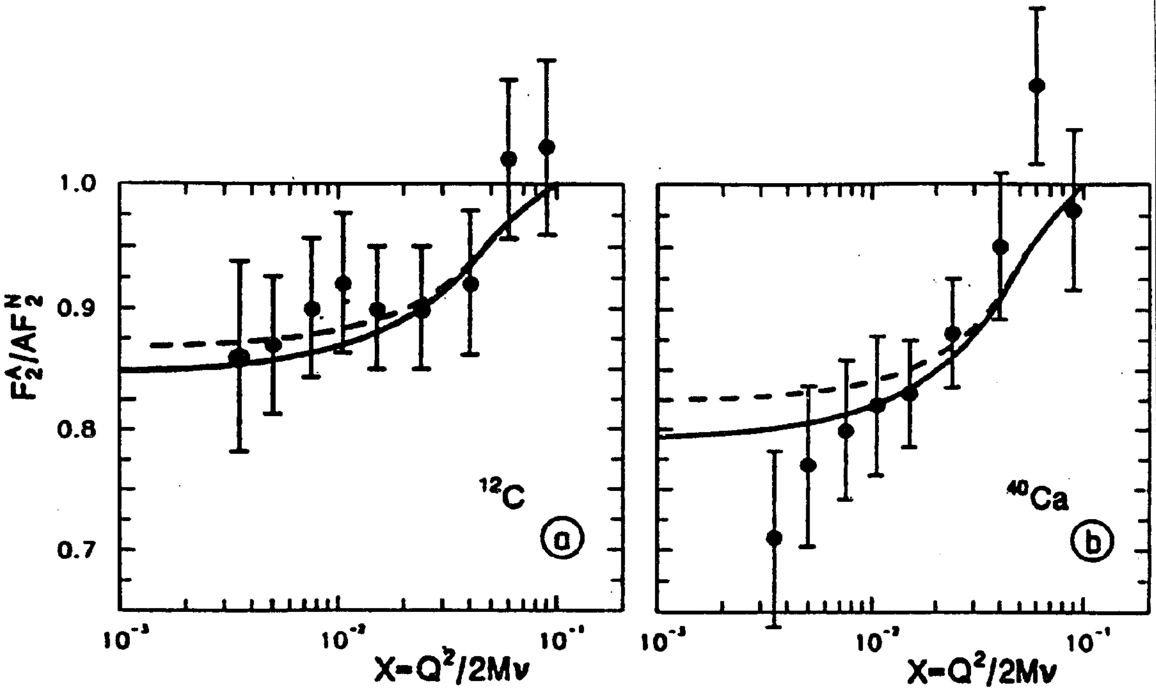

Figure 1.48: The predictions of the model of Piller *et al.* [171] compared with the EMC NA28 results [40]; the dashed curves are obtained if the low mass vector mesons ρ, ω and ϕ only are included (from [171])

is based on formula 1.49 where the effective vector meson-nucleon cross section $\sigma(M_V^2)$ is taken, here as well, as $\sim 1/M_V^2$. Predictions are given (fig. 1.48) for the ratio of the C and Ca to D structure functions.

In the framework of this model (and the previous one) the shadowing effect is dominated by the low mass vector mesons, as can be seen from the dashed lines in fig. 1.48. This is because the propagation length of these states is large compared to the nuclear size; in addition their mean free path in nuclear matter is smaller than that of the high mass components because of the $1/M_V^2$ behavior of the vector meson-nucleon cross section. The authors point out however that without the inclusion of the higher mass mesons it would not be possible to reproduce the Q^2 dependence of $\sigma_{\gamma N}$.

Figure 1.49 shows the Q^2 dependence expected in this model for the carbon and calcium to deuterium ratios. For Q^2 larger than 1 GeV^2 shadowing decreases nearly logarithmically with increasing Q^2. At very small Q^2 (< 1 GeV^2) and $x > 0.03$ the opposite trend is predicted, reflecting the Q^2 dependence of the coherence length $d(M_V^2, Q^2)$.

The EMC NA28 data have also been compared [174] with the predictions of the off-diagonal GVMD model of Ditsas and Shaw [175, 176]. The virtual photon-nucleon cross section is expressed here by means of a relation of the type 1.45, in which the sum is extended to a series of mesons equally spaced in mass; only diagonal and next-to-diagonal transitions are allowed, i.e. $i = j \pm 1$. Furthermore the diagonal vector meson-nucleon cross sections $\sigma_{V_iV_i} = \sigma_{V_i}$ are taken to be the same as that of the ρ^0, which is parametrized as

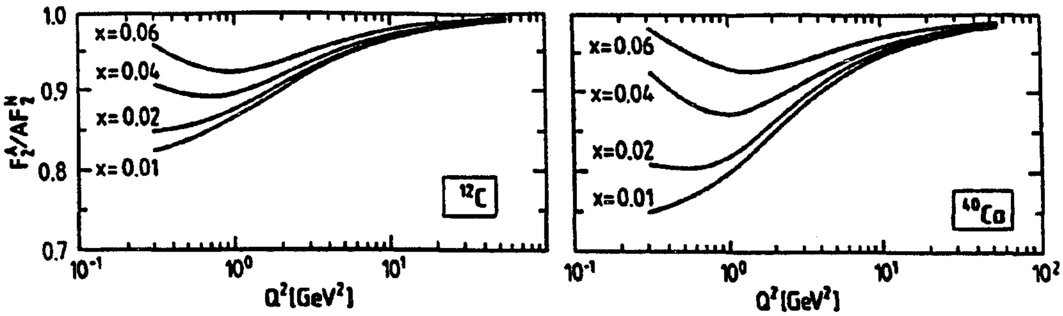

Figure 1.49: Predictions of the model of Piller *et al.* [171] for the Q^2 dependence of shadowing (from [173])

$$\sigma_\rho = a + \frac{b}{\sqrt{E}}, \tag{1.50}$$

where $E \approx \nu$ is the energy of the meson. Note that this behavior is rather different from the $\sigma_V \sim 1/M_V^2$ one of the other two models. When ν and Q^2 become large, the second term in 1.50 becomes small and shadowing is then approximately Q^2 independent, since at large Q^2 and fixed x the coherence length d is also roughly Q^2 independent. The amplitudes of the transitions $V_i \to V_j$ are adjusted so as to obtain Q^2 independence a large Q^2 and a good fit to the nucleon electroproduction data. Figure 1.50 shows the predictions of the model and the EMC NA28 data.

Partonic Models

The first discussion of shadowing in a partonic approach is the one of N.N. Nikolaev and V.I. Zakharov [177]. Parton-nucleus scattering is considered in the Breit frame, where the energy of the virtual photon is zero and the three-momentum of the scattered parton is exactly reversed by the collision. A parton carrying a fraction x of the nucleon's momentum P_N can only be localized longitudinally to within a distance $\Delta z \sim 1/(xP_N)$ (the "longitudinal dimension" of the parton), as can be seen by using the uncertainty principle. On the other hand the nucleons are separated by a distance

$$\Delta z_N \sim 2R_N$$

(with the nucleon radius $R_N \approx 1$ fm) in the laboratory frame or

$$\Delta z_N \sim 2R_N \frac{M}{P_N} \tag{1.51}$$

in the Breit frame. So for $x < x_N = 1/(2R_N M) \approx 0.1$ partons belonging to different nucleons at the same impact parameter start to overlap spatially. In fact, for x values smaller than $x_A = 1/(2R_A M) \approx x_N A^{-1/3}$ (R_A = the nuclear radius), Δz exceeds the Lorentz contracted nuclear diameter and partons from all nucleons (at the given impact parameter) overlap. Overlapping partons can interact and fuse, thereby reducing the parton density at small x.

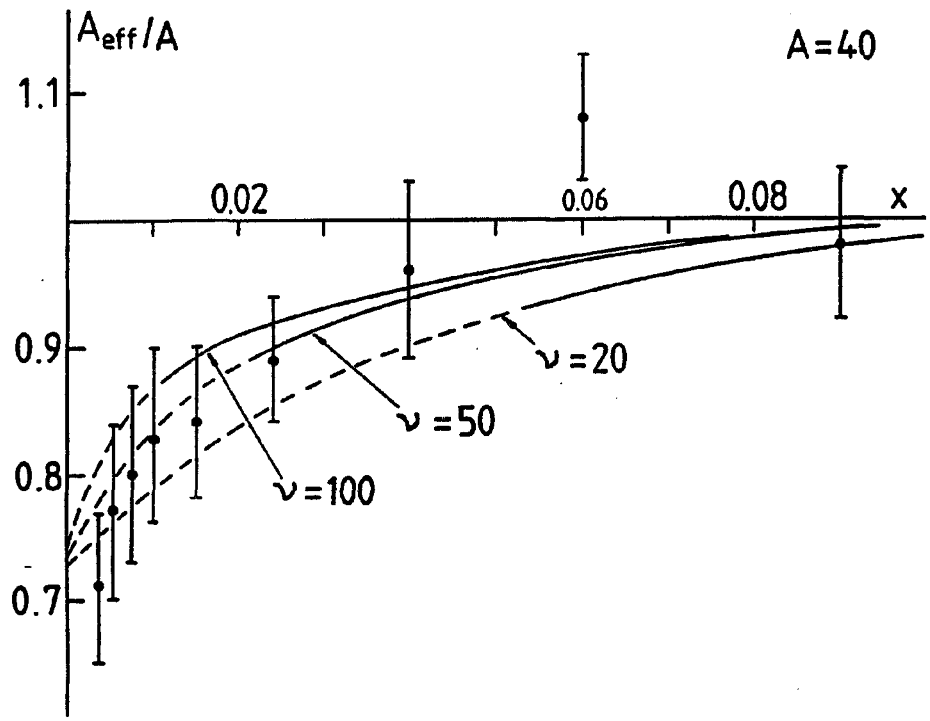

Figure 1.50: Comparison of the predictions of Shaw [174] with the NA28 results of fig. 1.16 for Ca (from [174])

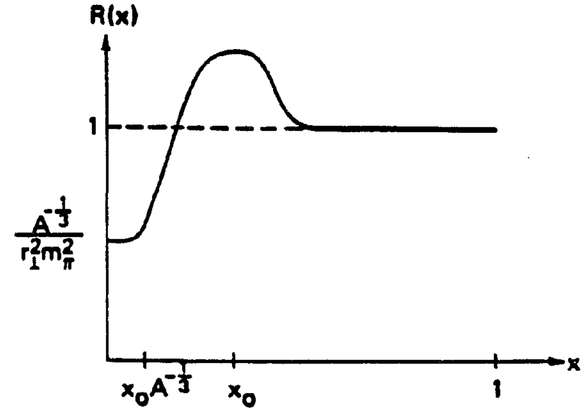

Figure 1.51: Qualitative features of the bound to free nucleon structure function ratio in the partonic model of Nikolaev and Zakharov [177] (from [177])

The total momentum carried by partons is not changed as a result of the fusion but is simply redistributed to different x regions. The depletion of low momentum partons due to the fusion process thus leads to an enhancement in the density of higher momentum partons, expected to be maximum around $x \approx x_N$.

Since in DIS the cross section is proportional to the parton distribution functions, the depletion of low x partons causes a depletion in the nuclear structure functions which starts somewhere below x_N and becomes maximum at $x \approx x_A$. Similarly the enhancement in the parton density at $x \approx x_N$ determines an increase of the bound nucleon structure functions with respect to the free nucleon ones, labelled "anti-shadowing". The prediction of anti-shadowing is a feature characteristic of the partonic approach. Also characteristic of this treatment, and in contrast with the VMD models, is the fact that shadowing and anti-shadowing do not disappear with increasing Q^2, but are rather functions of x alone (they "scale"). The qualitative trend of the ratio according to Nikolaev and Zakharov is shown in fig. 1.51.

More recently Müller and Qiu [178] approached parton fusion in a perturbative QCD framework and studied the consequences of gluon recombination. They derived modified, non-linear evolution equations which include gluon recombination effects. Such effects turn out to be significant only if evolution is started below ≈ 2 GeV^2. They concluded that the main consequence of gluon recombination is a depletion of the gluon distribution in nuclei at small x which reflects into a depletion of the sea quark density; the direct shadowing of sea quarks themselves appears instead to be a smaller effect.

By means of these modified Altarelli-Parisi equations, Qiu [179] focused on the Q^2 evolution of shadowing. The nuclear parton distribution functions used as an input are a product of a phenomenological shadowing function R_s and a parametrization of the parton distributions in the nucleon. The explicit form for R_s, often referred to in the later literature, is:

$$R_s(x, Q_0^2, A) = \begin{cases} 1 & x_N < x < 1 \\ 1 - K(A^{1/3} - 1)\frac{\Delta V_A}{V_A} & x_A < x < x_N \\ 1 - K(A^{1/3} - 1) & 0 < x < x_A \end{cases} \tag{1.52}$$

where the constant factor K is different for sea quark and gluon distributions and must be determined by comparison with the experimental data. The quantity

$$\frac{\Delta V_A}{V_A} = \frac{1/x - 1/x_N}{1/x_A - 1/x_N} \tag{1.53}$$

is a measure of parton overlap which is zero at $x = x_N$ and maximum at $x = x_A$. The term $(A^{1/3} - 1)$ gives the average number of shadowed nucleons: at very small x the photon cannot distinguish between partons of different nucleons at the same impact parameter; for large enough A, say $A > 8$, the effective number of nucleons thus equals the number of surface nucleons, $\approx R_A^2/R_N = A^{2/3}$, and the number of "shadowed" nucleons (per effective nucleon) is $n_s = (A - A^{2/3})/A^{2/3} = A^{1/3} - 1$. Note that expression 1.52 just parametrizes the x dependence of shadowing, does not predict it. The main conclusion of Qiu is that the Q^2 dependence of shadowing is very weak, in agreement with the original prediction of Nikolaev and Zakharov.

After the publication of the EMC NA2′ and NA28 results Berger and Qiu [180] elaborated on this approach, concentrating on the A dependence of the point where shadowing sets on. These authors observed that the average longitudinal distance between one parton from a nucleon and another from a neighboring nucleon is larger for nucleons on the surface of the nucleus than for nucleons well inside the nucleus. As a result of these surface versus volume effects, the onset of shadowing is seen to increase with A:

$$\hat{x}_N = \frac{1}{MR_N\left[1 + 3\frac{2}{A^{1/3}} - 3\left(\frac{2}{A^{1/3}}\right)^2 + \left(\frac{2}{A^{1/3}}\right)^3\right]}, \tag{1.54}$$

where the new symbol for the onset of shadowing is meant to emphasize the fact that $\hat{x}_N \neq 1/(2R_N M)$. The value of $\hat{x}_N$ rises from $\hat{x}_N = 0.08$ for ^{4}He to 0.1 for ^{12}C and 0.107 for ^{64}Cu. While this trend is in qualitative agreement with the data, it is not entirely clear however what the actual meaning of $\hat{x}_N$ is (whether for instance it should be identified with the x value corresponding to the maximum of the structure function ratio, in the anti-shadowing region, or with the point where the ratio is unity or, more probably, with some other point in between).

While retaining the partonic mechanism of Qiu [179], Close and Roberts [181] later attempted to justify the A dependence of the onset of shadowing with arguments based on the Q^2 rescaling model which, as we have seen, may be used to describe the structure function ratio for x values between 0.2 and 0.6. In this model the nuclear structure functions per nucleon at a specific Q^2 are given by the free nucleon structure functions at a larger value of Q^2:

$$F_2^A(x, Q^2) = F_2^N(x, \xi(Q^2)Q^2), \tag{1.55}$$

where the A dependence of the parameter ξ is controlled by the average nucleon density. If the density is high there is a sizable probability for the nucleons to overlap, thereby modifying the confinement scale of quarks. As the density of nucleons grows with increasing A, the distance between neighboring nucleons decreases; so does the distance between partons, thus making it more likely for them to fuse. As a consequence the onset of shadowing $\hat{x}_N$ grows with A. With the overlap probabilities evaluated in [103], the results found for carbon, copper and tin are $\hat{x}_N = 0.121, 0.130$ and 0.135, respectively. The trend is similar to that found by Berger

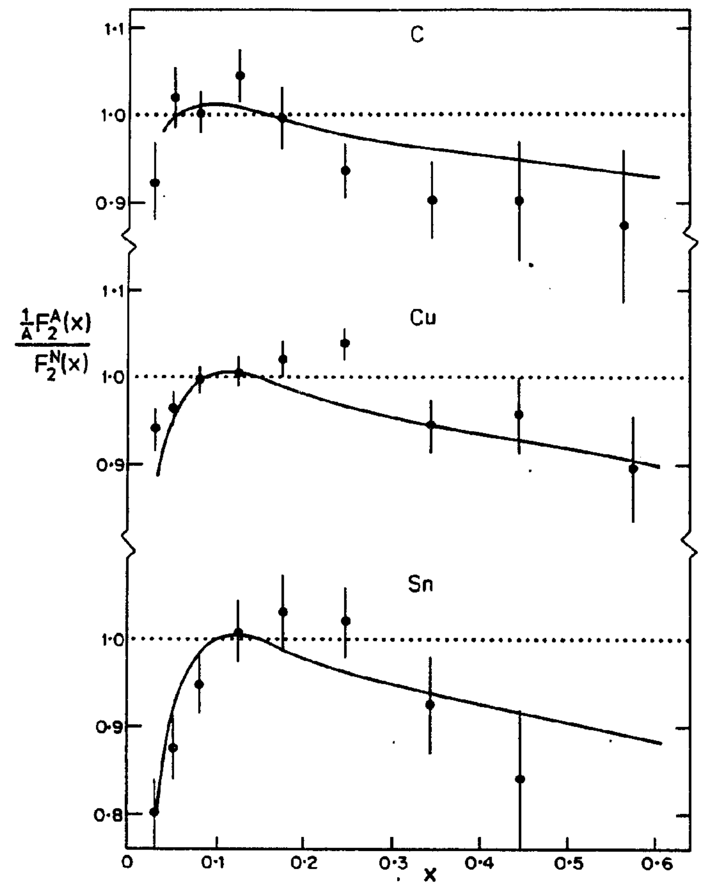

Figure 1.52: Comparison of the predictions of Close and Roberts [181] with the EMC NA2′ results [38] (from [181])

and Qiu [180] and also seen in the data. Again it is difficult to identify the actual meaning of $\hat{x}_N$ in terms of measured quantities, but the authors claim that at least its variation with A should be analogous to that of the point where the ratio equals unity. In the EMC NA2′ data [38, 39] this cross-over point moves by ≈ 0.06 in going from carbon to tin, as opposed to the predicted variation of $\hat{x}_N$, $\Delta\hat{x}_N = 0.014$. The discrepancy motivated Close and Roberts to propose that the value of x_A, where shadowing saturates, is A independent, unlike what was previously assumed. The A independence of x_A means that shadowing saturates already when Δz exceeds only few nucleon dimensions. The assumption is made that this occurs when at least 12 nucleons are involved. In other words x_A is taken to be a constant for $A > 12$; its value is set to $x_A = 1/(2MR_A)$ with R_A the radius of the carbon nucleus, resulting in $x_A \approx 0.043$. This assumption is combined with the A dependence of $\hat{x}_N$ found with the Q^2 rescaling hypothesis. The nuclear structure functions are then computed by applying Q^2 rescaling to the parton distributions at all x; furthermore the sea quark distribution in the nucleus is suppressed by the shadowing function 1.52, with $K \approx 0.1$ and the values of $x_N = \hat{x}_N$ and x_A just discussed. Figure 1.52 shows that the predictions thus obtained are in fair agreement with the data.

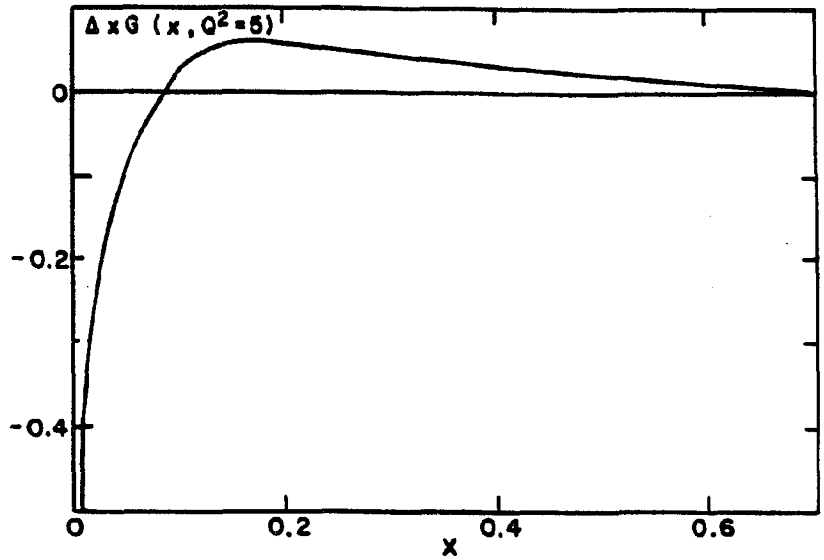

Figure 1.53: Parton recombination contribution to the gluon distribution $xG(x)$ at $Q^2 = 5$ GeV^2 (from [182])

In the papers just discussed ([178]-[181]) the x dependence of shadowing was essentially assumed by using phenomenological parametrizations. Close, Qiu and Roberts [182] attempted a semi-quantitative derivation of the shape of shadowing based on the parton fusion picture and corroborated by QCD arguments. The results can be summarized as follows. Perturbative QCD studies how parton distributions evolve as a consequence of quarks radiating gluons, gluons converting into $q\bar{q}$ pairs and gluons splitting into gluon pairs. Quarks and gluons can of course also fuse, but these diagrams are generally not studied individually; rather their effects are subsumed into the input parton distributions. Fusion diagrams are instead explicitely considered in this paper and the equivalent of the parton splitting functions for the fusion processes $qg \to q$, $gg \to g$ and $q\bar{q} \to g$ ("parton fusion functions") are evaluated.

The results are applied to the case of nuclear structure functions, starting from the situation in which gluons and sea quarks leak from a nucleon into a neighboring one and recombine with the quarks and gluons of that nucleon. Leakage of gluons and leakage of sea quarks are studied separately. Figure 1.53 shows the resulting effect on the gluon distribution $xG(x)$ for Fe at $Q^2 = 5$ GeV^2. The effect mainly arises from $gg \to g$ processes, rather than from $q\bar{q} \to g$ or $qg \to q$ ones. It turns out that only about 0.1% of the nuclear momentum is transferred from quarks to gluons: momentum conservation is thus assured almost separately within the individual parton species.

The distinction is made between "initial state recombination", with which this paper is concerned (fig. 1.54(b)), and the so-called "radiative recombination" (fig. 1.54(d)). Initial state recombination dominates at small Q^2; for higher Q^2 the net effect is a mix of the two types of recombination. The Q^2 dependence of radiative recombination was the subject of the papers of Qiu [179] and Müller and Qiu [178], presented above.

In principle one should thus first compute the effects of initial state recombination to obtain the x dependence of the parton distributions at some low scale Q_0^2; these should then be fed

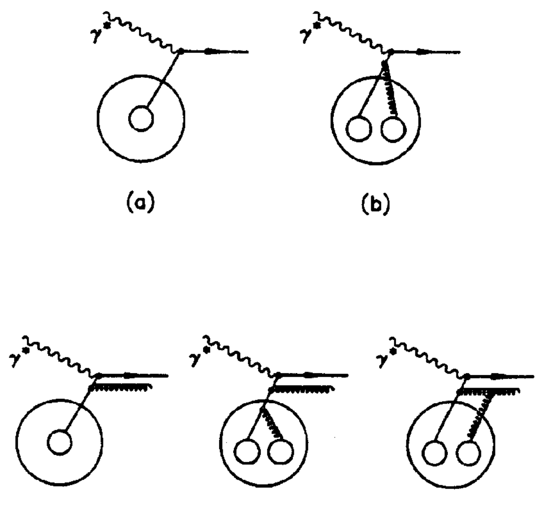

Figure 1.54: The leading contribution (a) and the leading fusion correction (b) to the effective nuclear parton distributions (initial recombination) at a given Q^2; the fusion occurring at a lower $Q^2 = Q_0^2$ affects the distribution at higher Q^2 via the input distribution at Q_0^2 (c); radiative recombination (d) (from [182])

into the evolution equations in order to obtain the parton distributions at larger Q^2.

The picture that emerges is consistent with the known experimental facts about shadowing. A quantitative evaluation of the shape of shadowing is however precluded by the ignorance of the value of Q_0^2 at which the initial recombination mechanism is dominant over the radiative one and from which evolution begins.

The view that interactions between gluons and sea quarks from neighboring nucleons give rise to shadowing is shared by Guanglie, Zhijun and Chasheng [183]. They proposed a phenomenological description of shadowing in which the bound nucleon structure functions are given by the free nucleon ones multiplied by the shadowing factor:

$$R_s(x, Q^2, A) = \begin{cases} 1 & x_N < x < 1 \\ 1 - K_A \frac{\Delta V_A}{V_A} & 0 < x < x_N, \end{cases} \tag{1.56}$$

where again $x_N = 1/(2R_N M)$. The parameter K_A is a function of A only. The parton overlap probability $\Delta V_A / V_A$ is similar to the one defined by Qiu [179] and discussed above, but is computed by assuming realistic nuclear density distributions. This description of the bound to free nucleon structure function ratio at small x is associated with a standard x rescaling model for the larger x region. The rescaling parameter is however different for valence and sea quarks so as to retain longitudinal momentum conservation (overall momentum conservation was not explicitely required in the models [178]-[181]).

Figure 1.55 compares the predictions thus obtained with the EMC NA2′ results. This model, while adopting a partonic mechanism to interprete shadowing, describes the enhancement region at intermediate x in terms of the interplay between shadowing at low x and rescaling at larger x. This is similar to what is done by Close and Roberts; here as well no mention is made of the possibility that the enhancement may be seen as anti-shadowing in the partonic sense, as discussed for instance by Nikolaev and Zakharov.

A somewhat different approach is the one developed by Zhu and collaborators [184]-[190] within the framework of the constituent quark model [191, 192]. In this approach the nucleon is viewed as composed of three constituent quarks or "valons". Valons are themselves composite objects, made up of the familiar quarks and gluons; the nucleon structure functions are thus the convolution of the constituent quark distribution G_N^c with the distribution F_N^c of the quarks and gluons in a constituent quark:

$$F_N(x, Q^2) = \sum_i \int_x^1 dy G_{N_i}^c(y) F_{N_i}^c(x/y, Q^2), \tag{1.57}$$

where the sum is over the three valons. The constituent quark distribution G_N^c is normalized to unity:

$$\int_0^1 G_N^c(y) dy = 1. \tag{1.58}$$

Furthermore each constituent quark is assumed to carry, on the average, 1/3 of the longitudinal momentum of the nucleon:

$$\int_0^1 G_N^c(y) y dy = 1/3. \tag{1.59}$$

The shape of G_N^c is determined by the interactions among the constituent quarks and is independent of the probe. The parton distribution F_N^c in a constituent quark depends instead on the Q^2 of the probe. At small Q^2 the virtual photon "sees" a structureless constituent quark (the valence quark, effectively); as Q^2 increases the structure of the constituent quark evolves according to QCD and the photon sees the usual sea quarks.

The nuclear medium influences both the structure functions F^c of the constituent quarks and the shape of their distribution functions G^c, but does not affect the two conditions 1.58 and 1.59.

Let us begin with F^c. The main point here is that the gluons and the sea quarks of the three constituent quarks recombine with those of other bound nucleons so that the sea distribution is hardened. This is the usual recombination approach and gives rise to shadowing and anti-shadowing.

More in detail, several mechanisms are at work. In the QPM with QCD, sea quarks are produced by the splitting process $g \to q\bar{q}$, while gluons essentially originate from the QCD bremsstrahlung of valence quarks. Shadowing of the sea quarks goes predominantly via $q\bar{q} \to g$ recombination and via the gluon-gluon fusion process $gg \to g$. Shadowing of the gluons proceeds instead only via gg fusion, since shadowing of the valence distribution is assumed to be negligible. It is thus expected that shadowing of the sea distribution is stronger than that of the gluons. Similar conclusions were also reached in [178, 179].

With increasing Q^2, the rate of $q\bar{q}$ and gg recombination processes increases since such processes are proportional to the q, $\bar{q}$ and g densities squared, which increase with Q^2. However,

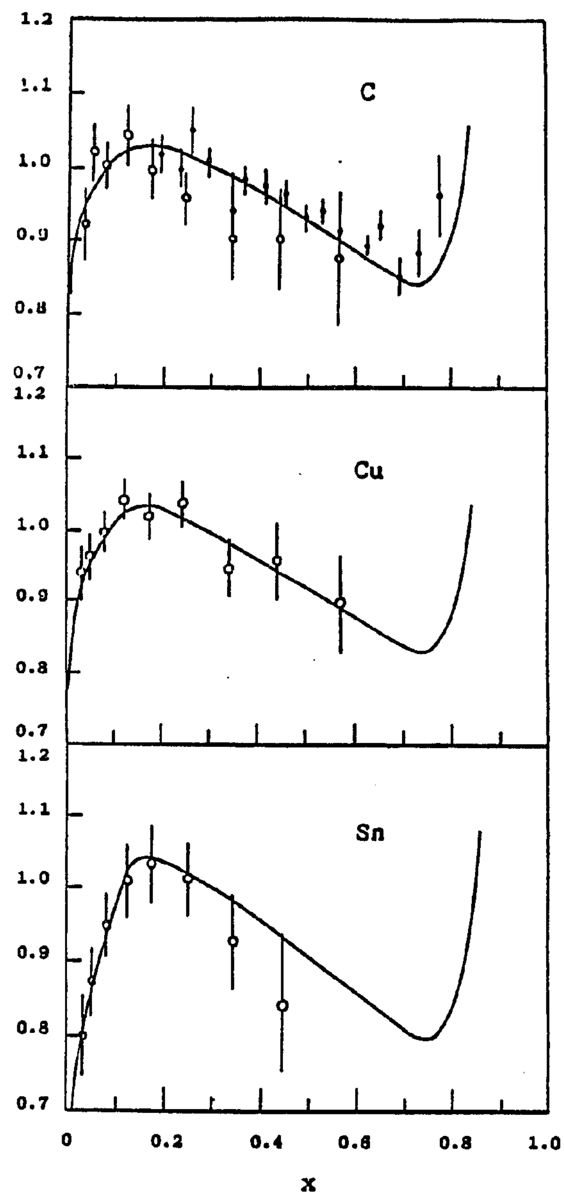

Figure 1.55: Comparison of the predictions of Guanglie *et al.* [183] with the EMC NA2′ results [38] (from [183])

the increase of the gluon density determines an increase of the $q\bar{q}$ production rate, which compensates for the enhanced rate of recombination; since gluons are less shadowed than sea quarks, there is in fact some over-compensation and a logarithmic decrease of the size of sea quark shadowing is expected. Remarkably also anti-shadowing is predicted to decrease and eventually disappear at large Q^2 values ($\sim$ 40 GeV^2). Notice that the $q\bar{q} \to g$ process transfers momentum from the quarks to the gluons and that the net momentum fraction transferred rises with Q^2. This conclusion is at variance with that reached by Close, Qiu and Roberts [182].

The x dependence of shadowing is obtained with a prescription similar to that of Müller and Qiu (cf. eq. 1.52): at $x = 0$ one has

$$F_A^c(Q^2) = F_N^c(Q^2)(1 - n_s K), \tag{1.60}$$

with n_s the number of shadowed nucleons (per surface nucleon), $n_s = (A^{1/3} - 1)$ for large A. For larger values of x the following ansatz is made:

$$F_A^c(x) = \begin{cases} \alpha(1-x)^\beta & 0 < x < x_N \\ \left[\alpha(1-x_N)^\beta - F^c(x_N)\right] f(x) + F^c(x) & x_N < x < 1 \end{cases} \tag{1.61}$$

where $F^c(x)$ is the distribution in the absence of shadowing and anti-shadowing. The function $f(x)$ gives the magnitude of anti-shadowing and is proportional to the gluon density squared at $x/2$: $f(x) \sim [G(x/2)]^2$.

We come now to the effects of the nuclear medium on G^c. The constituent quarks are assumed to be bound by a harmonic oscillator potential and the effect of the nuclear medium is expressed in terms of a weakening of the spring constant. This picture is not unique and an equivalent description can be obtained by increasing the constituent quark confinement size. The effect is in both cases a softening of the constituent quark distribution G^c; the degree of softening is related to the nuclear density. In practice then, like in many of the models discussed so far, the description of the shadowing mechanism is combined with a model of the EMC effect at larger values of x.

Figure 1.56 shows a comparison of the predictions of this model with the EMC NA2′ and NA28 results; the theoretical curves are for $Q^2 = 1$ GeV^2. Figure 1.57 shows the expected Q^2 dependence of the calcium to deuterium structure function ratio.

Castorina and Donnachie [193, 194] also argued that shadowing can be explained at the partonic level, but adopted a different framework. Their starting point is that the small x behavior of the structure function F_2 is controlled by pomeron exchange (see fig. 1.58). In this approach the virtual photon scatters off a pomeron emitted by the nucleon, thus probing the parton content of the pomeron rather than that of the nucleon itself. The authors suggest that in a nuclear environment the effective coupling β_q of the pomeron to a quark is suppressed because of nucleon overlap, i.e., with reference to fig. 1.58, $\tilde{\beta}_q < \beta_q$. This overlap effectively reduces the volume occupied by each nucleon and decreases the mean distance between the quarks of different nucleons. The hypothesis that the spatial separation between quarks (i.e. the radius of the hadron) determines the strength of the quark-pomeron coupling is consistent with the observation that the total hadron-hadron cross section is proportional to the squared radii of the interacting hadrons [195]. As the total cross section is also proportional to the effective quark-pomeron coupling, its variation can be interpreted in terms of a dependence of the pomeron coupling on the hadron radius [196, 197]. Quantitatively the structure functions

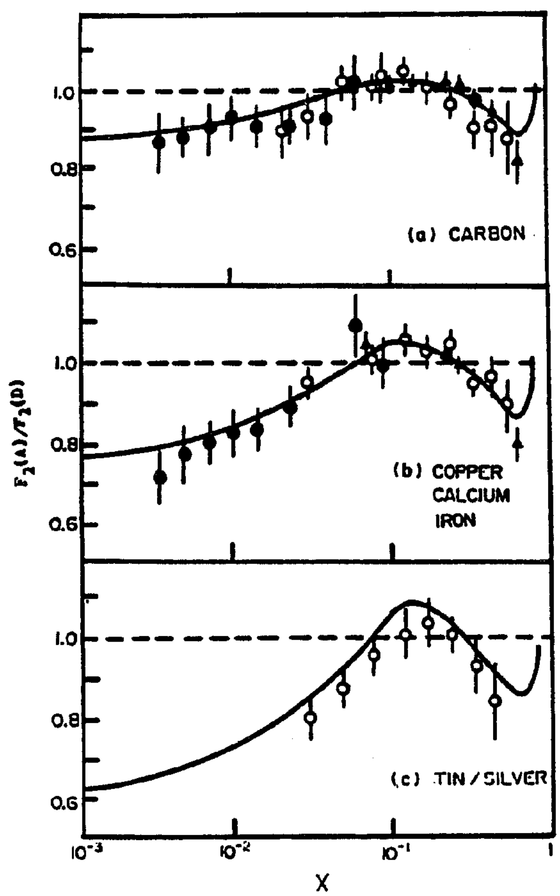

Figure 1.56: Comparison of the predictions of Zhu *et al.* [186] with the EMC NA2′ [38] and NA28 results [40] (from [186])

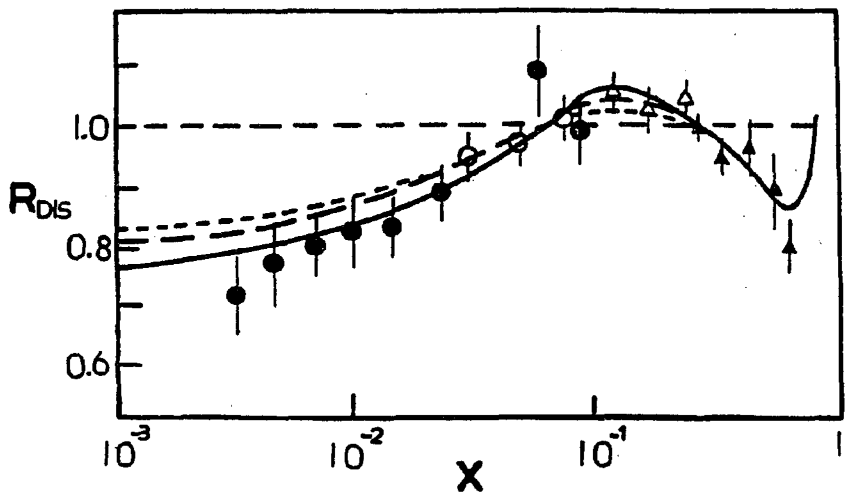

Figure 1.57: Predictions of the model of Zhu *et al.* [187] for the Q^2 dependence of the calcium to deuterium structure function ratio; continuous line: 1 GeV^2; dashed line: 10 GeV^2; dotted line: 40 GeV^2. The data points are the same as in fig. 1.56 (from [187])

at small x are then expected to be suppressed in a bound nucleon with respect to a free one by a factor proportional to the average nucleon-nucleon distance squared. This treatment of the low x behavior of nuclear structure functions is coupled with a description of the large x ($0.3 < x < 0.6$) behavior of the EMC effect based on the x rescaling model of Akulinichev *et al.* [79].

Once again the interpretation of anti-shadowing in partonic terms is abandoned and the description of the enhancement at intermediate x is left to the interplay between shadowing and x rescaling. The resulting prediction for the ratio of bound to free nucleon structure functions is shown in fig. 1.59.

Finally, Brodsky and Lu [198] proposed a semi-quantitative description of shadowing and anti-shadowing in a somewhat hybrid framework. The virtual photon is assumed to convert to a $q\bar{q}$ pair at a distance before the target proportional to $\sim 1/x$, in the laboratory frame. In the Bjorken limit and in an appropriate gauge the final state interactions of the quark can be neglected and effectively only the anti-quark interacts. The anti-quark-nucleus scattering amplitude is obtained from the anti-quark-nucleon one by means of Glauber's multiple scattering series. At very small x the $\bar{q}N$ amplitude is taken to be dominated by pomeron exchange and is mainly imaginary; as we emphasized earlier, this gives rise to shadowing. In order to reproduce the enhancement at larger values of x, the authors argue that the real part of the amplitude becomes important in this region; in the Regge language this amounts to describing the scattering process in terms of a superposition of reggeons.

Figure 1.60 compares the predictions of the model with the EMC NA2′ [38] and NA28 [40] data.

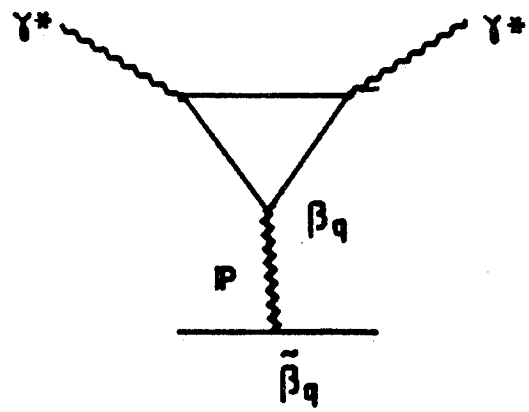

Figure 1.58: Compton scattering in the pomeron exchange picture (from [193])

Models which Combine the GVMD and the Partonic Approaches

Kwieciński and Badełek [199] proposed a model which combines both the rescattering of low mass vector mesons and the partonic mechanism of shadowing in order to describe nuclear structure functions in the region of $0.001 < x < 0.1$ and $0.1 < Q^2 < 10$ GeV^2. In their model, the structure function F_2^A of a bound nucleon is related to the free nucleon structure function by the following expression:

$$AF_2^A = AF_2^N - \Delta F_2^{(v)} - \Delta F_2^{(p)}; \tag{1.62}$$

$\Delta F_2^{(v)}$ and $\Delta F_2^{(p)}$ are the vector meson and partonic contributions to shadowing, respectively.

- The vector meson contribution $\Delta F_2^{(v)}$ is obtained as usual by means of relation 1.44; the sum is restricted to the ρ^0, ω and ϕ mesons only. The interactions of vector mesons with the nucleus are treated in the Glauber approximation and the nucleus is taken to be a sphere of uniform density and radius $R = r_0 A^{1/3}$.

- The partonic term $\Delta F_2^{(p)}$ is discussed in the pomeron exchange language used also by Castorina and Donnachie [193] and Brodsky and Lu [198]. Figure 1.61 shows the forward elastic photon-nucleon (Compton) scattering diagram; at small x the blob in the figure corresponds to the photon-pomeron interaction shown in fig. 1.62. When the target is a nucleus rather than a nucleon, the multiple scattering terms of fig. 1.63 must be considered, in which the double interaction diagram of fig. 1.64(a) dominates. At small x this process is controlled by the double pomeron exchange of fig. 1.64(b). The pomeron structure function in this figure has two major components: the triple pomeron (fig. 1.64(c)) and the quark box diagram contribution (fig. 1.64(d)).

In the region $0.75 < Q^2 < 1.5$ GeV^2 shadowing turns out to be practically independent of Q^2. The partonic contribution is instrumental in this respect, since the contributions due to the rescattering of vector mesons decrease significantly over this region of Q^2. Figure 1.65 shows a comparison of the model calculation with various data sets, including the EMC NA2′ and NA28 ones.

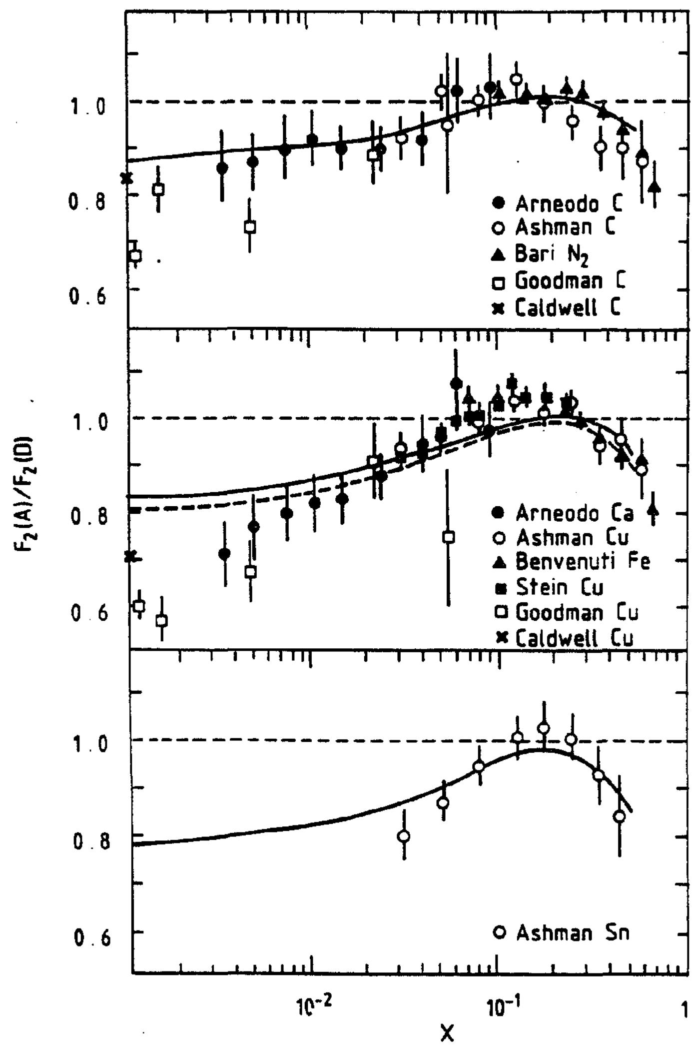

Figure 1.59: Comparison of the predictions of Castorina and Donnachie with a compilation of structure function ratio data, including the EMC NA2′ and NA28 ones (from [193])

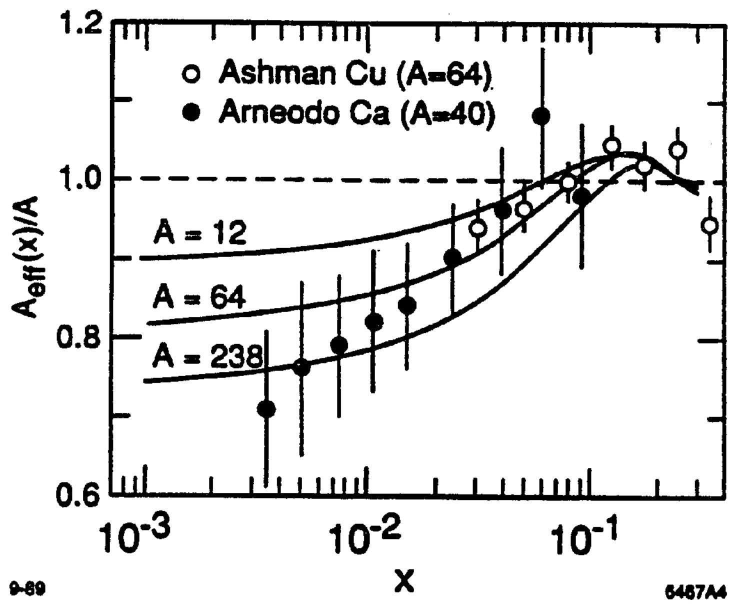

Figure 1.60: Predictions of Brodsky and Lu for $A_{eff}(x)/A$; the data points are from EMC NA2′ [38] and EMC NA28 [40] (from [198])

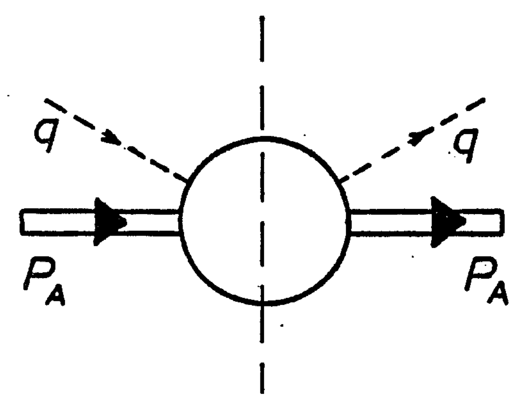

Figure 1.61: Forward elastic photon-nucleon scattering

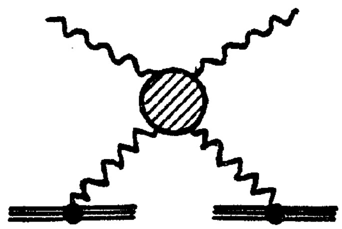

Figure 1.62: Photon-pomeron interaction

Figure 1.63: Multiple scattering terms in the pomeron picture of deep inelastic nucleus scattering

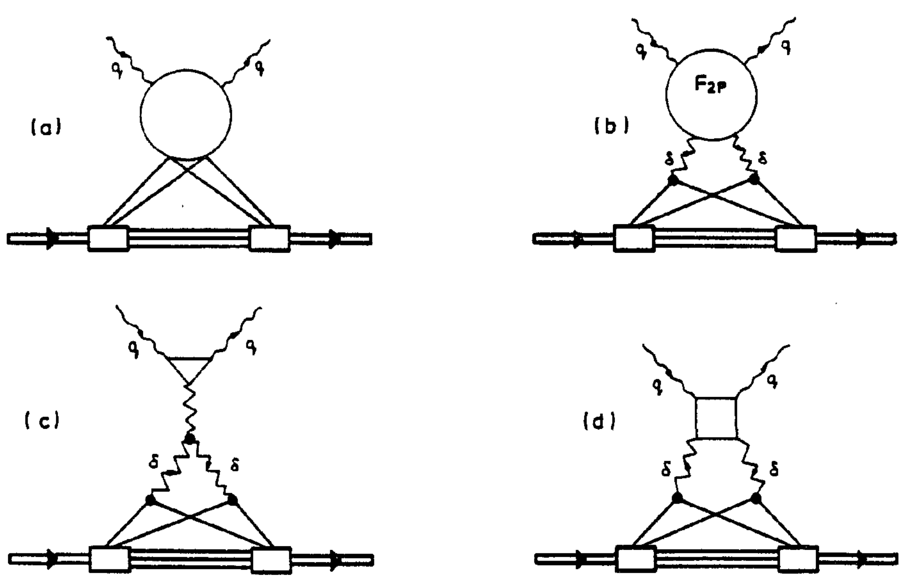

Figure 1.64: Double scattering diagrams for shadowing of a virtual photon. The zig-zag lines indicate the pomerons; see text for a discussion (from [199])

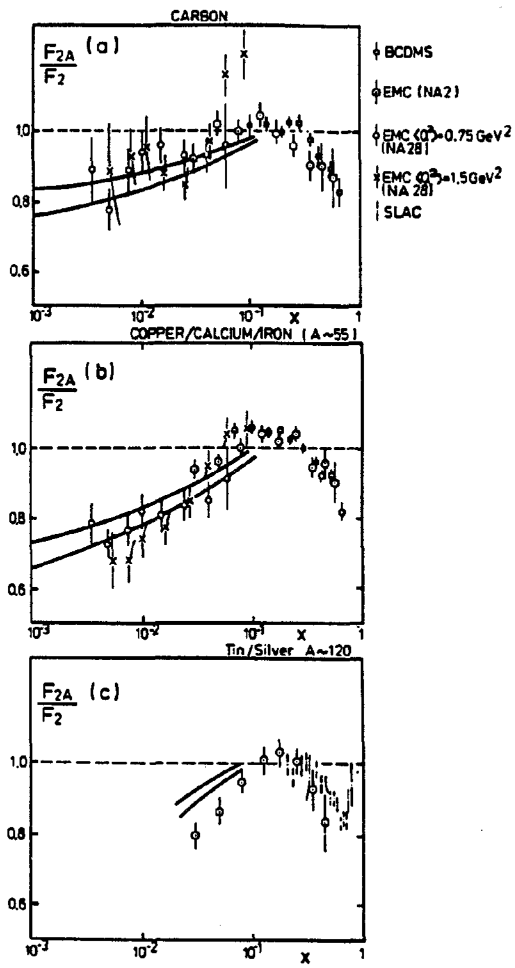

Figure 1.65: Predictions of the model by Kwieciński and Badełek compared with a compilation of data on shadowing. The upper and lower curves correspond to r_0 = 1.5 and 1.25 fm, respectively, in the formula for the nuclear radius, $R = r_0 A^{1/3}$ (from [199])

Kwieciński [200] later elaborated on the same approach in an attempt to establish a quantitative relationship between the shadowing corrections to nuclear parton distributions and the partonic content of the pomeron. Starting from the hypothesis that the pomeron is essentially composed of gluons at $Q^2 \approx 2$ GeV^2 (in the sense that gluons carry all the pomeron's momentum) and assuming specific momentum distributions for these gluons, the amount of shadowing in nuclei can be estimated. In particular, shadowing of the nuclear gluon distribution is shown to be substantial: at $x = 0.01$ in iron it amounts to as much as 50%.

Frankfurt and Strikman [201, 202] examined the nuclear effects on the quark distributions within a rather different model. The main points can be summarized as follows. At small x, in the laboratory frame, the virtual photon-nucleus interaction proceeds in two stages:

1. the virtual photon dissociates into a quark-anti-quark pair;
2. upon arrival on the nucleus, this virtual system interacts with the nucleons giving rise to the hadronic final state.

The interaction cross section of the $q\bar{q}$ pair is taken to be proportional to its transverse dimension squared, approximately given by $1/k_t^2$, with k_t the relative transverse momentum of the pair. Pairs with small k_t have large transverse size, comparable with that of a hadron, and indeed interact in a way resembling a hadron projectile. Symmetric, large k_t, pairs have transverse dimensions smaller than those of a ordinary hadron and their cross section with the nucleus is simply proportional to the number of nucleons. The decrease of the opacity of nuclear matter with decreasing transverse dimensions of the $q\bar{q}$ pairs is often referred to as "color-transparency". The distinction between low k_t asymmetric and large k_t symmetric pairs is a reformulation of the aligned jet model of Bjorken and Kogut [203], in which the nucleus was supposed to become less and less opaque to hadronic jets with increasing k_t of the jet. The idea of discriminating between symmetric and asymmetric pairs in order to give a description of shadowing was first proposed by Nikolaev and Zakharov [177].

Sea and valence quark distributions are treated separately.

- Sea quarks. For $x < x_A$ ($x_A = 1/(2MR_A)$) the cross section $\sigma_{\gamma A}$ reads:

$$\begin{aligned}\sigma_{\gamma A} &= \frac{\alpha}{3\pi}\int_{M_0^2}^{\infty}\frac{dM_V^2 R_{e^+e^-}(M_V^2)M_V^2}{(Q^2+M_V^2)^2}\left[\frac{3k_{t0}^2}{M_V^2}\right]\sigma_{VA} \\ &\quad +\lambda A\sigma_{\gamma N}(x,Q^2). \end{aligned} \tag{1.63}$$

The first term in 1.63 has the usual GVMD-like form and is the contribution of small k_t pairs, which behave like hadrons, in fact vector mesons of mass M_V. The second term is the contribution of high k_t pairs, which interact with non-hadronic, pointlike cross section.

Here $M_0^2 > m_\rho^2$ is the scale characteristic of soft hadronic processes and k_{t0} is a typical transverse momentum of such processes. The vector meson-nucleus cross section is σ_{VA} and the nuclear radius is indicated as before by R_A. The quantity $R_{e^+e^-}(M_V^2)$ is the ratio of $\sigma(e^+e^- \to \textit{hadrons})$ and $\sigma(e^+e^- \to \mu^+\mu^-)$. The main difference in the integrand in 1.63 with respect to that in formula 1.49 is the presence of the factor $3k_{t0}^2/M_V^2$, proportional to the phase space occupied by large transverse size pairs. This extra power of M_V^2 in the denominator of the integrand allows the $1/Q^2$ scaling behavior of $\sigma_{\gamma A}$ to be recovered using vector meson-nucleus (or -nucleon) cross sections which do not depend strongly on M_V^2, but are rather constant, as intuitively expected (cf. the discussion on page 64).

For $Q^2 \gg m_\rho^2$ and $x \ll x_A$, equation 1.63 predicts

$$\frac{A_{eff}}{A} = (1-\lambda)\frac{\sigma_{\rho A}^{tot}}{\sigma_{\rho N}^{tot}} + \lambda \simeq 1.3A^{-0.18}(1-\lambda) + \lambda, \tag{1.64}$$

provided that $A > 10$. The parameter λ can be extracted from the experimental data and is found to be $\lambda \approx 0.2$-0.3.

The x dependence of shadowing is computed, as usual, by means of Glauber's multiple scattering series. The region where shadowing starts to saturate moves to smaller x with increasing A; the dependence of this value of x on A is estimated to be slower than $\sim A^{-1/3}$.

- Valence quarks. Shadowing of the valence quark distribution V_A (i.e. of $\sigma_{W+A} - \sigma_{W-A}$) is calculated by applying Glauber's series to describe the interaction of the soft hadron component of the virtual bosons W^+ and W^-. At very small x ($\ll x_A$) and $Q^2 \approx 1$ GeV^2 the valence distribution is calculated to be also shadowed by as much as 0.6 for $A \approx 60$ and 0.5 for $A \approx 200$.

Figure 1.66 shows the predictions of Frankfurt and Strikman compared with the compilation of data of fig. 1.16. The solid curves show the shadowing due to sea quarks only; the dashed ones include the effect of the valence quarks as well. For both sea and valence distributions, the parameter λ is set to 0.2; if λ is changed to 0.3 the prediction for the structure function ratio is affected by up to 3% for $A = 20$ and $x > 0.03$.

In order to explore the region up to $x \approx 0.1$, Frankfurt and Strikman use momentum conservation

$$\int_0^A \frac{1}{A}[V_A + S_A + G_A]\,\xi_A d\xi_A = \int_0^1 [V_N + S_N + G_N]\,x dx \tag{1.65}$$

and baryon number conservation

$$\int_0^A \frac{1}{A} V_A d\xi_A = \int_0^1 V_N dx, \tag{1.66}$$

where $\xi_A = Ax$ and V, G and S are the valence quark, gluon and sea quark distributions, respectively.

Since the valence distribution is shadowed at small x, baryon number conservation implies that valence is enhanced at higher x. Likewise shadowing of the sea and momentum conservation imply an enhancement of the sea and/or of the gluon distribution at higher x.

Using the preliminary NMC results on F_2^{Ca}/F_2^D [204, 205], Frankfurt, Strikman and Liuti [206] have estimated the ratio of momentum fractions carried by gluons in Ca and D and found it to be larger than unity by 2-3%. Combining the conclusions reached above on the

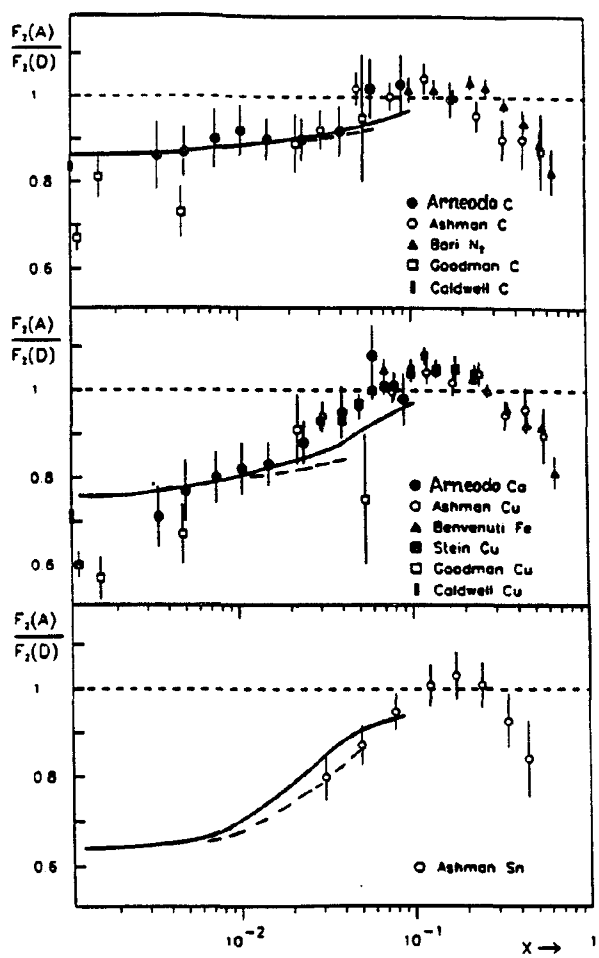

Figure 1.66: Predictions of Frankfurt and Strikman compared with the compilation of data of fig. 1.16. The solid curves show the shadowing due to sea quarks only; the dashed ones include the effect of the valence quarks as well (from [202])

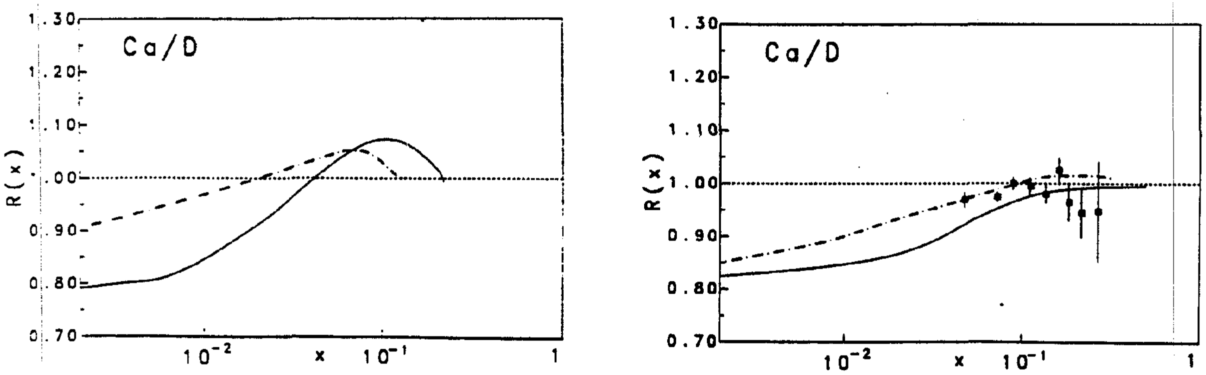

Figure 1.67: Predictions of Frankfurt, Strikman and Liuti [206] for the ratio of the Ca to D gluon (left) and sea quark distributions (right) (solid lines: $Q^2 = 2$ GeV^2; dot-dashed lines $Q^2 = 15$ GeV^2). The data points are from [61] (from [206])

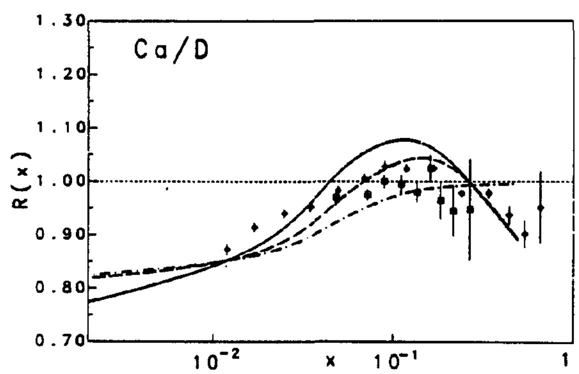

Figure 1.68: Predictions of Frankfurt, Strikman and Liuti [206] for the ratio of the Ca to D valence (solid line), sea (dot-dashed line) and total structure functions (dashed line). All curves are for $Q^2 = 2$ GeV^2 (from [206])

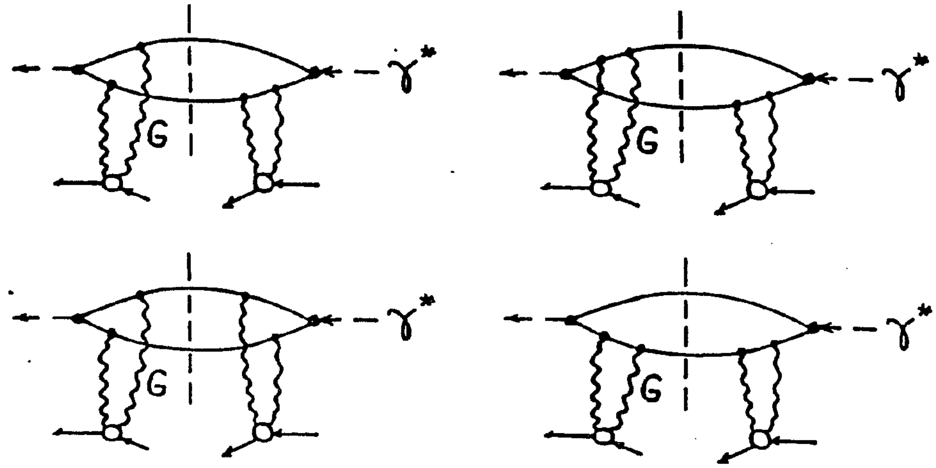

Figure 1.69: Perturbative QCD diagrams for the inclusive forward diffractive dissociation of the photon (from [207])

shadowing of sea and valence quark distributions with these findings, they derived the shape of the parton distributions in nuclei. The results are summarized in fig. 1.67 and fig. 1.68.

All parton distributions are thus shadowed at small x, while at larger x only the valence quark and gluon distributions are enhanced. The dynamical mechanism suggested to explain this pattern is once again parton fusion, when DIS is viewed in the Breit frame. Here shadowing of the valence distribution is the result of the absorption of gluons by valence quarks. For the sea two processes compete: $q\bar{q} \to g$, which depletes the sea quark distribution and $qg \to q$, which ehnances it.

A further contribution to the discusssion on shadowing came recently in two papers by N.N. Nikolaev and B.G. Zakharov [207, 208]. Once again shadowing is ascribed to the asymmetric, large size, $q\bar{q}$ component of the virtual photon. Symmetric pairs also contribute to shadowing, but their effect dies away quicky with increasing Q^2.

This description is made quantitative by means of perturbative QCD. The interaction of the virtual photon with the nucleons is described in terms of pomeron exchange. Pomerons are effectively treated as gluon pairs. Figure 1.69 shows the diagrams involved, in which the gluons of the pomeron interact with the $q\bar{q}$ state coming from the "diffractive" dissociation of the photon. In the calculation of the small x nucleon structure function, based on these diagrams, use is made of the spatial wavefunction of the $q\bar{q}$ fluctuations. The extension to the nuclear case is then made via Glauber's multiple scattering approximation. The QCD analysis confirms the near-scaling of shadowing and predicts only a slow ($\sim 1/\ln Q^2$) evolution with increasing Q^2. Figure 1.70 shows the predictions compared with the EMC NA28 results [40] as a function of Q^2. The authors point out the connection between this approach and the parton fusion one of [177]. For example the quarks in the $q\bar{q}$ loop of fig. 1.69 do not belong to either of the nucleons involved: in the language of [177], this is a typical fusion of the gluon of the first nucleon with the sea quark of the second nucleon, or vice versa.

In these papers Nikolaev and Zakharov also show that shadowing should be different for the transverse and longitudinal absorption cross sections, σ_L and σ_T: shadowing of longitudinal photons is expected to disappear more quickly with Q^2 than that of transverse photons. A

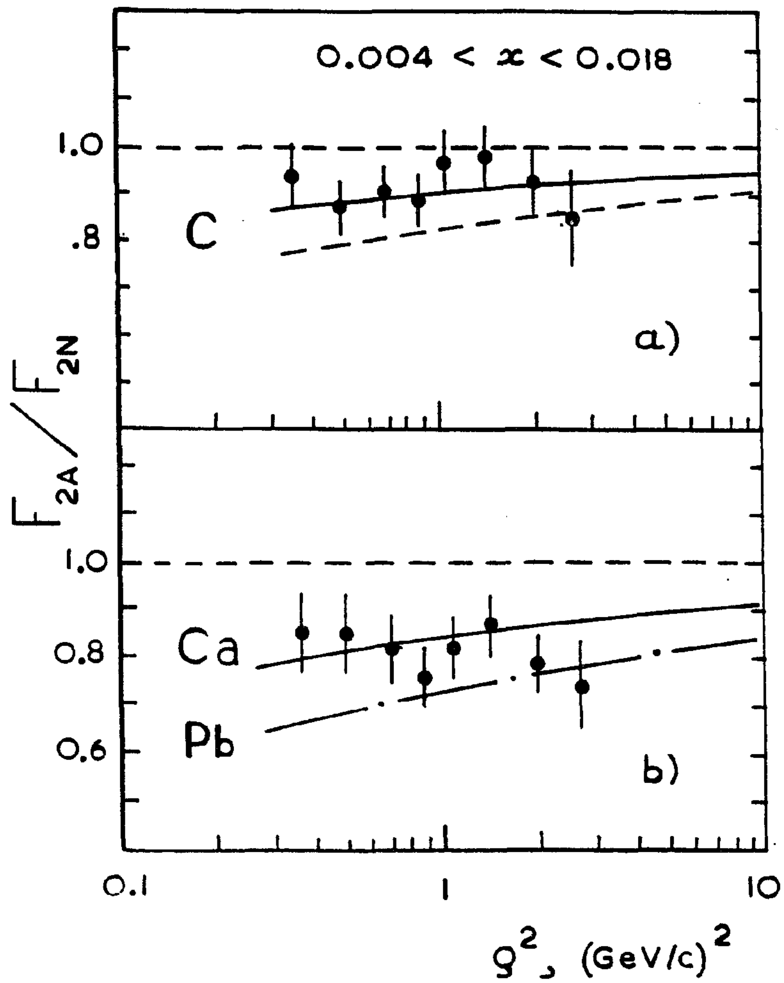

Figure 1.70: Predictions of Nikolaev and Zakharov for the A and Q^2 dependence of shadowing compared with the EMC NA28 data [40]. Solid and broken curves correspond to maximum allowed extension of the $q\bar{q}$ pair $R_c = 1.5$ fm and $R_c = \infty$, respectively (from [208])

consequence of this is the A dependence of $R = \sigma_L/\sigma_T$, which should vary by up to 10-15% in going from hydrogen to lead.

Finally, an explicit prediction is made for shadowing of the deuteron structure function:

$$\left(\frac{A_{eff}}{A} - 1\right)_D \approx 0.25 \left(\frac{A_{eff}}{A} - 1\right)_{^4He}. \tag{1.67}$$

The values of A_{eff}/A plotted in fig. 1.70 include such contribution.

Chapter 2

The Experimental Apparatus

"I must have two, you know — to come and go. One to come, and one to go" [209]

Introduction

The data discussed in this thesis were taken as a part of the experimental program of the New Muon Collaboration (NMC) which gathered in 1985 at CERN with the aim of investigating a wide range of physics topics in deep inelastic scattering [210].

Notably, the program comprises:

- a detailed study of shadowing and the EMC effect, including their A and Q^2 dependences;
- the measurement of $R = \sigma_L/\sigma_T$ as a function of A;
- the measurement of the gluon distribution in different nuclei by means of J/ψ production;
- a precise measurement of the neutron to proton structure function ratio;
- a low systematics determination of the nucleon structure functions.

The experiment, approved by CERN with the name NA37, used the CERN high energy muon beam and an upgraded version of the European Muon Collaboration (EMC) apparatus [211, 212]. The latter is a large magnetic spectrometer which combines a powerful bending magnet and a system of chambers providing long incident and outgoing track lever arms to obtain optimal Q^2 and ν resolution.

Special efforts were made to reduce systematic effects with particular emphasis on those relevant to the determination of cross section ratios (cf. for instance the peculiar target arrangement) and to the evaluation of absolute F_2's (cf. e.g. the increased accuracy in the beam momentum measurement and in the beam flux measurement).

Figure 2.1 shows schematically the general layout of the CERN site ca. 1986, while fig. 2.2 shows the NMC spectrometer, which was located in the Nord Area of CERN, on the Prévessin site.

This experiment took data between the years 1986 and 1989. The He/D data presented here were collected in the SPS-period P4A86, between September 10th and October 1st, 1986.

In the following we will discuss the main aspects of the experimental apparatus. We will not attempt to give a complete description of the mechanical and electronic characteristics of the detectors, but will rather concentrate on those aspects which are relevant to the analysis

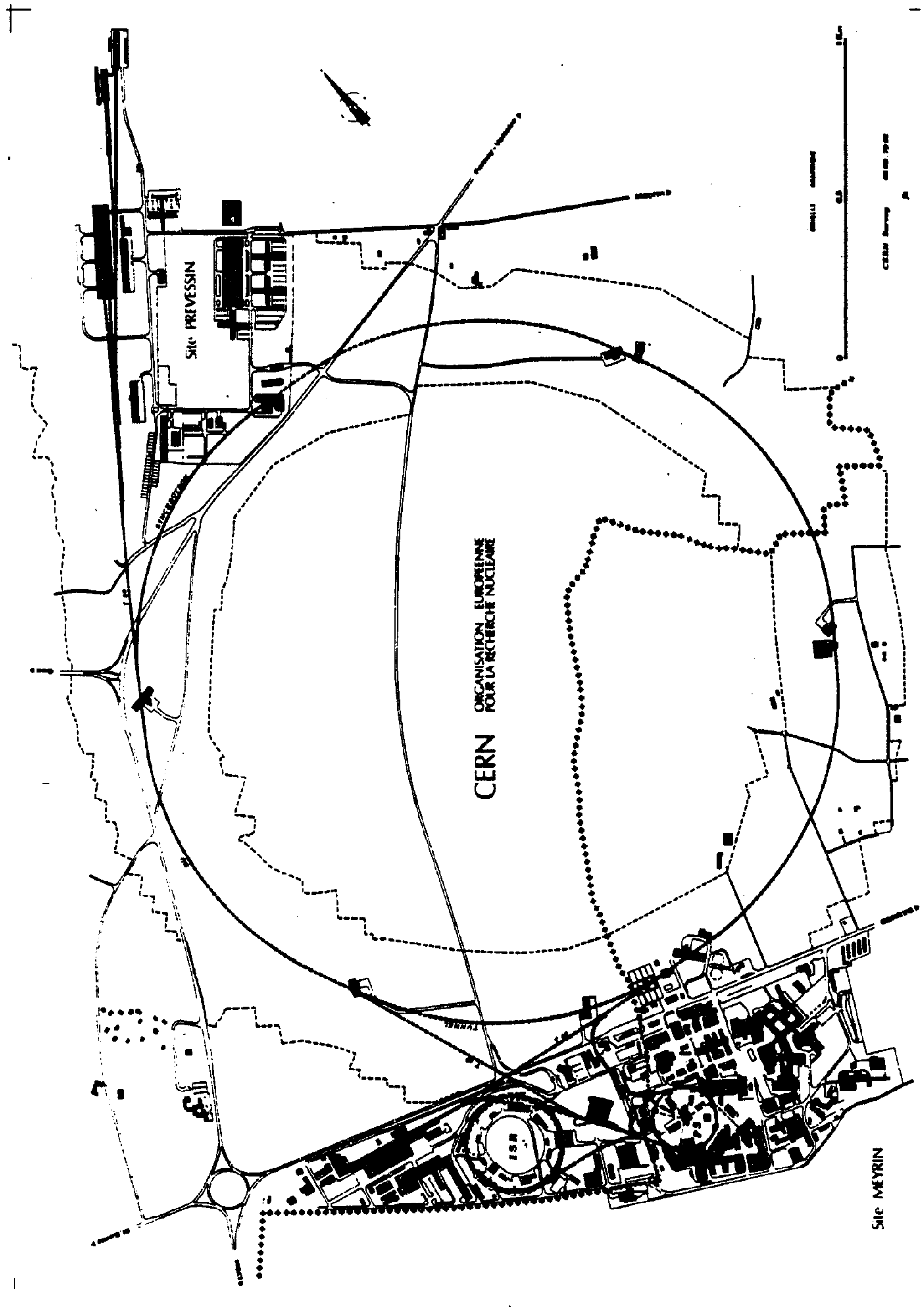

Figure 2.1: General layout of the CERN site ca. 1986

discussed in this work. Similarly we will restrict ourselves to a description of the apparatus as it was in P4A86 and will neglect changes or improvements which occurred after 1986 and did not affect the He/D data. A full account of the NA37 experimental set-up can be found elsewhere [213].

2.1 General Scheme of the Experiment

With reference to fig. 2.2, the muon beam enters from the left. The incoming muons are momentum analyzed by a focusing spectrometer, the Beam Momentum Station (BMS) and their trajectory is measured by the Beam Hodoscopes BHA and BHB. The beam traverses two target vessels, containing He and D, respectively; the vessels are frequently exchanged with two identical ones, in which the relative positions of He and D along the beam are inverted. As we discuss below, this "complementary" arrangement is instrumental in the measurement of structure functions ratios with small systematic errors.

Fast, forward produced, charged particles exiting the target region have their momentum measured by the Forward Spectrometer Magnet (FSM); their tracks are reconstructed in the the proportional chambers P0C and PV1, PV2 (in short PV12) upstream of the FSM and in P0D, P1, P2, P3 (P123) inside the magnet. After the FSM particles are tracked by a system of proportional and drift chambers: W1, W2 (W12), P0E and W4, W5 (W45), P4, P5 (P45), P0A. Hadrons, electrons and photons are then stopped by a calorimeter with electromagnetic and hadronic sections and by a thick iron absorber. Only muons survive and are detected by the drift chambers W6 and W7 (W67).

The read-out of the spectrometer is started by the passage of a scattered muon through a set of scintillation counters (H1H, H1V, H3H, H3V, H4H). Five planes of veto hodoscopes (V1, V1.5, V3, V2.1, V2) detect beam halo muons or knock-on electrons and inhibit the trigger. Upon receipt of a valid trigger signal the data acquisition computer writes all the chambers and hodoscopes information onto magnetic tape.

2.2 The NMC Reference Frame

We will often make use of the NMC reference frame. It is defined as follows (fig. 2.2): the nominal beam direction coincides with the x axis. The z axis is vertical and points upwards. The y axis is such as to make the system orthogonal and right-handed. A geographical nomenclature is often used in the EMC and NMC notes and internal publications: the positive y direction is referred to as the Jura side, the negative y direction as the Salève side.

The magnetic field in the FSM is always chosen so as to deflect beam muons towards the positive y direction.

2.3 A Historical Note

The EMC-NMC spectrometer is an outstanding example of longevity in experimental high energy physics. It was designed and built in the late 1970's and served the long and rich experimental program of the European Muon Collaboration through the NA2, NA9, NA28 and NA2′ experiments which were realized between 1978 and 1985. Originally conceived to study the nucleon structure function at large Q^2, in the perturbative QCD regime (NA2 [211]), it was later complemented by a vertex spectrometer with particle identification capabilities in order to investigate the hadronic final state in deep inelastic scattering (NA9 [212]). At the same time a sofisticated low angle trigger system enabled the study of nucleon and nuclear structure functions at very small x and Q^2 (NA28 [40, 214]). In 1984 and 1985, after the removal of the vertex spectrometer, NA2′ engaged in the measurement of polarized structure functions with a set of polarized proton targets [215] and simultaneously in the study of nuclear structure functions [38, 39].

The EMC program was extremely successful. We will only quote here the small value of the QCD scale parameter Λ found at the beginning of the 1980's [216], in contradiction with previously accepted results, the discovery of the EMC effect [14] and the finding that the polarized proton structure functions behave in an unexpected fashion at low x [215], breaking the Ellis-Jaffe sum rule.

The spectrometer was taken over by the NMC, which upgraded it, without however modifying its conceptual design and its basic performances. The most important contributions of the new collaboration were:

1. The "complementary" target system, which allowed accurate measurements of ratios of cross sections on different target materials, independently of the acceptance corrections and of the incoming beam flux.

2. Two small hadron calorimeters and a concrete absorber installed in the target region, used for the Be/C, Al/C, Ca/C, Fe/C, Sn/C and Pb/C high luminosity runs.

3. A small angle trigger which extended the sensitivity of the original EMC trigger system to smaller scattering angles and therefore smaller Q^2 values.

4. The Beam Calibration Spectrometer, designed to calibrate the incoming beam momentum measurement to the 10^{-3} level (critical for the nucleon absolute structure functions determination).

5. An additional beam flux normalization system, also very important for absolute structure functions.

6. A new data acquisition and on-line monitoring system (after 1987) using a network of microVAX computers and a FASTBUS event buffer.

Furthermore, pieces of the apparatus which had shown significant aging effects in the last years of the EMC running were replaced. We recall that

- the beam hodoscopes were entirely rebuilt;
- the PV1 chamber in front of the magnet was also rebuilt with smaller wire spacing (2 instead of 4 mm);
- the sense wires in the magnet chambers P123 were replaced;
- the W12 drift chambers were rewired;
- the W45 drift chambers were rewired;
- an extra P45 chamber was added in order to compensate for the efficiency deterioration of the large drift chambers W45.

While the NMC apparatus directly derived from the EMC one, there is only little overlap between NMC and EMC in terms of participating institutions and physicists (cf. appendix E), at least with respect to the NA2 and NA9 experiments. It is interesting to note that there are essentially two components in the new collaboration: on the one hand physicists with a high energy physics background, on the other nuclear physicists attracted by the possibility to probe the nucleus with somewhat unconventional tools. The merging of the two communities has proved fruitful and instructive for both.

Upon completion of the data taking program of NA37, the EMC-NMC spectrometer was taken over by the Spin Muon Collaboration (SMC) [217], which will exploit it for 4 more years at least in order to further investigate the structure functions of polarized nucleons. By then the spectrometer will have totalled 15 years of operation.

2.4 The Muon Beam

The CERN muon beam line M2 [218] is shown schematically in fig. 2.3. A high energy proton beam (400 GeV) is extracted from the SPS and made to impinge on a tungsten target (T6), thereby producing a high intensity pion/kaon beam. Muons originate from the weak decay in flight of the pions and kaons.

The beam line can be divided into four main parts:

1. Production and selection of the hadrons. The protons from the SPS interact on a production target (its length may vary from 40 to 500 mm, depending on the desired muon intensity). The outgoing secondary beam emerges within an energy-dependent solid angle of 10-20 μsr with respect to the incoming protons. Any remaining protons are removed by a combination of a momentum selecting magnet and a collimator which also acts as a dump for the proton beam. The magnet and the collimator select a pion/kaon beam of definite sign and with a momentum spread $\Delta p/p < 10\%$.

2. The decay channel. It consists of a 640 m long series of 16 large aperture (20 cm) quadrupole magnets set in alternate focusing and defocusing mode (FODO). The decay channel has been designed to transport both the parent hadrons and the decay muons with minimum losses. It can be shown that for a parent hadron momentum p (π, K), the momentum of the decay muons $p(\mu)$ lie within the range:

$$\left(\frac{m_\mu}{m_{\pi,K}}\right)^2 p(\pi,K) < p(\mu) < p(\pi,K),$$

   that is:

$$0.57p(\pi,K) < p(\mu) < p(\pi,K).$$

   At the end of the channel about 3% of the hadrons have decayed and typically 25% of the resulting muons lie within the momentum band which can be selected and transported to the experiment.

3. The hadron absorber. At the end of the decay channel the remaining hadrons are absorbed by 11 m of beryllium. The hadronic component of the beam is then attenuated by a factor 10^8, leaving a residual contamination of less than 10^{-6} hadrons per muon.

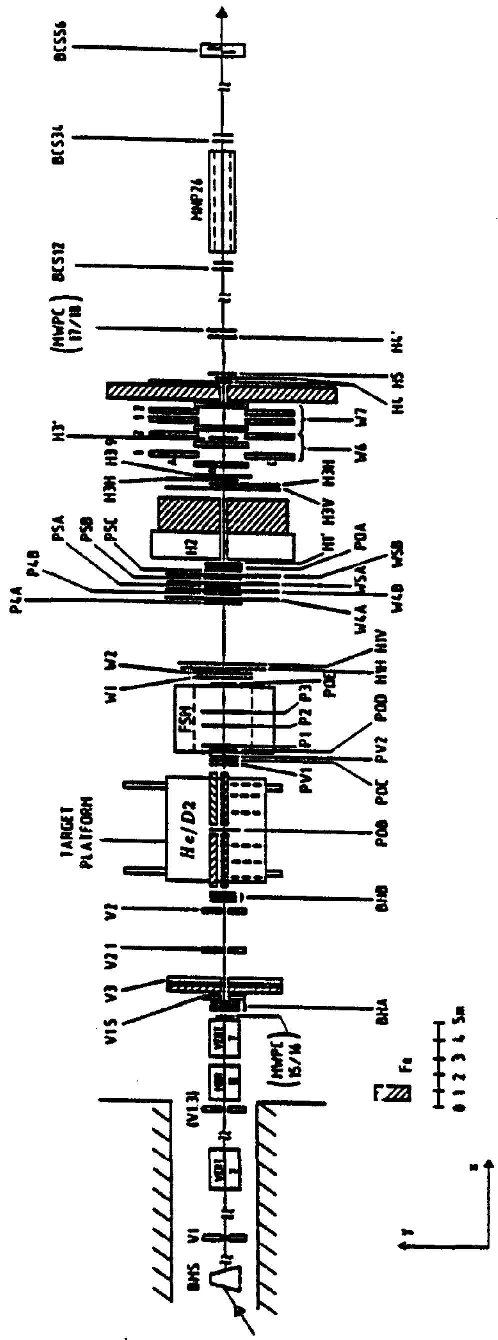

Figure 2.2: The NMC spectrometer

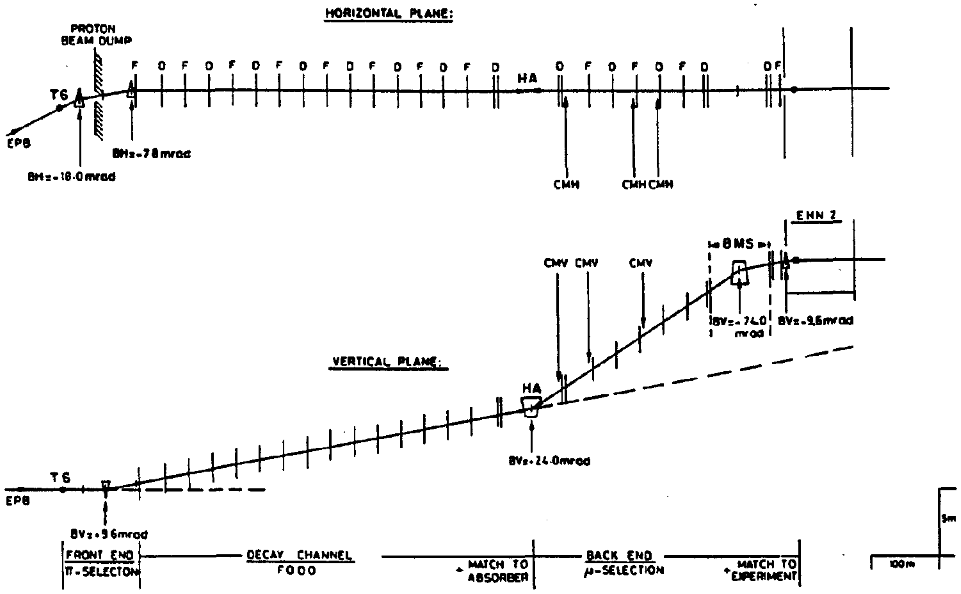

Figure 2.3: The M2 beam line

Beryllium was chosen because of its large ratio of radiation to attenuation length, in order to minimize multiple scattering of the muons. The muons of required momentum are focused onto a waist at the center of the absorber, thus reducing the beam emittance.

4. The end section. This part selects the muon momentum and transports the beam to the experimental hall. A momentum band $\Delta p/p \approx 5\%$ is defined by a bending magnet (24 mrad upwards) followed by a magnetized iron collimator. The beam is then transported through 3 periods of a 350 m FODO quadrupole sequence similar to the one in the decay channel. It is deflected back by -24 mrad by a second set of 3 magnets which remove the dispersion caused by the first bending. These magnets are part of a spectrometer (described in the next section) used to determine the beam momentum. The overall vertical displacement, following the two 24 mrad bends, is 7.5 m. Finally a series of quadrupoles and weak bending magnets are used to steer and focus the beam onto the experimental targets. The resulting muon beam has a minimal contamination of hadrons ($10^{-6}/\mu$) and electrons ($10^{-4}/\mu$).

Special attention has been paid to the reduction of halo muons; these are unwanted muons which do not lie in the required beam phase space region, in terms of momentum or position, but which nevertheless reach the experimental region. Eliminating such halo is a difficult task due to the penetrating nature of the beam particles: previous muon beams [219] were plagued by a halo as large as 50% of the useful flux. Three aspects of the design have been instrumental in reducing the halo:

1. The large aperture of the FODO optics, allowing the transport of muons in a wide momentum band with small losses.

2. The use of several magnetized iron collimators, installed just downstream of the hadron

absorber and in the end section. They clean the edges of the beam by deflecting outwards the halo muons close to the beam.

3. The two vertical bends which the beam undergoes before arriving to the experimental zone: they eliminate the "far" halo, which does not pass through the magnets.

In addition, halo particles remaining within the acceptance of the experimental apparatus are detected in a series of veto counters which will be described in section 2.10.3.

It is interesting to note that the muon beam is naturally polarized thanks to the parity non-conserving nature of weak interactions. The muon helicity is fixed in the parent hadron frame: the muons decaying forward with respect to the hadron direction then have large momentum in the laboratory frame and negative polarization. Conversely muons moving backward with respect to the beam direction have lower momentum and positive polarization. It is therefore possible to select the muon polarization by appropriately choosing the hadron average energy in the first section of the beam line and the muon momentum in the end section. Polarizations of up to 85% can be obtained [220]. This possibility has been exploited several times in the long history of the M2 beam line [221, 215], and will again be used in a forthcoming experiment on the same line [217].

NMC took data with 90, 120, 200 and 280 GeV beams. Typical intensities varied between 2×10^7 μ/spill (one spill being about 2 s long) and 4×10^7 μ/spill, depending on the beam momentum (intensity decreases with increasing momentum) and on the beam muon sign (intensity is larger for positive muons).

In the period analyzed here the nominal beam momentum was 200 GeV, corresponding to a pion/kaon momentum of about 220 GeV. The beam intensity was $\approx$ 2-3 $\times 10^7$ μ/spill, corresponding to $\approx$ 60-100 $\times 10^{11}$ protons/spill on the production target T6.

Figure 2.4 shows the typical beam phase space at the experiment.

2.5 The Beam Momentum Station

As mentioned in the previous section, the beam undergoes a 24 mrad vertical bend before being finally steered and focused onto the targets. The three dipoles giving the deflection, together with 4 sets of scintillation counters hodoscopes, form a spectrometer which measures the momentum of each beam muon. The set-up is complemented by two quadrupole magnets, necessary to control the beam phase space.

The four hodoscope planes provide an over-constrained momentum measurement, a critical feature given the multiple hit environment resulting from the high muon intensity. Each plane is composed of 64 horizontal strips, each of 5 mm width. There is a small overlap between adjacent strips, to ensure maximum efficiency. The element size is such that the individual rates do not exceed 3×10^7 Hz. The scintillator thickness is 2 cm, thus providing a large light output, important to achieve accurate timing. Each scintillator is seen by a photomultiplier, coupled to an electronic chain [222] designed to have the smallest possible dead time. The chain ends with a Time to Digital Converter (TDC) measuring the time interval between the trigger and the phototube signal in a 60 ns time window. The time resolution of each tube is $\approx$ 150 ps; all channels are timed with respect to one another with a similar precision. The relative timing between different channels is achieved by using a laser illuminating a scintillator block, which is in turn coupled to the tubes by means of optical fibers. The observed timing differences are then corrected for with computer controlled delay lines. The relative timing is

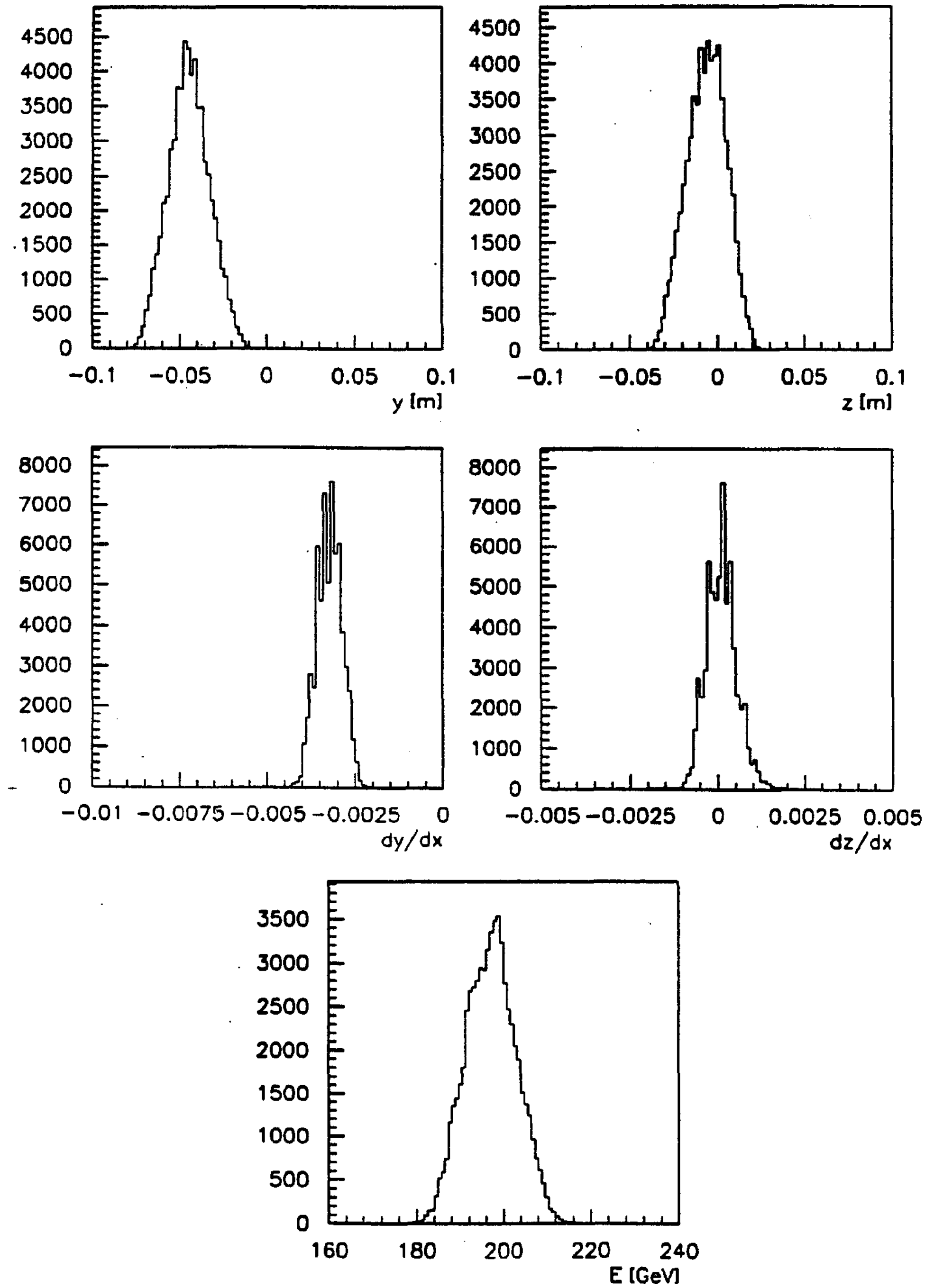

Figure 2.4: Beam phase space: y and z distributions at the upstream target, y and z slopes distributions, beam energy distribution

further measured and corrected for in the off-line analysis. Each plane is then also timed with respect to the trigger with an accuracy of $\approx$ 300 ps.

Notice that precise timing is essential in the high intensity environment in which these hodoscopes work; hits are associated to beam tracks on the basis of their timing. Similarly beam tracks are associated to events on the basis of the relative timing between BMS and trigger: this is a powerful tool to select the incoming muon in events with multiple beam tracks.

Once the correct beam track has been selected, its momentum can be computed. The technique used is the following: for each beam energy and sign a Monte Carlo program simulating the beam line is run. For each simulated track both the momentum and the hodoscopes hits are known and a relationship between hit coordinates and momentum can be found. This is done using a principal component analysis followed by a multi-dimensional least squares fit. The set of numbers defining a specific parametrization is often referred to as "the BMS coefficients" and is a part of the alignment file (cf. section 3.6). The parametrization obtained from the Monte Carlo events is then used for the real data (in the reconstruction program PHOENIX, see chapter 3) to obtain the track momentum from the hits in the BMS hodoscopes.

2.6 The Beam Calibration Spectrometer

The Beam Calibration Spectrometer (BCS) was designed to provide a means to calibrate the BMS to high accuracy ($\Delta p/p \sim 10^{-3}$).

It consists of a dipole magnet (often referred to with its serial number: MNP26) giving a horizontal bend and a set of 6 multi-wire proportional chambers (see fig. 2.2). The spectrometer is located at the downtream end of the NMC apparatus, along the trajectory of the beam deflected by the FSM.

The MNP26 magnet is a 6 m, 11.5 Tm dipole with a 48 cm $\times$ 10 cm aperture. It provides a maximum bend of 18 mrad at 200 GeV.

The full length of the hall gives a downstream lever arm of approximately 35 m, with a displacement of 0.60 m at 200 GeV. At both ends of the magnet there are 2 wire chambers, with 1 mm wire spacing measuring y and z coordinates, respectively. Two additional wire chambers on a moving chariot are placed side by side (with no overlap) at the very end of the experimental hall and measure the y coordinate only.

Each chamber has 96 sense wires and is read out by preamplifier-discriminator cards [223]. The discriminated pulses are read out by standard CERN RMH modules [224].

The system is used in dedicated calibration runs: data are taken with the BCS magnet off, for chamber alignment, and then at the three currents for which field maps are available: 550 A, 960 A and 1800 A. The field integrals at the three currents are 5.04 Tm, 8.5 Tm and 11.5 Tm, respectively. The sign of the magnet excitation current is always chosen so that the field deflects the beam towards the negative y direction (the Salève side).

For a detailed description of the analysis of the BCS calibration runs and a discussion of the results the reader is referred to appendix A.

2.7 The Beam Hodoscopes

The Beam Hodoscopes (BH) measure the direction of the incoming beam muons. They consist of two groups of four planes of scintillation counters, BHA and BHB, separated by a distance of approximately 6 m; BHB is just upstream of the upstream targets.

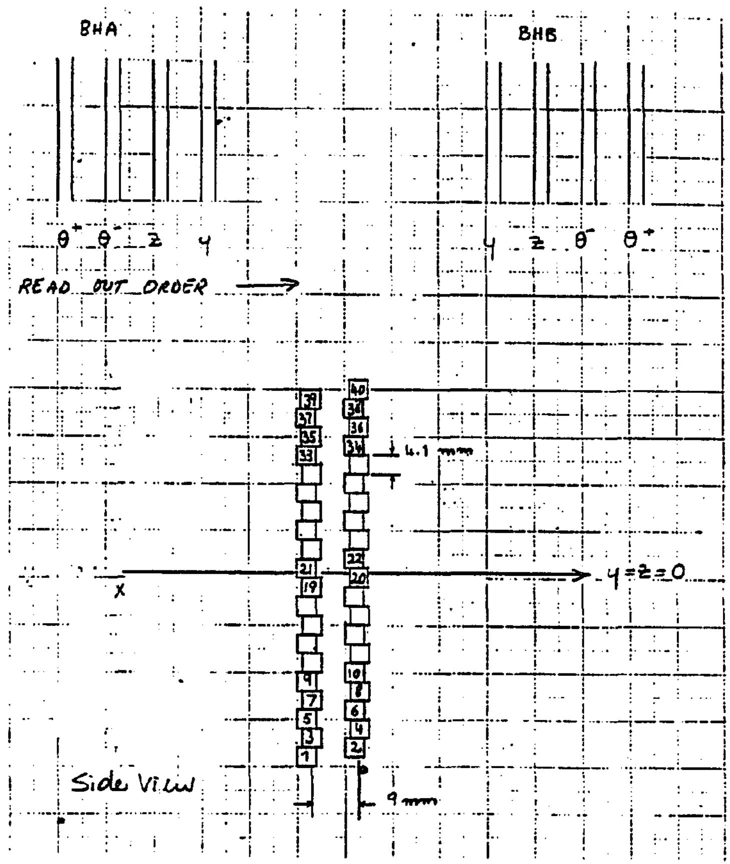

Figure 2.5: The beam hodoscopes layout

The four planes in each set have horizontal, vertical and ±45° scintillator strips, respectively. Each plane has 40 strips, 4 mm wide, 4 mm thick and 9 cm long. The 40 strips in a plane are divided into two sub-planes of 20 strips; the two sub-planes are shifted with respect to each other by a half strip width (fig. 2.5), thereby achieving an effective strip pitch of 2 mm and eliminating any dead region between neighboring channels. The resulting angular resolution is ≈ 0.15 mrad. The active area of a plane is 8×8 cm^2.

Each scintillator strip is seen by a fast photomultiplier. The analog signal is discriminated and fed into a TDC, which measures the time interval between the trigger and the hit in a 60 ns time window. The time resolution of a single channel is about 0.6 ns, but the timing of a beam track is effectively determined to much better accuracy as it is measured independently in up to 16 channels. Relative timing differences between channels are measured and corrected for off-line (see chapter 3).

Here again the accuracy of the timing is a critical factor: hits are associated to tracks on the basis of their timing; a BH track is attributed the momentum measured by the BMS only if the respective timings fall within a narrow window. Finally, as mentioned above, a beam track is associated to an event depending on the difference between the trigger and the BH, BMS times.

Appendix B contains a more detailed description of the BH hardware and software.

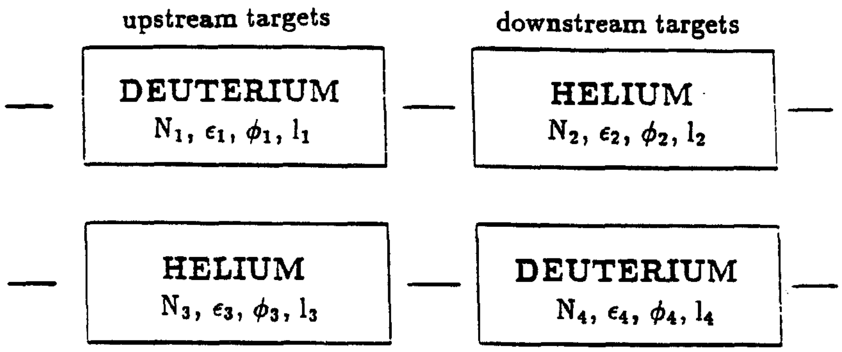

Figure 2.6: The complementary target set-up

2.8 H5 and H6 Hodoscopes

Non-interacting beam tracks are detected by the H5 and H6 hodoscopes, situated at the downstream end of the NMC spectrometer.

H5 consists of two planes with 4 and 5 vertical elements, respectively; the element sizes are such that the rate per element never exceeds $\sim 10^7$/s.

H6 (not shown in fig. 2.2) is composed of 72 scintillator elements arranged in a mosaic pattern; the central 64 channels are in use, covering a roughly circular area with diameter $\sim$ 14 cm centered on the beam axis.

H5 and H6 provide a rough on-line monitoring of the beam flux and of the beam position. H5 is also used to define a beam transmission trigger (T5, see below).

2.9 The Targets

2.9.1 The Complementary Target Method

As mentioned in the introduction, one of the goals of the NA37 experiment is to measure ratios of cross sections with very good control of the systematic errors, notably those arising from the beam flux measurement and the spectrometer acceptance calculation. To this purpose a peculiar target arrangement is used.

Two targets are simultaneously in the beam (He and D, in this case); they are thus necessarily exposed to the same muon flux. These two targets are frequently exchanged with two "complementary" ones (fig. 2.6), in all respects identical, except for the fact that the positions of He and D are interchanged along the beam direction. With reference to fig. 2.6, the number of events coming from each of the four targets is, respectively:

$$N_1 = \sigma_D \epsilon_1 \phi_1 N_{Av} l_1 \rho_D \frac{A_D}{M_D} \quad (2.1)$$

$$N_2 = \sigma_{He} \epsilon_2 \phi_2 N_{Av} l_2 \rho_{He} \frac{A_{He}}{M_{He}} \quad (2.2)$$

$$N_3 = \sigma_{He} \epsilon_3 \phi_3 N_{Av} l_3 \rho_{He} \frac{A_{He}}{M_{He}} \quad (2.3)$$

$$N_4 = \sigma_D \epsilon_4 \phi_4 N_{Av} l_4 \rho_D \frac{A_D}{M_D}, \quad (2.4)$$

where ϵ_i is the apparatus acceptance for the i-th target, ϕ_i is the total number of muons traversing the i-th target, N_{Av} is the Avogadro number and l_i the length if the i-th target; ρ_D and ρ_{He} are the densities of the liquid deuterium and helium targets, respectively; A_D, A_{He} are the atomic numbers of deuterium and helium and M_D, M_{He} their atomic weights. In writing 2.1-2.4 the definition of cross section was used:

$$N = \sigma \times L$$

where L is the luminosity:

$$L = \left(\frac{\phi}{S}\right) \times (number\ of\ scattering\ centers) =$$

$$= \left(\frac{\phi}{S}\right) \times \rho \frac{(Sl)}{M_A} N_{Av} A,$$

with S the cross sectional area of the target.

In 2.1-2.4 $\phi_1 = \phi_2$, as we said, and similarly $\phi_3 = \phi_4$. Furthermore the upstream acceptances ϵ_1, ϵ_3 must be equal (as long as they depend on geometry only); on the same grounds $\epsilon_2 = \epsilon_4$.

The following ratio can then be taken:

$$\frac{N_2 N_3}{N_1 N_4} = \left(\frac{\sigma_{He}}{\sigma_D}\right)^2 \left(\frac{\rho_{He}}{\rho_D}\right)^2 \left(\frac{A_{He}}{A_D}\frac{M_D}{M_{He}}\right)^2$$

from which we obtain:

$$\frac{\sigma_{He}}{\sigma_D} = \sqrt{\frac{N_2 N_3}{N_1 N_4}} \frac{\rho_D}{\rho_{He}} \frac{A_D}{A_{He}} \frac{M_{He}}{M_D}. \tag{2.5}$$

We see than that the cross section ratio is independent of the integrated muon flux and of all acceptance and efficiency corrections, in so far as they are target material independent. In addition, any time dependent effects in the apparatus acceptance and efficiency also cancel due to the frequent target exchange (typically once every 30 minutes, a total of a few hundred times).

2.9.2 The He and D Targets

The method outlined above requires the use of four target vessels, mounted on a moving platform, allowing rapid and precise exchange of the two complementary configurations. Liquid helium and liquid deuterium were used.

The upstream targets were situated between BHB and P0B, while the downstream ones sat between P0B and P0C.

Figure 2.7 shows schematically the mechanical layout of the targets. The liquid helium and deuterium were contained in vessels about 3 m long and 10 cm in diameter. The inner target walls were particularly thin, amounting to 0.0598 g/cm^2 of mylar (250 μm) and 4.05×10^{-5} g/cm^2 aluminum (180 μm); these should be compared with a total He thickness of 37.8 g/cm^2 and a total D thickness of 48.8 g/cm^2. The vessels were inside vacuum tight hard paper containers; the containers had a diameter of 30 cm and their thickness was 1.4 cm, except in the region traversed by the beam, were the hard paper was replaced by 250 μm thick mylar windows.

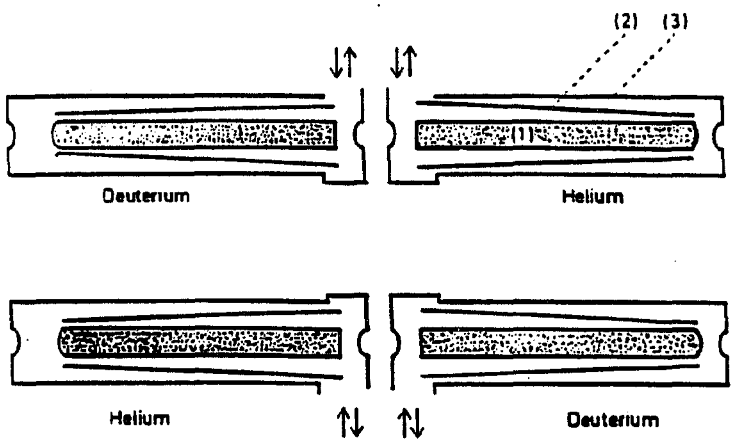

Figure 2.7: The mechanical layout of the targets: (1) vessel, (2) aluminum cryogenic shielding, (3) container

A critical issue is the measurement of the target densities: we see in formula 2.5 that the cross section ratio is directly proportional to the density ratio. The target densities were obtained starting from the measured values of the saturated vapor pressure in each target. The vapor pressure is in fact uniquely related to the temperature and the latter in turn determines the density of the liquid materials (see [225] for deuterium and [226] for helium; see also [227]-[233]). In deriving the deuterium density from the measured D vapor pressure the assumption was made that the liquid is in the so-called "equilibrium" state (97.8% ortho-deuterium, 2.2% para-deuterium), reached some time after liquefaction, as opposed to the "normal" state (2/3 ortho, 1/3 para-deuterium) in which deuterium is at liquefaction.

The densities were found to be ρ_{He}=0.12580 ± 0.0004 g/cm^2 and ρ_D=0.16252 ± 0.0005 g/cm^2, respectively. The value obtained for the deuterium density takes into account the HD contamination of the liquid D_2, discussed in detail below.

2.9.3 Hydrogen Admixture in the Deuterium Target

The liquid deuterium used as a target was not pure but contained a 3% fraction of HD molecules [234]:

$$\epsilon = \frac{HD}{HD + D_2} = 0.0300 \pm 0.0024.$$

The HD contamination of the deuterium has three consequences:

1. The deuterium density is different from the one that could be computed directly from the vapor pressure measured inside the deuterium vessel and an iterative procedure must be used to find the true deuterium density.

   From the measured vapor pressure P_{meas} the approximate temperature T of the HD, D_2 admixture was obtained. From the latter the HD vapor pressure P_{HD} was found by means of the following empirical parametrization [225]:

$$\log_{10} P_{HD} = 5.04964 - \frac{55.2495}{T} + 0.01479\,T.$$

An estimate of the actual deuterium vapor pressure P_{D_2} was then obtained assuming

$$nP_{meas} = n_{HD}P_{HD} + n_{D_2}P_{D_2}$$

($n = n_{HD} + n_{D_2}$, with n_{HD} and n_{D_2} the number of HD and D_2 moles, respectively). From P_{D_2} a new estimate of the temperature was found and the procedure repeated until convergence. The final temperature of the admixture was found to be 23.872 °K; the corresponding deuterium and HD molar volumes are $U_{D_2} = 24.8097$ and $U_{HD} = 27.2915$ cm^3/mole, respectively. The HD molar volume was obtained from the following parametrization [225]:

$$U_{HD} = 24.886 - 0.30911\,T + 0.01717\,T^2.$$

The deuterium density thus found is $\approx 0.2\%$ higher than that computed without iteration.

2. The number of target nucleons is smaller (a HD molecule contains 3 nucleons instead of 4 and occupies about the same volume as a D_2 one). The correct number of target nucleons can be obtained by imposing that the sum of the volumes occupied by HD and by D_2 equals the actual vessel volume V:

$$V = n_{HD}U_{HD} + n_{D_2}U_{D_2}.$$

The correction found for the deuterium luminosity is thus

$$\left[1 + \epsilon\left(2\frac{U_{HD}}{U_{D_2}} - 1\right)\right]^{-1},$$

amounting to about -0.18%.

3. The observed yield from deuterium contains unwanted events in which the scattering has occurred on an isolated proton. The observed number of events from deuterium N is thus the sum of the true deuterium events N_t and of the proton events N_p:

$$N = N_t + N_p.$$

It is easy to find that the correction to the measured yield is:

$$\left[1 + \frac{\epsilon}{1 + \sigma_n/\sigma_p}\right]^{-1}.$$

The correction is a function of σ_n/σ_p, the neutron to proton cross section ratio. For the latter the BCDMS parametrization [268] was used:

$$\frac{\sigma_n}{\sigma_p} = 1 - 1.85x + 2.45x^2 - 2.35x^3 + x^4.$$

The overall correction to the ratio due to three effects discussed above is about -1% and depends weakly on x because of σ_n/σ_p.

2.10 The Trigger System

The data analyzed in this work have been collected with two different types of triggers, the first sensitive mainly to large scattering angles (> 10 mrad), the other effective in the small angle region (between 4 and 15 mrad). They will be hereafter referred to as Trigger 1 (T1) and Trigger 2 (T2), respectively.

T1 uses three sets of scintillation counter hodoscopes (H1, H3, H4, fig. 2.2) to provide a fast measurement of the horizontal and vertical coordinates of the track trajectory at different x positions downstream of the FSM. T1 is designed to guarantee a good coverage of the high Q^2 region, while suppressing the rate of low Q^2 events which tend to dominate, as the cross section is proportional to $1/Q^4$. To this purpose it imposes a cut on the scattered muon angle with respect to the beam axis; since the beam divergence is very small this effectively translates into a cut on the scattering angle ϑ and therefore on $Q^2 \approx EE'\vartheta^2$.

T2 extends the sensitivity of the trigger down to smaller scattering angles by means of three more hodoscopes, H1′, H3′ and H4′, which are located near the T1 set but are of smaller dimensions and closer to the beam. T2 is sensitive down to to scattering angles of $\approx$ 4 mrad with respect to the beam direction.

More in detail, for both T1 and T2 the scattered particle must be identified as a muon and therefore detected in the H3 and H4 (H3′, H4′ for T2) hodoscopes, downstream of the calorimeter H2 and of the hadron absorber. The H3, H4 (H3′, H4′) information is then used with that from H1 (H1′) in order to insure that the muon comes from the target region. Further, the requirement is imposed that no signals be detected in the veto hodoscopes (V1, V1.5, V3, V2.1, V2) thus rejecting events caused by halo muons which may not have interacted in the target and yet may have succesfully gone through the H1, H3 and H4 (H1′, H3′, H4′) trigger logic.

It is interesting to compare the kinematic regions covered by the two triggers in terms of the Bjorken variable x and Q^2 (fig. 2.8). At small x both triggers extend down to 1-2 $\times 10^{-3}$, with T2 reaching only slightly smaller x values. The T2 events however realize a given value of x by smaller Q^2 and therefore smaller y values than the T1 ones. As we discuss later in more detail, this entails two advantages:

1. Since the low x T2 events have smaller y than the T1 ones, they also have smaller radiative corrections (see section 4.2) and therefore smaller systematic errors.

2. In a given x bin the T2 events extend the Q^2 range of the data towards lower values, thereby allowing a more sensitive study of the Q^2 dependence of the EMC effect.

2.10.1 The T1 Hodoscopes

Five planes of trigger hodoscopes are used for T1: H1V, H1H, H3V, H3H, H4H.

The hodoscopes H1H and H1V (H1 in short) are located at the magnet exit, upstream of the drift chambers W1 and W2. H3H and H3V (H3) are behind the iron absorber, while H4H (H4) is at the end of the spectrometer.

H1H, H3H and H4H consist of a plane of horizontal elements each, and provide three measurements of the vertical coordinate of the scattered muon. H1V and H3V have vertical elements and thus measure the horizontal coordinate.

Table 2.1 summarizes the main characteristics of the trigger counters. The width of the elements is a compromise between spatial resolution and the number of channels; seen from the target it corresponds to a 0.5° angle.

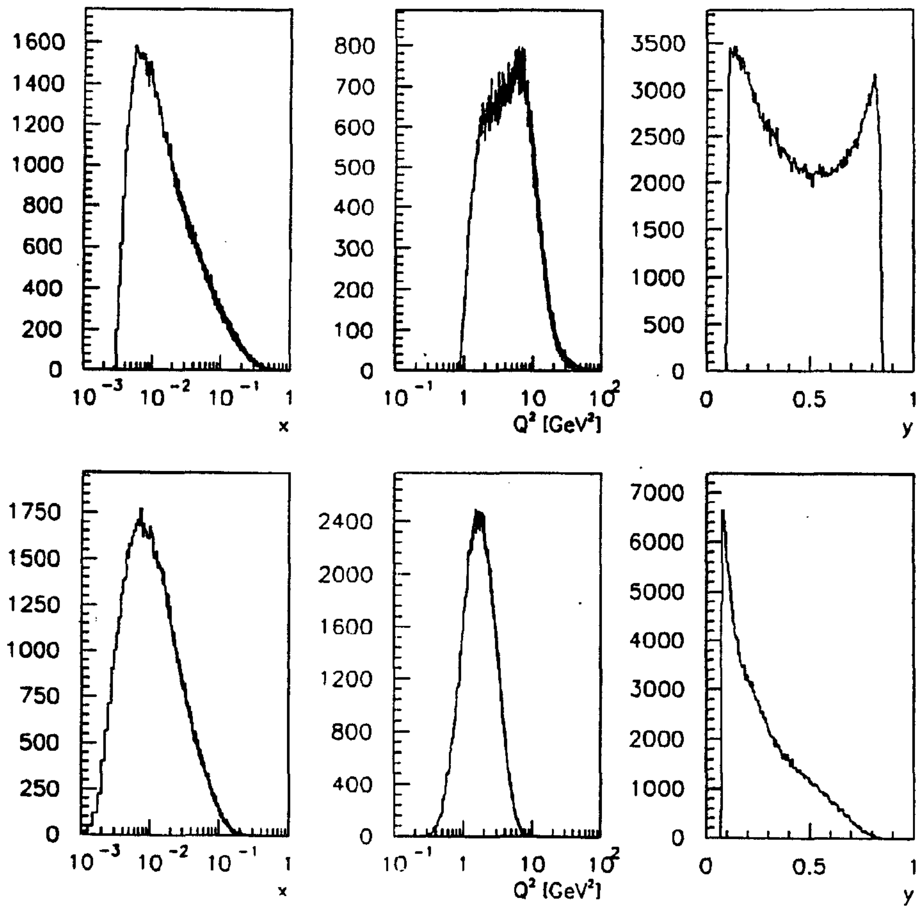

Figure 2.8: The x, Q^2 and y distributions for T1 (top) and T2 (bottom) events

	No. of planes	No. of elements per plane	Scint. thickness (cm)	Area of one element ($y \times z$ cm^2)	Total area per plane (cm^2)	PM type	PM ø (mm)
BMS	4	64	2.0	$(10-60) \times 0.5$	120×100	RT C1910	13
BHA/B	4/4	40	0.4	8×8	12.0×0.4	EMI 9826A	19
V1	1	4	1.0	70×70	120×120 (min.)	XP 2020	50
V2	1	4	0.5	25×25	30×30 (min.)	XP 2020	50
V3	1	< 96	2.0	50×100	1000×450 (max.)	EMI 9813 KB	50
H1H	1	18	0.5	250×7	250×125	EMI 9813 KB	50
H1V	1	36	1.0	7×130	250×130	EMI 9813 KB	50
H3H	1	2×23	2.0	390×13	765×345	EMI 9813 KB	50
H3V	1	50	2.0	15×340	750×340	XP 2020	50
H4H	1	2×29	2.0	500×15	996×430	EMI 9813 KB	50
H1′	1	24	1.0	50×1.4	50×29	EMI 9826B	19
H3′	1	24	1.0	50×1.4	50×29	EMI 9826B	19
H4′	1	32	1.0	50×1.4	50×38.6	RCA C31005B	19
H5	2	4/5	1.0	$(1-8) \times 20$	19×20	XP 2020	50
H2	3 sections	40/20/20	1.0	280×28	560×280	RCA 4522	125

Table 2.1: Main characteristics of some scintillation counters

The length of an element may reach 4 m, a distance that light covers in 20 ns. The timing of a hit will then be known to 10 ns at best, too long a time with respect to the resolution of the veto hodoscopes and to the response time of the coincidence matrices (see below). Each channel is therefore read out by two phototubes, one at each end of the scintillator strip (with the exception of the H1V strips around the beam hole which have only one tube per channel). The signals from the two phototubes are discriminated and sent to a mean timer (Le Croy LRS 624) which gives an output signal after a constant delay with respect to the passage of the particle, irrespective of where the strip has been traversed. The residual timing uncertainty is reduced to ≈ 1 ns. The timing of H3V is recorded by TDC's and gives the actual timing of the event: this is used for example in the selection of the beam track, as discussed previously.

2.10.2 The T2 Hodoscopes

The T2 hodoscopes are composed of 24 (H1′, H3′) or 36 (H4′) partially overlapping horizontal scintillator strips, each read out by a single phototube. The strip dimensions are 50 cm $\times$ 1.4 cm $\times$ 1 cm: the 1.4 cm element width (in y) is smaller than that of the T1 hodoscopes, therefore allowing better spatial resolution. This is important in order to reduce the number of spurious triggers: the problem is more critical for these low angle hodoscopes than for the T1 ones, as the rate is larger at small angles.

Each hodoscope is split up into two halves leaving a gap in the beam region. The gap sizes are are 17, 25 and 30 cm for the three hodoscopes, respectively, and define a minimum scattering angle of about 4 mrad.

2.10.3 The Veto Hodoscopes

Broadly speaking we classify as halo all particles which do not pass through the beam momentum station or through the beam hodoscopes BHA, BHB. The halo rate is about 10^6 particles per spill outside a circular surface of 10 cm radius around the beam axis, for a beam intensity of 10^7 muons per spill. A veto inefficiency as low as 10^{-6} is thus needed to provide the necessary suppression [235]. Halo particles are detected by a set of five scintillation counters (V1, V1.5, V2, V2.1, V3), perpendicular to the beam direction, situated at various positions along the beam line upstream of the targets.

- V1 is located downstream of the last vertical and horizontal bends of the muon beam. It vetoes the small angle, near-beam halo. It is composed of four 1 cm thick counters with a square beam hole of approximately 10×6 cm^2 area.
- The large veto wall V3 is immediately downstream of BHA. It covers an area of 6.5×4 m^2 with a central hole for the beam and is composed of 92 counters partly overlapping, so as to avoid any holes in the vetoing efficiency. An iron wall upstream of V3 cuts out the soft component of the halo (electrons, photons and hadrons generated by decays and interactions with beam line elements), so that V3 sees only the high energy halo muons.
- V1.5 is situated upstream of the iron wall, 50 cm away from V3. It has four rectangular elements of 0.5×1 m^2 area; the central hole has variable size and can be adjusted by displacing the individual elements. It is intended to veto the halo component emerging from the hall floor and produced upstream in the beam line, typically somewhere in the decay channel.
- The other two veto hodoscopes V2.1 and V2 are each composed of four elements with an adjustable central beam hole of ≈ 6 cm diameter. They are placed just upstream of BHB and detect muons outside a 6 cm diameter cylinder coaxial with the targets; they can therefore be used to reject beam tracks which might miss one of the targets.

2.10.4 The Programmable Coincidence Matrices

The matrices allow the N_1 discriminated signals of a hodoscope plane to be correlated with the N_2 of another [236]: individual coincidences between elements in the two planes are masked by a pattern of allowed coincidences (the "matrix pattern") which can be computer loaded. The maximum number of input channels, $N_1 \times N_2$, is 36×25. A matrix produces a set of N_1 output signals, one for each of the N_1 channels of the first of the two hodoscopes. The i-th output signal is non-zero if the following conditions are satisfied:

1. The channel in question is in coincidence with at least one channel of the second hodoscope (i.e. if the two signals overlap in time).
2. The coincidence in 1. is allowed by the matrix pattern.

The outputs of a matrix can be fed into another matrix, in order to impose further conditions. Each matrix also produces an extra output signal by forming the total OR of all the individual coincidences and the matrix pattern. This is used to form the final YES signal which is put in anti-coincidence with the OR of the veto signals to give a T1.

The time resolution of the matrix coincidences is 8 ns; the input rate can be up to 120 MHz and the transit time is 48 ns, which allows several matrices to be cascaded to define correlations among more than two hodoscope planes.

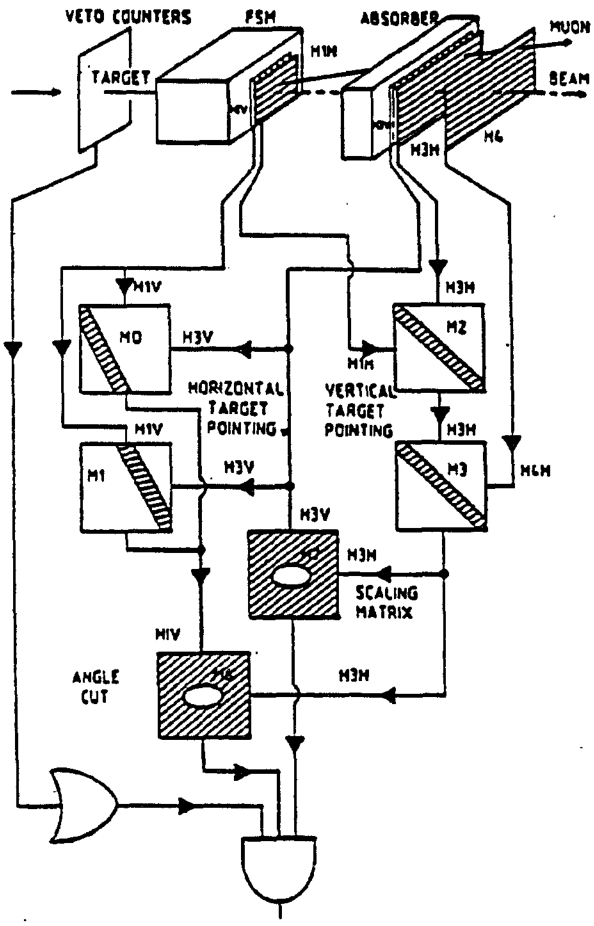

Figure 2.9: The trigger 1 conditions

2.10.5 The Trigger 1 Conditions

As we said before the spectrometer is read out upon detection of a muon track coming from the target region and passing through the five planes of the trigger hodoscopes. Muons are identified on the basis of their penetrating power: hadrons and electrons are expected to be stopped by the calorimeter and the absorber. The iron wall immediately upstream of H4 further improves the trigger efficiency by absorbing the soft electromagnetic showers originating from interactions on the edge of the absorber hole or in the W67 chambers. The signals from the trigger hodoscopes are input to a chain of coincidence matrices (fig. 2.9) with patterns predetermined by Monte Carlo simulations. The conditions imposed are listed below.

- Horizontal Target Pointing. Target pointing in the horizontal plane (this is the bending plane of the FSM) is achieved by combining the information of H1V and H3V (the only two trigger hodoscope planes with vertical strips) in the M0 and M1 matrices. M0 and M1 are effectively used as a single 36 $\times$ 50 matrix.

- Vertical Target Pointing. The H1H and H3H hits are combined in M2; the H3H hits, masked by M2 are then combined with the H4H ones in M3 in order to impose the target pointing condition in the vertical plane. Better precision in the pointing can be achieved in this projection as tracks are not bent by the FSM field.

- Minimum Angle Cut. This cut is applied by the M6 matrix which puts in coincidence the H1V and H3H hits after they passed both the horizontal and the vertical target pointing requirements. The minimum scattering angle acceped after this cut is $\approx 0.5°$ (depending on the position of the vertex, of course).

- Scaling. M7 provides an additional angle cut for low momentum muons at small scattering angles. Such muons mainly originate from the decay of pions and kaons produced in the interaction or from radiative processes in which the incoming or the outgoing muon radiate a photon. In these events the muon may go through the H1 hole and hit H3, thereby faking a trigger in conjuction with other tracks detected in H1.

  M7 is programmed to remove the region of H3 where such unwanted events cluster. The inputs to M7 are the H3V signals and the H3H ones, after the vertical target pointing conditions. Special studies were made before the beginning of the NMC data taking in order to optimize the M7 setting; the main point was to improve the suppression of the low Q^2, high ν radiative events. As a result the trigger rate reduction was about 30% with respect to the EMC setting, with an estimated loss of good events of $\approx 4\%$.

- Absence of Halo Muons. Finally the logical OR of all the veto hodoscopes is put in anti-coincidence with the AND of M6 and M7 to produce a trigger 1.

2.10.6 The Trigger 2 Conditions

The T2 strategy is similar to that of T1, except for the use of different trigger hodoscopes. Figure 2.10 shows the trigger 2 logic scheme.

From a logical and electronic point of view the upper and lower halves of the T2 hodoscopes are treated separately. Within each half the H3′ and H4′ signals are fed into a coincidence matrix (M8) which imposes a vertical angle cut and (vertical) target pointing. No horizontal target pointing can be checked as none of the T2 hodoscope planes has vertical elements.

The vertical angle cut and the target pointing conditions are then applied once more using H1′ coupled with H3′ and separately with H4′. A MLU-PLU combination (MLU stands for Memory Look-up table, while PLU means Programmable Logical Unit) replaces the matrices. MLU's are computer controlled CAMAC units which contain the allowed coincidence patterns; upon receipt of a strobe (the M8 output, in this case), they load the pattern into the PLU, which uses it to mask the coincidences between the hodoscope signals. The MLU-PLU combination effectively acts as a matrix. Finally the PLU outputs are ANDed together and put in anti-coincidence with the OR of the veto hodoscopes to produce a Trigger 2.

2.10.7 The Other Triggers

Besides the physics triggers T1 and T2 described above, a number of other triggers are implemented. They serve various purposes, notably beam flux measurement (T3, T4, T10), detector spatial alignment and timing (T5, T6, T7, T8) and trigger hodoscopes efficiency measurement (T11, T12). A random trigger (T9) is also available.

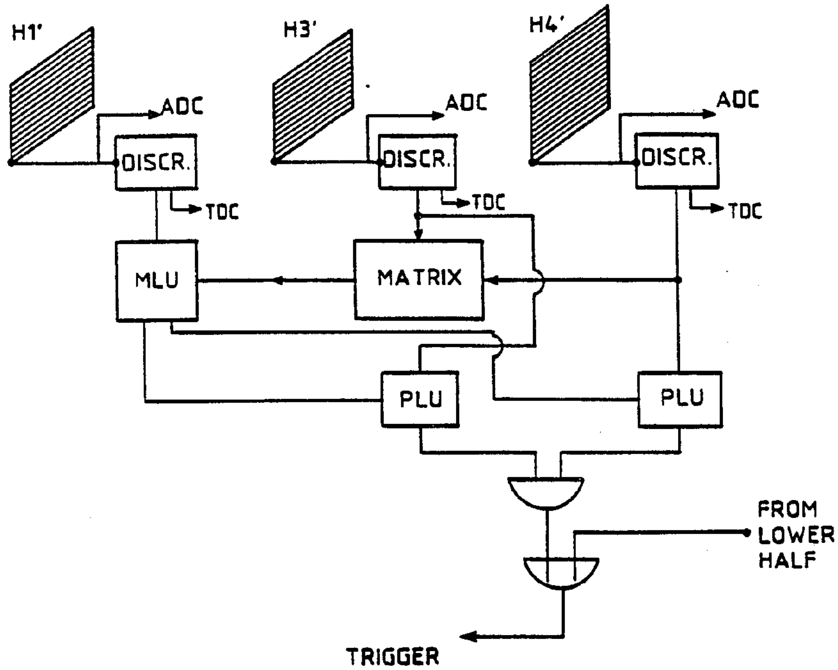

Figure 2.10: The trigger 2 conditions

The Normalization Triggers: T10 and T3-4

The precise measurement of the incoming muon flux is a very difficult task if conventional techniques are used: at beam intensities of 2×10^7 muons/s (i.e., on the average, one muon every 50 ns) scintillators and phototubes easily become saturated and knock-on electrons have to be eliminated by fast logic. Two different methods have been devised to measure the useful incoming flux; both exploit the fact that none of the beam measuring detectors (BMS, BH's) is used in the definition of the physics triggers.

Ratios of structure functions are independent of the integrated fluxes when the complementary target method is used (section 2.9.1); furthermore the T3-4 information was not available for the data taking period analyzed in this work. We nonetheless briefly describe the two techniques, as they are interesting in their own right.

A first method (T10) [237], already implemented in the EMC experiments, consists of starting the BMS and the BH TDC's during the spill with a random signal (average frequency $f \approx 8$ Hz), in anti-coincidence with the OR of the veto hodoscopes. All beam tracks arriving within a given time window (of width τ) are recorded and processed through the same analysis chain used for physics triggers. The integrated reconstructable flux ϕ is then given by

$$\phi = \frac{\textit{Number of Reconstructed Beam Tracks}}{\tau f}. \tag{2.6}$$

In order to minimize correlations between the trigger and the beam, an americium radioactive source is used as random generator; for the same reason the read-out electronics of the source is placed underground, several hundred meters away from the beam line. Statistical accuracies of $\approx 1\%$ for the integrated flux measurement for one data-taking period can be achieved.

An alternative and independent method to measure the useful beam flux was developed by the NMC. Hits in the central 16 strips of BHA3 (z) and BHB1 (y) are counted by scalers. Every 2.56×10^6 scaler counts in BHA3 (z) (BHB4 (y)) a T3 (T4) is issued and the BH and BMS information is written to tape (provided there is no in-time signal from the veto hodoscopes). From these data the probability that a scaler count represents a useful incoming muon can be determined. The integrated recostructable flux is then obtained by multiplying the integrated scaler content by the probability that a scaler count corresponds to a useful beam track.

Both T3-4 and T10 have the advantage that the treatment of beam tracks is the same as for the physics triggers events. Inefficiencies due both to hardware and software are thus directly included in the measured muon flux, thus making the knowledge of the absolute flux unnecessary.

The Alignment Triggers: T5, T6, T7, T8

- The beam Trigger: T5.

  T5 is defined as $\overline{VETO} \times$ H5; it is used for the on-line monitoring and off-line alignment of the beam hodoscopes and P0 chambers. A small fraction of T5's is always written to tape (typically 5-10 per spill) in order to allow a run by run monitoring of BMS and BH timing.

- The Tilted Beam Trigger: T6.

  It is given by the condition T6 = Σ V2 $\times$ H3.9 $\times$ H1H$_{center}$; it is operational only during alignment runs and depends on a deflected beam to produce muon tracks which pass through the beam chambers and the live regions of W12, P45, W45.

- The Near Halo Trigger: T7.

  T7 = H3H $\times$ H4H$_{center}$ $\times$ H3V$_{center}$ $\times$ Σ V3$_{center}$

  Its purpose is to monitor the big proportional chambers (PV12, P123) together with W12, W45 and the central module of W67; it is also used off-line for the alignment and efficiency calculation of such chambers.

- The Far Halo Trigger: T8.

  T8 = $\overline{T7}$ $\times$ H3H $\times$ H4H $\times$ Σ H3V

  Trigger 8 is used for on-line monitoring of the outer regions of the W12, W45 and W67 chambers. Like T7 it is also used off-line in the chamber alignment and efficiency calculation. Also the H3V timing is checked with these triggers. Both T7 and T8, like T5, are written to tape (typically a few per spill) also during standard data taking runs.

The Trigger Hodoscopes Efficiency Trigger: T11

Trigger 11 is defined as HiH $\times$ ΣV3, with i = 3 or 4; it is principally used in the off-line calculation of the trigger 1 hodoscopes efficiency.

A similar trigger (T12) is now available for the T2 hodoscopes efficiency measurement. It was however not yet implemented in 1986 when the data discussed here were taken.

The Random Trigger: T9

Trigger 9 is produced using a pulse generator at ≈ 10 Hz and reads out the whole apparatus. The presence of other triggers within the data acquisition system randomizes the number of T9 events written to tape in each spill. On-line monitoring tasks are run on T9 in the absence of beam.

2.11 The Tracking System

It is important to achieve very good resolutions on the scattered muon momentum and scattering angle since the cross section varies very quickly as a function of these variables.

The angles and momenta of the particles emerging from the target region are measured by a classical spectrometer built around a large aperture air-core dipolar magnet (the Forward Spectrometer Magnet, FSM).

The lever arm in front of the magnet is provided by the proportional chambers PV1 and PV2, which completely cover the magnet aperture. The two small chambers P0B and P0C, the first between the upstream and downtream targets, the second close to PV12, are especially designed to work up to intensities $\sim 10^8\mu/s$ and insure track reconstruction in the beam region. The chamber P0B detects the particles scattered at low angles when the vertex is in the upstream targets; it is used to further constrain the beam track in the events occurring in the downstream targets.

The back arm consists of the drift chambers W1 and W2 just behind the FSM, W4 and W5 some 5 m downstream and the large W6 and W7 chambers situated behind the iron absorber. The central regions of W45, where the rate is high and the efficiency of the drift chambers is low, are also covered by the proportional chambers P4 and P5. The proportional chambers P0E (close to W12) and P0A (in the W45 region), similar to P0B and P0C, allow tracking in the beam region, in which W12, W45 and P45 are made insensitive because of the high rate. Tracking in the FSM is made possible by the three proportional chambers P1, P2 and P3; their central region is desensitized and is covered by P0D at the magnet entrance.

Typical accuracies attained are $\delta(p)/p \approx (0.66p(\text{GeV}) + 25.1) \times 10^{-4}$ for the momentum and $\delta(\vartheta) \approx 10^{-4}$ rad for the scattering angle [8].

2.11.1 The Forward Spectrometer Magnet

The Forward Spectrometer Magnet (FSM) is a classical air-core dipole with an aperture of 2×1 m^2 and 4.3 m length along the beam direction. Two water-cooled copper coils allow a maximum operating current of 5000 A, corresponding to a field integral of ≈ 5 Tm. The working current is however chosen depending on the beam energy: 2000 A for 90 and 120 GeV, 4000 A for 200 GeV and 5000 A for 280 GeV; the deflection for the beam muons is therefore about the same at the different energies and amounts to ≈ 6.5 mrad. At 4000 A the momentum cut-off imposed by the magnet aperture is ≈ 4 GeV: lower momentum particles are deflected against the inside walls of the magnet and do not reach the downstream chambers. The magnet field has been mapped [238] and the integral of the field $\int B dx$ is supposed to be known to a fractional accuracy of $\sim 2 \times 10^{-3}$. More comments on this can be found in appendix A.

2.11.2 The Proportional Chambers

Proportional chambers have been adopted everywhere the high track multiplicity or the presence of a magnetic field forbids the use of drift chambers, which allow in principle better spatial resolution and are cheaper to instrument. Table 2.2 summarizes some of the proportional chambers characteristics.

- PV1 and PV2 (PV12 in short). These chambers located upstream of the FSM and have a sensitive area of 1.50 × 0.94 m^2 and 1.54 × 1.00 m^2, respectively. The sense wires are vertical and at ±10° for PV1; they are vertical and at ±18°, ±45° with respect to the vertical for PV2. The wire spacing is 2 mm and the wire diameter is 20 μm. The central area of PV2, where the beam passes, is made insensitive by the insertion of kapton cylinders glued to the cathode wires.

  The PV1 gas mixture is 65% argon and 35% isobuthane, while the PV2 one is 71.5% argon, 23.8% isobuthane, 4% methylal and 0.7% freon.

  Hybrid amplifier-discriminators [239] are mounted directly on the chambers. The output signals are fed into 100 m of twisted-pair delay cable, and finally end up in standard receiver modules (RMH [224]) which gate the hits from the chamber with a strobe derived from the trigger and encode them.

- P1, P2 and P3 (P123) are placed inside the magnet and have a sensitive area of 1.8 × 0.8 m^2, thus filling most of the magnet aperture.

  Each chamber consists of three planes of signal wires: horizontal, vertical and inclined by ±20° to the vertical, respectively. The anode planes are made of 20 μm diameter gold-plated tungsten wires with a 2 mm pitch; they are 8 mm away from the cathode planes which consist of horizontal arrays of 100 μm diameter Cu-Be wires with 1 mm spacing. Anode and cathode planes are soldered and glued to machined epoxy-glass frames which are bolted onto two stainless steel frames. The central areas of the chambers are made insensitive with a technique similar to that used for PV2.

  The gas mixture and the read-out system used are the same as those of PV2.

- The P4 and P5 proportional chamber systems (P45) consist altogether of five chambers interspersed between the drift chambers W45. Their installation was decided by the EMC during the NA9 experiment, in order to compensate for the efficiency deterioration of W45 in a region of about 30 cm radius around the beam axis. Each chamber has two planes, one vertical and one at 60° to the vertical. The sensitive area is of dodecagonal shape of about 45 cm effective radius and is covered by 448, 20 μm thick sense wires with 2 mm pitch. The cathode plane consists of 25 μm kapton foil coated with a thin layer of carbon. The central region of the chambers is normally made insensitive by appropriately reducing the voltage on the central part of the cathode plane in order to avoid damages caused by the high beam rate; this region is however rendered alive during low intensity alignment runs.

  An argon, isobuthane, freon mixture is used; the relative percentages are 78%, 20% and 2%, respectively.

  These chambers are read out by hybrid amplifier-discriminator cards, which are placed on the chambers themselves. The signals are then encoded by the RMH [224] modules mentioned before.

  At the very beginning of the SPS period in which the data discussed in this thesis were taken, the chambers P4A and W4A caught fire and were not available for the whole period.

Name	Type	Active area	Number of planes	Wire spacing
P0B, P0C	Prop.	14.4 cm ⌀	$2y$, $2z$, 4ϑ	1 mm
PV1	Prop.	$160 \times 65\,\text{cm}^2$	$2y$, 2ϑ	2 mm
PV2	Prop.	$160 \times 65\,\text{cm}^2$	$2y$, 4ϑ	2 mm
P0D	Prop.	14.4 cm ⌀	$2y$, $4z$, 2ϑ	1 mm
P1, P2, P3	Prop.	$182 \times 80\,\text{cm}^2$	$1y$, $1z$, 1ϑ	2 mm
P0E, P0A	Prop.	14.4 cm ⌀	$2y$, $2z$, 4ϑ	1 mm
W12	Drift	$225 \times 125\,\text{cm}^2$	$4y$, $4z$, 8ϑ	2 cm
W45	Drift	$520 \times 260\,\text{cm}^2$	$6y$, $6z$, 4ϑ	4 cm
P45	Prop.	90 cm ⌀	$5y$, 5ϑ	2 mm
W67	Drift	W6: $288 \times 348\,\text{cm}^2$ W7: $348 \times 432\,\text{cm}^2$	W67B: $6y$, $6z$, 4ϑ W67A,C: $4y$, $4z$, 3ϑ	12 cm

Table 2.2: Main parameters of the forward spectrometer wire chambers

- The P0 chambers (P0B, P0C, P0D, P0E, P0A) are multi-plane proportional chambers, designed to stand particle fluxes up to $10^8\,\mu/\text{s}$. Each plane is composed of 144 gold-plated tungsten wires 10 μm in diameter with 1 mm pitch. Two planes measuring the same coordinate within a given chamber are shifted with respect to each other by half the wire spacing, thereby reducing the effective pitch to 0.5 mm. Each sense plane is enclosed by two cathode planes, made of a graphite-mylar sheet, to which the negative high voltage is applied. Within a chamber there are 8 planes; the wires are vertical, horizontal and at $\pm 30°$ with respect to the vertical.

  The gas used is a mixture of argon, freon and isobuthane. The relative proportions are 74%, 25% and 1%, respectively; a small ($< 1\%$) fraction of methylal is also present.

  The read-out system [240] is designed to minimize the chambers dead time and is based on hybrid low-impedance amplifiers designed at Rutherford Laboratory, similar to (but not compatible with) the P45 ones.

2.11.3 The Drift Chambers

Drift chambers are used in the spectrometer downstream of the FSM, where the low energy particles produced in the interaction have been swept out of the apparatus acceptance by the magnetic field, with a drastic reduction of the charged multiplicity. Typical multiplicities upstream of the FSM, say in PV1, may be as high as 15; downstream of the magnet they are reduced by more than a factor two. Due to the lower number of sense wires drift chambers can be used to cover larger areas. Table 2.2 summarizes some of the drift chambers characteristics.

- W1 and W2 (W12 in short) are immediately downstream of the FSM. They nearly cover the whole magnet aperture, being $2.2 \times 1.2\,\text{m}^2$ in area. W12 consists of 16 anode planes, divided in four modules with independent gas volumes. Sense wires are vertical, horizontal and at $\pm 60^\circ$ to the vertical. A 12 cm diameter circular region at the center has been made insensitive by electroplating the sense wires with silver.

- W4 and W5 (W45) are similar in construction to W12 but have a wider sensitive area: 2.6×5.2 m^2. Sense wires are vertical, horizontal and at 30° to the vertical. Here again the central region is desensitized, by means of polyamide foils glued to the sense wires. We mentioned already that W4A was not in function during the SPS period P4A86.

- W6 and W7 (W67) are situated at the end of the spectrometer, downstream of the calorimeter and of the iron absorber. In order to cover the angular aperture of the FSM they have to extend over a very wide area, 10×4.4 m^2; for this reason they are divided in smaller sections (A, B and C). Each consists of four modules (see fig. 2.2), with the plane structure summarized in table 2.2. The modules are staggered in order to maximize the track finding efficiency. The central section, B, has more planes than the others (16 instead of 11), due to the larger halo flux to which it is exposed. Sense wires are vertical, horizontal and at 60° to the vertical. The beam region is desensitized with the same technique used for W45.

The structure of the drift cells of W12, W45, W67 is shown in fig. 2.11. The chosen drift spaces represent a compromise between economy of electronics and rate on the individual wires, mainly dominated by in-time halo muons. The sense wires of all drift chambers are made of 20 μm gold-plated tungsten, while the potential wires consist of 100 μm Cu-Be except for W1 where three 50 μm diameter wires are used. The cathode planes are made of Cu-Be wires 50 μm thick, with the exception of the W67 chambers which have 3 mm wide Cu strips.

The gas mixtures are supplied by a servo-valve (Rota-meter) system. An argon-methane-isobuthane mixture (78.5%-19.5%-2%) is used for W12 and W45 and an argon-ethane (65%-35%) one is used for W67.

All chambers have amplifier-discriminator cards (CERN types 4241, 4242, 4243) mounted directly on the frames. The discriminated signals are fed, via twisted-pair cables, to the Drift Time Recorders (CERN DTR type 247), which have a time resolution of $\approx$ 4ns. Due to limitations of the amplifiers, the inter-signal dead time is $\approx$ 60 ns which corresponds to a minimum track separation of 3 mm.

For a beam intensity of 10^7 muons/s the plane efficiencies range typically from 93% to 99%, yielding more than 99% efficiency for each set of chambers to detect a track. Typical spatial resolutions (averaged over one plane) are 0.3 mm in W45 and 0.4 mm for W67.

2.12 Particle Identification

Particle identification in the NMC spectrometer is limited to muons, electrons and photons. Muons are filtered out by the combination of the calorimeter H2 and the hadron absorber; electrons and photons are singled out from hadrons by the calorimeter H2.

2.12.1 The Hadron Absorber

The iron absorber is located downstream of W45 and just upstream of H3. It consists of a 2 m thick iron wall covering an area of 8×3.5 m^2, with a hole for the beam in the center. Together with the calorimeter H2 it provides $\approx$ 15 absorption lengths, reducing the background from electromagnetic showers and hadron punch-through to a minimum. Muons, on the other hand,

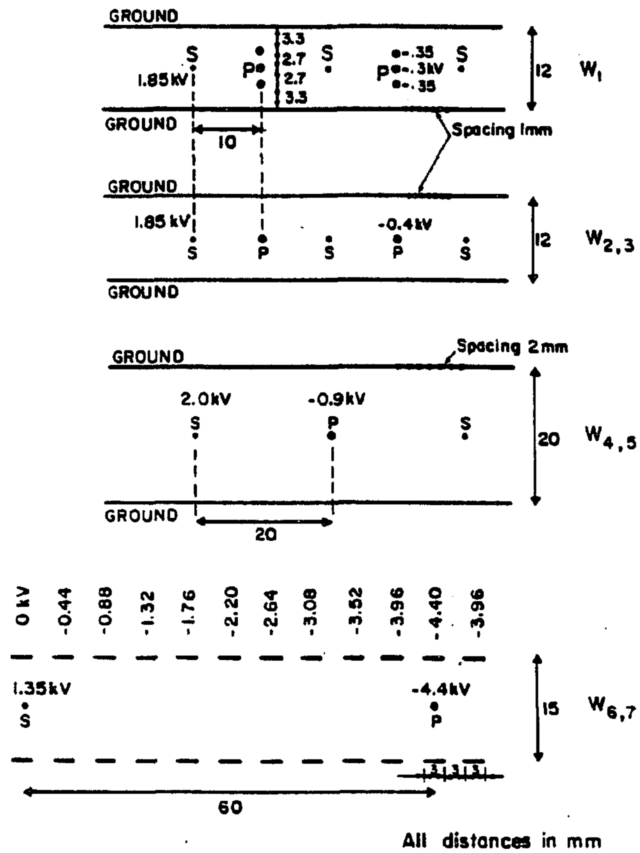

Figure 2.11: The drift cell structures for the various chambers (from [211])

pass with minimal energy loss and some multiple scattering which, for a momentum of 50 GeV, causes an uncertainty in the scattering angle of about 5 mrad.

The hadron absorber was originally intended to be magnetized with opposite horizontal fields in the upper and lower halves. The aim was to deflect vertically the muons so as to suppress the triggers due to low energy particles, mostly coming from the decay in flight of pions and kaons produced in the interaction. The obtained suppression was not as effective as expected, the field being much less homogeneous than foreseen and the field was definitely turned off already in 1979. A residual field has however remained in the absorber [241] and must be taken into account in the track linking between W67 and W45.

2.12.2 The Calorimeter H2

H2, just upstream of the absorber, provides some calorimetric capability for neutral particles within the acceptance of the spectrometer as well as a means of identifying muons, electrons and hadrons.

The calorimeter (fig. 2.12) is divided into two halves, to the left and the right of the beam, and each half is divided longitudinally in three sections. A 20 cm diameter hole is left for the beam.

The upstream section (the electromagnetic part) is composed of lead sheets interspersed with plastic scintillator blades, 1 cm thick, 28 cm wide and 2.8 m long. Planes with horizontal and vertical blades are interleaved in the longitudinal direction. The blades from a plane are grouped together to form forks, each of which is coupled to a single 125 mm phototube. The lead in this section combined with the steel face plates (see fig. 2.12) amounts to 20 radiation lengths and 0.95 interaction lengths of material, thus assuring containment of all electromagnetic showers. In this section hadrons produce signals equivalent to a few minimum ionizing particles.

The two downstream modules (the hadronic section of the calorimeter) have horizontal and vertical blades, respectively, and the passive material is steel in the form of 4 cm thick plates. The total thickness of the electromagnetic section plus the two hadronic sections is $\approx$ 5.5 interaction lengths.

The energy resolution of H2 is $\sigma/E = 0.4/\sqrt{E\ (GeV)}$ for electrons in the lead section alone and $\sigma/E = 1.5/\sqrt{E\ (GeV)}$ for the hadronic energy, measured as the sum of the energies deposited in each module.

2.13 The Data Acquisition and On-line Monitoring

At the time when the data discussed in this thesis were taken the acquisition and on-line monitoring system was still the same as the one developed and used by the EMC [242]. It was based on a network of four PDP 11/70 computers, labelled DAC, U0, U1 and U2, interconnected using 5 Mbaud OMNET serial links [243] via a small PDP 11/10 computer (MPX), which acted as a multiplexer and an interface to the CERNET network. The latter gave access to the central CERN IBM 370/168 computer.

The main data-acquisition computer (DAC) acquired data during the beam spill, stored them temporarily into a 160 Kbyte buffer before transferring them onto tape. Data acquisition and tape writing were overlapped during the spill. Outside the spill the DAC wrote any unrecorded data to tape and then distributed samples of complete events to the monitoring tasks running on the other three computers.

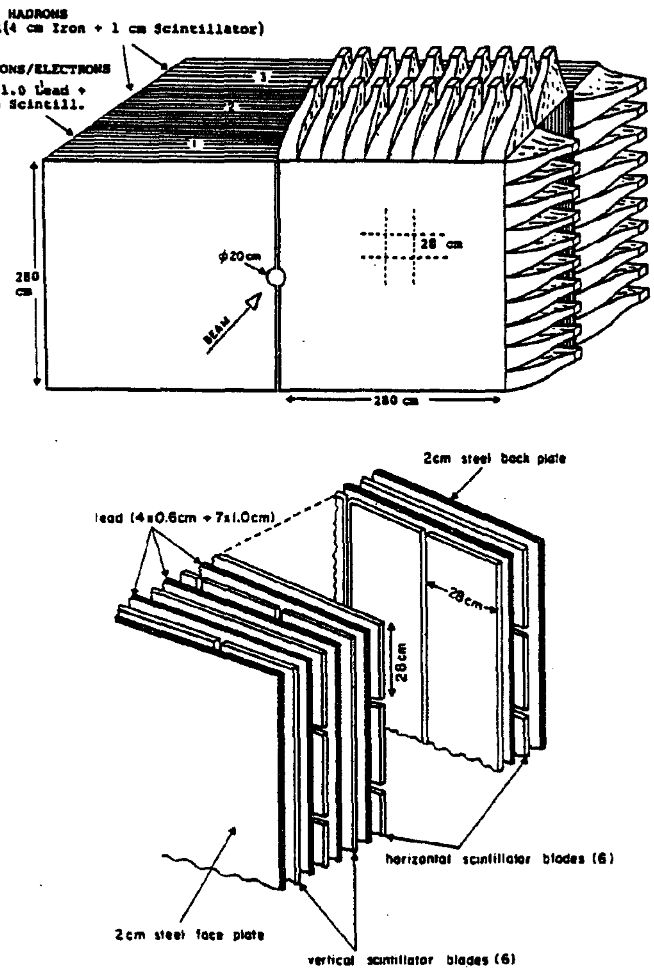

Figure 2.12: The H2 calorimeter (from [211])

U0 and DAC had a common CAMAC interface to the read-out. U0 was used to read and check the hodoscopes high voltages, inject pulses into the chambers read-out system and to read the currents in the beam line magnets. U1 and U2 had no direct access to the read-out system and were used exclusively to run tasks monitoring the performance of various pieces of the apparatus by means of event samples obtained from the DAC.

Each detector had typically several on-line tasks which monitored its performance and reported any malfunctioning to the experimental log and to a TV status screen. Any serious faults produced an audible alarm and, if necessary, suspended the data-taking. As an example the beam hodoscopes had (and still have, in the new system which replaced the old EMC one) three programs associated with them. The program BHHV was used to set the high voltages and to check them periodically. BHCHK fired every scintillator strip with LED's outside the spill, read out the beam hodoscopes TDC's and looked for dead channels. BHMON sampled real events and plotted the beam profiles and the stop time of the BHA and BHB TDC's separately.

Samples of several thousands events were periodically sent to the central CERN IBM computer in order to reconstruct them and perform efficiency calculations. The outputs of these jobs were automatically printed in the counting room.

The read-out system used was the CERN-developed ROMULUS [244]. This is a read-only CAMAC-based system which allows the acquisition of data from many CAMAC crates with minimum dead time. The read-out is logically divided into a number of distinct sub-branches, each being associated with a piece of apparatus. These sub-branches can be enabled or disabled via control lines connected to the associated ROMULUS Branch Driver (ROBD) so that an event can consist of any combination of the available and enabled pieces of the equipment. Up to 16 different trigger conditions can be defined, each with a different set of detectors read out. Any combination of triggers may then be chosen to be written onto tape.

Direct memory access to the computer allowed data transfer from CAMAC at a rate of up to 1.5 μs per 16 bit word. This produced a dead time of about 3.5 ms for the read-out of a complete event of about 1200 16 bits words.

Chapter 3

The Data Reduction Chain

"Mine is a long and a sad tale" said the Mouse [...]
"It is a long tail, certainly," said Alice [...],
but why do you call it sad ?" [245]

Introduction

The extraction of physics results from the raw-data tapes is a long and complex procedure. It involves decoding the raw-data, reconstructing track segments in the individual detectors and joining them into tracks traversing the whole spectrometer. Tracks are then fitted and momentum analyzed. The interaction point is found and the full event topology and kinematics are determined. The information thus gathered about each event is very detailed but much too extensive for a physics analysis. The relevant results are therefore filtered out and stored in a highly compact form. Only at this point can physics analysis begin.

All NMC programs are written in FORTRAN and use the CERN developed offline editor PATCHY [246]. Extensive use is made of the dynamic memory managment package ZBOOK [247] and of the histogramming package HBOOK [248]. Input/output at all stages is carried out using the standard, machine independent, EPIO format [249].

A large fraction of the software chain used by the NMC was originally developed for the EMC experiment. Additions have however been made at various stages, mostly in connection with new or modified hardware (e.g. the beam hodoscopes, trigger 3-4, the beam momentum calibration station etc.).

We will now discuss the various steps in the data reduction process (the data "production", in the experimentalists' jargon). The final analysis program will be the subject of the next chapter.

3.1 Pattern Recognition: PHOENIX

The pattern recognition program Phoenix uses the beam hodoscopes and BMS information to reconstruct the beam tracks. It also reconstructs the outgoing muon and hadron tracks using the wire chamber information.

The event pattern recognition starts from the incoming beam: tracks are reconstructed in the beam hodoscopes and matched to the relative BMS information. Failure to find a beam track causes the event to be rejected.

Once the beam track has been reconstructed, Phoenix proceeds to find and reconstruct the scattered muon. A particle is presumed to be a muon when it is detected downstream of the hadron absorber. Track segments are therefore first looked for in the W67 chambers. Candidates are then extrapolated backwards through the absorber and a search is made for the corresponding lines in W45/P45, W12/P0E, in the magnet chambers P0D, P1, P2, P3 and upstream of the magnet in the PV1, PV2 and P0C chambers. If at any stage the muon track is lost and none of the original W67 candidates survives, the event is rejected.

For the events with at least one reconstructed muon track hadrons are searched for starting from W45 and again proceeding backwards to the FSM and the target region.

In what follows we will describe in some detail the different parts of the event reconstruction procedure. Before we embark in this, we recall here that raw-data information cannot be directly input to the pattern recognition software. Each event on a raw data tape presents itself as a sequence of numbers separated by "marker words" which identify the various pieces of equipment in the apparatus (BMS, BHA/B, W12, ...). The first operation done by Phoenix is therefore the decoding of the raw-data information. This is carried out by a specific set of routines (the Decoding Package) which translate the raw-data referring to a given detector into wire numbers, hodoscope channels, DTR and TDC readings. This mapping of the numbers written by the read-out system into physical information is strictly time dependent: cables may be swapped, individual detectors may be modified in the course of time etc.

Not all events are successfully reconstructed. The overall fraction of triggers rejected by Phoenix (no scattered muon, no beam track or simply impossibility to decode the event) amounts to $\approx 51\%$ for T1 and $\approx 45\%$ for T2.

3.1.1 Beam Muon Reconstruction

The Beam Momentum Station information is processed first; tracks with at least one signal in three out of the four BMS hodoscopes are assigned a momentum according to the procedure outlined in section 2.5. Hits are selected on the basis of the timing information: hits in different planes may be associated to the same line only if their timings fall within a window 1.3 ns wide. In case of ambiguities the combination closest in time is chosen. The fraction of events with at least one track accepted and measured in the BMS is typically $\approx 94\%$; 4-hit and 3-hit tracks are $\approx 67\%$ and $\approx 39\%$, respectively.

After evaluating momentum of the incoming muon, Phoenix proceeds to determine its direction using the beam hodoscopes. For the details of the pattern recognition in the beam hodoscopes we refer the reader to appendix B. A beam muon is successfully recostructed in the beam hodoscopes in about 95% of the T1 and T2 events.

Tracks found in the beam hodoscopes are extrapolated to P0B and hits in P0B tagged. A global fit (BH + P0B) is not attempted here but is left to the Geometry program.

At this point BMS and BH results are matched: a track in the beam hodoscopes is attributed the momentum found by the BMS if the timings from the two detectors differ by less than 2 ns. About 90% of the events have at least one correlated (BMS + BH) track; about 18% have more than one. Events in which no acceptable combination of BMS and BH tracks is found are assigned the nominal beam momentum (200 GeV, in this case). In the present analysis such events were however discarded at the Snomin stage (section 3.3).

3.1.2 Scattered Muon Reconstruction

Reconstruction in W67

The W67 pattern recognition is a complex procedure mainly because of the large width of the W67 drift cells (6 cm, cf. table 2.2) which translates into a long drift time ($\approx$ 1200 ns). During this time the chambers are sensitive to spurious tracks, for instance uncorrelated electromagnetic showers coming from the region of the absorber hole. This adds to the well known left-right ambiguity, a problem common to all drift chambers, which effectively increases the number of hits by a factor two. Whenever possible the information of the trigger hodoscopes is used to resolve the ambiguity.

Recostruction is attempted for the three W67 modules (A, B, C) independently, first in the z and then in the y projection; the lines found in the two projections are later associated using the ϑ planes. The minimum plane requirements in W67 (i.e. the minimum number of planes with at least one hit attributed to the track) are the following:

1. W67 A: 3/4 y planes, 3/4 z planes, 2/3 ϑ planes;
2. W67 B: 4/6 y planes, 4/6 z planes, 3/4 ϑ planes;
3. W67 C: 3/4 y planes, 3/4 z planes, 1/3 ϑ planes.

About 8% of the T1 events have no W67 line and are therefore abandoned; this fraction rises to 37% for T2.

Reconstruction in W45/P45

Lines which have been successfully recostructed in W67 are extrapolated to the W45 region, with due allowance for multiple scattering in the iron absorber and in the calorimeter. Hits in the W45 and P45 chambers are searched for within an appropriate distance ("road-width") from the extrapolated W67 track, are tagged and used for recostruction, according to the procedure outlined below. Non-tagged hits will be subsequently used for hadron reconstruction. Tracks in W45/P45 fall in one of three classes:

1. W45 only: tracks reconstructed using W45 hits only;
2. W45 + P45: tracks for which the W45 minimum plane requirement was fulfilled, but for which hits were found in P45 and were included in the global fit;
3. P45 + W45: tracks which satisfied the full P45 minimum plane requirement and only a reduced W45 one (see below).

Similarly to what happens in W67, W45 tracks are first found and fitted in the y and z projections separately and later associated using the ϑ hits. For P45 the situation is slightly more complicated due to the absence of z planes: ϑ coordinates need to be converted into z coordinates using the y hits. This determines a y-ϑ correlation and produces a number of ghost z lines. For a given P45 y line, each z line is extrapolated to W45 and a global 3-dimensional fit is made including the W45 hits, if there. The correct P45 z projection is taken to be the one which gives the smallest χ^2.

Notice that no global W45/P45-W67 fit is attempted here, due to the multiple scattering in H2 and in the absorber: it is left to Geometry (section 3.2.3) to decide which of the W45/P45 and W67 line segments really belong to the same track.

We recall that chambers W4A and P4A were not operational during the data taking period considered here: this means that the number of useful W45 y planes was reduced from 6 to 4; the same reduction applied to the z planes. In P45 the loss amounted to one y and one ϑ plane. The minimum plane requirements for W45 in the current analysis are therefore looser than normal. We list them here, together with the P45 ones (which were instead the standard ones):

- W45: 3/6 y planes (instead of 4/6), 3/6 z planes (instead of 4/6), 3/4 ϑ planes;
- P45 + W45: 3/4 y planes, 3/4 ϑ planes in P45;

  2/6 y planes, 4/10 z-ϑ planes in W45.

About 20% (25%) of the W67 lines are lost at this stage of the reconstruction, for T1 (T2) events.

Reconstruction in W12/P0E

W45/P45 lines are extrapolated to the W12/P0E chambers and hits inside the roadwidth are tagged. Pattern recognition is very similar to that in W45. If the minimum plane requirement is satisfied in W12 or P0E (10/16 and 5/8 planes, respectively), a global W12/P0E-W45/P45 fit is made.

For T1 events about 90% of the W45/P45 tracks are found in the W12/P0E chambers; the percentage is 94% for T2.

Reconstruction in the Magnet

Tracking in the magnet is made difficult by the presence of the magnetic field which bends the particle trajectories in the y plane. The magnet aperture is covered by the P1, P2, P3 chambers, except for the central region which is covered by P0D.

Tracking in the z projection, where the bending is negligible, is attempted first: W12/P0E-W45/P45 lines are extrapolated, hits found inside the roadwidths are tagged and a z line is fitted if the minimum plane requirement in the P123 or P0D chambers is met. Note that the result of the W12/P0E-W45/P45 fit, extrapolated at the position of W12/P0E, is used as a point in the new fit: this allows to demand only at least 2 (out of 3) z planes in P123 and 3 (out of 4) in P0D.

For each of the z lines thus found (there can be more than one for a given W12/P0E-W45/P45 line) pattern recognition is attempted in the y and ϑ planes according to the following procedure:

1. If the z line is in P0D, all the y and ϑ hits in P0D (at least 3/4, with at least one ϑ) are searched for and buffered.

   For each P0D point a circle passing through the point itself and tangent to the W12/P0E-W45/P45 line is extrapolated to P123, demanding at least 1 out of 3 planes in each chamber for which the prediction is outside the dead region.

2. If the z line is in P123 then:

   i) All the y and ϑ hits in P1 are searched for and buffered. A circle is fitted to each P1 point and to the W12/P0E-W45/P45 line. The circle is extrapolated to P2 and P3 and hits within the roadwidth are tagged (at least 1 out of 2 y and ϑ planes in P2 and P3 are required).

ii) All the y and ϑ hits in P2 are searched for and buffered. A circle is fitted to each P2 point and to the W12/P0E-W45/P45 line. The circle is extrapolated to P1 and P2 and hits within the roadwidth are tagged (at least 1 out of 2 y and ϑ planes in P1 and P2 are required).

iii) All the y and ϑ hits in P3 are searched for and buffered (except those used in i)), again a circle is fitted to the point and to the W12/P0E-W45/P45 line, and hits are looked for in P1 and P2 (at least 1 out of 2 y and ϑ planes in P1 and P3 are required).

This procedure reduces the ambiguous situations to:

1. A given z line has more than one y-ϑ line associated with it.
2. A given W12/P0E-W45/P45 line corresponds to more than one z line.

Such ambiguities are resolved by a quintic spline fit which uses the full FSM field map; the correct track is selected on the basis of the χ^2 of the fit. Quintic spline fits are extensively used in the Geometry program; we refer the reader to section 3.2.2 for a description.

Reconstruction upstream of the FSM

The spline fit results are extrapolated to PV12 and P0C and the usual tagging procedure is applied to find hits, the only difference being that the roadwidths now depend on the spline fit error and therefore vary from track to track. At least 5 (of which one y) out of 10 planes are required to have acceptable hits in PV12; 5 out of 8 are needed in P0C. A muon must have one line segment in either PV12 or P0C (or both).

The fraction of W12/P0E muon tracks which survive both the magnet and the PV12/P0C reconstruction is $\approx 83\%$ for T1 and $\approx 95\%$ for T2.

Reconstruction is then finally attempted in P0B by repeating the spline fit with the PV12, P0C points and extrapolating back to P0B. Track segments found in this way mainly belong to events occurred in the downstream target (rather than to beam tracks). No decision is made however at this level on where the interaction took place: the question will be settled later by the vertex processor in the Geometry program.

3.1.3 Hadron Reconstruction

Once the scattered muon has been found and reconstructed, the remaining hits in the chambers upstream of the calorimeter H2 and of the absorber are used to reconstruct hadron tracks. The procedure is very similar to the one outlined above with the following notable differences:

1. The most downstream hits for a track are presumed to be in W45 and not in W67. The track reconstruction therefore starts from W45 and then proceeds upstream as in the muon case.
2. There may be incomplete hadron tracks (i.e. not seen in all detectors).
3. Roadwidths are in general larger than in the muon case, especially in the PV12 and P0C chambers where the pattern recognition is made more complex by the existence of

tracks originating from secondary vertices, not necessarily inside the targets. Furthermore hadron tracks are in general slower than muon tracks: they therefore undergo more multiple scattering and are bent more by the FSM. Both these facts increase the difficulty of the pattern recognition and call for larger roadwidths.

3.2 Event Fitting: GEOMETRY

The events surviving the selection operated by Phoenix are written to an intermediate tape and serve as input to Geometry. Here track segments found by Phoenix are fitted together and assigned to vertices. From the overall event topology the kinematics of the event (scattered muon momentum, Q^2, ν etc.) is determined.

The output of Geometry consists of all the fit results worked out by the program plus the results of Phoenix and the raw data. Everything is written out to the so-called maxi-Data Summary Tapes (maxi-DST): maxi-DST's contain the maximum amount of information per event available during the production chain.

The overall fraction of events rejected by Geometry amounts to $\approx 40\%$ for T1 and $\approx 20\%$ for T2.

3.2.1 The Beam Processor

All beam tracks found by Phoenix are scanned. First the relative H3V-BH or H4′-BH (for T2) timing is checked. A track is kept if it is in time with H3V (H4′ for T2) within a 10 ns window. If several tracks in time with H3V or H4′ are found, they are considered pairwise. If two are too close in time (less than 2 ns), one of them is probably a knock-on electron. Since it is not possible to single out the correct track, both are flagged as bad. Analogously, if two tracks are too close in space in the target region (less than 4 mm), both are rejected, on the grounds that it would be impossible for the vertex processor to distinguish the correct one. About 5% of the events are lost due to the beam processor cuts.

All tracks left after these cuts are kept. The final choice will be made by the vertex processor (section 3.2.5) by selecting the beam muon which has the best combination of timing difference with H3V (H4′ for T2) and distance of approach to the scattered muon.

3.2.2 The Spline Fit

The quintic spline method [250] consists in using "spline" functions to relate the track parameters (momentum, slopes etc.) and the magnetic field. A spline function is a continuous function used to interpolate between two given points. A spline of degree N has its first $N-1$ derivatives everywhere continuous while the Nth derivative may be discontinuous on the points themselves.

Let us suppose that we measure the coordinates $y(x)$ and $z(x)$ of a set of points along the trajectory of a charged particle. The trajectory of the particle can then be written, in appropriate units, as

$$Py'' = \sqrt{1+y'^2+z'^2}[B_x z' + B_y y'z' - B_z(1+y'^2)]$$

$$Pz'' = \sqrt{1+y'^2+z'^2}[-B_x y' - B_y y'z' + B_y(1+z'^2)],$$

where

$$y' = \frac{dy}{dx},$$

$$y'' = \frac{d^2y}{dx^2},$$

P is the momentum and B is the magnetic field.

Let us assume further that B_x, B_y, B_z, y' and z' are known at each of the measured points. Two cubic spline functions $A(x)$ and $C(x)$ can then be found such that:

$$Py''(x) = A(x)$$

$$Pz''(x) = C(x).$$

Upon integration we obtain:

$$y(x) = a_1 + a_2x + \frac{Y(x)}{P}$$

$$z(x) = b_1 + b_2x + \frac{Z(x)}{P},$$

where

$$Y(x) = \int_{u=x_1}^{u=x} du \int_{v=x_1}^{v=u} dvA(v)$$

and $Z(x)$ is defined in a similar way. The functions $A(x)$ and $C(x)$ are continuous up to and including their second derivatives. The functions $Y(x)$ and $Z(x)$ are therefore expected to be continuous up to and including their fourth derivatives while the fifth is continuous only between the measured points. The trajectory is thus represented by quintic spline functions (hence the name).

The 5 parameters a_1, a_2, b_1, b_2 and P define the track and can be determined by least squares fitting to the n measured points (the system is evidently overconstrained as soon as n is greater than 3).

Having found the 5 track-defining parameters, we may recompute B, y', z' for all points by using the new trajectory $y(x)$, $z(x)$ and iterate the procedure until the results become stable. It is possible to evaluate the contribution of each hit to the global χ^2 and reject the hits which contribute most (typically sparks accepted by Phoenix because they are inside the roadwidths but which do not actually belong to the track). A significant improvement of the track χ^2 may be obtained by rejecting up to 4 planes.

At the end of the procedure each track is identified by its y and z intercepts at a given point (e.g. at a certain plane of a detector outside the magnetic field), its slopes y', z' and the reciprocal of its momentum $1/P$.

Before the method is applied, the hits found by Phoenix are first refitted on a detector by detector basis. The output of the fit is a point for P0B, P0A and P123; it is a line for all the other chambers. These points/lines serve as input to the quintic spline fit.

Note that up to here hadron and muon tracks are treated in the same way: the W67 information is not used in the spline.

3.2.3 The W45-W67 Link

All the W45/P45 tracks are in turn fitted to the W67 line(s), taking into account multiple scattering, energy loss and the residual absorber magnetic field. The combination with the best χ^2 (provided it is below a certain cut) is kept and henceforth defined as a muon.

3.2.4 The Trigger Processor

Once the muon has been identified through the link procedure, Geometry verifies that it really satisfies the trigger conditions.

It may occur in fact that a hardware trigger is faked by some combination of spurious hits which do not belong to a scattered muon track. On the other hand the particle that Geometry has defined as muon may not necessarily be the one which has caused the trigger. The T1 or T2 conditions are therefore applied software-wise and the event is rejected if they are not fulfilled. About 76% (95%) of the T1 (T2) events survive this cut.

The muon track is then extrapolated to the trigger hodoscope planes and record is kept of whether the expected hodoscope elements did have a hit or not. This is later used to cross-check the trigger hodoscopes efficiencies (determined with T11/T12 events, section 2.10.7).

3.2.5 The Vertex Processor

The last delicate task of Geometry is to find where the interaction occurred (the primary vertex). Secondary vertices (e.g. decays, reinteractions etc.) are also looked for.

The primary vertex is given to first approximation by the intersection of the beam track and the fastest muon with the same sign as the beam; this criterion minimizes the contribution of muons coming from hadron decays, which usually have large angles and small momentum and fake large Q^2 scatterings. Vertices found using the beam and the scattered muon only are called of type 1. Vertices of type 1 to which hadrons or other muons have been attached are classified as type 3. It should be noted that during the vertex fitting procedure the tracks themselves are not forced to go through a common point. Only about 90% of the events input to the vertex processor are assigned a vertex.

Secondary vertices are looked for by considering the tracks not used for the primary fit. Such tracks are associated pairwise and their point of closest approach is calculated. A list of tentative vertices is thus formed with the best combinations. Examples of possible secondary vertices are two oppositely charged hadrons with no incoming track (a V^0, vertex type 4), a beam muon plus one oppositely charged muon (type 5), a charged hadron decay (type 6).

3.3 Data Compactification: SNOMUX and SNOMIN

The maxi-DST's contain much more information than is generally needed for the physics analysis. Furthermore there are as many maxi-DST's as there are raw data tapes, 154 in our case: this is too large a number for a physics analysis.

Snomux reduces the number of tapes by about a factor 10 by dropping the raw-data and by packing the ZBOOK banks in a compact form for the events which survived the Phoenix and Geometry selection. The condensed output of Snomux is written onto the "mini-DST's".

Snomux also has a number of dedicated processors:

- The scaler processor deals with the decoding of the scaler information in the Start-Of-Burst (SOB) and End-Of-Burst (EOB) records. SOB and EOB records contain for instance the number of triggers (of all types) per spill, the raw ones and those which were actually treated by the data acquisition system (fewer, due to the acquisition system dead time), the number of vetoes per spill etc. Scaler contents integrated every 100 bursts are written to tape.

- The T10 processor selects the T10 scalers information from the SOB and EOB records and writes out two files. The first contains the number of T10's in each spill and is used to compute the T10 rate (no. of T10's per second). Bad T10 bursts are defined here as those in which the T10 rate is more that 5 standard deviations away from the average. The second file contains the full information about all T10 events and is used to tune the timing of the veto hodoscopes among themselves (using vetoed T10 tracks) and between the veto and the beam hodoscopes (using vetoed T10 tracks traversing both the veto and the beam hodoscopes): this timing is important because good T10 beam tracks are those which are found within a time window around the T10 time, provided that there is no in-time signal from the veto hodoscopes.

- The T3-4 processor analyzes all T3-4 events, processes the normalization scalers and verifies that the T3-4 electronics was functioning correctly (essentially by checking the prescale factors). It also writes a "rate-file" from which the weights (i.e. the probability that a scaler count represents a useful incoming muon) are computed.

- The H2 processor calculates, on a track by track basis, the amount of energy seen in the electromagnetic and hadron sections of the calorimeter and attempts pattern recognition in the electromagnetic sections.

Mini-DST's are in turn read by Snomin which operates a further compactification by selecting only what is relevant to a specific analysis. The data are written out in a highly compact form (micro-DST's) by packing several pieces of information into single 32 bit words.

Similarly to Snomux, Snomin also contains a series of dedicated processors. We list them here:

- The T10 processor computes the weight (i.e. the integrated reconstructable flux represented by the track) for each track, given the width of the T10 window and the T10 rate (see formula 2.6, page 112). Kinematic information plus weights for tracks passing the cuts are then written onto micro-DST. A separate file is also written containing the accepted T10 tracks. This is used as input to the Monte Carlo.

- The T3-4 processor finds the beam track which has actually caused the trigger 3 or 4 and attaches the proper weight to it. The track is written onto micro-DST if it passes the beam processor cuts.

- The beam processor applies the final cuts (y slope, z slope, radius at V2 etc.) on the beam phase space for physics (T1, T2) and normalization (T10, T3-4) events. We emphasize that the beam cuts must be the same in the two cases for the normalization to be correctly computed.

- The efficiency package determines (independently of the micro-DST writing procedure) the single wire and global efficiency for all planes of each chamber (section 3.6.3), which are then input to the Monte Carlo program.

3.4 The micro-DST

The micro-DST's are used for the final physics analysis and contain only selected information, in a higly compacted format, for specific types of data evaluation. ZBOOK banks are finally abandoned and the relevant data are stored in a few FORTRAN COMMONs.

Two types of micro-DST's were written for the P4A86 data: the so-called "muon" and "hadron" ones.

The muon micro-DST contain T1, T2, T10 and T3-4 events. For each physics event the full kinematics and topology (Q^2, ν, beam phase space, vertex coordinates and errors) is stored, together with a limited amount of detector specific information: beam and scattered muon track fit probabilities, y and z W45-W67 link χ^2's, BMS and H3V (H4$'$ for T2) times, scattered muon track parameters at various planes in the spectrometer. All the data necessary to compute the incoming muon flux via T10 or T3-4 is also present, as well as some alignment information (detector x-positions, target description etc). Two tapes (6250 bpi) were sufficient for the whole period.

The hadron micro-DST's contain, in addition to the event kinematics, detailed information concerning the main vertex and all secondary vertices. The parameters for all tracks (muons and hadrons) and the energy deposited in the electromagnetic and hadronic sections of H2 are also available. In order to limit the number of hadron micro's to be written, only T1 and T2 events were selected. A total of 4 (6250 bpi) tapes were necessary for P4A86.

3.5 The Monte Carlo

A full simulation of the experimental set-up is generally an essential tool to evaluate the acceptance of the apparatus, the efficiency of the software chain and hence the cross section for the process under investigation. This is for instance the case for the determination of absolute structure functions.

The situation is greatly simplified however in our case as we measure ratios of cross sections (rather than absolute cross sections) using the complementary targets arrangement. As we discussed in detail in section 2.6, acceptance corrections and beam flux automatically cancel from the ratio. It is therefore possible to reach physically interesting results without depending on Monte Carlo simulations, a rather exceptional (and fortunate) situation, seldom encountered in high energy physics experiments.

The use of the Monte Carlo program in the present analysis has indeed been very limited. We will therefore give here only a very brief overview of the program; a complete description can be found elsewhere [251]. A short account of the modified (and simplified) version used in the BCS analysis is presented in appendix A.

The simulation of the experiment can be summarized as follows. The parameters of the beam track are read off the T10 file mentioned previously: the beam phase space is in this way guaranteed to be exactly the same as the real one. The incident muon is then propagated to an interaction point randomly chosen in the target region. The Q^2 and ν of the event are selected at random and the scattered muon and virtual photon 4-vectors are determined accordingly. Each event is assigned a weight proportional to the value of the cross section $d^2\sigma/dQ^2d\nu$. Optionally hadrons may also be produced according to the Lund model [252]. All particles are then tracked through the apparatus and the chambers response is simulated by generating hits on the appropriate wires or scintillator elements; in doing this account is taken of the measured chamber efficiencies. The trigger conditions are also applied and the trigger hodoscope efficiencies are included.

The Monte Carlo simulated data are at this point processed through the full software chain, from Phoenix through Geometry all the way to the micro-DST's. The software efficiency is thus automatically taken into account.

3.6 The Data Production

Having described the programs used for the data production, we now briefly outline the sequence of steps that brings from the raw data tapes to the micro-DST's.

The precise location of all the detectors must first be determined: reference points on the frames of all chambers and hodoscopes are surveyed and their positions measured with respect to the FSM. From these data the position of all wires and scintillator strips is in principle known; it is however critical to check and improve these numbers by making sure, for instance, that straight tracks are really measured and recostructed as such. Special low intensity alignment runs are therefore taken with the FSM off. These runs are also used to determine the relative timing of the hodoscopes, to calibrate drift chambers etc. All the relevant information is then stored into the "alignment file".

Furthermore, before actual data production begins, Phoenix and Geometry need to be tuned: parameters like the road-widths used in the reconstruction, the minimum plane requirements etc. must be adapted to the specific conditions of the period being analyzed.

At this point raw data tapes are processed through Phoenix and Geometry, and the maxi-DST's are written. In the present case the production was done using two 370E emulators [253] at the M.P.I. in Heidelberg and two at CERN. Mini and micro-DST's were instead produced on the CERN IBM 3090/600 computer.

The CPU time to process one tape (about 50,000 triggers) through Phoenix and Geometry on an emulator was $\approx$ 12 hours. Several months of real time were necessary to process the whole P4A86 period (154 tapes) also because the entire production from Geometry to the mini-DST's had to be re-done following the discovery of an error in the Geometry vertex processor. The micro-DST's were finally ready before the end of 1987, more than a year after the data had been taken. This time may seem extremely long: it is unfortunately a feature of many high-energy physics experiments that the actual data evaluation starts only long after the data have been collected. In this respect NMC has been fortunate enough to inherit a large quantity of software from EMC: most of the programs were ready and extensively tested well before the data were taken.

Once the mini-DST's are available the full chamber efficiency evaluation may begin. Chamber efficiencies, as we said, are input to the Monte Carlo and can be determined by counting, on a plane by plane basis, the number of tracks for which an associated hit was found (success) and those for which the hit was not found (failure). Efficiencies are obtained as the ratio of successes to the total number of tracks (successes + failures). The Monte Carlo simulation can at this stage finally be run.

Details of the alignment, tuning and efficiency determination are given below. As the Monte Carlo was used only marginally in this analysis, the description of the efficiency evaluation will be short. More details can be found elsewhere [254].

3.6.1 Alignment and Calibration

Alignment runs are taken with the FSM field off, so that muons traverse the apparatus along straight trajectories, except for multiple scattering mainly in the calorimeter and the absorber.

Let us assume, for example, that all detector planes in the spectrometer are perfectly aligned except for one y plane. A straight track is extrapolated to that plane and the extrapolated y coordinate is compared with the position of the actual hit. The plane in question is aligned only when the residuals (fit−hit) distribution is centered on zero. This distribution has always a finite width, reflecting the detector resolution and the effects of multiple scattering. The procedure is evidently an iterative one, starting from the surveyed detector positions, typically accurate to about 1 mm in y and z, and ending with relative accuracies of order 300 μm. While excellent accuracies in the y and z alignment can be achieved using straight tracks, it is virtually impossible to determine the position of any detector along the beam starting from the data alone: x alignment has therefore to rely on the surveyors' results.

As we said, alignment runs are also important in order to calibrate the drift chambers. The goal of this calibration is to obtain the set of coefficients that allow to translate the timing recorded by the DTR's into the distance D to the sense wire of the point where the particle passed. Ideally $D = V_0 \times (T - T_0)$, where T is the DTR reading, T_0 is an offset that corrects for the delays introduced by cables and electronics and V_0 is the drift velocity. However, as the drift velocity is not constant throughout the drift-cell, non-linear terms must be included in the time versus distance relationship. The parameters V_0, T_0 and the coefficients of the non-linear terms are obtained by fitting an appropriate function to the D versus T data. It is evident that the drift chambers calibration and their alignment is an iterative procedure.

Finally, alignment tapes are used to time in all the scintillation counter hodoscopes which are read out by TDC's: the BMS, the BH's, H3V and H1$'$, H3$'$, H4$'$. As in the drift chamber case, this essentially amounts to finding, for each channel, the offset time T_0 which has to be subtracted from the TDC reading in order to obtain physically meaningful times. Alignment runs are ideal for this purpose: the beam intensity is very much reduced (typically $\sim 10^5$ muons per spill) with respect to the standard one ($\sim 10^7$ muons per spill) and generally only one scintillator strip per plane is hit, thus avoiding any ambiguity. Apart from one overall additive constant, the T_0's are then the quantities needed to have all channels hit by the same track give the same time (after the time of flight subtraction).

The first of the alignment runs to be used is the one which contains events defined by trigger 7 (for a description of the hardware definition of T7 and of the other alignment triggers, see section 2.10.7). These are near-halo events, mainly almost parallel tracks which satisfy the condition of not passing through the central hole in the big veto wall V3: they are used for the alignment and calibration of the drift chambers W12, W45 and the B module of W67. T7 is also used for the alignment of PV12, P123 and P45. The external modules of W67 (A and C) are instead aligned and calibrated with the far halo trigger T8.

The beam trigger, T5, is composed of tracks going through the beam hodoscopes and the P0 chambers. T5 tracks pass through the dead regions of all other proportional chambers, with the exception of PV1 (which has no dead region) and of the P45 chambers (which are made sensitive in the center during these runs). T5 is used therefore to align and time in all the beam detectors (BMS, BH, P0's) with respect to each other.

At this point the spectrometer is split into two distinct sections: the large proportional and drift chambers, aligned with T7 and T8, and the beam detectors aligned with T5. T6 enables the relative alignment of the beam detectors and the big chambers: to this end tilted beam tracks are used which go through the beam hodoscopes, the P0's and W12, P45, W45. Tracks at such large angles are obtained by appropriately changing the currents in the last few bending magnets of the beam line. Three T6 alignment runs are made with the beam tilted upwards, downwards and horizontally to the right.

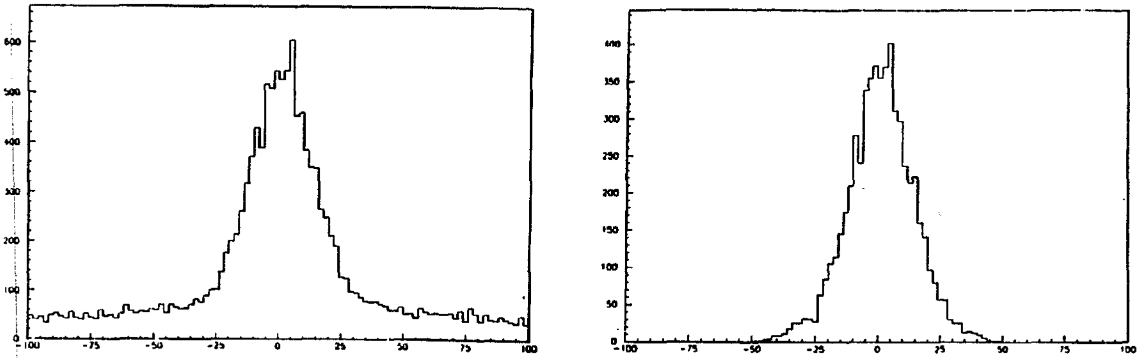

Figure 3.1: Time differences for key-plane hits in the BH: all hits (left) and hits belonging to good tracks only (right). Units are tenths of ns

3.6.2 Tuning

Both Phoenix and Geometry contain a large number of tunable quantities which depend among other factors on the specific running conditions, like beam energy, and on the general status of the apparatus, e.g. the number of dead planes. All these parameters must be fixed before production is begun. A few runs are therefore selected throughout the period and such parameters are optimized.

In Phoenix all roadwidths are tunable parameters. Other tunable quantities are the minimum plane requirements, the time window in which BH or BMS hits are considered, the minimum χ^2 probability for BMS tracks, the maximum allowed time separation between hits on different BH planes.

As an example fig. 3.1 shows the time differences of all hits belonging to pairs of certain planes in the BH (the "key-planes", cf. section B.6 for a detailed discussion). The distribution for hits belonging to reconstructed tracks is presented in the same figure. Pairs of hits are accepted only if they occur within a given time window. Based on plots like the ones shown, the window width was chosen to be from -5 to 5 ns.

A discussion of the tuning procedure for the pattern recognition in the forward spectrometer chambers can be found in [255]. The tuning of the BH recostruction is presented in appendix B.

Examples of tunable parameters in Geometry are:

- the minimum track time and space separations used in the beam processor and described in section 3.2.1;
- all the individual plane r.m.s. errors used in the fits within a given detector (these are the fits preliminary to the spline);
- the lowest acceptable value of the χ^2 probability for the W45-W67 link.

An important step in the Geometry tuning procedure is the checking and refining of the alignment of chambers and hodoscopes. Residuals (fit$-$hit) are plotted at all detectors; if their distribution is not centered on zero the alignment may need some corrections.

3.6.3 Efficiencies

The first phase of the efficiency determination is to find chamber regions where the efficiency is very small or zero *tout-court*. These may occur for instance at the chamber edges or close to the support wires or anywhere in correspondence of a wire or of a group of wires whose electronics is not functioning properly; in the latter case the inefficiency may be time-dependent. Regions of zero (or close to zero) efficiency are spotted by visual inspection of wire maps, merely using the decoding package. This information is stored in a preliminary efficiency file used as input to Phoenix: hits in these regions, if at all there, are killed and no longer used in the reconstruction, as often spurious and due to electronics cross-talk, amplifier oscillations etc.

The efficiencies of all the other (non-dead) wires are determined at the mini-DST level from a sample of fully reconstructed hadron and muon tracks. A conceptual difficulty in the efficiency evaluation is that the total number of tracks is not known, only the measured tracks being available, of course. Hence, for a given plane, tracks are used which would satisfy the minimum plane requirement even if the plane in question had not recorded a hit. The efficiency is then defined as the ratio:

$$\epsilon = \frac{GOOD}{GOOD + BAD},$$

where GOOD are the tracks that have a hit at the plane being studied and BAD are those that do not.

In general the efficiency of a particular detector plane (apart from dead wires, edges etc.) is taken to be isotropic around its central dead area; the radial efficiency for each plane is then fitted to an analytic function. Regions close to the sense and potential wires of drift chambers often show a drop in efficiency; such structure is therefore also parametrized and folded in with the radial efficiency.

The efficiencies of the trigger hodoscopes are evaluated with a procedure similar to the one outlined for the wire chambers. T11 (or T12 for T2) tapes are used in this case [256].

Chapter 4

Analysis and Results

"That seems to be done right — " [Humpty Dumpty] began.
"You're holding it upside down !" Alice interrupted. [257]

Introduction

Once the data are on micro-DST, the final analysis leading to the extraction of the physics results may commence.

Events are first assigned to targets by means of vertex cuts. Events belonging to regions where the apparatus response is poor or where there is a large contamination of background are then rejected. The measured yields are corrected to take into account the contribution of electromagnetic processes of order higher than that of the Born term (the one given in fig. 1.1, page 2). Finally cross section ratios are computed using formula 2.5, page 103.

While the extraction itself of the results from the micro-DST is a straightforward and fast operation, the definition of the best combination of cuts to be applied may require several iterations. Even longer and more complicated is the estimation of the systematic errors. This proceeds through the investigation of a variety of possible sources, including radiative corrections, vertex smearing, uncertainties in the target densities and lenghts. It also requires a critical examination of the results themselves, in order to evaluate their stability with respect to the cuts, their correlation with kinematic and apparatus variables and their dependence on the set of detectors used in the event reconstruction.

4.1 Data Selection

Particular care is exercised both at the trigger level and later at the data production stage in order to retain only genuine deep inelastic events in the final data sample. However micro-DST's still contain data that must be rejected before physics results can be safely extracted. The data selection procedure includes the following steps:

- the elimination of possibly "bad" runs, in which some of the hardware is suspected to have malfunctioned;
- the rejection of events in which the interaction has occurred outside the helium or deuterium targets, e.g. in the beam hodoscopes, in the chambers P0B, P0C etc.;

- the rejection of events belonging to kinematic regions in which the apparatus is known to have poor resolution or rapidly varying acceptance (typically near the edges of the accessible kinematic range);
- the rejection of events belonging to kinematic regions in which the contamination of background events is large (e.g. coherent or quasi-elastic radiative events faking a deep inelastic scattering).

4.1.1 Bad Run Rejection

In order to single out bad runs, the following quantities were examined as a function of the run number:

1. the ratio of upstream to downstream target yields (for the two target positions independently);
2. the yield in each target position (helium + deuterium), normalized to the incoming flux;
3. the beam muon fit probability (for each of the four targets);
4. the scattered muon fit probability (for each of the four targets);
5. the vertex fit probability (for each of the four targets);
6. the W45 y and z-link probabilities (for each of the four targets).

The ratio of upstream to downstream event rates (1.) and the number of triggers for a given target position, normalized to the incoming muon flux (2.) were used as monitors of the trigger system. The fit probabilities (3. to 6.) were instead used to detect malfunctionings of the tracking system. The runs in which one of the quantities above significantly departed from the average were rejected.

As an example fig. 4.1 shows the ratio of the upstream to downstream yields for target pos. #1[1] as a function of the run number. For the period under discussion run numbers range from 339 to 493.

The following runs were rejected and not used for the extraction of the results:

- trigger 1
  - 363, 400, 409, 412, 436 (trigger problems);
  - 387, 398, 442, 459, 493 (various combinations of tracking system problems);
  - 339 through 343 (anomalously low scattered muon fit probability due to problems in P0C);
  - 476 through 480 (anomalously low beam muon fit probability due to problems in the beam hodoscopes);
- trigger 2
  - 400, 409, 412, 413, 423, 439 (trigger problems);

[1]Target position # 1 has deuterium upstream and helium downstream. Target position # 2 has helium upstream and deuterium downstream.

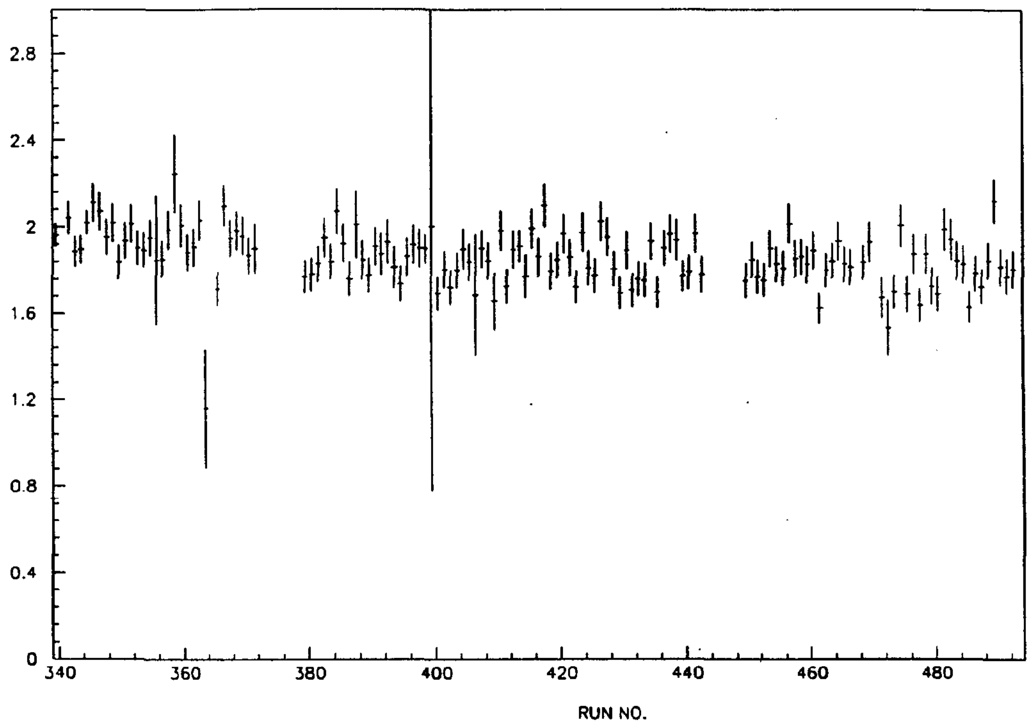

Figure 4.1: The ratio of upstream to downstream T1 events for target position #1

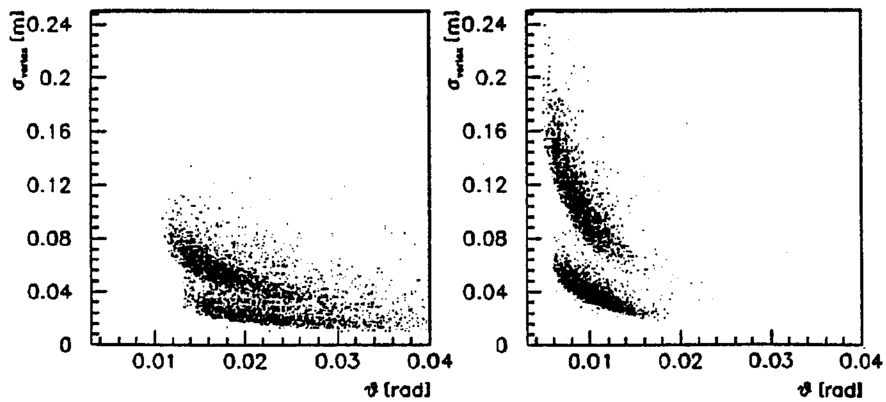

Figure 4.2: The error on x_{vertex} as a function of ϑ for T1 (left) and T2 (right) events. The upper and lower bands in each plot correspond to the upstream and downsream targets, respectively

- 387, 391, 398, 399, 409, 442, 459, 493 (various combinations of tracking system problems);
- 476 through 480 (anomalously low beam muon fit probability due to problems in the beam hodoscopes).

Furthermore, all runs before no. 390 were discarded from the T2 analysis, so as to exclude the trigger 2 setting-up phase.

4.1.2 The Vertex Cuts

Vertex cuts are applied in order to assign events to specific targets. The problem arises because of the finite resolution of the spectrometer; the vertex coordinates found by Geometry are affected by errors and it may happen that events which occurred, say, in the upstream deuterium target are in fact assigned a vertex in the beam hodoscopes, in the P0B chamber or inside the downstream helium vessel. Figure 4.2 shows the errors on the fitted value of x_{vertex} as a function of the scattering angle for T1 and T2 events.

Vertex cuts must at the same time meet contrasting requirements. On the one hand, the least amount of good data should be rejected by the cuts; on the other hand, the contamination of events coming from foreign target materials should be kept to a minimum.

Figures 4.3 and 4.4 show the distributions of the reconstructed vertices along the beam direction for T1 and T2 events, for both target positions. The shape of these distributions is a consequence of the acceptance of the spectrometer, folded with the different densities of the liquid He and D targets (the density of He is lower than that of D, cf. section 2.9.2, page 103). The figures show that acceptance tends to be lower for the downstream targets, for which muons scattered at small angles go into the central holes of the trigger hodoscopes and are therefore not detected. Acceptance clearly varies with x_{vertex} in a different way for T1 and T2. The continuous lines are the results of fits to a superposition of several box functions plus the convolution of gaussian and Breit-Wigner type functions [258]. A gaussian or a Breit-Wigner alone would reproduce the experimental distributions poorly close to the minima.

Events were assigned to the upstream targets if

- T1:

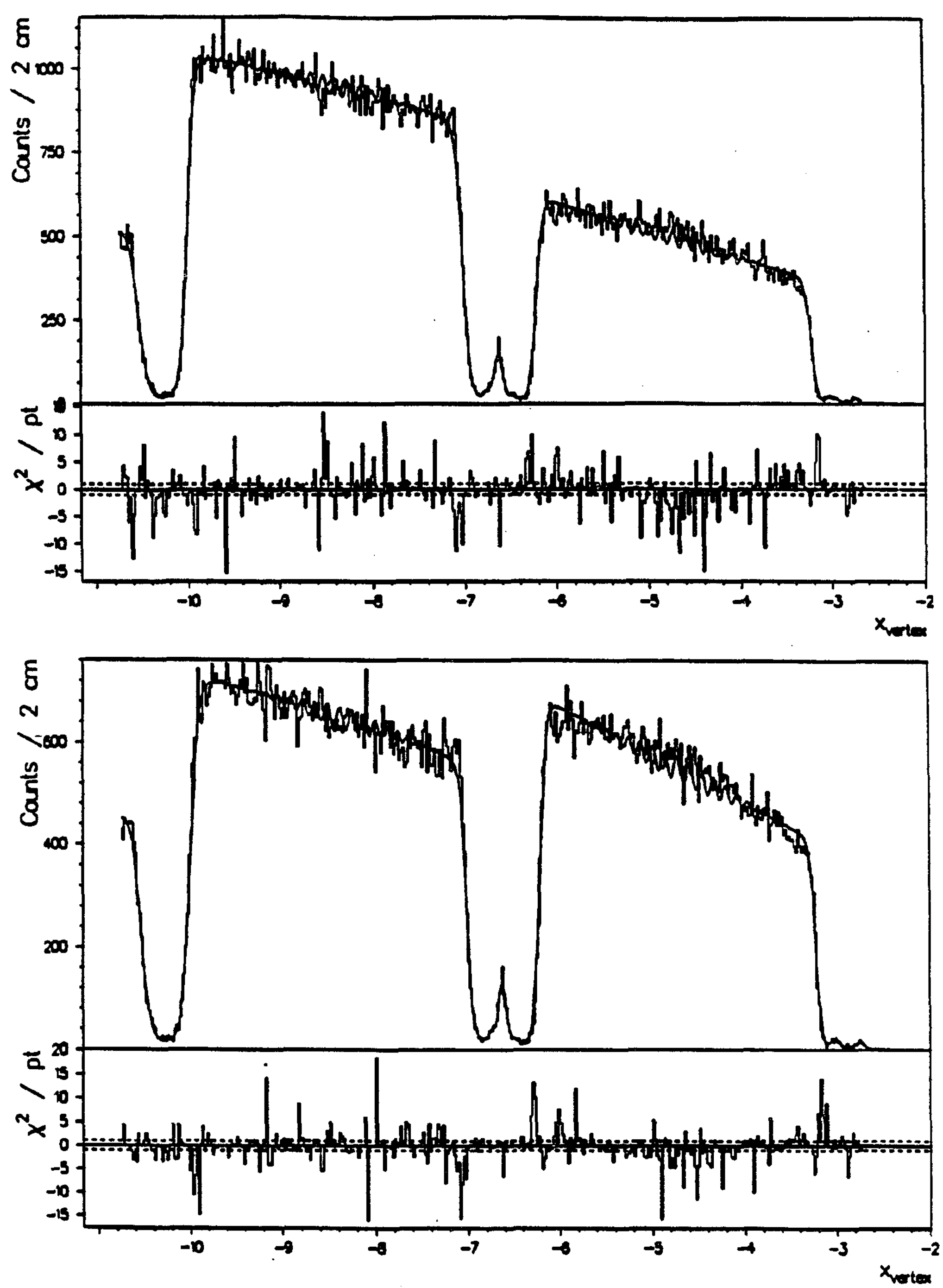

Figure 4.3: Distribution of x_{vertex} for T1 events, target pos. #1 (top) and target pos. #2 (bottom). The continuous line is the fit described in the text. The lower part of each plot shows the χ^2 of the fit as a function of x_{vertex}

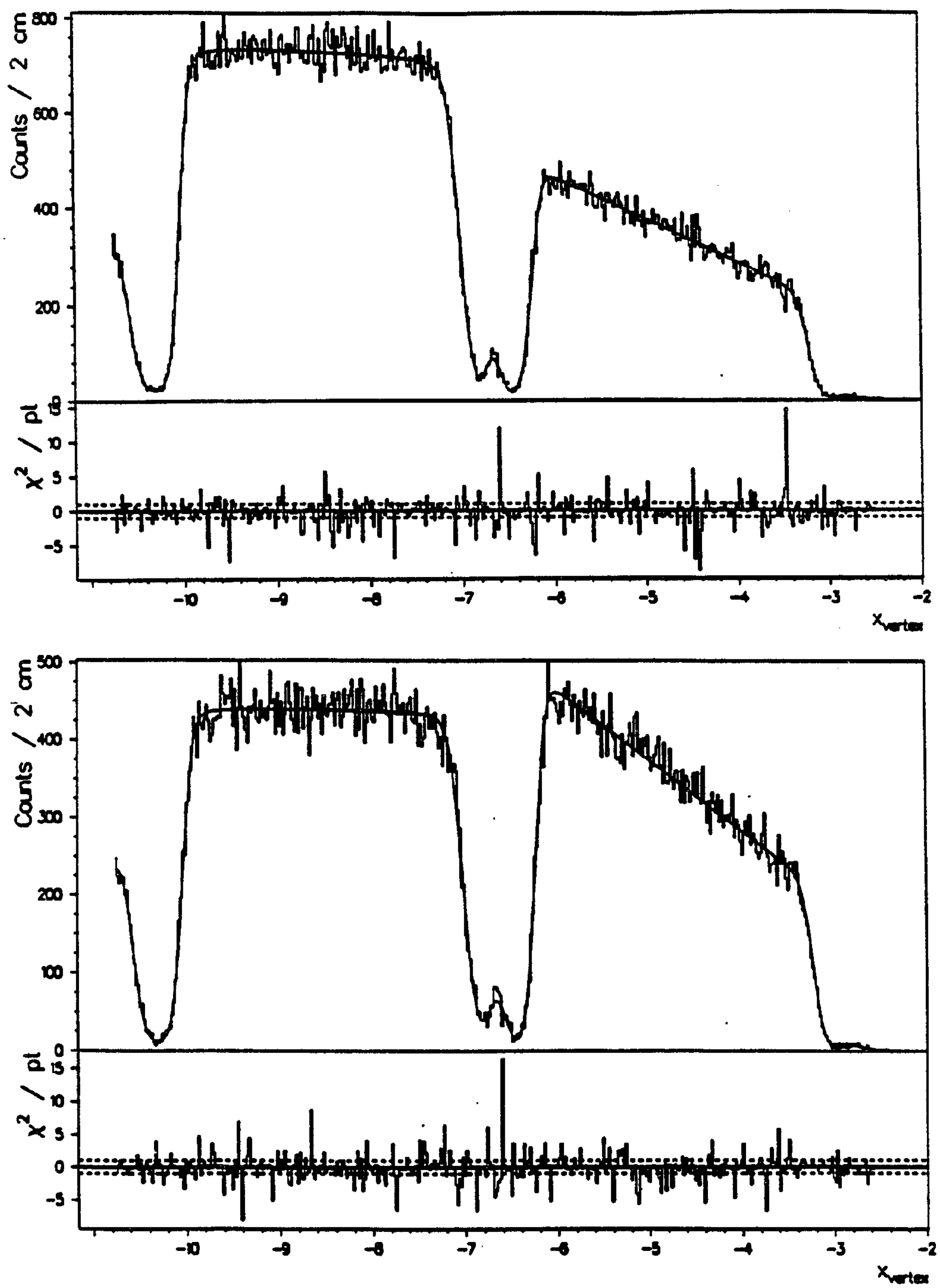

Figure 4.4: Distribution of x_{vertex} for T2 events, target pos. #1 (top) and target pos. #2 (bottom). The continuous line is the fit described in the text. The lower part of each plot shows the χ^2 of the fit as a function of x_{vertex}

$$-10.29m < x_{vertex} < -6.83m$$

- T2:

$$-10.31m < x_{vertex} < -6.81m.$$

They were assigned to the downstream targets if

- T1:

$$-6.40m < x_{vertex} < -3.09m$$

- T2:

$$-6.45m < x_{vertex} < -2.97m.$$

These values correspond to the minima of the fits to the experimental vertex distributions closest to the nominal target edges. The maximum number of events is thus kept, while keeping vertex smearing corrections small (see section 4.4.2).

4.1.3 Kinematic Cuts

Figures 4.5(a)-(b) show the (x, y) distribution of the T1 and T2 events, respectively, after the application of the vertex cuts defined in the previous section (x and y are the scaling variables defined on page 2). The kinematic cuts summarized in table 4.1 were then applied to these data. Table 4.2 shows their effect on the event counts. We briefly comment on these cuts.

- In the small ν region the virtual photon kinematics is affected by large errors: ν is in fact obtained in this case as the difference of two quantities, the incoming and the outgoing muon energies, both large and of similar magnitude. Low ν events were therefore discarded.

- Events with small scattered muon momentum were also rejected, as they are contaminated by muons from π and K decays.

- A minimum scattering angle ϑ was demanded in order to avoid events in which the scattered muon passes very close to the trigger hodoscopes edges; the apparatus acceptance is very small and changes rapidly in this region. Furthermore the spectrometer resolution is poorest at small scattering angles: vertex coordinates are affected by large errors and therefore the assignment of events to specific targets becomes difficult. Different ϑ cuts were applied to the downstream and upstream targets, as a consequence of the different angles under which the spectrometer is seen by the two targets.

- The region where the radiative corrections for the helium nucleus (which requires a larger correction than deuterium) exceeded a given threshold was also excluded. In practice this cut rejected events at large y and low x.

Figures 4.5(c) and (d) show the event distributions in the (x, y) plane after applying the cuts. The total number of events left after cuts is 0.65×10^6. The counts are roughly equally divided between T1 and T2.

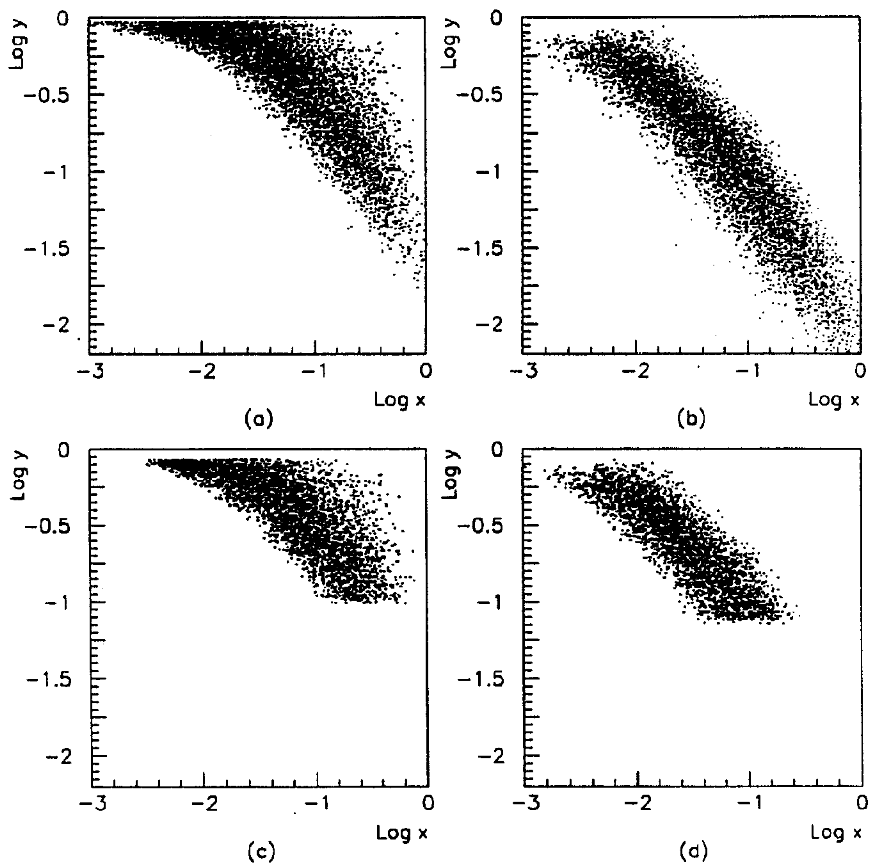

Figure 4.5: Effects of the cuts. Event distributions for T1 (a) and T2 (b) before the cuts. Event distributions for T1 (c) and T2 (d) after the cuts

	T1	T2
ν_{min}/GeV	20	15
E'_{min}/GeV	30	30
$\vartheta^{(u)}_{min}$/mrad	11	5
$\vartheta^{(d)}_{min}$/mrad	13	6
η^{He}_{min}	0.6	0.6

Table 4.1: Kinematic cuts on the energy transfer ν, the scattered muon energy E', the scattering angle ϑ for upstream (u) and downstream (d) targets, and on the weight factor η^{He} of the radiative corrections for helium (see below formula 4.1 for the definition of η^{He})

	T1	T2	total
before cuts	517,776	464,438	982,214
vertex cuts	497,737	449,712	947,449
ν_{min}	455,763	271,087	726,850
E'_{min}	388,041	271,041	659,082
ϑ_{min}	380,734	267,146	647,880
η^{He}_{min}	377,943	267,143	645,086

Table 4.2: Effects of the cuts on the event counts

4.2 Radiative Corrections

The observed cross section includes contributions from an infinite series of electro-weak processes of order higher than that of the Born term represented by the one-photon exchange graph of fig. 1.1 and fig. 4.6(a). The diagrams of some of these processes are shown in figures 4.6(b)-(l). Corrections must be applied in order to extract the one-photon exchange contribution from the observed cross section: they are known as "radiative" corrections.

The graphs of fig. 4.6 can be grouped into few main classes:

- radiation of real photons from the muon lines (b,c);
- lepton vertex correction (d) and vacuum polarization (e,f);
- two photon exchange (g);
- radiation of photons from the hadron vertex (h,i);
- pair production (j,k);
- Z^0 exchange (l).

In the graphs of figures 4.6(b,c) and (k) a photon is radiated from the incoming or outgoing muon line. The true four-momentum of the exchanged virtual photon is thus different from the one that can be computed from the experimentally measured four-momenta of the beam and scattered muon: the apparent kinematics of the event is therefore wrong. The measured ν is for example always larger than the true one.

In these graphs the virtual photon may interact directly with a quark (deep inelastic scattering); it may also scatter elastically off a nucleon inside the nucleus (quasi-elastic scattering) or off the whole nucleus (coherent scattering). In the latter cases the nucleon (the nucleus) on which the interaction has taken place emerges intact from the scattering. As a consequence of the smearing of the kinematic variables due to the radiation of a real photon, also these coherent and quasi-elastic events (in addition to the truly deep inelastic ones) contribute to the measured experimental yield. In other words events which appear as deep inelastic may originate from:

1. truly deep inelastic scattering of the virtual photon off a quark, with no radiated photons (the one photon exchange diagram, fig. 4.6(a));
2. truly deep inelastic scattering of the virtual photon off a quark, in which however the measured kinematics has been distorted by the radiation of the photon ("inelastic tail");

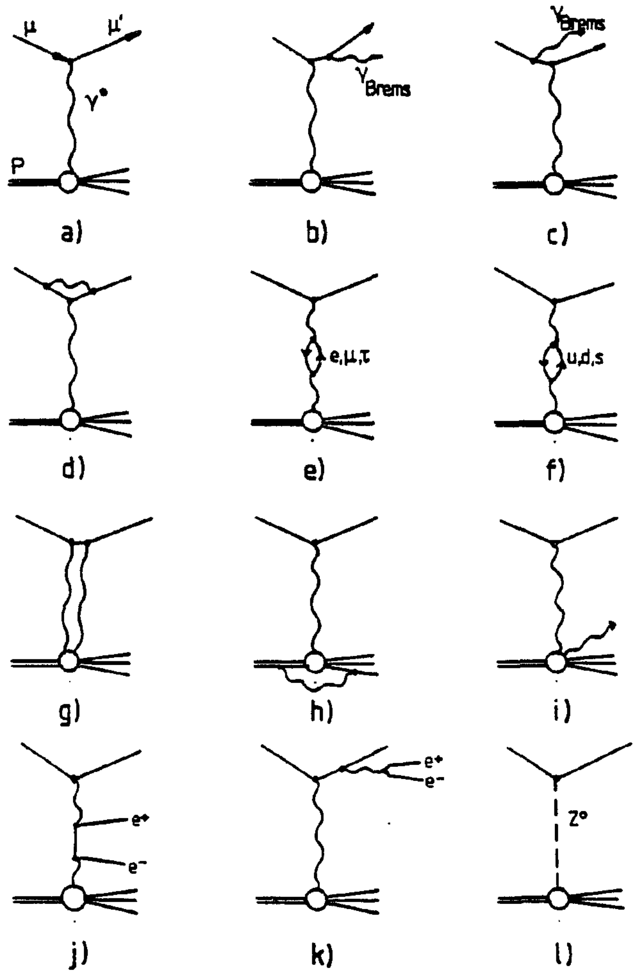

Figure 4.6: One photon exchange (a) and higher order contributions to the observed yields

3. elastic scattering of the virtual photon off a nucleon ("quasi-elastic tail") or
4. off the nucleus ("coherent tail").

In contrast to the photon radiation, which modifies the kinematics, the vertex graphs of fig. 4.6(d,h) and the vacuum polarization ones of fig. 4.6(e,f) mainly contribute by changing the cross section, via interference with graph 4.6(a).

As far as the radiation from the hadron vertex is concerned (fig. 4.6(i)), the basic amplitudes for radiation from a quark or from a lepton are the same. The hadronic final state is however simply integrated over and the kinematics of the event – as determined from the incoming and outgoing muon four-momenta – is also not modified. The resulting corrections are small [259].

Also small, at the Q^2 of interest here, are the electro-weak interference effects (due e.g. to the interference of graphs 4.6(a) and 4.6(l)), since $Q^2 \ll M_{Z^0}^2$.

The problem of determining radiative corrections is trivial at the theoretical level, all the graphs involved being QED or at most electro-weak ones. Uncertainties are however present in practice because of the parameters needed as inputs to the calculation. As we discuss below, detailed knowledge of the nuclear and nucleon form factors is in fact needed, as well as of the nucleon and nuclear structure functions over as wide a kinematic range as possible.

4.2.1 The Radiative Corrections Program: FERRAD

The NMC radiative corrections program, Ferrad, is based on the formalism originally developed by Tsai [260] for the coherent and quasi-elastic radiative tails and by Mo and Tsai for the inelastic tail [261]. It includes also the vertex correction and the vacuum polarization contribution for electron and muon loops.

For a given (x, y) point the program produces a multiplicative correction factor (weight) η. The observed cross section must be multiplied by η in order to obtain the one-photon exchange cross section.

The procedure is to first run the program for a sufficiently fine grid of points in the (x, y) plane and produce a table of radiative corrections. For each of the events passing the vertex and kinematics cuts described in the previous sections, η is then computed by interpolating the radiative correction table.

The expression for η has the following form:

$$\eta = \frac{\sigma_{1\gamma}}{\sigma_{measured}} = \frac{\sigma_{1\gamma}}{F_r(1+\delta_{vac}+\delta_{vertex}+\delta_{small})\sigma_{1\gamma}+(T_{inel}+T_{quasi-el}+T_{coherent})}. \tag{4.1}$$

- $\sigma_{1\gamma}$ is the cross section for the one-photon exchange process (fig. 4.6(a)).
- δ_{vac} is the vacuum polarization contribution, for the electron and muon loops of fig. 4.6(e). Tau and quark loops are neglected. The size of δ_{vac} is small compared to unity.
- δ_{vertex} is the vertex contribution (fig. 4.6(d)). The size of δ_{vertex} is also small compared to unity.
- δ_{small} is also very small. Its definition is somewhat involved and we refer the reader to the paper by Tsai [260] (equations 2.12 and 2.14) for a discussion of its meaning.
- F_r is related to the renormalization of the divergencies in QED. Its value is close to unity and depends on the cut-off parameter Δ discussed below, as well as on the event kinematics.

- T_{inel}, $T_{quasi-el}$ and $T_{coherent}$ are the inelastic, quasi-elastic and coherent tail contributions, respectively.

Formula 4.1 shows clearly two distinct types of contributions to $\sigma_{measured}$. The term

$$F_r(1 + \delta_{vac} + \delta_{vertex} + \delta_{small})\sigma_{1\gamma}$$

would be the whole story if the event kinematics were not modified by the graphs (b) and (c). The effect of these graphs is to bring in the contributions of the tails:

$$T_{inel} + T_{quasi-el} + T_{coherent}.$$

Figures 4.7-4.10 show the size of the various terms, averaged over the accepted events: $T_{coherent}/\sigma_{1\gamma}$ (dashed lines), $T_{quasi-el}/\sigma_{1\gamma}$ (dotted lines), $T_{inel}/\sigma_{1\gamma}$ (dash-dotted lines above zero) and $[F_r(1+\delta_{vac}+\delta_{vertex}+\delta_{small})-1]$ (dash-dotted lines below zero). The full correction is also plotted (continuous line) as $1/\eta - 1$; a value of $1/\eta - 1 = 0.5$, for example, means that the measured cross section must be *reduced* by a factor 1.5 in order to obtain the one photon exchange cross section.

From the figures it is clear that the helium data require more sizable corrections than the deuterium ones. The difference is a consequence of the fact that the coherent, the quasi-elastic and the inelastic tails are different for the two nuclei. The term $[F_r(1+\delta_{vac}+\delta_{vertex}+\delta_{small})]$ is instead largely independent of the target.

As a rule the corrections are large at large y and small x; here the weight η is smaller than unity, which means that the number of one photon exchange DIS events belonging to this region is smaller than the one actually measured.

The size of the correction to the ratio in a bin is approximately given by the ratio of the helium and deuterium corrections, η_{He}/η_D, and it is then much closer to unity than the individual corrections. It is shown as a function of x in fig. 4.11. As we explained, the main contributions to the correction for the ratio come from the radiative tails, which are different for the two target materials.

We shall now describe at some length the calculation of the tails. The subject of radiative corrections will be taken up also later, during the discussion of the systematic studies, in section 4.5.3, and in appendix C. More details will be given there about the input to the program and comparisons will be made between the NMC method and other available procedures.

The Inelastic Tail

In this case the virtual photon scatters off a quark in the target, but the incoming or the outgoing muon radiate a real photon. The inelastic tail contribution is computed by numerically integrating the cross section for photon radiation from the incoming or outgoing muon line over all the allowed hadronic final state masses W and over all photon emission angles. Consider for example fig. 4.12 and suppose that the inelastic tail contribution must be computed for an event of given Q^2 and ν (the point (Q^2, ν) in the figure). In this case the integration must be carried out over all possible points on the plane from which the given Q^2 and ν can be reached upon emission of a photon (regions A and D in fig. 4.12).

In practice the integration is carried out separately for photon energies E_γ smaller than a cut-off Δ and photon energies larger than Δ. The reason for this is that the integrand diverges when the photon energy tends to zero: the energy spectrum of the emitted photons has a $1/E_\gamma$

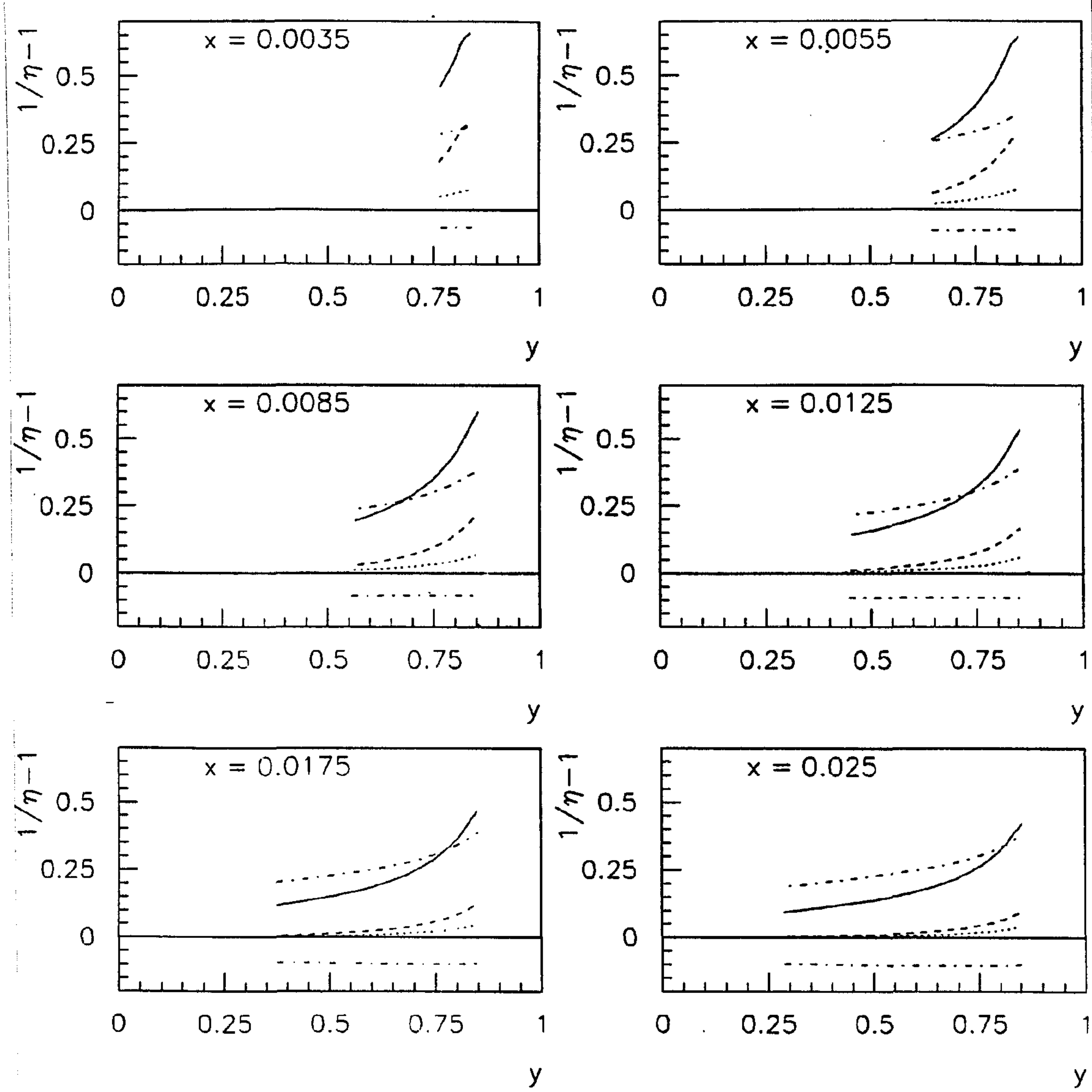

Figure 4.7: Size of the average radiative corrections for T1 helium events as a function of y for different x bins: full correction (continuous line), coherent tail (dashed line), quasi-elastic tail (dotted line), inelastic tail (dash-dotted line above zero). The dash-dotted line below zero is described in the text

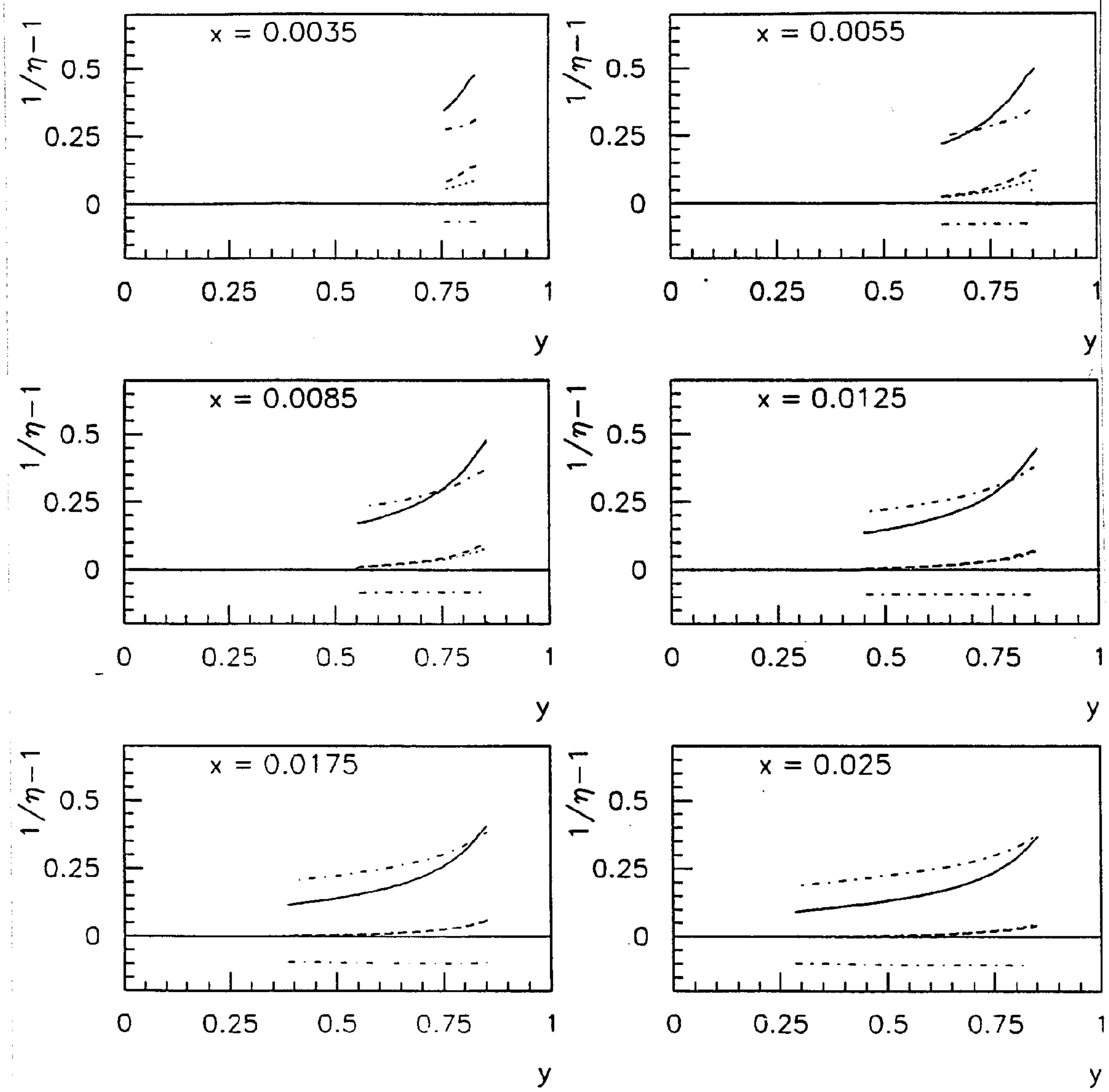

Figure 4.8: Size of the average radiative corrections for T1 deuterium events as a function of y for different x bins: full correction (continuous line), coherent tail (dashed line), quasi-elastic tail (dotted line), inelastic tail (dot dashed line above zero). The dot dashed line below zero is described in the text

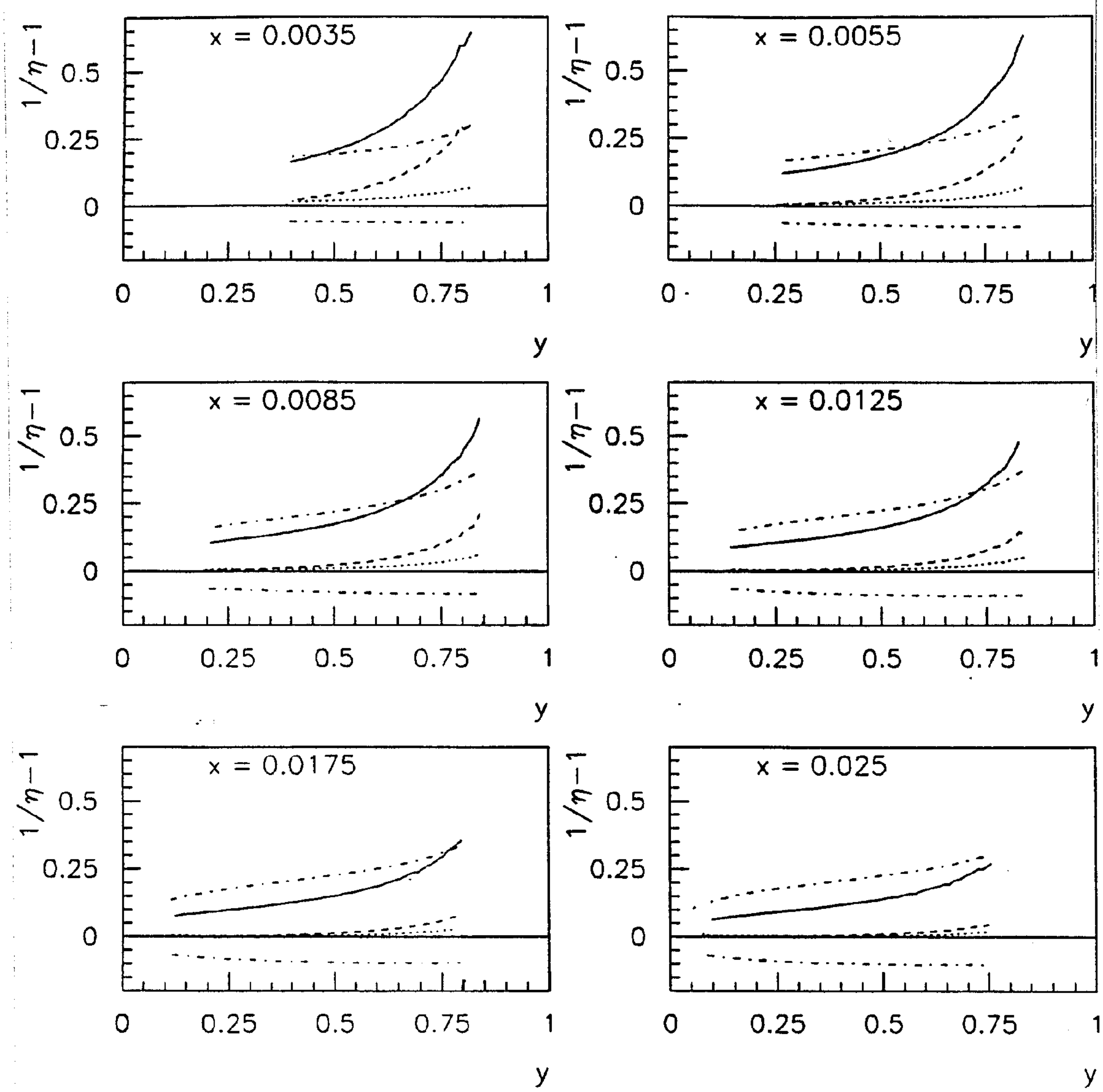

Figure 4.9: Size of the average radiative corrections for T2 helium events as a function of y for different x bins: full correction (continuous line), coherent tail (dashed line), quasi-elastic tail (dotted line), inelastic tail (dot dashed line above zero). The dot dashed line below zero is described in the text

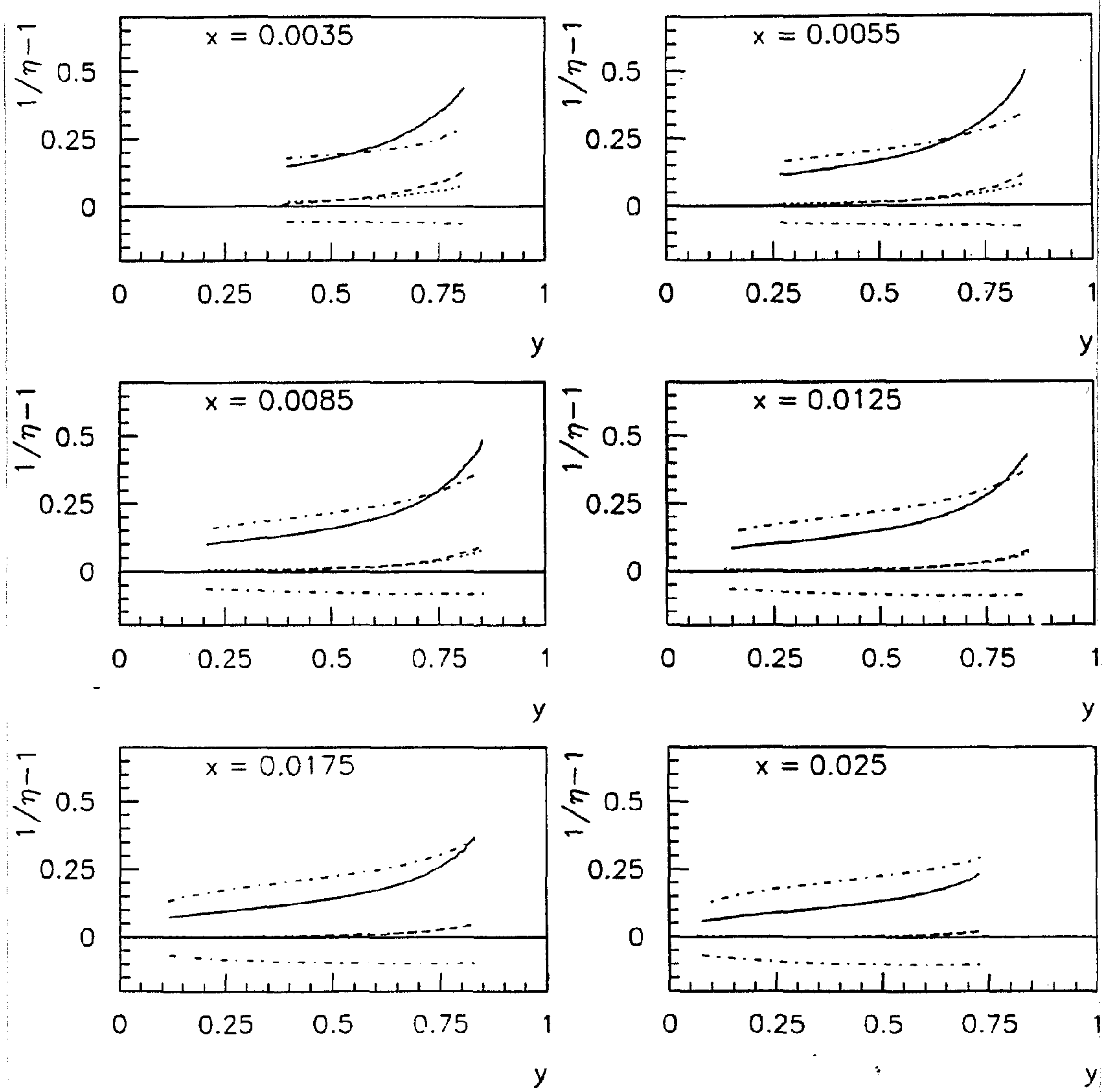

Figure 4.10: Size of the average radiative corrections for T2 deuterium events as a function of y for different x bins: full correction (continuous line), coherent tail (dashed line), quasi-elastic tail (dotted line), inelastic tail (dot dashed line above zero). The dot dashed line below zero is described in the text

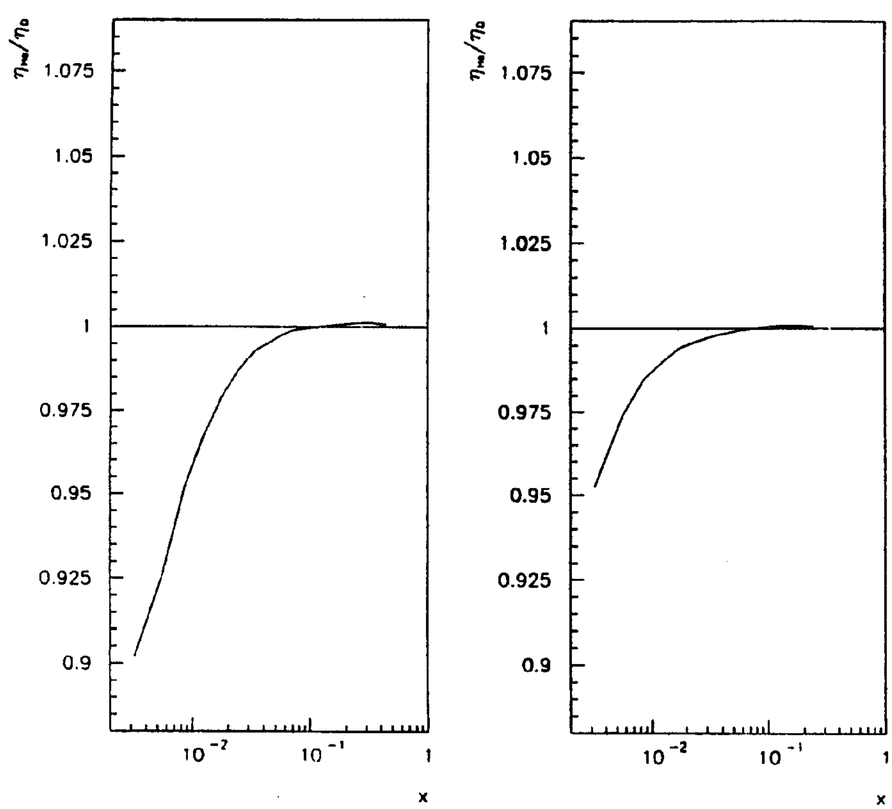

Figure 4.11: Size of the average radiative correction to the cross section ratio as a function of x, for T1 (left) and T2 (right) events

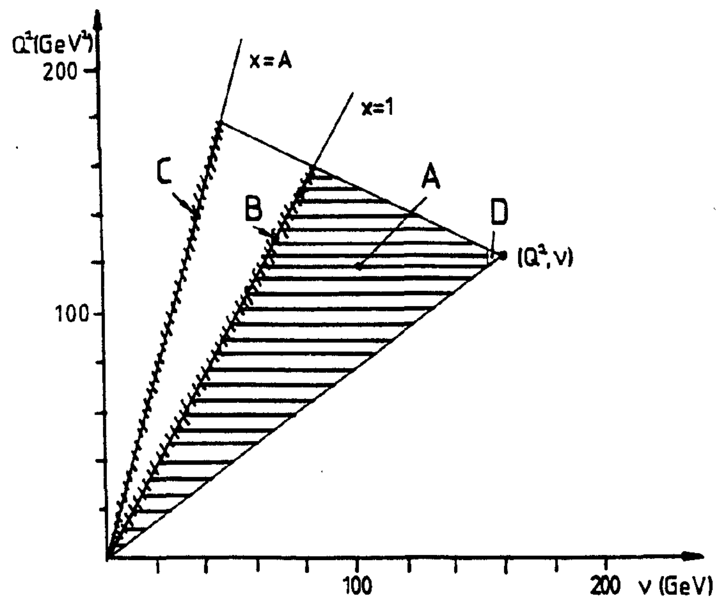

Figure 4.12: Integration region for the evaluation of the inelastic tail

behavior[2]. Therefore, while the high energy part of the integration can be carried out exactly (over the shaded area A in fig. 4.12), the integration from zero to Δ (over the non-shaded area D in fig. 4.12) is evaluated only approximately and contributes the factor F_r mentioned above. Radiative corrections should not depend on the value of Δ. This requires some tuning; in our case $\Delta \simeq 0.1\%$ of the incident muon energy.

In the calculation of the inelastic tail contribution, higher order diagrams where photon radiation occurs together with vacuum polarization or with vertex loops are also included.

In order to carry out the integration (and in order to compute $\sigma_{1\gamma}$) the knowledge of both $R = \sigma_L/\sigma_T$ and F_2 is required. In the present analysis a phenomenological fit to SLAC and CERN results for R [46, 47] was adopted, while a fit to the results of deep inelastic scattering experiments and to data in the resonance region was used for F_2^D (see 4.5.3 and appendix C for a discussion). The helium structure function F_2^{He} was taken as

$$F_2^{He} = F_2^D \times \frac{F_2^{He}}{F_2^D},$$

where F_2^{He}/F_2^D is a fit to the measured cross section ratio and to the SLAC E139 results [35] for $x > 0.3$. An iterative procedure was therefore necessary.

We note that the integration over the photon emission angles is carried out exactly, and no use is made of the "peaking" approximations common in electron scattering experiments. Photon emission angles are peaked around the incident or the scattered muon directions giving rise to the "s-peak" and "t-peak", respectively; a third peak around the direction of the virtual

[2] As it is well known, the divergence appears because we have only considered the diagrams of fig. 4.6(b,c); the interference of diagrams of fig. 4.6(a) and (d) leads in fact to another divergence which cancels the bremsstrahlung one.

photon becomes important at high y. The order of magnitude of the s and t-peak widths is given by $\sqrt{m/E}$ and $\sqrt{m/E'}$ where m is the lepton mass, E is the beam energy and E' is the scattered muon energy. Peaking approximations [260, 261] consist in computing the integrals over the photon directions assuming emission at the s and t-peaks. The use of such approximations is forbidden in the muon case, the peak widths being too large as a consequence of the the larger mass of the scattered lepton.

The Quasi-elastic Tail

In this case the virtual photon scatters elastically off one of the nucleons in the nucleus. The apparent kinematics is however that of a deep inelastic event with $x < 1$ (and not $x = 1$, as expected for elastic scattering off a nucleon) because of the radiation of a real photon by the beam or by the scattered muon. The final state being fixed here ($W = M_{nucleon}$, line B in fig. 4.12) the only integration which must be carried out is over the kinematics of the real photon.

The quasi-elastic cross section is given to first approximation by the cross section for elastic scattering of the virtual photon off a free nucleon. It is thus proportional to the nucleon form factor squared. The binding forces between the nucleons tend however to make it less likely for the photon to scatter off a nucleon without affecting the other nucleons. The photon-nucleon cross section is thus reduced in nuclei, particularly at small Q^2.

In nuclei larger than deuterium, the Pauli exclusion principle imposes a further reduction of the cross section, because final states already occupied by other nucleons in the nucleus are excluded. In a Fermi gas model of the nucleus this extra suppression is a function of the nuclear Fermi momentum k_F: the suppression is largest at $Q^2 = 0$ and goes to zero around $Q^2 = (2k_F)^2$.

In Ferrad the distinction is made between the electric and the magnetic suppression factors, allowing for the fact that the effects of electric and magnetic interactions of nucleons are different. In order to define the electric and the magnetic suppression factors, we first recall the expression of the Rosenbluth formula which describes the scattering of a muon (or an electron) off a nucleon or a nucleus:

$$\frac{d\sigma}{d\Omega} = \left(\frac{d\sigma}{d\Omega}\right)_{Mott} [A(Q^2) + 2B(Q^2)\tan^2(\vartheta/2)] \tag{4.2}$$

with

$$A(Q^2) = \frac{G_e^2 + \frac{Q^2}{4m^2} G_m^2}{1 + \frac{Q^2}{4m^2}} \tag{4.3}$$

and

$$B(Q^2) = \frac{Q^2}{4m^2} G_m^2 \left(1 + \frac{Q^2}{4m^2}\right), \tag{4.4}$$

where G_e and G_m are the electric and magnetic nucleon or nucleus form factors, and where the mass m equals that of the nucleon or that of the nucleus.

We will take helium as an example. Let A_{He} and B_{He} be the values of the functions $A(Q^2)$ and $B(Q^2)$ for helium, when both coherent scattering off the nucleus and quasi-elastic scattering off the nucleons (i.e. coherent scattering off the individual nucleons) are included. Let $A_{coherent}$ and $B_{coherent}$ be the same functions but for the coherent nuclear scattering case only; $B_{coherent} = 0$ for helium, which is a spin-0 nucleus. Finally we introduce $A_{incoherent}$ as the incoherent sum of the quasi-elastic contributions

$$A_{incoherent} = ZA_{proton} + NA_{neutron},$$

and likewise for $B_{incoherent}$.
The electric suppression factor is then defined as

$$S_E = \frac{A_{He} - A_{coherent}}{A_{incoherent}}. \tag{4.5}$$

Similarly the magnetic suppression factor is

$$S_M = \frac{B_{He} - B_{coherent}}{B_{incoherent}}. \tag{4.6}$$

In order to obtain the quasi-elastic cross section the functions $A(Q^2)$ and $B(Q^2)$ should be multiplied by the electric and magnetic suppression factors, respectively; the cross section has still the form 4.2, but $A(Q^2)$ and $B(Q^2)$ now read:

$$A_{QE}(Q^2) = S_E \frac{G_E'^2 + \frac{Q^2}{4M^2} G_M'^2}{1 + \frac{Q^2}{4M^2}} \tag{4.7}$$

and

$$B_{QE}(Q^2) = \frac{Q^2}{4M^2} S_M G_M'^2 \left(1 + \frac{Q^2}{4M^2}\right), \tag{4.8}$$

with

$$G_E'^2 = G_E^2 \frac{Z}{A}, \tag{4.9}$$

$$G_M'^2 = G_E^2 \frac{Z\mu_p^2 + N\mu_n^2}{A}. \tag{4.10}$$

The quantity G_E is the proton electric form factor and $\mu_p = 2.79$, $\mu_n = -1.91$ are the proton and neutron magnetic moments in units of the nuclear magneton.

In the present analysis the suppression factors for both helium and deuterium were obtained from a paper by Bernabeu [276]. The calculation of Bernabeu is based on the nuclear shell model with spin and isospin correlations between the nucleons built in. The model explicitely assumes that the suppression factors are zero at $Q^2 = 0$ and tend to unity for $Q^2 \to \infty$. The results of the calculation are in good agreement with the existing measurements of A_{QE} in deuterium ($0.06 < Q^2 < 0.179$ GeV^2) [277]. We refer the reader to section 4.5.3 and appendix C for a comparison with other approaches.

For the nucleon form factors necessary in equations 4.7 and 4.8, the parametrizations of Gari and Krümpelmann [272] were taken. These parametrizations were obtained from a simultaneous fit of the nucleon form factors $G^{p,n}_{M,E}$ to recent data. The fitted functions are based on an extended vector meson dominance model, which incorporates quark dynamics at large Q^2 via perturbative QCD.

The Coherent Tail

In coherent events the virtual photon scatters coherently off the whole nucleus. Again the apparent x is smaller than unity as a consequence of photon radiation from the muon. The formalism for the calculation of this tail is the same as that for $T_{quasi-el}$; in this case of course $W = M_{nucleus}$ (line C in fig. 4.12). The coherent nuclear scattering cross section is used and the nuclear coherent form factors are needed (fit no. 1 from [299] for D and parametrization [305] for He, see section 4.5.3 and appendix C for a discussion).

4.3 Correction of the Beam and Scattered Muon Momenta

The beam muon momentum, as measured by the BMS, was recomputed, event by event, using the calibration obtained from the BCS calibration runs for this period and discussed in appendix A.

The scattered muon momentum was rescaled by 1.007 ± 0.002, in agreement with the shift seen in the J/ψ mass and ascribed to a wrong setting of the FSM current [314, 315].

The effect of these corrections is small and only affects the high x bins.

4.4 The Cross Section Ratio σ^{He}/σ^{D}

The events which passed the selection criteria described above were radiatively corrected and then binned in x and Q^2, for each of the four targets separately (He upstream, He downstream, D upstream, D downstream). The cross sections ratio was then obtained in each bin by means of formula 2.5, page 103. A few corrections were applied to the ratio thus found.

4.4.1 Correction for the Hydrogen Admixture in the Deuterium Target

We mentioned already in chapter 2 that the liquid deuterium used as a target was not pure but contained a 3% fraction of HD molecules. As discussed in point 3. of section 2.9.3 (page 104), this entails a correction to the observed deuterium yield and therefore to the ratio. The size of the correction is slightly x dependent and amounts to about -1%.

4.4.2 Vertex Smearing

As we described in section 4.1.2, events are assigned to targets on the basis of the vertex cuts. It is clear that, because of the finite vertex resolution, events occurring in one target material may be assigned a value of x_{vertex} outside the target cuts. These events are thus lost. Events from foreign material, e.g. the beam hodoscopes, P0B, P0C, etc. may instead occasionally appear to have originated within the helium or deuterium targets.

In order to estimate the loss of good helium or deuterium events and the gain of spurious ones, the fits of figures 4.3 and 4.4 were repeated for the data belonging to different ϑ intervals.

ϑ range	$C-1$
0 – 8 mrad	$-0.3\% \pm 0.3\%$
8 mrad – 16 mrad	$-0.1\% \pm 0.1\%$
16 mrad – 110 mrad	$-0.04\% \pm 0.04\%$

Table 4.3: Vertex smearing corrections

The fitted contributions of the BH, the upstream target, P0B, the downstream target and P0C were integrated inside and outside the vertex cuts for target position #1 and #2 separately.

For each of the four targets (He_{up}, He_{dw}, D_{up} and D_{dw}), the following quantities were computed in each ϑ bin:

- $N_{measured}$, the integral of all contributions within the vertex cuts for a given target;
- N_{extra}, the integral of all the foreign material contributions within the vertex cuts: as an example, for the upstream He target, N_{extra} is the sum of the BH, P0B, downstream deuterium and P0C contributions integrated within the upstream vertex cuts.
- N_{lost}, the integral of the contributions of a given target outside the vertex cuts.

The true number of events is thus given by

$$\begin{aligned} N_{true} &= N_{measured} + N_{lost} - N_{extra} \\ &= N_{measured}\left(1 + \frac{N_{lost} - N_{extra}}{N_{measured}}\right) \\ &= N_{measured}(1+\zeta). \end{aligned}$$

The measured yield in a given target must be thus multiplied by $(1+\zeta)$ in order to correct for the vertex smearing effects. Keeping in mind expression 2.5 (page 103) for the extraction of the cross section ratio, the correction applied to the ratio in a given ϑ bin reads:

$$C = 1 + \frac{1}{2}(\zeta_{He_{up}} + \zeta_{He_{dw}} - \zeta_{D_{up}} - \zeta_{D_{dw}}).$$

The corrections decrease with increasing ϑ and are generally small (0.3% at most). They are listed in table 4.3.

4.4.3 Effects of the Target Walls and of Shrinking of the Target Vessels

The target walls fall inside the vertex cuts and act as foreign, unwanted target material. Let the extra events from the target walls be N'; the total number of observed events N_{obs} is then given by

$$N_{obs} = N_{true} + N', \tag{4.11}$$

where N_{true} is the number of events actually coming from helium or deuterium.

Expression 4.11 can be rewritten as

$$N_{obs} = N_{true}\left(1 + \frac{\sigma' L'}{\sigma_{true} L_{true}}\right), \tag{4.12}$$

where we have set $N' = \sigma' L'$, with $\sigma' L'$ the product of the cross section and the luminosity for the target walls and similarly $N_{true} = \sigma_{true} L_{true}$. If we neglect nuclear effects and set $\sigma'/\sigma_{true} = 1$, we obtain

$$N_{obs} = N_{true}\left(1 + \frac{\rho' l'}{\rho_{true} l_{true}}\right), \tag{4.13}$$

where ρl is the thickness in g/cm^2.

Using the target thicknesses of section 2.9.2, we find

$$\frac{\rho' l'}{\rho_{He} l_{He}} = 0.41\% \pm 0.09\% \tag{4.14}$$

and

$$\frac{\rho' l'}{\rho_D l_D} = 0.32\% \pm 0.07\%. \tag{4.15}$$

Taking also into account the effect of target shrinking [316], slightly different (0.03%) for helium and deuterium because of the different operating temperatures, we finally obtain an overall x independent correction to the ratio of -0.06%.

4.4.4 Apparatus Smearing

Since the apparatus resolution is finite, kinematic variables may be incorrectly measured. A given bin of the variable ξ may thus contain events for which ξ_{true}, the *real* value of ξ, differs from $\xi_{measured}$ and actually belongs to a nearby bin. Likewise the bin in question may lose events to neighboring ones. The balance between gained and lost events may be not even in the case of steep distributions, thus leading to a distortion of the distributions themselves (which are then said to be smeared).

While the problem may be serious when computing absolute differential cross sections, it is less critical in the evaluation of cross section ratios, as smearing effects largely cancel out in the ratio. In our case smearing corrections essentially originate from the small differences between the distributions of the kinematic variables in helium and deuterium.

Smearing may be computed by means of Monte Carlo simulation. We briefly outline the procedure [317].

The number of events measured in a bin of size $\Delta\xi$ may be written as

$$N = L \int_{\Delta\xi} d\xi \int_a^b d\xi' P(\xi|\xi') \sigma_{tot}(\xi') \epsilon(\xi'), \tag{4.16}$$

where for brevity we used $\xi = \xi_{measured} = \xi_{smeared}$ and $\xi' = \xi_{true}$; ξ' may take values in all of the allowed kinematic range $a \le \xi' \le b$. The function $P(\xi|\xi')d\xi$ is the probability that the measured value of ξ occurs in the interval $\xi \pm d\xi/2$ if the true one is at ξ'. The symbol σ_{tot} is a short-hand notation for the total differential cross section $d\sigma_{tot}/d\xi'$, ϵ is the acceptance and L is the luminosity.

As we explained before every event is weighted by the radiative corrections weight $\eta = \sigma_{1\gamma}/\sigma_{tot}$. Formula 4.16 for the weighted events reads:

$$W = L \int_{\Delta\xi} d\xi \int_a^b d\xi' P(\xi|\xi')\sigma_{tot}(\xi') \left\{ \frac{\sigma_{1\gamma}(\xi)}{\sigma_{tot}(\xi)} \right\} \epsilon(\xi'). \tag{4.17}$$

If we take the binwidth $\Delta\xi$ small enough that $\sigma_{1\gamma}(\xi)$ is nearly constant inside the bin, then relation 4.17 becomes:

$$W = L\sigma_{1\gamma}(\bar{\xi}) \int_{\Delta\xi} d\xi \int_a^b d\xi' P(\xi|\xi') \frac{\sigma_{tot}(\xi')}{\sigma_{tot}(\xi)} \epsilon(\xi') \tag{4.18}$$

where $\bar{\xi}$ is the average of ξ inside the bin. Let the value of the double integral in 4.18 be I. Taking then the ratio of W_{He} to W_D, the values of W for helium and deuterium, respectively, we get:

$$\frac{W_{He}}{W_D} = \frac{L_{He}}{L_D} \frac{\sigma_{1\gamma}^{He}}{\sigma_{1\gamma}^{D}} \frac{I_{He}}{I_D}, \tag{4.19}$$

from which we obtain the cross section ratio as

$$\frac{\sigma_{1\gamma He}}{\sigma_{1\gamma D}} = \left\{ \frac{W_{He}}{W_D} \frac{L_D}{L_{He}} \right\} \left\{ \frac{I_D}{I_{He}} \right\}. \tag{4.20}$$

Relation 4.20 shows that the cross section ratio is proportional to the ratio of the helium to deuterium yields weighted by the radiative corrections, times the factor $S = I_D/I_{He}$ which is due to the apparatus smearing effects. The ratio I_D/I_{He} can be computed by means of the full Monte Carlo simulation of the experiment described in chapter 3. Each Monte Carlo event is used twice, once weighted proportionally to the helium cross section and once proportionally to the deuterium one. This introduces a correlation between I_{He} and I_D which reduces the statistical error on their ratio.

The resulting corrections are everywhere small and are at most 0.2% at large x.

4.4.5 Bin Centering Corrections

Formula 2.5 (page 103) is applicable to a certain x bin under the assumption that the events coming from the four targets have the same average value of x. As a consequence of the different spectrometer acceptance for the upstream and downstream targets, the average x, $\bar{x}$, in a given x bin may be different for the upstream and downstream events. This may be taken into account by means of the following relationship [318]:

$$r_{true}(\bar{x}) = r_{measured}(\bar{x}) \cdot \sqrt{1 - \left[\frac{\frac{dr}{dx}(\bar{x})}{2r(\bar{x})} \cdot (\bar{x}_u - \bar{x}_d) \right]^2} \tag{4.21}$$

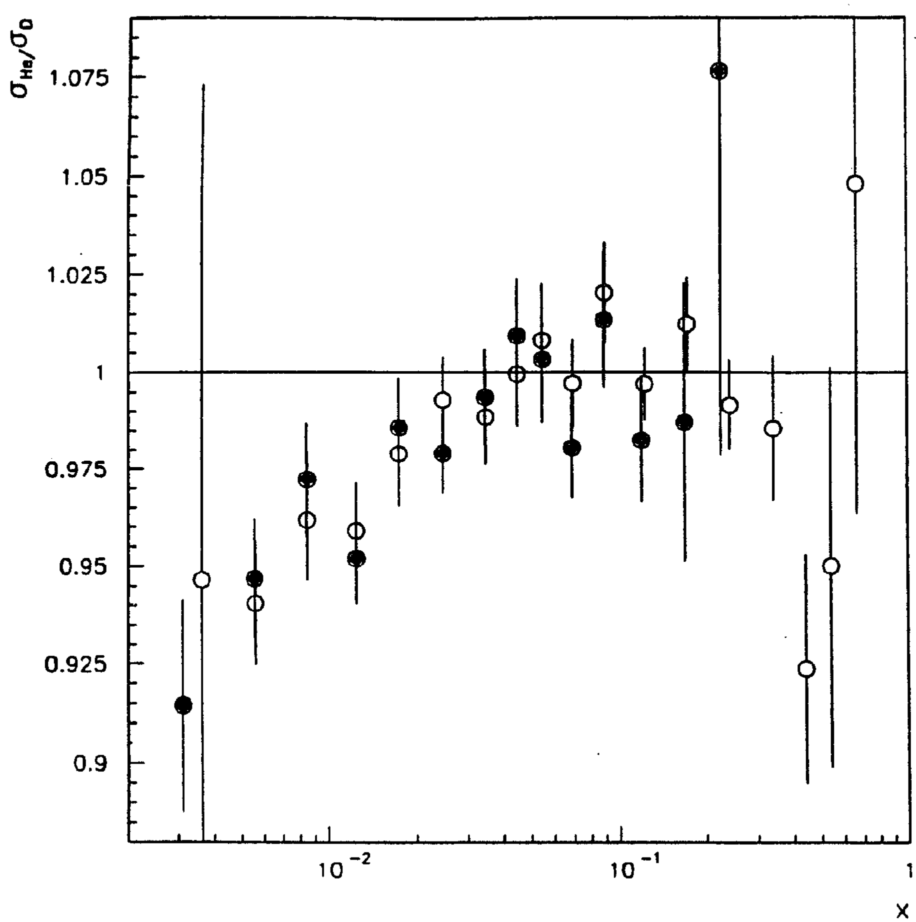

Figure 4.13: The ratio σ^{He}/σ^D as a function of x. The open circles refer to the T1 data, the solid ones refer to the trigger 2 data. Only statistical errors are shown

where $r = \sigma^{He}/\sigma^D$.

Bin centering corrections, i.e. $r_{true} - r_{measured}$, are very small ($< 10^{-7}$) and will henceforth be neglected.

4.4.6 The Results

The T1 and T2 events were binned in x and the cross section ratio was computed in each bin by means of formula 2.5 (page 103) after applying the corrections described above. Figure 4.13 and tables 4.4 and 4.5 show the T1 and T2 results as a function of x. The errors are statistical only. Tables 4.4 and 4.5 also indicate the average scattering angle ϑ, the Q^2 range, the average Q^2, y and radiative correction factor η in each x bin. The same ratios are shown as a function of Q^2 in each x bin in figures 4.14-4.16.

Trigger 1 and trigger 2 events were merged together and treated as single data sample. Figure 4.17 and table 4.6 show the resulting ratio as a function of x.

Finally figures 4.18-4.20 show the ratio derived from the merged T1 and T2 data as a function of Q^2 in each x bin. The continuous lines are the results of fits of the type $\sigma^{He}/\sigma^D =$

$\langle x \rangle$	$\langle \vartheta \rangle$[mrad]	$\langle Q^2 \rangle$[GeV^2]	Q^2 range [GeV^2]	$\langle y \rangle$	$\langle \eta \rangle$	σ^{He}/σ^D	stat.
0.00363	12.0	1.1	1.1 – 1.2	0.80	0.67	0.946	0.127
0.00560	14.2	1.6	1.2 – 2.2	0.79	0.70	0.940	0.016
0.00850	16.0	2.4	2.0 – 3.1	0.75	0.74	0.962	0.015
0.01244	17.5	3.2	2.4 – 4.4	0.71	0.78	0.959	0.012
0.01744	18.7	4.2	2.8 – 6.2	0.66	0.82	0.979	0.014
0.02485	20.0	5.5	3.3 – 9.2	0.60	0.85	0.993	0.011
0.03488	21.1	7.0	3.9 – 12	0.55	0.87	0.989	0.012
0.04489	21.5	8.2	4.7 – 15	0.49	0.89	0.999	0.013
0.05486	21.7	9.1	4.6 – 18	0.45	0.90	1.008	0.015
0.06964	21.9	10	4.7 – 24	0.40	0.92	0.997	0.011
0.08967	22.0	11	5.6 – 25	0.35	0.93	1.020	0.013
0.12314	22.4	13	5.6 – 43	0.29	0.95	0.997	0.009
0.17318	23.2	15	6.9 – 46	0.24	0.97	1.012	0.012
0.24255	25.0	19	8.5 – 62	0.21	0.99	0.991	0.012
0.34203	27.9	24	13 – 86	0.19	1.01	0.986	0.019
0.44159	31.2	31	17 – 87	0.19	1.03	0.924	0.029
0.54039	34.5	38	21 – 90	0.19	1.04	0.950	0.051
0.66560	36.9	44	27 – 64	0.18	1.07	1.048	0.085

Table 4.4: The cross section ratio σ^{He}/σ^D obtained from the T1 data

$\langle x \rangle$	$\langle \vartheta \rangle$[mrad]	$\langle Q^2 \rangle$[GeV^2]	Q^2 range [GeV^2]	$\langle y \rangle$	$\langle \eta \rangle$	σ^{He}/σ^D	stat.
0.00312	6.8	0.70	0.5 – 1.1	0.61	0.79	0.914	0.027
0.00556	7.8	1.1	0.7 – 1.9	0.54	0.83	0.947	0.015
0.00849	8.6	1.5	0.9 – 2.7	0.47	0.86	0.972	0.015
0.01244	8.9	1.8	1.1 – 3.7	0.39	0.88	0.952	0.012
0.01743	9.1	2.1	1.1 – 4.6	0.33	0.90	0.986	0.013
0.02474	9.2	2.4	1.1 – 5.4	0.26	0.91	0.979	0.010
0.03477	9.2	2.6	1.1 – 5.4	0.21	0.93	0.994	0.012
0.04480	9.3	2.8	1.3 – 6.5	0.17	0.94	1.009	0.014
0.05479	9.5	3.0	1.5 – 6.5	0.15	0.95	1.003	0.016
0.06918	9.9	3.4	1.8 – 6.5	0.13	0.96	0.980	0.013
0.08920	10.4	3.8	2.4 – 6.5	0.12	0.97	1.013	0.017
0.11978	11.3	4.5	2.9 – 6.6	0.10	0.98	0.982	0.016
0.16915	12.7	5.8	4.7 – 6.6	0.09	0.99	0.987	0.036
0.22460	14.2	7.2	5.9 – 8.1	0.09	1.00	1.076	0.098

Table 4.5: The cross section ratio σ^{He}/σ^D obtained from the T2 data

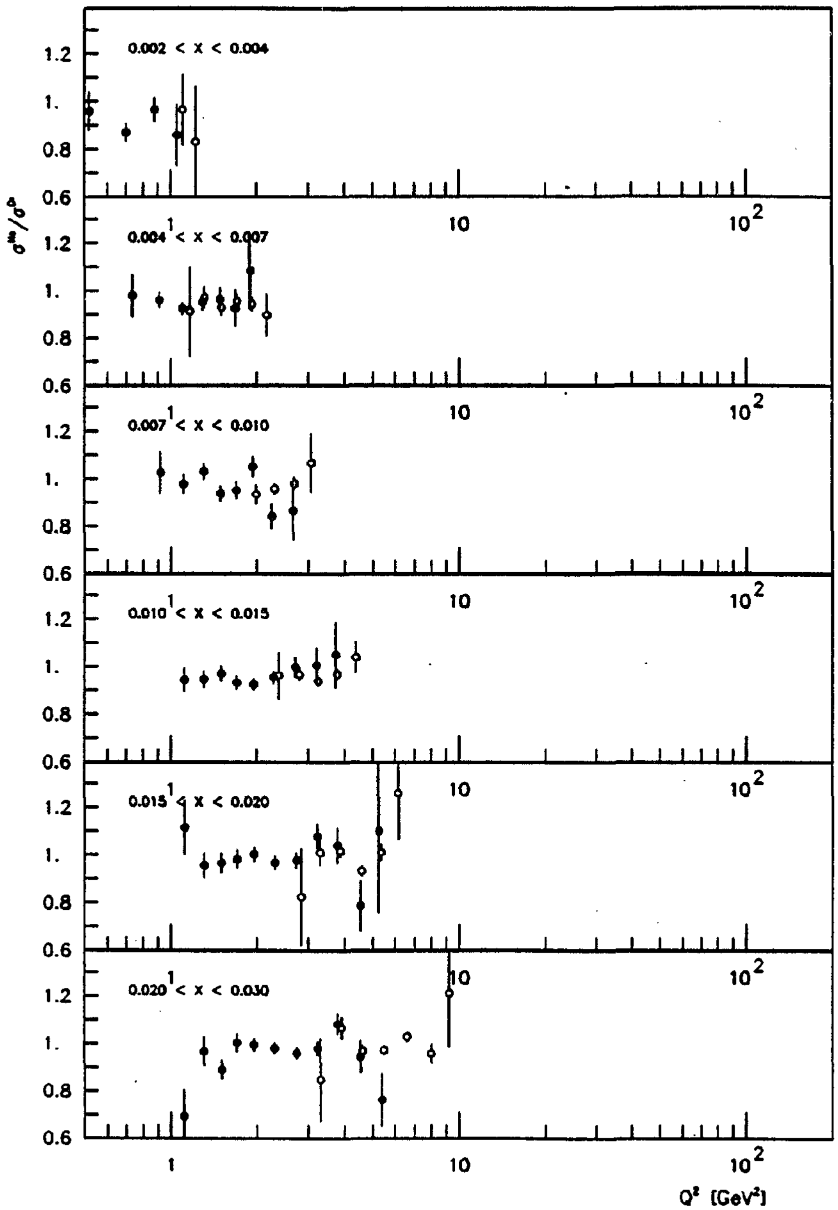

Figure 4.14: The ratio σ^{He}/σ^{D} as a function of Q^2 in each x bin. The open circles are from T1, the solid ones are from T2 ($0.002 < x < 0.03$)

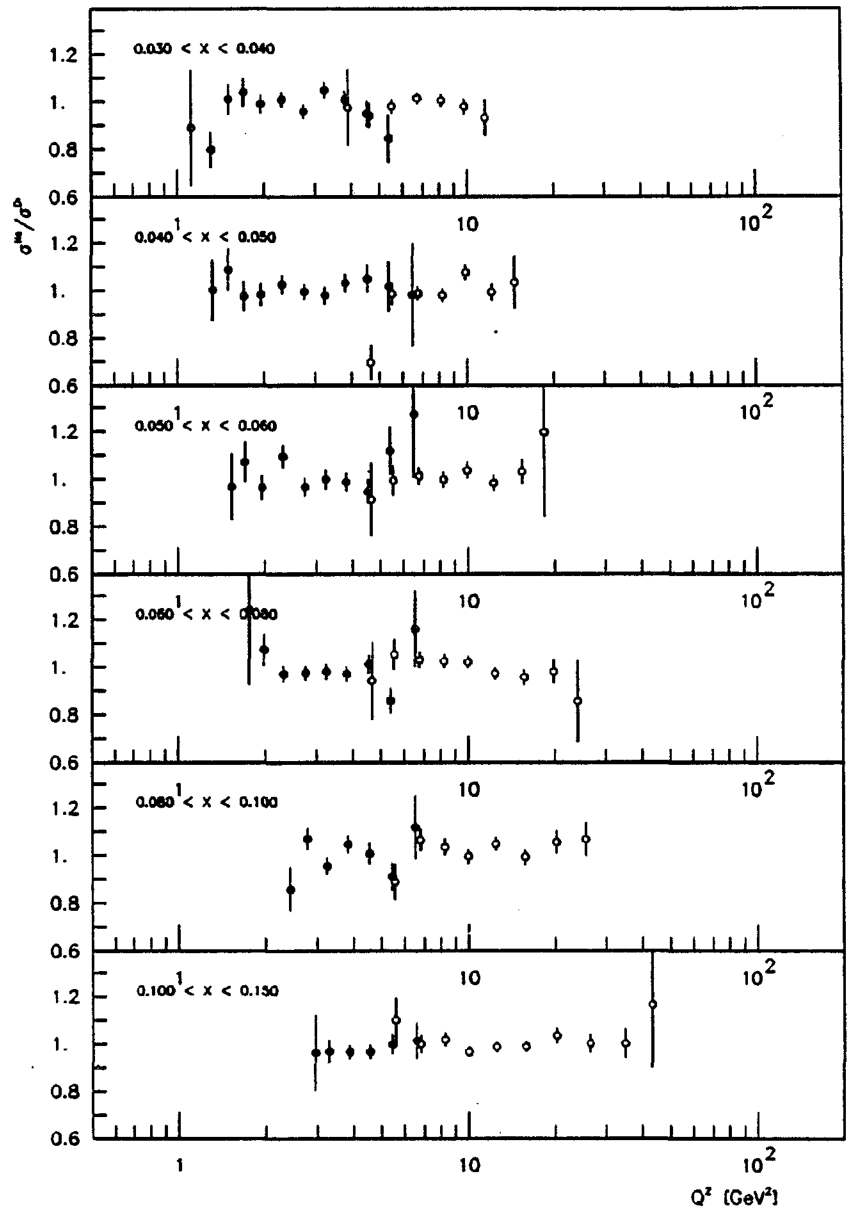

Figure 4.15: The ratio σ^{He}/σ^{D} as a function of Q^2 in each x bin. The open circles are from T1, the solid ones are from T2 ($0.03 < x < 0.15$)

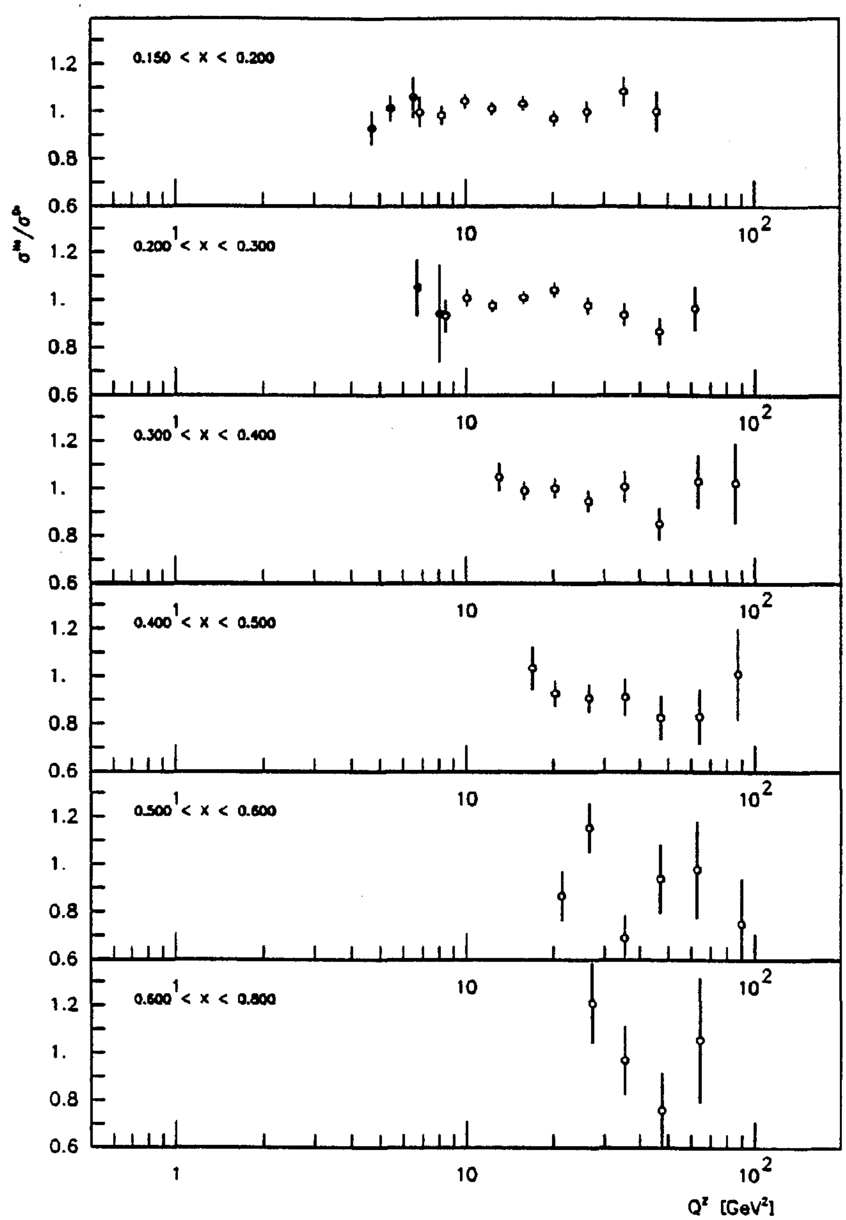

Figure 4.16: The ratio σ^{He}/σ^{D} as a function of Q^2 in each x bin. The open circles are from T1, the solid ones are from T2 ($0.15 < x < 0.8$)

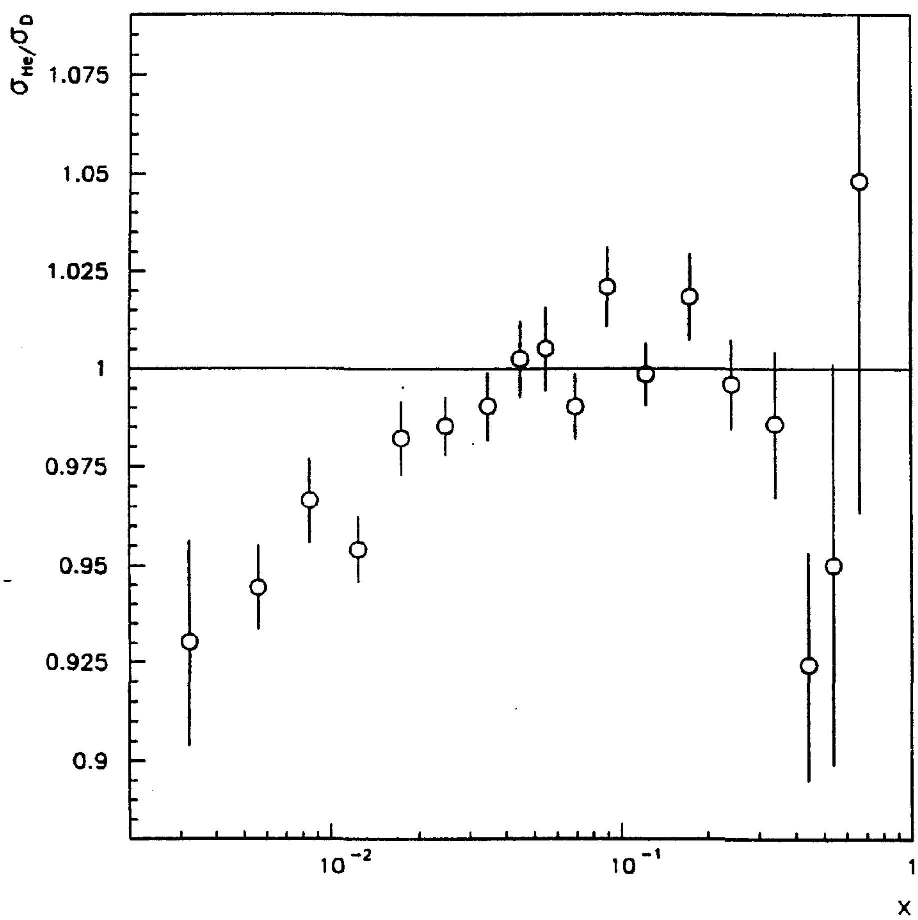

Figure 4.17: The cross section ratio σ^{He}/σ^{D} obtained from the merged T1 and T2 data

$\langle x\rangle$	$\langle\vartheta\rangle$[mrad]	$\langle Q^2\rangle$[GeV^2]	Q^2 range [GeV^2]	$\langle y\rangle$	$\langle\eta\rangle$	σ^{He}/σ^D	stat.
0.00322	7.7	0.77	0.5 – 1.2	0.65	0.77	0.930	0.026
0.00558	10.6	1.3	0.7 – 2.2	0.65	0.77	0.944	0.011
0.00849	11.8	1.8	0.9 – 3.1	0.59	0.80	0.966	0.011
0.01244	12.6	2.4	1.1 – 4.4	0.53	0.84	0.954	0.009
0.01743	13.2	3.0	1.1 – 6.2	0.47	0.86	0.982	0.009
0.02479	14.0	3.8	1.1 – 9.2	0.42	0.88	0.985	0.008
0.03482	14.9	4.7	1.1 – 12	0.37	0.90	0.990	0.009
0.04485	15.6	5.6	1.3 – 15	0.34	0.91	1.003	0.010
0.05483	16.0	6.3	1.5 – 18	0.31	0.92	1.005	0.011
0.06945	16.8	7.3	1.8 – 24	0.29	0.93	0.990	0.009
0.08950	17.9	8.7	2.4 – 25	0.26	0.94	1.021	0.010
0.12231	19.6	11	2.9 – 43	0.24	0.95	0.999	0.008
0.17275	22.1	14	4.7 – 46	0.22	0.97	1.018	0.011
0.24204	24.7	19	5.9 – 62	0.21	0.99	0.996	0.011
0.34200	27.9	24	13 – 86	0.19	1.01	0.986	0.019
0.44158	31.2	31	17 – 87	0.19	1.03	0.924	0.029
0.54039	34.5	38	21 – 90	0.19	1.04	0.950	0.051
0.66560	36.9	44	27 – 64	0.18	1.07	1.048	0.085

Table 4.6: The cross section ratio σ^{He}/σ^D obtained from the merged T1 and T2 data

$a + b\ln Q^2$ to the data in each bin separately. The logarithmic slopes b are given in table 4.7 and are plotted in fig. 4.21 as a function of x. Only statistical errors are shown.

4.5 Systematic Studies on the Radiative Corrections

4.5.1 General Remarks

Radiative corrections are a crucial step in the determination of structure function ratios. In the small x region there is little resemblance between the uncorrected ratios and the final results, especially in the T1 case. Figures 4.22 and 4.23 show the corrected and uncorrected ratios for the T1 and T2 data, respectively. Corrections grow with decreasing x and are thus important in the region where statistics is largest. It is clear that the size of the shadowing signal will be incorrectly estimated if radiative corrections are wrong.

Before we enter the discussion on the systematics of radiative corrections, an important conclusion can be drawn already from fig. 4.13. Trigger 1 and trigger 2 events have a large region of overlap in x; T2 events have however smaller Q^2 and ν than T1 events at the same value of x. Lower ν implies lower y and therefore smaller radiative corrections. A comparison of the y distributions for T1 and T2 is shown in fig. 2.8 (page 107) and for $x < 0.04$ in fig. 4.24. The agreement of the T1 and T2 results at small x thus suggests that, at least in the region of overlap, radiative weights are calculated correctly.

A similar conclusion can be drawn by comparing the standard results to those obtained when applying a stricter cut on the radiative corrections, $\eta_{min} = 0.8$, instead of $\eta_{min} = 0.6$. Figure 4.25 shows that removing events with large radiative corrections does not change the results, within the errors.

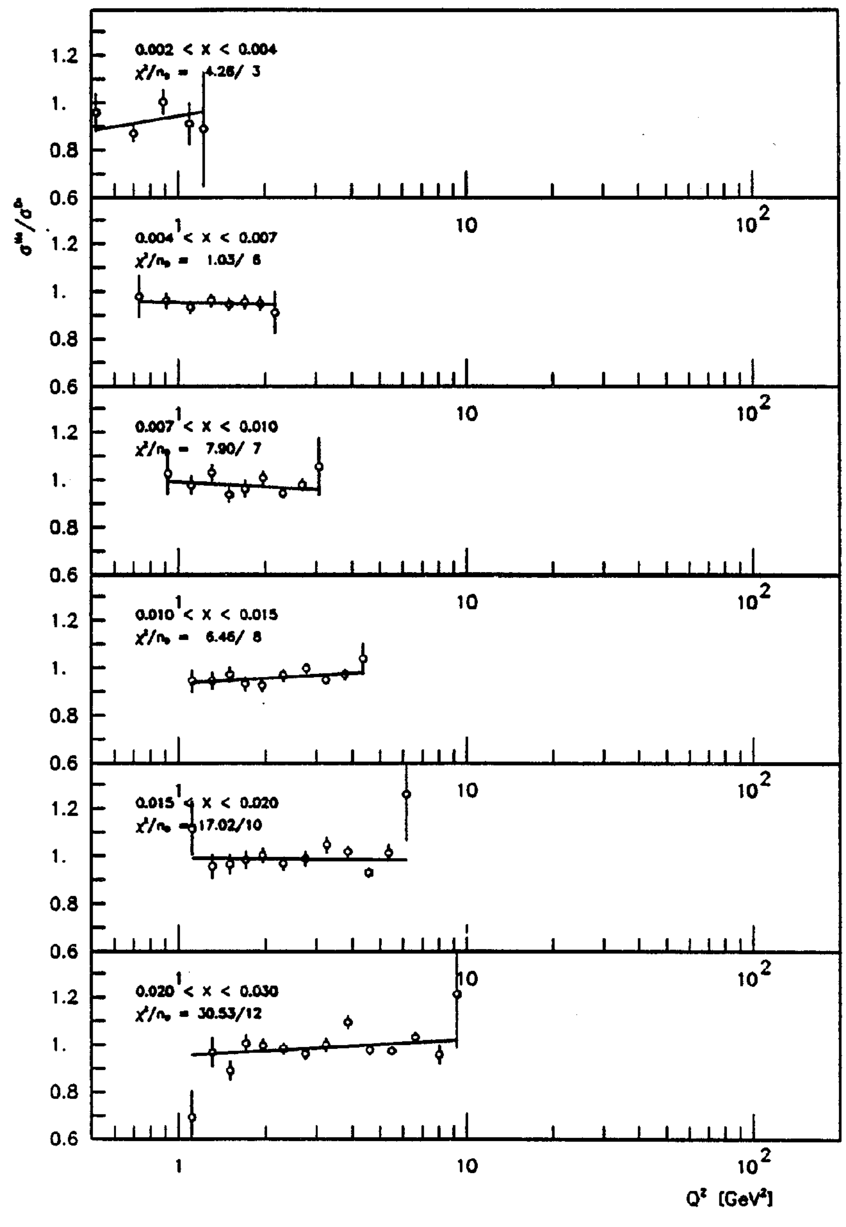

Figure 4.18: The ratio σ^{He}/σ^D as a function of Q^2 in each x bin, for the merged T1, T2 data $(0.002 < x < 0.03)$. The continuous lines are the results of the fits described in the text

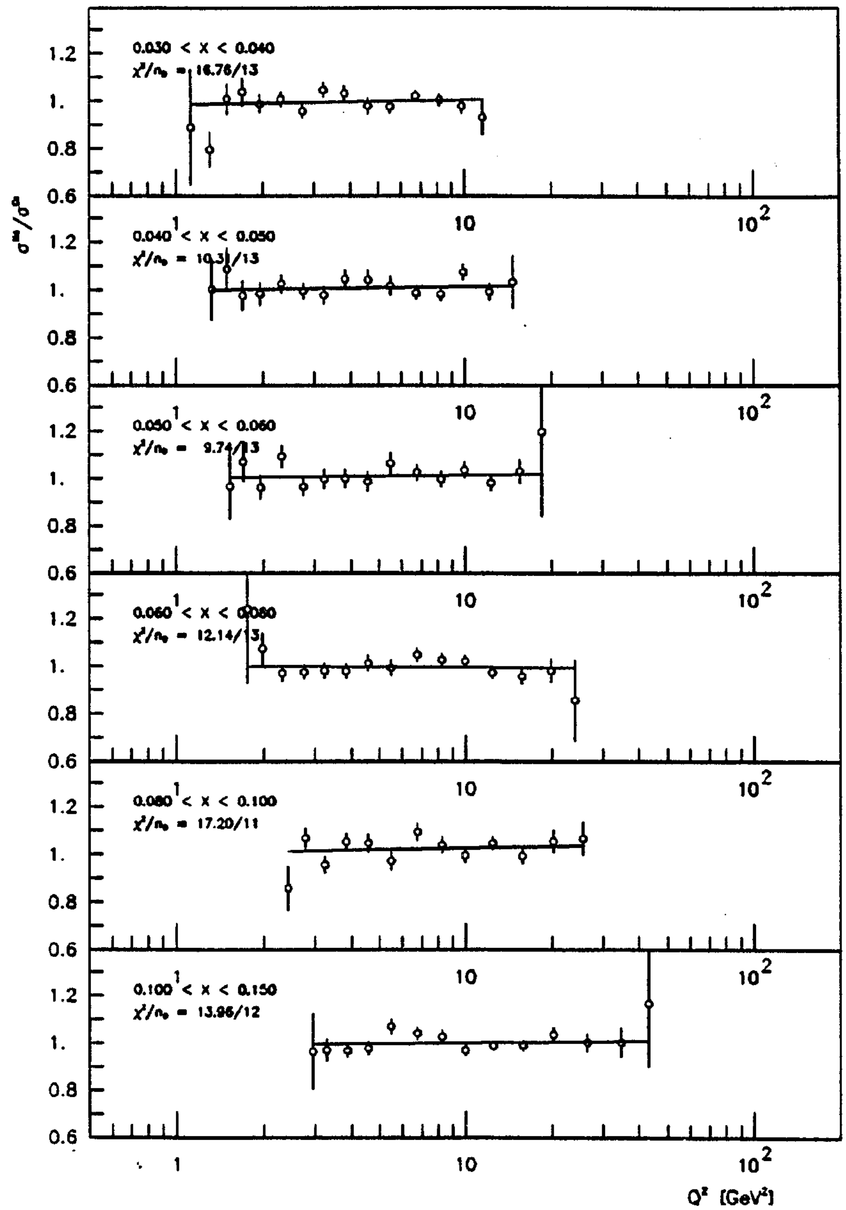

Figure 4.19: The ratio σ^{He}/σ^{D} as a function of Q^2 in each x bin, for the merged T1, T2 data ($0.03 < x < 0.15$). The continuous lines are the results of the fits described in the text

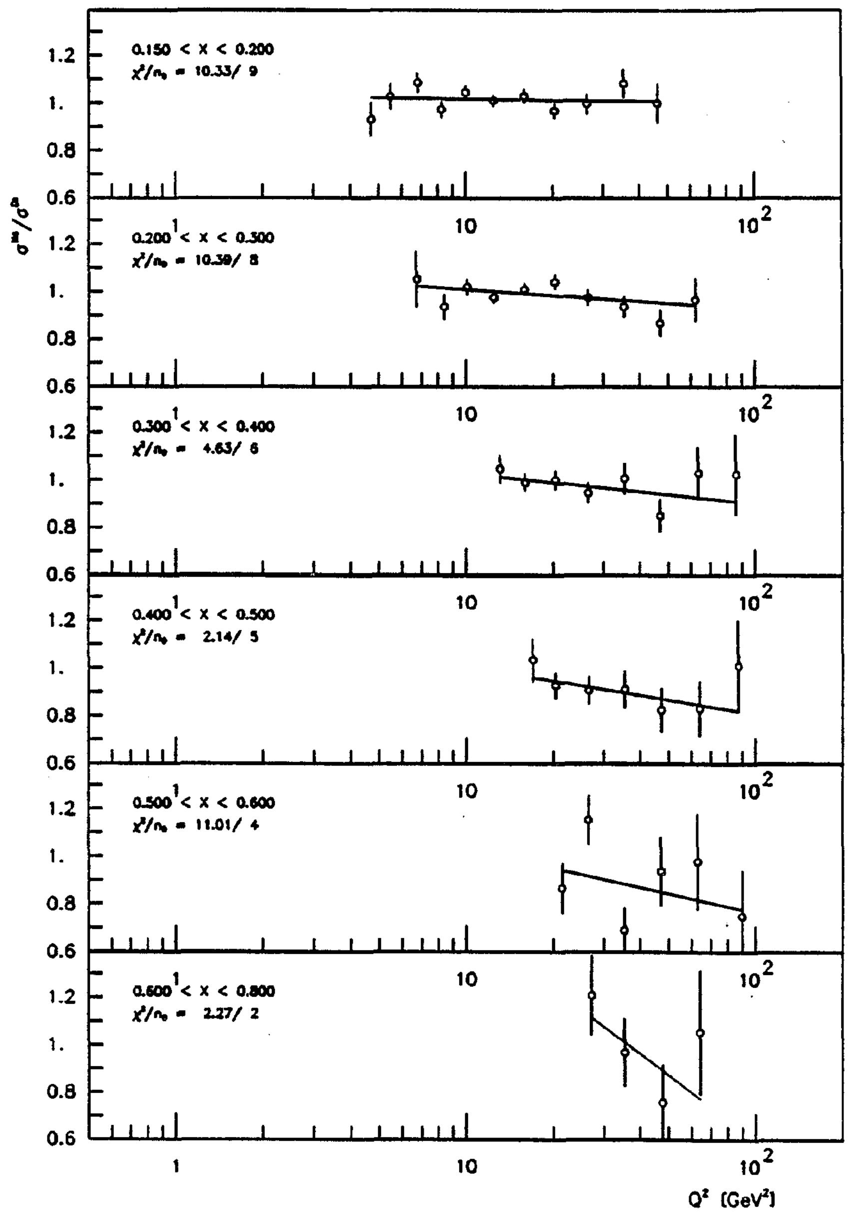

Figure 4.20: The ratio σ^{He}/σ^{D} as a function of Q^2 in each x bin, for the merged T1, T2 data $(0.15 < x < 0.8)$. The continuous lines are the results of the fits described in the text

x	b	stat.
0.0035	0.088	0.132
0.0055	−0.009	0.044
0.0085	−0.030	0.037
0.0125	0.029	0.024
0.0175	−0.004	0.023
0.025	0.029	0.017
0.035	0.008	0.016
0.045	0.007	0.017
0.055	0.004	0.018
0.070	−0.002	0.014
0.090	−0.010	0.017
0.125	0.004	0.014
0.175	−0.006	0.022
0.25	−0.037	0.024
0.35	−0.054	0.044
0.45	−0.085	0.071
0.55	−0.114	0.123
0.65	−0.401	0.312

Table 4.7: The slopes $b = d(\sigma^{He}/\sigma^{D})/d(\ln Q^2)$ as a function of x. Only statistical errors are shown

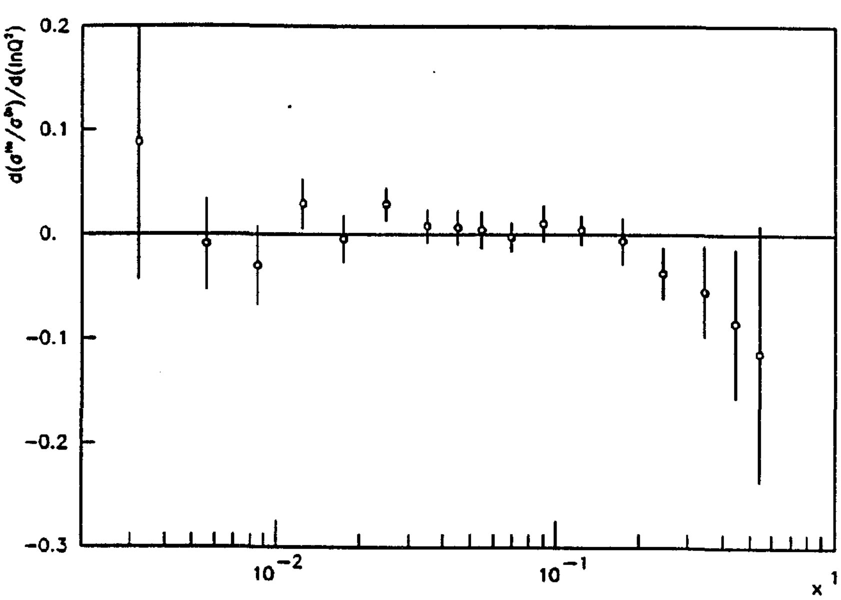

Figure 4.21: The slopes $b = d(\sigma^{He}/\sigma^{D})/d(\ln Q^2)$ in each x bin. Only statistical errors are shown

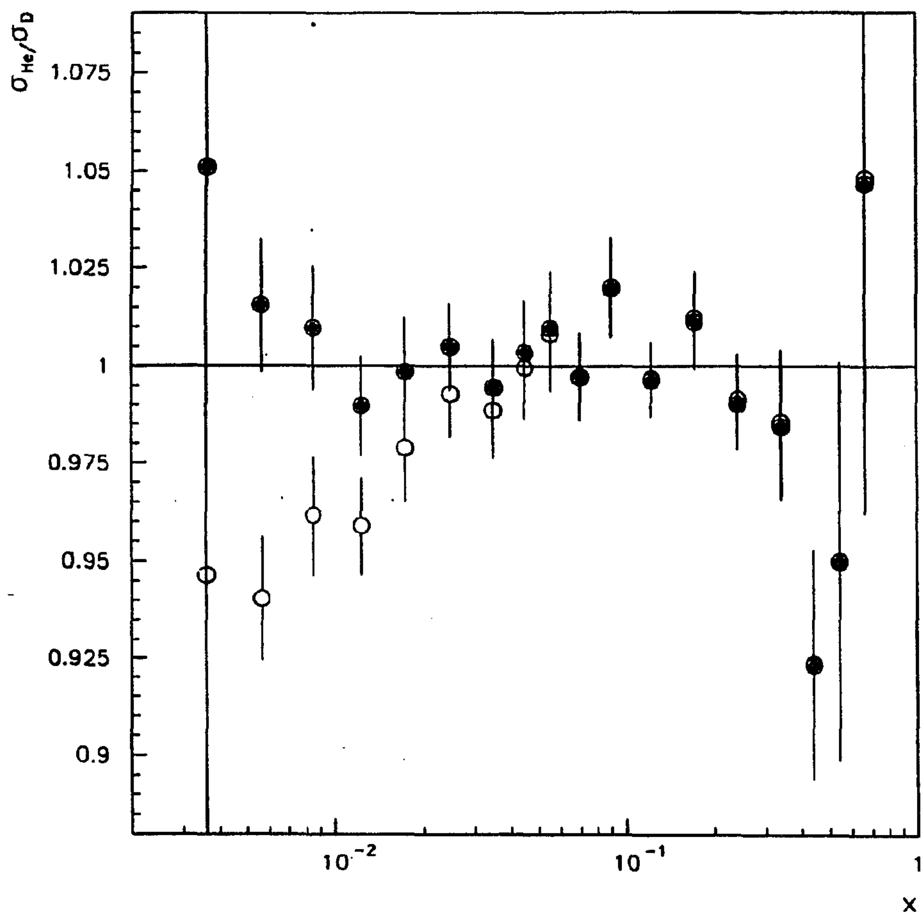

Figure 4.22: The ratio σ^{He}/σ^{D} as a function of x, with (open symbols) and without (full symbols) radiative corrections for the T1 events

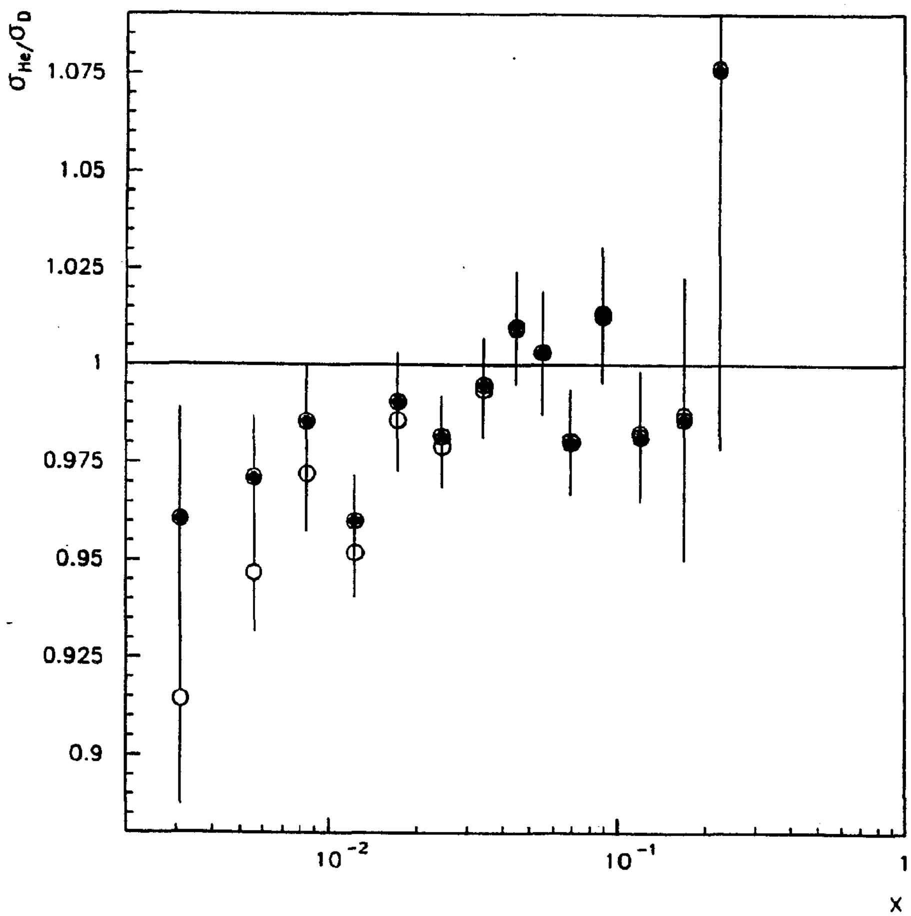

Figure 4.23: The ratio σ^{He}/σ^{D} as a function of x, with (open symbols) and without (full symbols) radiative corrections for the T2 events

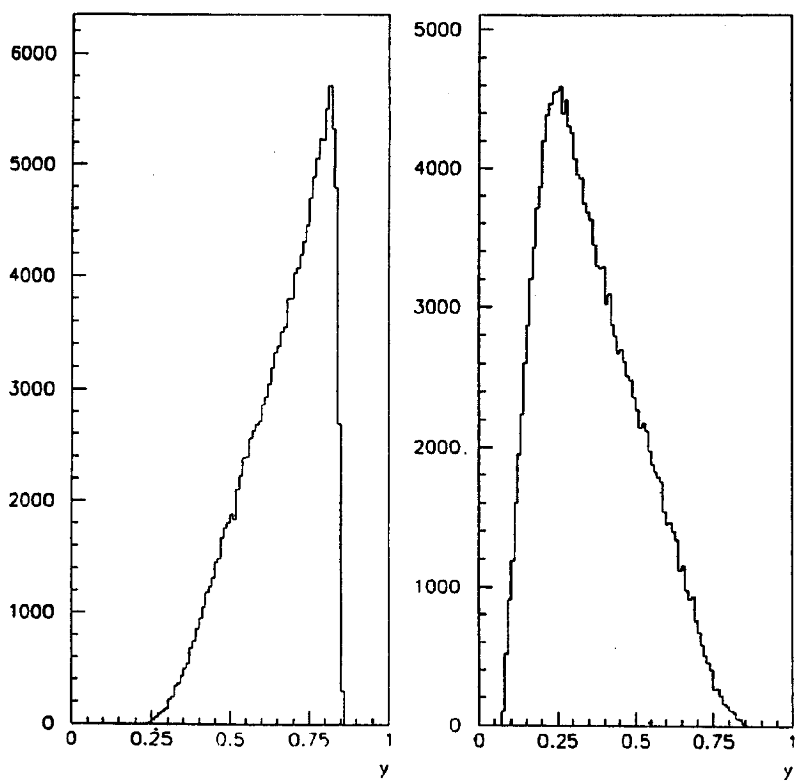

Figure 4.24: Distribution of y for T1 (left) and T2 (right) events ($x < 0.04$)

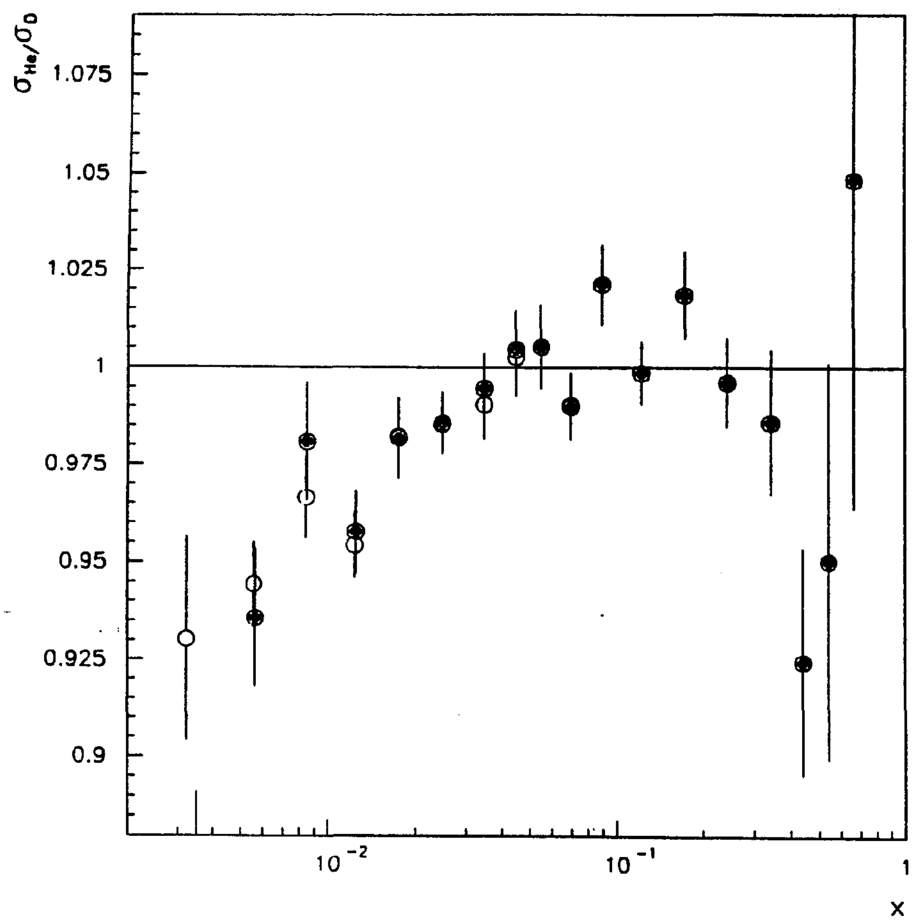

Figure 4.25: The ratio σ^{He}/σ^{D} as a function of x. The open symbols are for the standard results (η_{min} = 0.6); the full symbols are for the η_{min}=0.8 results

In the following we compare the NMC radiative corrections procedure with other available ones. We also present a detailed evaluation of the effect of modifying the input parameters to the NMC Ferrad program.

4.5.2 Comparison with Other Procedures

The NMC radiative correction procedure is based on the Tsai [260], Mo and Tsai [261] formalism, originally developed for the SLAC electron scattering experiments and subsequently adapted by EMC for use with muon beams. It includes, as we saw, an exact treatment of the elastic and quasi-elastic radiative tails, an approximate treatment of the inelastic tail, vacuum polarization loops for electrons and muons and partial treatment of $O(\alpha^4)$ contributions to the lepton current. The BCDMS group, within the NA4 experiment at CERN developed a procedure based on the more recent calculations of Bardin and collaborators [259, 319]. The latter feature:

- a covariant treatment of all processes,
- vacuum polarization loops for electrons, muons, taus and light quarks;
- complete evaluation of the $O(\alpha^4)$ contributions to the lepton current;
- complete evaluation of the $O(\alpha^3)$ contributions to the hadron current;
- calculations of electro-weak (γ-Z^0) interference.

The major differences between the two approaches come from the inclusion of the tau and quark vacuum polarization contributions, the $O(\alpha^3)$ corrections at the hadronic vertex and the electro-weak interference effects. The differences in the treatment of the elastic and inelastic tails are small, the main point being a formal one: the formulae applied are Lorentz invariant and do not contain the (unphysical) cut-off parameter Δ for radiation of soft photons.

Extensive comparisons have been made between the two programs [320, 321]. Although there are significant differences in how the corrections are calculated, the effects tend to cancel when the different contributions are summed. All analyses show that there are no large discrepancies between the results in the kinematic region of interest here, provided the input parametrizations for form factors, structure functions etc. are the same.

A disagreement is apparent only at large x and large Q^2 where the Bardin corrections are a few per cent larger than the EMC-NMC ones. The discrepancy is mainly due to the electro-weak interference effects, neglected in Ferrad, and reaches 4% at $x = 0.8$ and $Q^2 = 200$ GeV^2 [321]. Note that the quoted disagreement applies to the full corrections (i.e. the corrections to the absolute structure functions). In taking the ratio of structure functions the corrections largely cancel and the residual difference is smaller. In the high x and high Q^2 region the NMC statistical errors are anyway large and the discrepancy is thus of marginal significance.

The EMC-NMC evaluation of radiative tails has also been checked experimentally, in a wide kinematic range (down to $x \simeq 0.006$ and up to $y \simeq 0.9$). The yield of wide angle bremsstrahlung photons (with $z = E_\gamma/\nu > 0.7$) was measured by EMC NA2 [322, 323] and compared with the predictions of the Ferrad program. The studies had been stimulated, at the time, by the suggestion of Chahine [324] that the Mo and Tsai formalism does not properly take into account multiple radiation of soft photons. The results of the measurements are consistent with the Mo and Tsai calculations; in particular, the conclusion was reached [323] that the experimental yields of bremsstrahlung photons disagree with the predictions of Chahine.

A further check was made by EMC NA28 [40] by comparing the fractions of events with hadrons from calcium and deuterium targets, as a function of ν. Bremsstrahlung events (fig. 4.6(b,c,k)) contain only the scattered muon and no secondary tracks apart from those due to the photon converting into an electron-positron pair. The ratio of the fraction of events with no secondary track from calcium to the fraction from deuterium was observed to rise sharply with ν. The observed rise agreed with that expected from the Ferrad program.

A study was carried out along similar lines by both EMC NA2′ [325] and by NMC [326, 327]. In these analyses the presence of at least one measured hadron track in the event was explicitely required, thereby excluding coherent and quasi-elastic events and insuring that a genuine deep inelastic interaction had occurred. The corrections for the coherent and quasi-elastic tails were thus no longer necessary and the size of the residual correction was significantly reduced; furthermore the residual correction was largely target material independent. The results for the structure function ratios obtained in this way were shown to agree with those found using the standard radiative correction procedure.

4.5.3 Sensitivity to the Input Parameters

Having discussed the reliability of the procedure, we now address the question of the dependence of the results on the the input parameters, e.g. the parametrization of F_2, the form factors, etc. As we mentioned, it is essentially the uncertainty in these quantities that determines the uncertainty on the radiative corrections and hence on the structure function ratio. The subject is covered in detail in appendix C; here we summarize the conclusions relevant to the systematic error evaluation.

We concentrate on the radiative tails, since – as we saw – they are the main cause of the difference between helium and deuterium radiative corrections and thus of the fact that the correction to the structure function ratio is non-zero.

- Inelastic tail. The knowledge of the structure functions F_2^D and F_2^{He}, as well as of the ratio $R = \sigma_L/\sigma_T$ is required.

  - F_2

    For F_2^D a fit to the results of several deep inelastic scattering experiments and to small W data in the resonance region was used. The fitted function, the input data sets and an estimate of the uncertainty on the resulting parametrization are presented in appendix C.

    The helium structure function F_2^{He} was obtained as $F_2^{He} = F_2^D \times (F_2^{He}/F_2^D)$, where (F_2^{He}/F_2^D) is a fit to the measured ratio. The uncertainty of the F_2^D parametrization thus reflects on that for F_2^{He}.

    The overall effect of these errors on the structure function ratios is at most 0.5% at small x.

    Additional variations of up to 0.3-0.4% are found if different functional forms are used to fit the measured ratio F_2^{He}/F_2^D; the reader is referred to appendix C for more details.

  - R

    We used a parametrization based on the most precise data currently available (R^{1990} [46, 47]). This parametrization covers a wide kinematic region, down to

$Q^2 \approx 0.3$ GeV^2, with small errors. If R is modified within these errors the resulting changes in the structure function ratios are smaller than 0.1%. The results are essentially not sensitive to the value of R below $Q^2 = 0.3$ GeV^2.

The assumption was made that R is not a function of A. As we argued before (cf. section 1.2.3, page 16), this is consistent with the results of the SLAC E140 experiment, which measured $R^{Fe} - R^D$ and $R^{Au} - R^D$ for $0.2 < x < 0.5$ and $1 < Q^2 < 5$ GeV^2.

- Quasi-elastic tail. The nucleon elastic form factors and the quasi-elastic suppression factors are required for the calculation of this tail.
  - Nucleon elastic form factors are well known. The existing parametrizations differ very little from each other. The resulting uncertainty on the radiative corrections is very small, below the 0.1% level.
  - Quasi-elastic suppression factors are less well known. For deuterium we used the results of Bernabeu [276], based on a shell model calculation. Alternative choices are based on the nuclear closure approximation (cf. appendix B of [24]) and on a calculation of Arenhövel [278], respectively. The corresponding changes in the radiative corrections are 0.2% at most.

    For helium the results of Bernabeu [276] were used as well. The other available approaches [279, 281] are based on a Fermi gas description of the nucleus. If these suppression factors are used instead of that of Bernabeu, radiadive corrections change by as much as 1%, at small x.

- Coherent tail. The essential ingredient for the evaluation of this contribution is the nuclear coherent form factor. The helium and the deuterium form factors have been measured by many experiments up to Q^2 of a few GeV^2. Several parametrizations exist for both form factors (cf. appendix C for a detailed discussion), but they do not differ significantly for $Q^2 < 1$ GeV^2. Radiative corrections do not vary by more than 0.1% when any of the available parametrizations is used instead of the standard ones. The uncertainty on the structure functions ratio originating from the coherent tail is thus negligible.

Table 4.8 summarizes the effects of the modifications just discussed on the measured ratio. The largest change (about 1% at small x) is the one due to the helium suppression factor (second and third column). Smaller variations, 0.2-0.5%, are due to the modifications in the deuterium suppression factor (third column), in the parametrization for F_2^D (fifth and sixth column) and in the functional form used for the fit to the measured cross section ratio (last column).

4.5.4 Overall Uncertainty on the Ratio Due to Radiative Corrections

We discussed in section 4.5.3 and in appendix C the effect of the uncertainty on the input parameters to the radiative corrections program. In each case the effect is to either increase or decrease the ratio by an amount which becomes smaller with increasing x (cf. table 4.8). The sign of this change does not vary with x, only its magnitude. We used this fact to evaluate the systematic error on the radiative corrections, which were recomputed with two different sets of input parameters. In the first one we grouped all sources which make the cross section ratio

x	He supp. [279] vs [276]	He supp. [281] vs [276]	D supp. [278] vs [276]	F_2^D upper limit vs standard	F_2^D lower limit vs standard	x, Q^2 fit C.4 vs fit C.2
0.0035	−0.012	−0.010	−0.002	0.005	−0.003	−0.004
0.0055	−0.013	−0.009	−0.002	0.004	−0.002	−0.003
0.0085	−0.009	−0.006	−0.002	0.002	−0.001	−0.003
0.0125	−0.006	−0.004	−0.001	0.001	−0.001	−0.003
0.0175	−0.004	−0.003	−0.001	0.001		−0.003
0.025	−0.002	−0.002				−0.003
0.035	−0.001	−0.001				−0.003
0.045	−0.001	−0.001				−0.003
0.055	−0.001					−0.003
0.070						−0.003
0.090						−0.002
0.125						−0.002
0.175						−0.002
0.25						−0.001
0.35						−0.001
0.45						−0.001
0.55						
0.65						

Table 4.8: Amount by which σ^{He}/σ^D changes due to modifications of some of the input parameters to the radiative corrections program. Changes smaller than 0.001 are not indicated. This table is the same as table C.3

increase. In the second set we grouped instead all sources which make the ratio decrease. In practice this means:

1. First set
   - For deuterium: the upper limit on F_2^D, the lower limit on R, the coherent deuterium form factor given in equation C.11.
   - For helium: the upper limit on F_2^D, the lower limit on R, the coherent helium form factor given in equation C.15.
2. Second set
   - For deuterium: the D suppression factor of Arenhövel [278], the lower limit on F_2^D, the upper limit on R.
   - For helium: the helium suppression factor based on a Fermi gas model [281], the (x, Q^2)-dependent fit to the cross section ratio described in appendix C, eq. C.4, the lower limit on F_2^D, the upper limit on R, the coherent helium form factor given in equation C.14.

All parameters not mentioned were left as in the standard calculation.

Two radiative correction tables were thus produced. The cross section ratios obtained by using these two tables (after the appropriate iteration) define the range in which the ratio may vary as a consequence of the uncertainty on the radiative corrections. The amount by which the upper and lower limit of the ratio differ from the standard results is shown in table 4.9. The corresponding changes in the logarithmic slopes $b = d(\sigma^{He}/\sigma^D)/d(\ln Q^2)$ are given in table 4.10. The errors obtained for the ratio are close to the linear sum of the individual contributions, as a comparison with table 4.8 demonstrates.

x	$\Delta(\sigma^{He}/\sigma^{D})$	
0.0035	−0.022	+0.008
0.0055	−0.018	+0.006
0.0085	−0.013	+0.004
0.0125	−0.010	+0.002
0.0175	−0.008	+0.001
0.025	−0.007	+0.001
0.035	−0.005	
0.045	−0.005	
0.055	−0.004	
0.070	−0.004	
0.090	−0.003	
0.125	−0.003	
0.175	−0.002	
0.25	−0.001	
0.35	−0.001	
0.45	−0.001	
0.55		
0.65		

Table 4.9: The errors on the cross section ratio due to the uncertainty on the radiative corrections. Values smaller than 0.001 are not indicated

x	Δb	
0.0035	−0.019	+0.011
0.0055	−0.017	+0.008
0.0085	−0.019	+0.008
0.0125	−0.012	+0.004
0.0175	−0.008	+0.003
0.025	−0.005	+0.001
0.035	−0.003	+0.001
0.045	−0.001	
0.055		
0.070	+0.001	
0.090	+0.001	
0.125	+0.001	
0.175	+0.001	
0.25	+0.001	
0.35	+0.001	
0.45	+0.001	
0.55	+0.001	
0.65		

Table 4.10: The errors on the logarithmic slopes $b = d(\sigma^{He}/\sigma^{D})/d(\ln Q^2)$ due to the uncertainty on the radiative corrections. Values smaller than 0.001 are not indicated

4.6 Apparatus Studies

4.6.1 Acceptance

Geometrical acceptance effects automatically should cancel upon use of formula 2.5 (page 103) which exploits the complementary targets set-up. Residual effects may be target material dependent. Assume for example that the angular distributions of the scattered muons were significantly different in helium and deuterium, so as to illuminate entirely different regions of the spectrometer. The apparatus efficiency might be different in the two regions and acceptance corrections would then no longer cancel completely when taking the cross section ratio.

Such effects are small; this can be seen in several ways.

- The agreement of the T1 and T2 results, in the region of overlap, represents by itself an important verification of the acceptance effects cancellation: the two triggers illuminate in fact regions of the apparatus where acceptance is very different; if residual effects were left, they might be expected to be of different magnitude in the two cases.

- In section 4.4, formula 2.5 was applied directly to the x distribution in order to obtain σ^{He}/σ^{D} as a function of x. One can instead apply the same formula to each (x, Q^2) bin, thus obtaining the results plotted in fig. 4.18-4.20. In this case acceptance effects cancel in each (x, Q^2) bin separately. These results can then be averaged[3] over Q^2 to recover the ratio as a function of x. The differences between the cross section ratio thereby obtained and that of table 4.6 may be taken as an indication of residual acceptance effects. The second column of table 4.11 shows the differences found. The differences are small except in the last few x bins, where statistical fluctuations dominate. The latter are due to the fact that in this region there are (x, Q^2) bins in which not all four targets have events. In this case the ratio cannot be derived and the corresponding events are effectively lost. Note that the averaging procedure assumes that the errors for the (squared) ratios are distributed along a gaussian.

- As a check of the validity of formula 2.5, the cross section ratio can be computed by considering the upstream and downstream target pairs separately. The complementary target set-up cannot then be exploited here and formula 2.5 is not applicable. With reference to formulae 2.1-2.4, page 102, the cross section ratio for the upstream targets is obtained as:

$$\frac{\sigma_{He}}{\sigma_D} = \frac{N_3}{N_1}\frac{\rho_D}{\rho_{He}}\frac{A_D}{A_{He}}\frac{M_{He}}{M_D}\frac{\phi_1}{\phi_3}. \tag{4.22}$$

The flux ratio $\phi_1/\phi_3 = \phi_{pos\#1}/\phi_{pos\#2}$ can be determined by means of T10. Similarly, for the downstream targets we have:

$$\frac{\sigma_{He}}{\sigma_D} = \frac{N_2}{N_4}\frac{\rho_D}{\rho_{He}}\frac{A_D}{A_{He}}\frac{M_{He}}{M_D}\frac{\phi_4}{\phi_2}, \tag{4.23}$$

with $\phi_4/\phi_2 = \phi_{pos\#2}/\phi_{pos\#1}$.

[3] We performed a weighted geometrical average à la Bodek [328] of the ratios squared.

x	average over Q^2	norm. with T10
0.0035	−0.009	0.003
0.0055	0.003	−0.001
0.0085	0.004	−0.003
0.0125	0.005	−0.001
0.0175	0.003	−0.003
0.025	0.006	−0.002
0.035	0.007	−0.001
0.045	0.007	−0.002
0.055	0.003	−0.008
0.070	0.002	−0.002
0.090	0.000	−0.001
0.125	−0.002	−0.001
0.175	−0.003	0.000
0.25	−0.009	0.001
0.35	−0.010	0.000
0.45	−0.018	−0.001
0.55	−0.135	0.002
0.65	−0.136	0.000

Table 4.11: Amount by which σ^{He}/σ^D changes due to modifications in the procedure used to evaluate it (see text)

The results obtained for the upstream and downstream targets are then averaged. The results differ from those of section 4.4 by a few tenth of a per cent typically, as table 4.11 (third column) demonstrates.

- Relations 2.1-2.4 can be used to determine the flux ratio squared:

$$\left(\frac{\phi_{pos\#1}}{\phi_{pos\#2}}\right)^2 = \frac{N_1 N_2}{N_3 N_4}\frac{\epsilon_1\epsilon_2}{\epsilon_3\epsilon_4} \tag{4.24}$$

which is a function of the acceptances only. Note however that the combination $\epsilon_1\epsilon_2/(\epsilon_3\epsilon_4)$ appearing in 4.24 is not the same as $\epsilon_2\epsilon_3/(\epsilon_1\epsilon_4)$ which is assumed to equal unity in 2.5. Yet it is important to verify that the quantity 4.24 is constant and does not depend on any kinematic variable. Figures 4.26 and 4.27 present such a ratio as a function of x and Q^2, respectively.

4.6.2 Dependence of the Results on Variables Other than x and Q^2

The cross sections ratio σ^{He}/σ^D is normally presented as a function of x and Q^2. It is interesting to evaluate it as a function of other physics and apparatus variables, as anomalous correlations of the ratio with some of them might indicate problems in the apparatus or in the analysis.

The following quantities were considered:

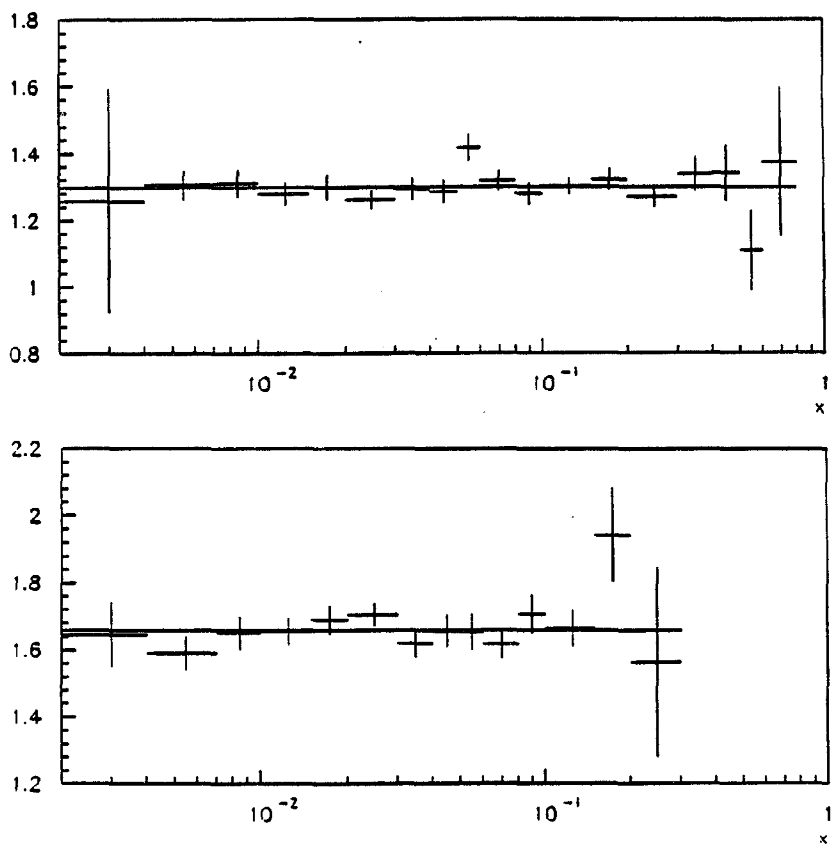

Figure 4.26: T1 (top) and T2 (bottom) flux ratio squared as a function of x. The horizontal line is the result of a fit to the points

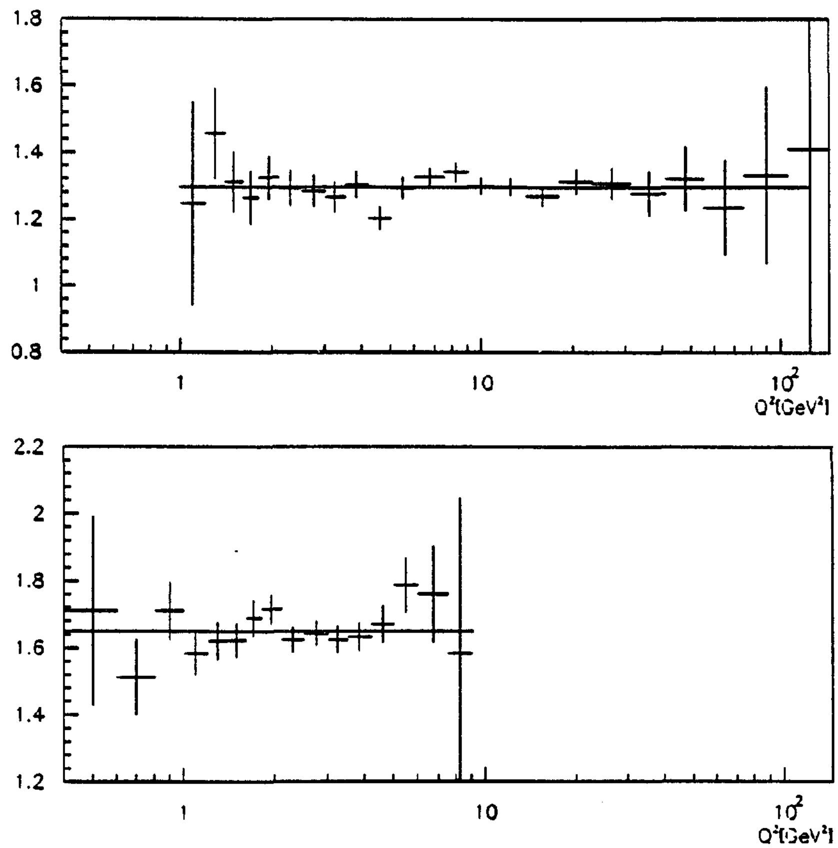

Figure 4.27: T1 (top) and T2 (bottom) flux ratio squared as a function of Q^2. The horizontal line is the result of a fit to the points

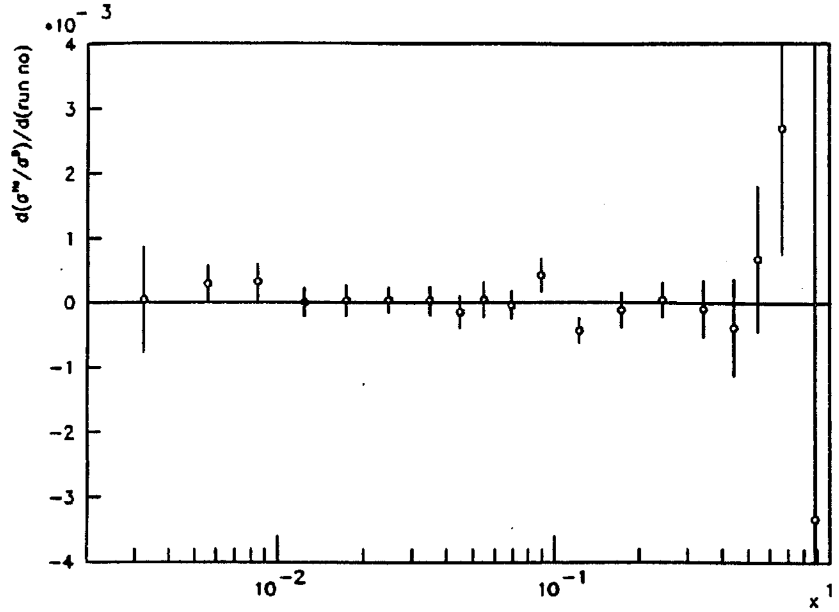

Figure 4.28: The slopes $d(\sigma^{He}/\sigma^{D})/d(run\ no.)$ as a function of x for the merged T1 and T2 data

1. physics variables: Q^2, y, E', W, ϑ and the azimuthal angle ϕ around the incoming beam direction;
2. beam variables: E, y and z beam slopes, BMS time and χ^2 of the beam track fit;
3. scattered muon variables: χ^2 probability of the track fit, χ^2 probability of the y and z W45-W67 links and H3V or H4′ time;
4. vertex variables: vertex fit probability, error on x_{vertex} and radial distance of the vertex from the beam axis;
5. run number.

The ratio σ^{He}/σ^{D} was studied as a function of all the above variables both using the complementary target method and treating the upstream and downstream targets separately, by means of formulae 4.22 and 4.23. Problems which affect the upstream or downstream targets only should show up more distinctly in the latter way.

It is particularly important to verify that the cross section ratio is constant with respect to quantities uncorrelated with x and Q^2, like the azimuthal angle ϕ, run number (i.e. time), vertex fit χ^2 probability, beam and muon track fit χ^2 etc. No unexpected correlation with these or other variables is detectable in the data. Figures 4.28 and 4.29 show some of the relevant plots.

4.6.3 Dependence of the Results on the Detectors Used for the Scattered Muon Reconstruction

The scattered muon track may be reconstructed using different combinations of detectors, depending on the trigger and on the kinematics of the event. The results obtained by selecting

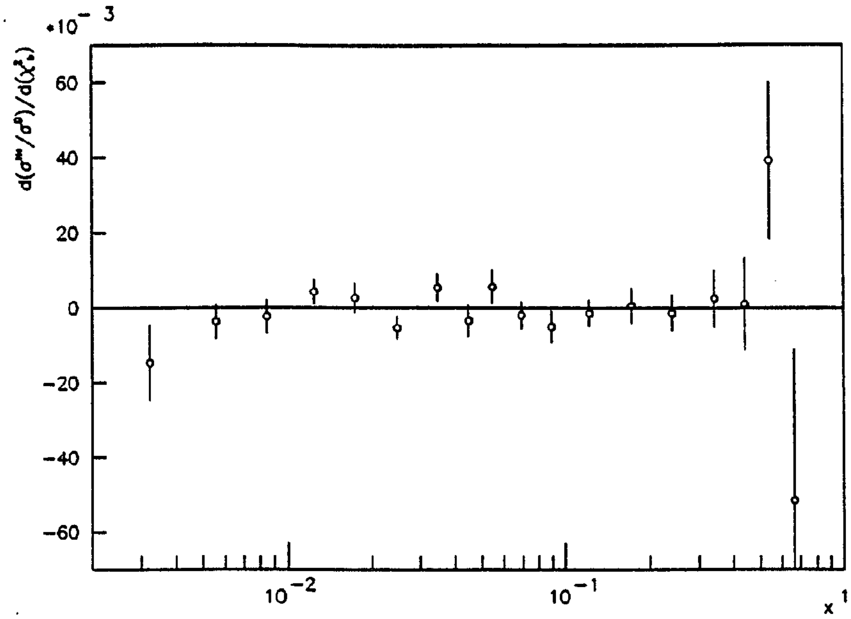

Figure 4.29: The slopes $d(\sigma^{He}/\sigma^{D})/d(\chi^2\, beam\, fit)$ as a function of x for the merged T1 and T2 data

events reconstructed with specific detector sets can be used to look for systematic problems in the data.

We briefly go through the event classes considered.

- W45/P45. We recall from section 3.1.2 that tracks reconstructed in the W45/P45 chamber system may belong to three classes: W45 only, W45+P45, P45+W45. The ratio was computed excluding in turn the events in one of these classes. Note that in trigger 1 (for the events surviving the cuts listed at the beginning of this chapter)

  1. W45 only events are 9% of the total upstream and 6% downstream;
  2. W45+P45 events are 65% of the total upstream and 72% downstream;
  3. P45+W45 events are 26% of the total upstream and 22% downstream.

  No systematic effects can be seen when any one of the three sets of events is excluded.

  Unlike T1 events, all T2 ones fall in the P45+W45 class.

- W12/P0E. All trigger 1 muon tracks are found in W12.

  About 3% of the upstream trigger 2 events are reconstructed using P0E; the fraction rises to 20% for the downstream events. No appreciable effect is apparent when either of the two classes is excluded.

- Magnet Reconstruction. Pattern recognition in the magnet is complicated and different reconstruction classes are present. A muon may have been reconstructed in the FSM by means of:

  1. P0D only. This hardly ever occurs in T1. In T2 P0D only events are 6% of the total upstream events and 33% of the downstream ones.

2. P0D+P123. In T1 these are 2% of the total upstream events and 57% of the downstream ones. In T2 the fractions are 70% and 66%, respectively.
3. A point in P1. In T1 these are 5% of the total upstream events and 2% of the downstream ones. In T2 the fraction for the upstream events is 1%; less than 1% of the downstream events belongs to this class.
4. A point in P2. In T1 these are 69% of the total upstream events and 32% of the downstream ones. In T2 the fractions are 19% and 1%, respectively.
5. A point in P3. In T1 these are 24% of the total upstream events and 9% of the downstream ones. In T2 the fraction for the upstream events is 4%; less than 1% of the downstream events belongs to this class.

The events belonging to each of the classes listed were in turn excluded. Some systematic effect was detected in the T1 data. Notably if the P0D+P123 or the P3 events are excluded, all points in the ratio shift by $\approx 0.5\%$.

- P0C/PV12. Tracks upstream of the FSM may be found in P0C or in the PV12 chambers or both. Here again no systematic effects are apparent in the T2 events; in T1 the largest systematic shifts are of the same order of magnitude as those observed in the magnet reconstruction (of which they are a reflection).

4.6.4 Overall Uncertainty on the Ratio Due to Residual Apparatus Effects

It is difficult to give a quantitative estimate of the consequences of a non-complete cancellation of acceptance, reconstruction efficiency or other apparatus effects.

The comparison of the standard results of table 4.6 with those given in table 4.11 suggests that these effects may be of the order of a fraction of a per cent. This is the same amount by which the results are seen to vary systematically if specific muon reconstruction classes are selected.

4.7 Systematic Errors

We are now able to discuss the total systematic errors on the results. The contributions taken into account were the following:

1. Radiative corrections. The discussion of section 4.5.4 applies here. For the systematic errors due to the uncertainty on the radiative corrections we conservatively took a symmetric contribution equal to the larger of the errors given in table 4.9; for example in the lowest x bin the error was taken to be ± 0.022

2. Residual acceptance/reconstruction effects. Based on the apparatus studies described in section 4.6 and on the conclusions drawn in section 4.6.4, we took a $\pm 0.5\%$ systematic error over the whole x range as an estimate of the uncertainty of the complementary target method used to extract the ratio.

3. Vertex smearing. The systematic errors due to the vertex smearing corrections are those indicated in table 4.3. They are very small (at most $\pm 0.3\%$) and essentially contribute to the error in the first few x bins only.

$\langle x \rangle$	$\langle Q^2 \rangle$[GeV^2]	Q^2 range [GeV^2]	$\langle y \rangle$	σ^{He}/σ^D	stat.	syst.
0.00322	0.77	0.5 – 1.2	0.65	0.930	0.026	0.022
0.00558	1.3	0.7 – 2.2	0.65	0.944	0.011	0.018
0.00849	1.8	0.9 – 3.1	0.59	0.966	0.011	0.014
0.01244	2.4	1.1 – 4.4	0.53	0.954	0.009	0.011
0.01743	3.0	1.1 – 6.2	0.47	0.982	0.009	0.009
0.02479	3.8	1.1 – 9.2	0.42	0.985	0.008	0.008
0.03482	4.7	1.1 – 12	0.37	0.990	0.009	0.007
0.04485	5.6	1.3 – 15	0.34	1.003	0.010	0.007
0.05483	6.3	1.5 – 18	0.31	1.005	0.011	0.007
0.06945	7.3	1.8 – 24	0.29	0.990	0.009	0.006
0.08950	8.7	2.4 – 25	0.26	1.021	0.010	0.006
0.12231	11	2.9 – 43	0.24	0.999	0.008	0.006
0.17275	14	4.7 – 46	0.22	1.018	0.011	0.005
0.24204	19	5.9 – 62	0.21	0.996	0.011	0.005
0.34200	24	13 – 86	0.19	0.986	0.019	0.005
0.44158	31	17 – 87	0.19	0.924	0.029	0.005
0.54039	38	21 – 90	0.19	0.950	0.051	0.005
0.66560	44	27 – 64	0.18	1.048	0.085	0.005

Table 4.12: The cross section ratio σ^{He}/σ^D obtained from the merged T1 and T2 data. The systematic errors are also shown. The 0.4% normalization uncertainty is not included

4. Muon momentum calibration. The uncertainties on the beam momentum calibration discussed in appendix A were used (section A.4). The uncertainty on the rescaling of the FSM field was taken to be $\pm 0.2\%$, as discussed in section A.5. The overall effect of these uncertainties on the ratio σ^{He}/σ^D amounts to 0.001 in the range $0.35 < x < 0.65$. It is negligible everywhere else.

5. Target densities (see section 2.9.2). Unlike the previous ones, these errors do not depend on x and contribute an overall normalization uncertainty which amounts to 0.4%.

The contributions 1.-4. were taken as uncorrelated and summed in quadrature. The results for each x bin are presented in the last column of table 4.12 and in fig. 4.30, where the inner error bars indicate the size of statistical errors and the outer error bars indicate that of statistical and systematic errors added in quadrature. The 0.4% normalization uncertainty is not included.

The effect of all the above uncertainties on the logarithmic slopes $b = d(\sigma^{He}/\sigma^D)/d(\ln Q^2)$ is always smaller than the statistical errors. The largest contribution comes from the radiative corrections and has already been shown in table 4.10.

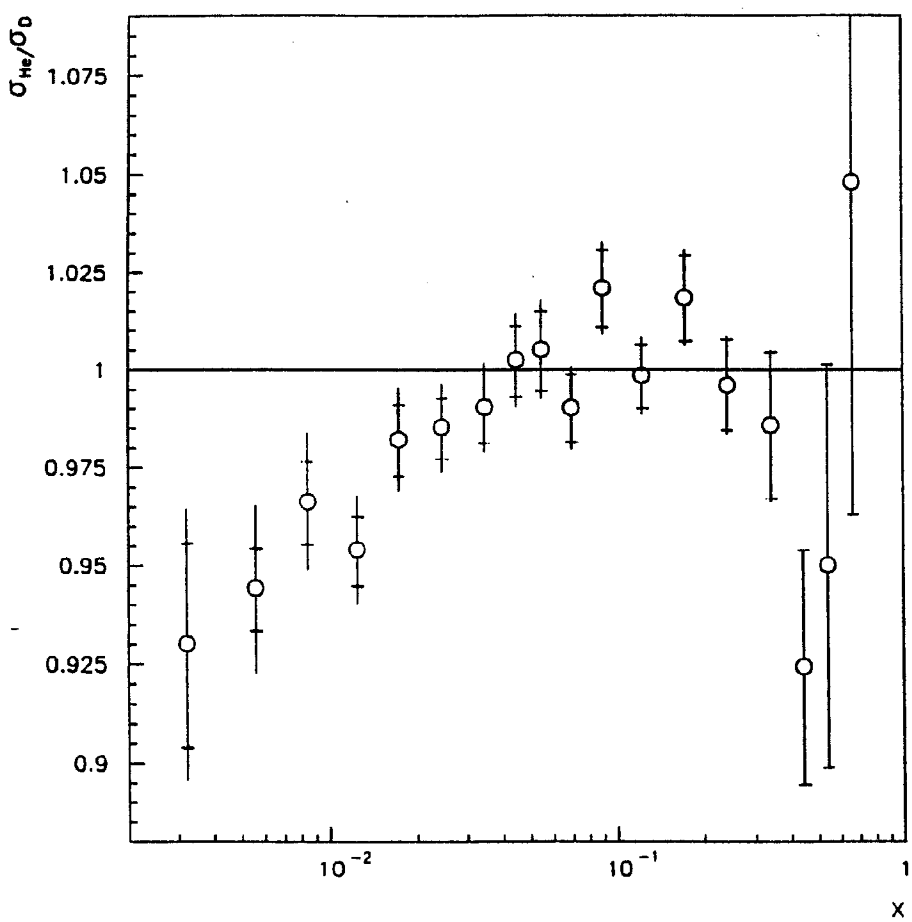

Figure 4.30: The cross section ratio σ^{He}/σ^{D} obtained from the merged T1 and T2 data. The inner error bars indicate the size of the statistical errors. The outer error bars include statistical and systematic errors added in quadrature. The 0.4% normalization uncertainty is not shown

Chapter 5

Discussion of the Results

Introduction

Having reported on the F_2^{He}/F_2^D results in the previous chapter, we now widen our discussion and present the results – also obtained by the NMC – on the carbon and calcium to deuterium structure function ratios (section 5.1). The three ratios have been used to study the A dependence of nuclear effects in structure functions at small values of x. The results of this study are presented in section 5.2. Section 5.3 then compares the NMC results on F_2^A/F_2^D with those of previous experiments.

From the structure function ratios and a parametrization of $F_2^D(x, Q^2)$ the integrals of the structure function differences $F_2^A - F_2^D$ can be computed. In the quark-parton model these integrals measure the difference between the momentum fraction carried by charged partons in a bound and in a free nucleon. We discuss the extraction of these integrals from the data and comment on the results in section 5.4.

Finally we compare our results with the available theoretical models in section 5.5 and we draw some general conclusions in section 5.6.

5.1 The Ratios F_2^{He}/F_2^D, F_2^C/F_2^D and F_2^{Ca}/F_2^D

The NMC published the F_2^{He}/F_2^D ratio presented in chapter 4 together with the ratios F_2^A/F_2^D for the isoscalar nuclei C and Ca [329]. Helium, carbon and calcium have comparable densities and binding energies E_B per nucleon, while their mass numbers differ considerably (see table 5.1).

The experimental set-up used for the C/D and Ca/D measurement was similar to that used

	D	He	C	Ca
M_A [AMU]	2.0140	4.0026	12.0110	39.9626
$<r^2>^{1/2}$ [fm]	2.10	1.68	2.47	3.48
$A/Volume$ [fm^{-3}]	0.05	0.21	0.19	0.23
E_B [MeV]	2.3	28.3	92.2	342.1
E_B/A [MeV]	1.2	7.1	7.7	8.6

Table 5.1: Atomic weight, radius, density and binding energy of the deuterium, helium, carbon and calcium nuclei

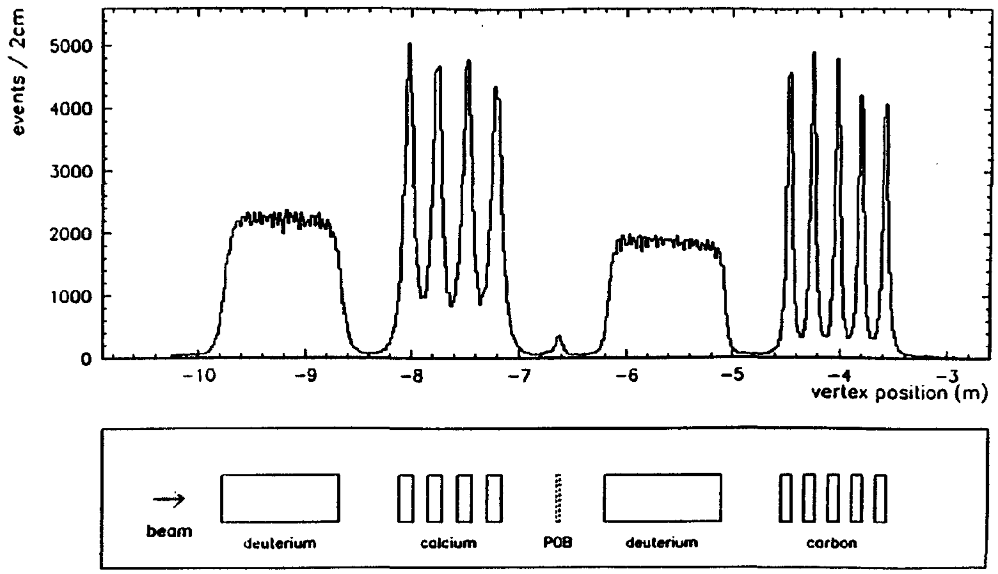

Figure 5.1: Distribution of reconstructed vertices along the beam direction in the measurement of Ca/D and C/D. The cylindrical liquid deuterium targets and the solid targets, which consisted of four calcium and five carbon slices, are clearly resolved. The small peak in the centre results from events scattered off the proportional chamber P0B

for the F_2^{He}/F_2^D one. Two 1.1 m long liquid deuterium targets were interspersed with sets of C and Ca targets (fig. 5.1), which consisted of several equally spaced slices distributed over a 1.1 m distance. The target thicknesses were in this case 18.7 g/cm^2 (C), 20.3 g/cm^2 (Ca) and 17.6 g/cm^2 (D). The calcium targets were kept in an argon atmosphere to avoid oxidation. The C and Ca targets were of natural isotopic composition.

The kinematic cuts and the radiative correction procedure were also very similar to those presented in the previous chapter for F_2^{He}/F_2^D. So was the determination of the systematic errors.

Table 5.2 and figure 5.2 show the results for the three ratios. In each x bin the ratios were extrapolated from the bin average to the bin center by using fits to the data with the function C.2 (see appendix C) so as to make the three results directly comparable. The corrections were always very small and for the helium to deuterium ratio amounted to 0.1% at most.

The three structure function ratios show a characteristic x dependence. There is a drop below unity at small x, which increases with decreasing x. The size of the depletion is about 7%, 12% and 22% in the lowest x bin for He/D, C/D and Ca/D, respectively. The results thus show a clear difference in shadowing between nuclei of similar binding energies and nuclear densities but of considerably different mass numbers.

The data also show an enhancement of the ratios with respect to unity at intermediate x, of about 2% for C/D and Ca/D, and possibly less for He/D. The fits to the x dependence of

x	$\langle Q^2\rangle$[GeV^2]	Q^2 range [GeV^2]	$\langle y\rangle$	F_2^{He}/F_2^D	stat.	syst.
0.0035	0.77	0.5 - 1.2	0.65	0.931	0.026	0.022
0.0055	1.3	0.7 - 2.2	0.65	0.944	0.011	0.018
0.0085	1.8	0.9 - 3.1	0.59	0.986	0.011	0.014
0.0125	2.4	1.1 - 4.4	0.53	0.954	0.009	0.011
0.0175	3.0	1.1 - 6.2	0.47	0.982	0.009	0.009
0.025	3.8	1.1 - 9.2	0.42	0.986	0.008	0.008
0.035	4.7	1.1 - 12	0.37	0.991	0.009	0.007
0.045	5.6	1.3 - 15	0.34	1.003	0.010	0.007
0.055	6.3	1.5 - 18	0.31	1.006	0.011	0.007
0.070	7.3	1.6 - 24	0.29	0.990	0.009	0.006
0.090	8.7	2.4 - 25	0.26	1.021	0.010	0.006
0.125	11	2.9 - 43	0.24	0.998	0.008	0.006
0.175	14	4.7 - 46	0.22	1.018	0.011	0.005
0.25	19	5.9 - 62	0.21	0.995	0.011	0.005
0.35	24	13 - 66	0.19	0.985	0.019	0.005
0.45	31	17 - 87	0.19	0.923	0.029	0.005
0.55	38	21 - 90	0.19	0.949	0.051	0.005
0.65	44	27 - 64	0.18	1.049	0.065	0.005

x	$\langle Q^2\rangle$[GeV^2]	Q^2 range [GeV^2]	$\langle y\rangle$	F_2^C/F_2^D	stat.	syst.
0.0035	0.74	0.5 - 0.9	0.62	0.879	0.018	0.016
0.0055	1.2	0.7 - 1.9	0.57	0.906	0.011	0.010
0.0085	1.7	0.9 - 2.7	0.54	0.909	0.011	0.008
0.0125	2.3	0.9 - 4.3	0.51	0.915	0.009	0.007
0.0175	3.0	1.1 - 6.2	0.47	0.944	0.010	0.006
0.025	3.8	1.1 - 9.2	0.42	0.949	0.008	0.006
0.035	4.9	1.3 - 12	0.38	0.976	0.009	0.005
0.045	6.0	1.7 - 15	0.37	0.989	0.010	0.005
0.055	7.2	2.0 - 16	0.36	0.996	0.012	0.005
0.070	8.8	2.4 - 24	0.34	1.018	0.010	0.005
0.090	11	3.3 - 26	0.33	1.031	0.012	0.005
0.125	14	4.0 - 35	0.31	1.019	0.009	0.005
0.175	17	5.9 - 46	0.27	1.017	0.012	0.005
0.25	21	8.5 - 60	0.23	1.001	0.012	0.005
0.35	26	13 - 80	0.21	0.968	0.018	0.005
0.45	31	17 - 84	0.19	1.011	0.030	0.006
0.55	37	21 - 88	0.19	0.980	0.046	0.006
0.65	42	27 - 86	0.17	0.843	0.062	0.007

x	$\langle Q^2\rangle$[GeV^2]	Q^2 range [GeV^2]	$\langle y\rangle$	F_2^{Ca}/F_2^D	stat.	syst.
0.0035	0.60	0.5 - 0.8	0.47	0.760	0.021	0.019
0.0055	0.94	0.7 - 1.6	0.46	0.782	0.009	0.013
0.0085	1.4	0.7 - 2.6	0.43	0.831	0.009	0.010
0.0125	1.9	0.8 - 3.7	0.41	0.859	0.007	0.006
0.0175	2.5	0.9 - 5.2	0.40	0.899	0.008	0.007
0.025	3.4	0.9 - 9.2	0.38	0.938	0.006	0.006
0.035	4.7	1.3 - 12	0.36	0.949	0.007	0.005
0.045	5.7	1.6 - 15	0.35	0.978	0.009	0.005
0.055	6.8	2.0 - 18	0.34	0.966	0.010	0.005
0.070	8.1	2.4 - 24	0.32	0.988	0.008	0.005
0.090	9.7	3.3 - 25	0.30	1.020	0.010	0.005
0.125	12	4.0 - 34	0.26	1.022	0.008	0.005
0.175	14	5.9 - 45	0.23	1.034	0.010	0.005
0.25	19	8.4 - 61	0.21	0.983	0.010	0.005
0.35	24	13 - 79	0.19	0.984	0.017	0.006
0.45	30	17 - 83	0.19	0.929	0.027	0.006
0.55	35	21 - 85	0.18	0.869	0.042	0.006
0.65	41	27 - 85	0.17	0.917	0.067	0.007

Table 5.2: The structure function ratios F_2^A/F_2^D averaged over Q^2. The normalization uncertainty of 0.4% is not included in the systematic errors

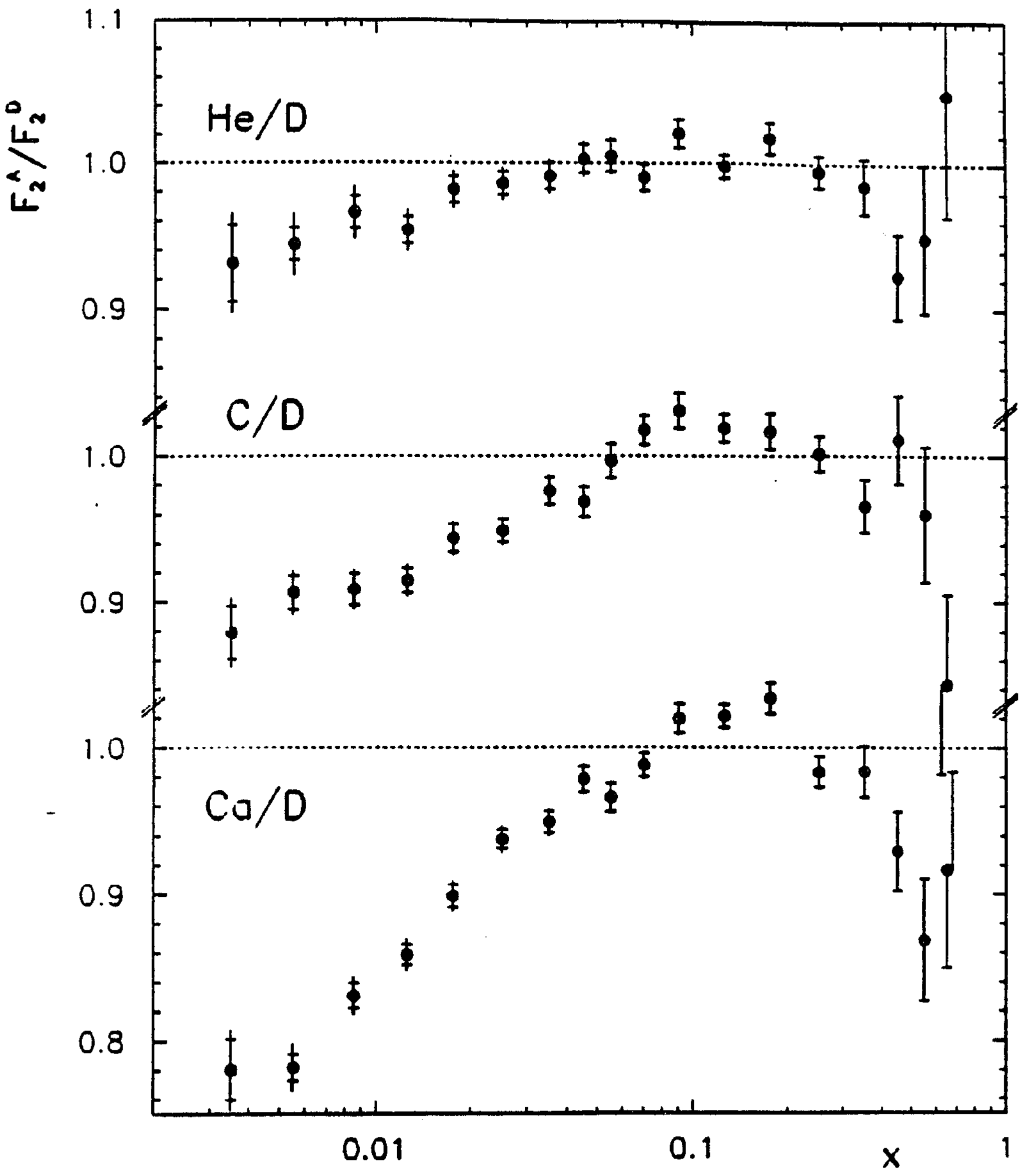

Figure 5.2: Structure function ratios F_2^A/F_2^D as functions of x, averaged over Q^2. The inner error bars indicate statistical errors only, the outer ones include the systematic errors added in quadrature. The 0.4% normalization uncertainty is not included

He/D	C/D	Ca/D
1.010 ± 0.004	1.025 ± 0.005	1.019 ± 0.005

Table 5.3: Maximum values of the ratios in the enhancement region obtained by fits of the type C.2 to the data. Only statistical errors were used in the fits

He/D	C/D	Ca/D
0.048 ± 0.010	0.058 ± 0.005	0.059 ± 0.003

Table 5.4: x values of the points where the ratios are equal to unity at small x obtained by fits of the type C.2 to the data. Only statistical errors were used in the fits

the ratios carried out with equation C.2 yield for the maxima in the enhancement region the values reported in table 5.3. Only statistical errors were used in the fits.

The same functions were used to estimate the x values of the points where shadowing turns into an enhancement (i.e. where the ratios are equal to unity at low x). Table 5.4 shows the results, which do not indicate a strong A dependence.

In the measured Q^2 range there is little indication of a Q^2 dependence of the ratios. Figures 5.3-5.5 show the three structure function ratios as a function of Q^2 for fixed values of x. The He/D points are the same as those plotted in figures 4.18-4.20.

The logarithmic slopes b obtained from fits of the type $F_2^A/F_2^D = a + b \ln Q^2$ in each bin separately are shown in fig. 5.6 for x up to 0.45. Again the He/D points are the same as those shown in fig. 4.21. For He/D and C/D no significant Q^2 dependence is observed. In the case of Ca/D negative slopes are found over a large fraction of the x range. Only in a few bins in the enhancement region, however, are they different from zero in a statistically significant way.

5.2 A Dependence

Figures 5.7-5.9 show the F_2^{He}/F_2^D, F_2^C/F_2^D and F_2^{Ca}/F_2^D ratios of fig. 5.2 plotted as a function of A in each x bin. The continuous lines are the results of fits of the form $F_2^A/F_2^D = \alpha + \beta \ln A$ in each bin separately. Only the statistical errors were used in the fits.

The figures show that at small x the size of shadowing in each x bin is consistent with a linear behavior in $\ln A$. For $0.07 < x < 0.1$, inside the enhancement region, the ratios are A independent; between $x = 0.1$ and $x = 0.2$, also in the enhancement region, the ratios increase slightly with increasing A, but the effect is of little statistical significance. For $x > 0.2$ the error bars become large and no conclusion can be drawn.

The results of the fits for the slopes $\beta = d(F_2^A/F_2^D)/d \ln A$ are shown as a function of x in fig. 5.10. As we have seen in chapter 1, structure function ratios are sometimes parametrized as

$$\frac{A_{eff}}{A} = \frac{F_2^A}{F_2^D} = A^{\epsilon}. \tag{5.1}$$

From this relation we see that $\beta = \epsilon F_2^A/F_2^D$. The function $\epsilon(x)$ has a shape similar to that of F_2^A/F_2^D, as relation 5.1 shows: $\epsilon(x)$ is negative in the shadowing region, where F_2^A/F_2^D is

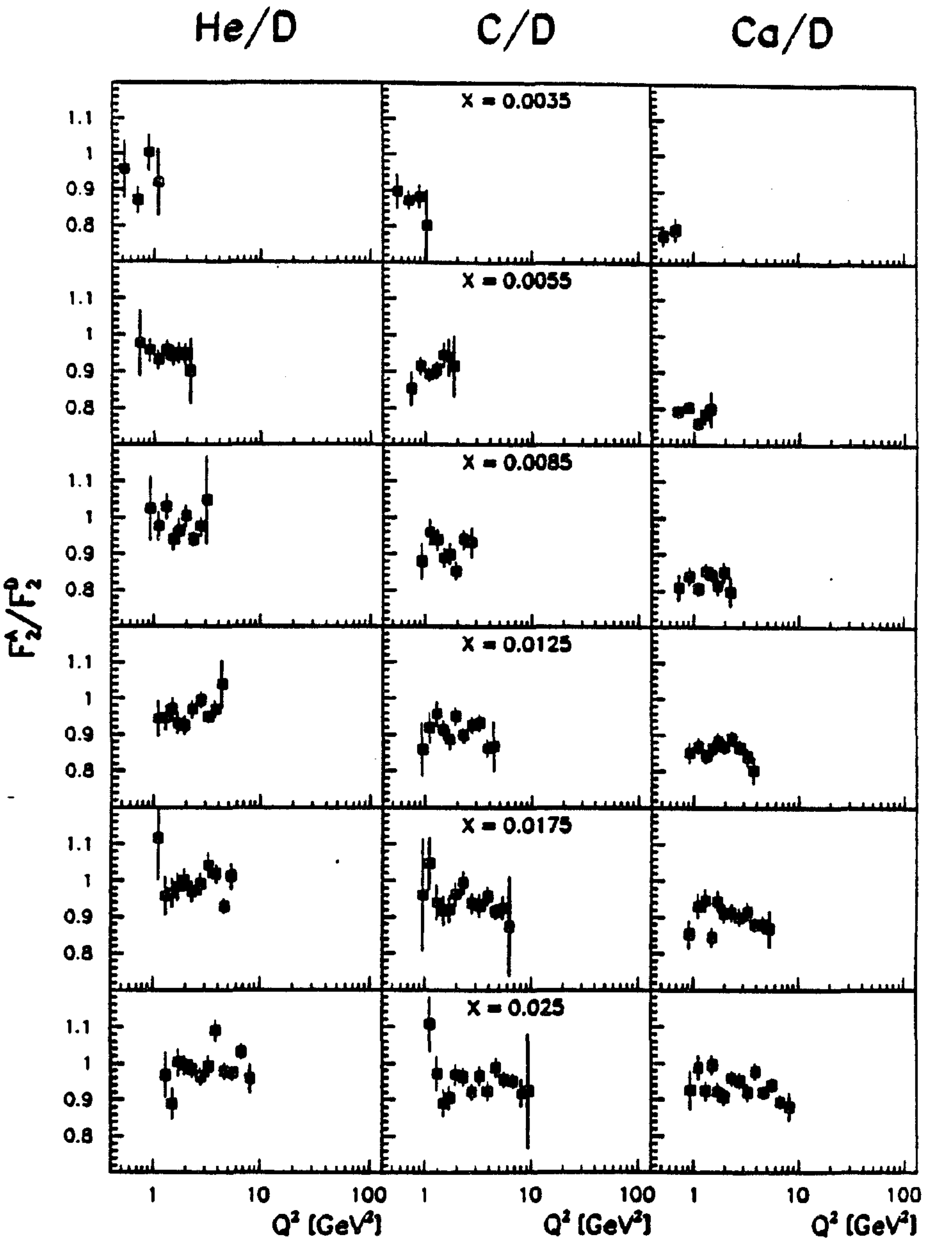

Figure 5.3: The structure function ratios as a function of Q^2 for $0.0035 < x < 0.025$. The errors shown are statistical only

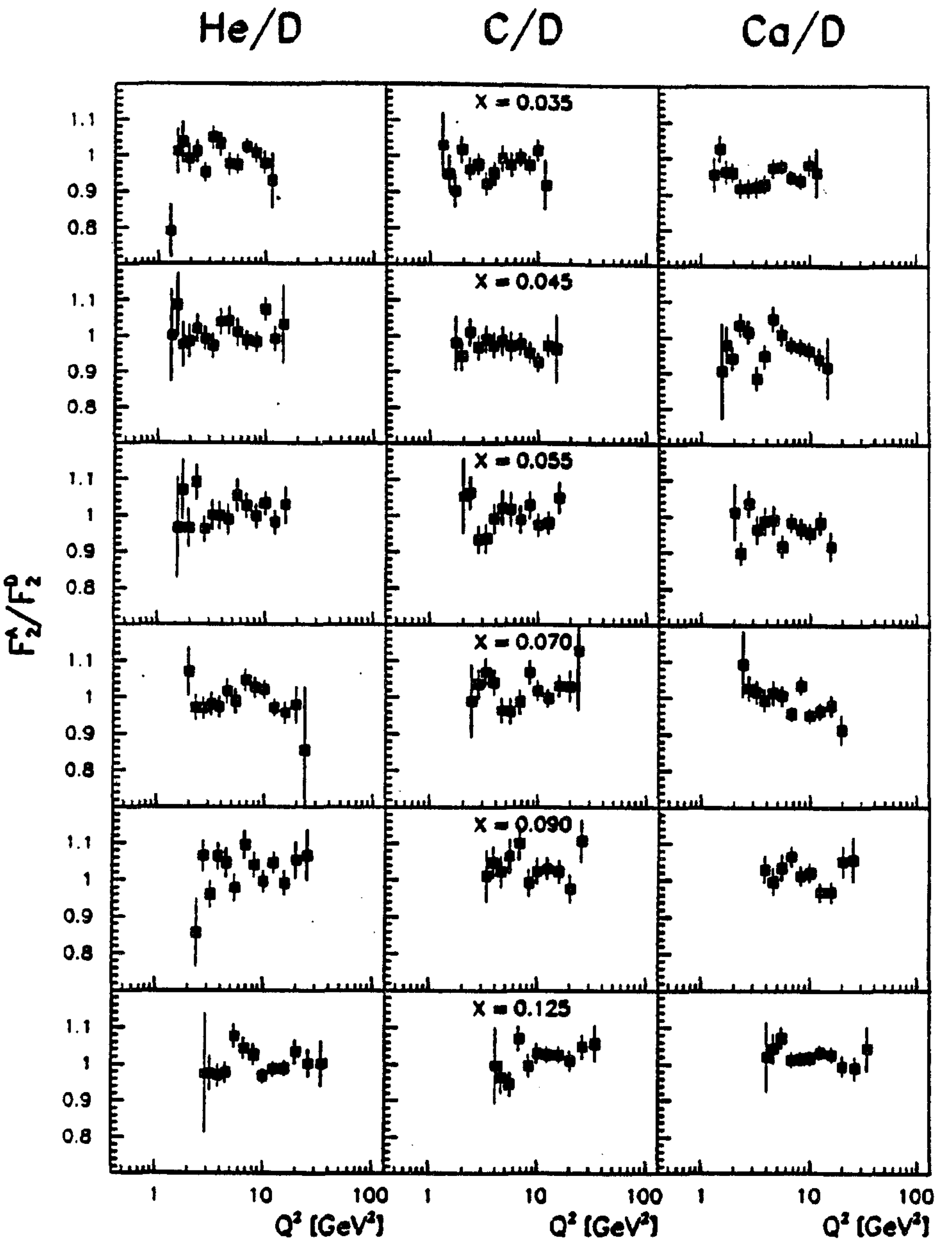

Figure 5.4: The structure function ratios as a function of Q^2 for $0.035 < x < 0.125$. The errors shown are statistical only

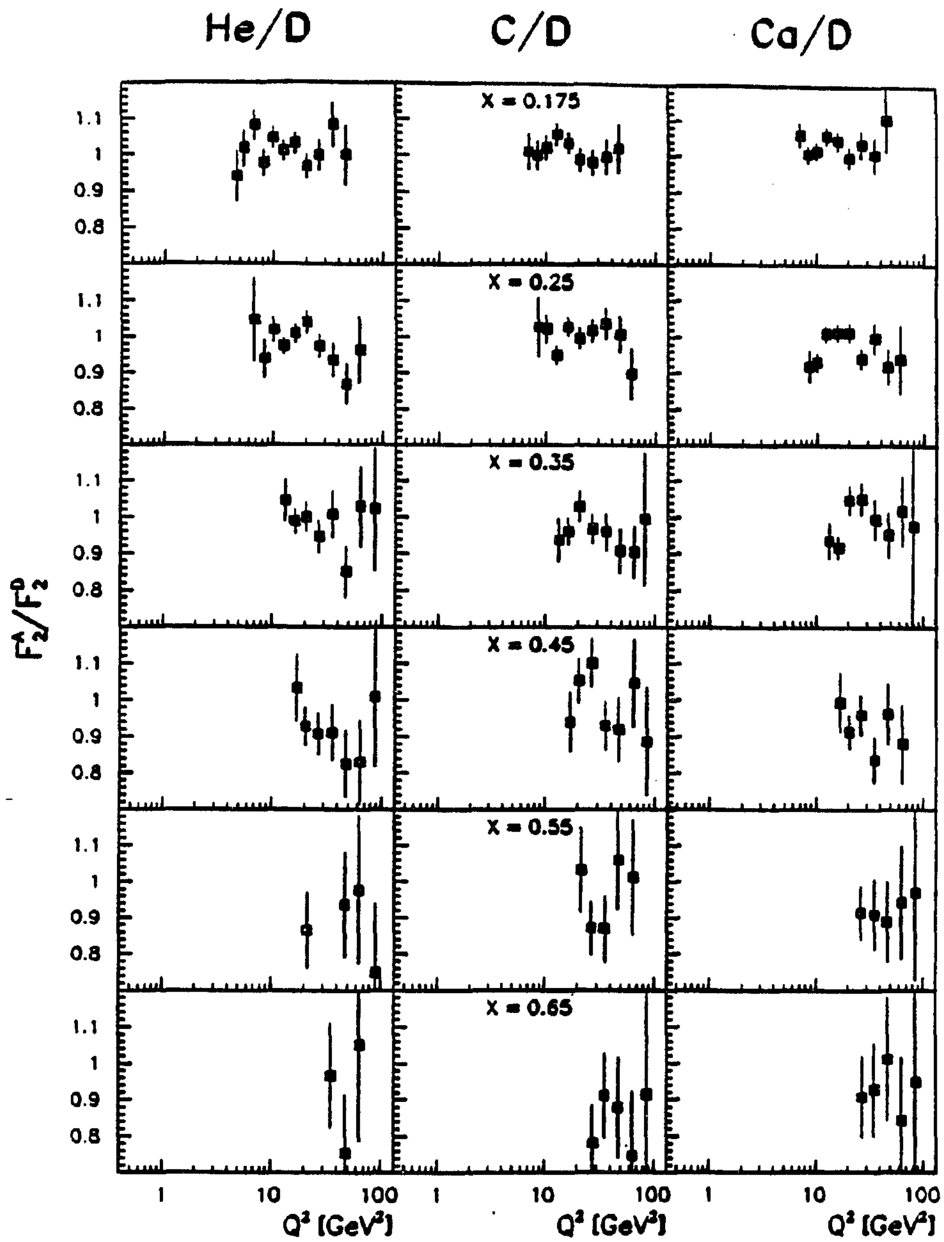

Figure 5.5: The structure function ratios as a function of Q^2 for $0.175 < x < 0.65$. The errors shown are statistical only

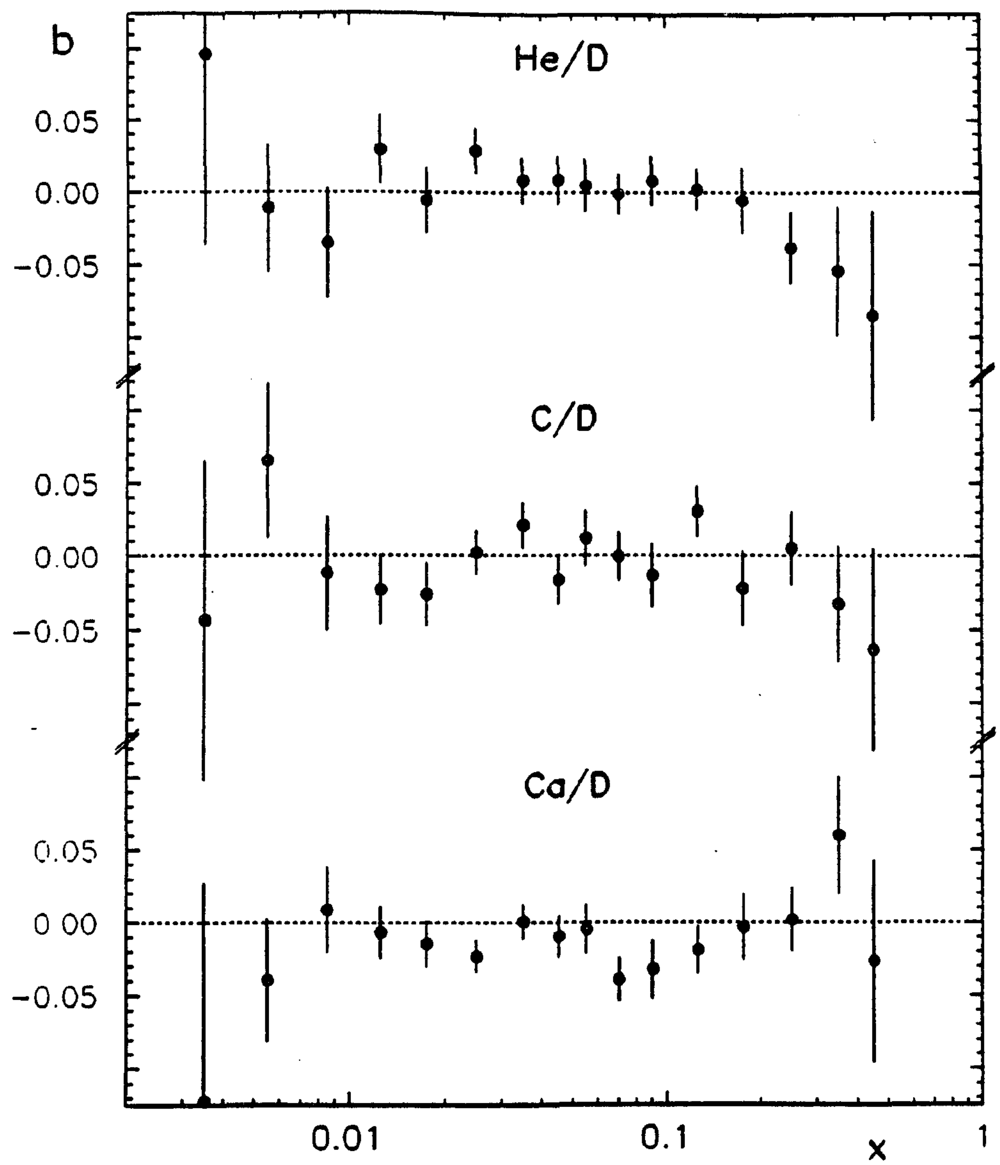

Figure 5.6: The slopes b from a linear fit in $\ln Q^2$ for each x bin separately, up to $x = 0.45$. The errors shown are statistical only

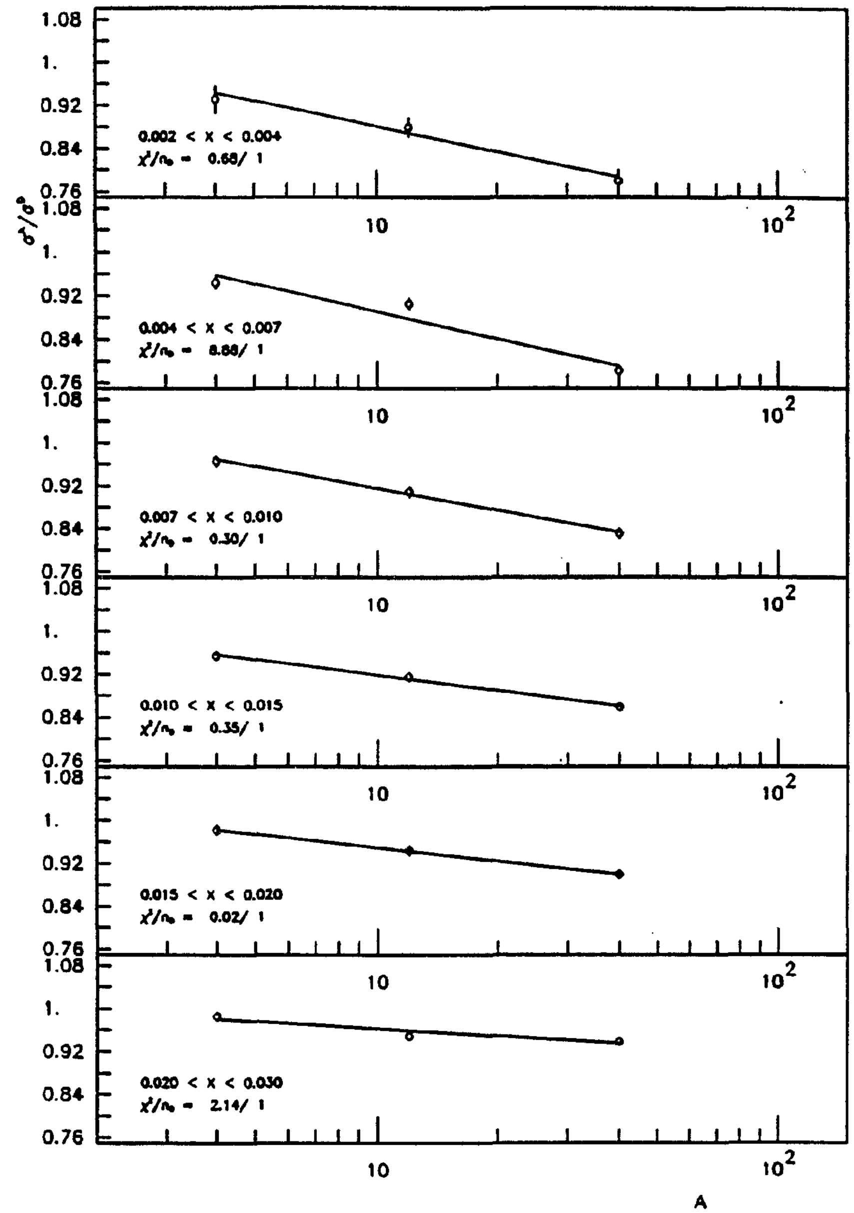

Figure 5.7: The structure function ratios as a function of A for $0.0035 < x < 0.025$. The errors shown are statistical only. The continuous line is the result of the fit described in the text

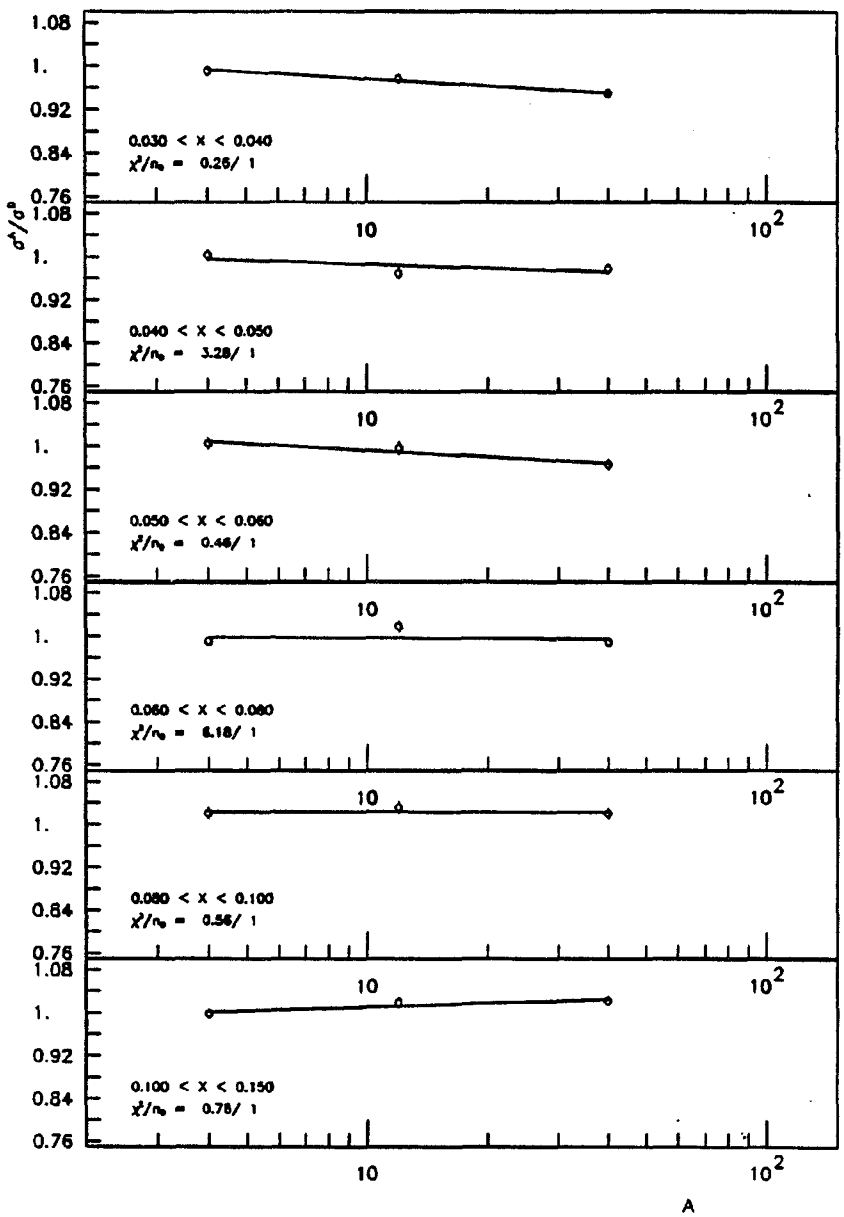

Figure 5.8: The structure function ratios as a function of A for $0.035 < x < 0.125$. The errors shown are statistical only. The continuous line is the result of the fit described in the text

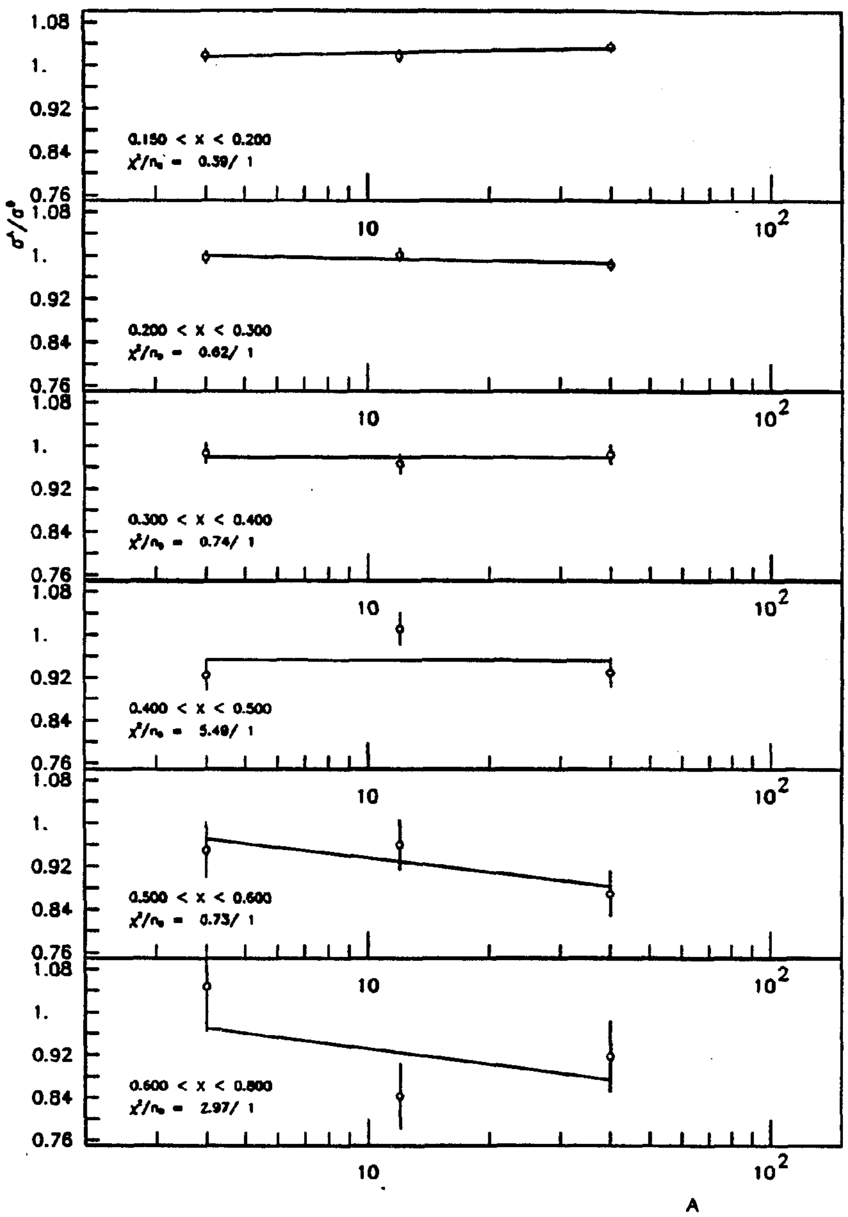

Figure 5.9: The structure function ratios as a function of A for $0.175 < x < 0.65$. The errors shown are statistical only. The continuous line is the result of the fit described in the text

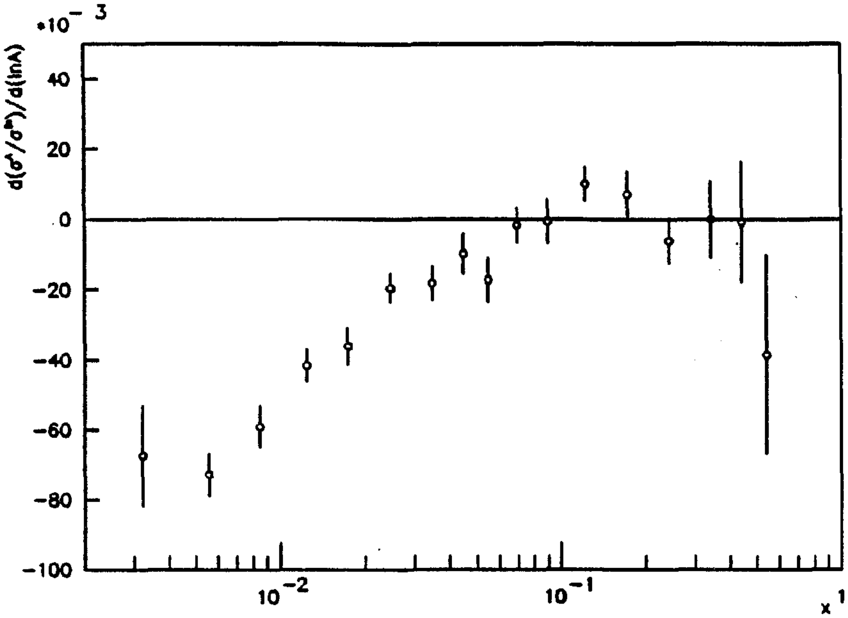

Figure 5.10: The slopes $\beta = d(\sigma^A/\sigma^D)/d(\ln A)$ as a function of x. Only statistical errors are shown

smaller than unity, becomes positive in the enhancement region and then turns negative again for $x > 0.2$. It is then not astonishing that $\epsilon F_2^A/F_2^D$ has a behavior similar *in shape* to that of F_2^A/F_2^D, as fig. 5.10 shows.

5.3 Comparison with Other Experiments

In fig. 5.11 we compare the x dependence of our data to that measured by previous measurements. For He/D only the SLAC E139 results [35] are available. The NMC C/D ratio is presented together with the EMC NA2′ [38] and EMC NA28 [40] results as well as with the BCDMS ones for F_2^N/F_2^D [36]. Finally, the Ca/D ratio is compared with the EMC NA2′ [38] and EMC NA28 [40] results.

The NMC results for He/D are the first to cover the low x region. In the same region the C/D and Ca/D ratios were previously measured by the EMC NA28 [40], but the NMC data are significantly more precise.

In the intermediate x region, where the data were so far inconclusive, an enhancement of the C/D and Ca/D ratios above unity is now clearly visible. The data suggest also some A dependence of the enhancement size.

At large x, the NMC results are consistent with the well known EMC effect shape.

In fig. 5.12 the slopes $\beta = d(\sigma^A/\sigma^D)/d(\ln A)$ obtained from the NMC data and already shown in fig. 5.10 are compared to those extracted from the SLAC E139 data [35] for the ratios of the He, Be, C, Al, Ca, Fe, Ag and Au to deuterium cross sections. The NMC and SLAC data have little overlap. Together they provide an accurate picture of the A dependence of nuclear effects in DIS.

As far as the Q^2 dependence is concerned, the NMC data show no significant effect in the shadowing region. This confirms – with increased accuracy – the observations previously made

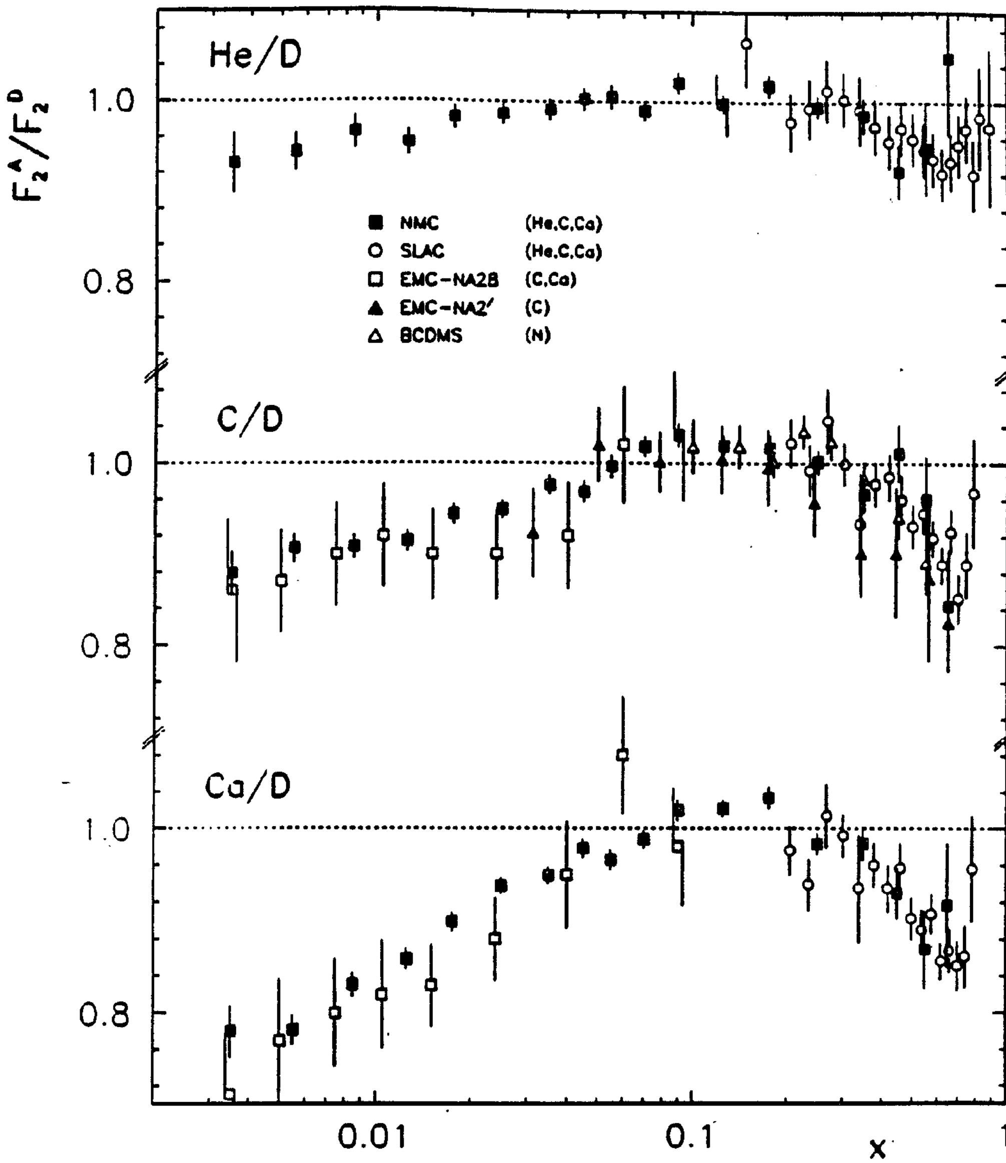

Figure 5.11: Comparison of the NMC structure function ratios with corresponding results from other experiments: SLAC-E139 [35], EMC-NA2′ [38] and EMC-NA28 [40]. Also shown are the F_2^N/F_2^D data from BCDMS [36]. The error bars show the statistical and systematic errors added in quadrature

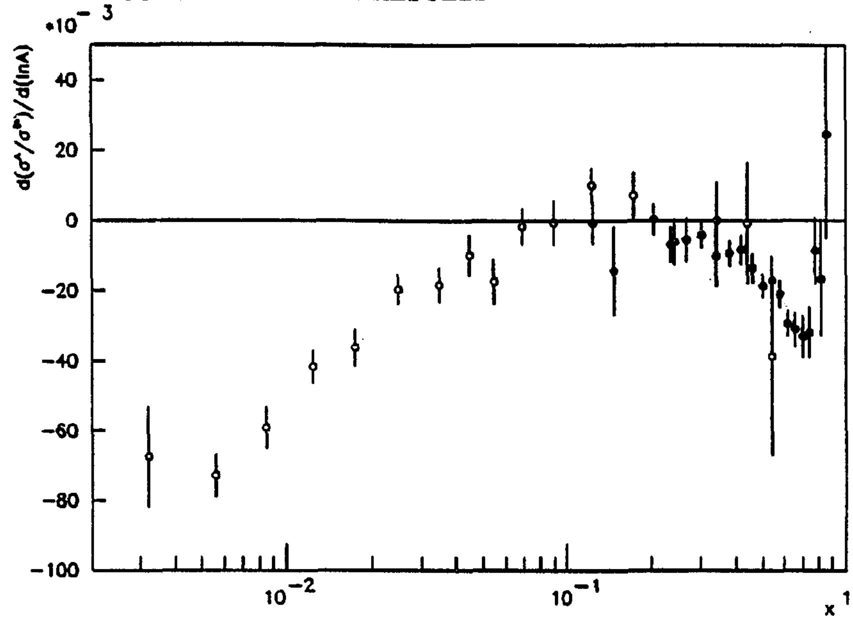

Figure 5.12: The slopes $\beta = d(\sigma^A/\sigma^D)/d(\ln A)$ as a function of x. Only statistical errors are shown

by EMC NA28 [40] and FNAL E665 [41] and also suggested by the agreement between the SLAC E61 [24], SLAC E139 [35] experiments, at small Q^2, and EMC NA2', at higher Q^2.

Also at larger values of x the He/D and the C/D ratios do not show any significant Q^2 dependence. It is however interesting to note that for $0.2 < x < 0.4$ both the NMC and the SLAC E139 [35] data on helium indicate negative Q^2 slopes. The SLAC results are plotted together with the NMC ones in fig. 5.13[1].

The Ca/D data show instead that the structure function ratio in the region $0.070 < x < 0.125$ decreases with increasing Q^2. This is marginally in agreement with the behavior observed for Fe/D by SLAC E139 (squares in the Ca/D plot). Both results are plotted in fig. 5.13. In the same figure the SLAC E139 results for the Q^2 dependence of the gold to deuterium cross section ratio are also presented.

5.4 The Integrals of the Structure Function Differences $F_2^A - F_2^D$

From the structure function ratio and the absolute structure function F_2^D, the difference $F_2^A - F_2^D$ can be evaluated as $(F_2^A/F_2^D - 1)F_2^D$ and thus the integral $\int (F_2^A - F_2^D)dx$ can be computed. In the framework of the quark-parton model this integral, evaluated over the full x range, represents the difference of the momentum fraction carried by charged partons in bound nucleons relative to that for deuterium.

The evaluation of this integral involves some subtleties. We present a detailed discussion of the subject in appendix D. Here we only recall that the quantity in which we are interested

[1]The SLAC Q^2 slopes have not been published. We extracted them from table III in the second of the two references [35]. The slopes for the SLAC Fe/D data, also shown in fig. 5.13 (squares in the Ca/D plot) and previously presented in [39], had been derived in a similar way.

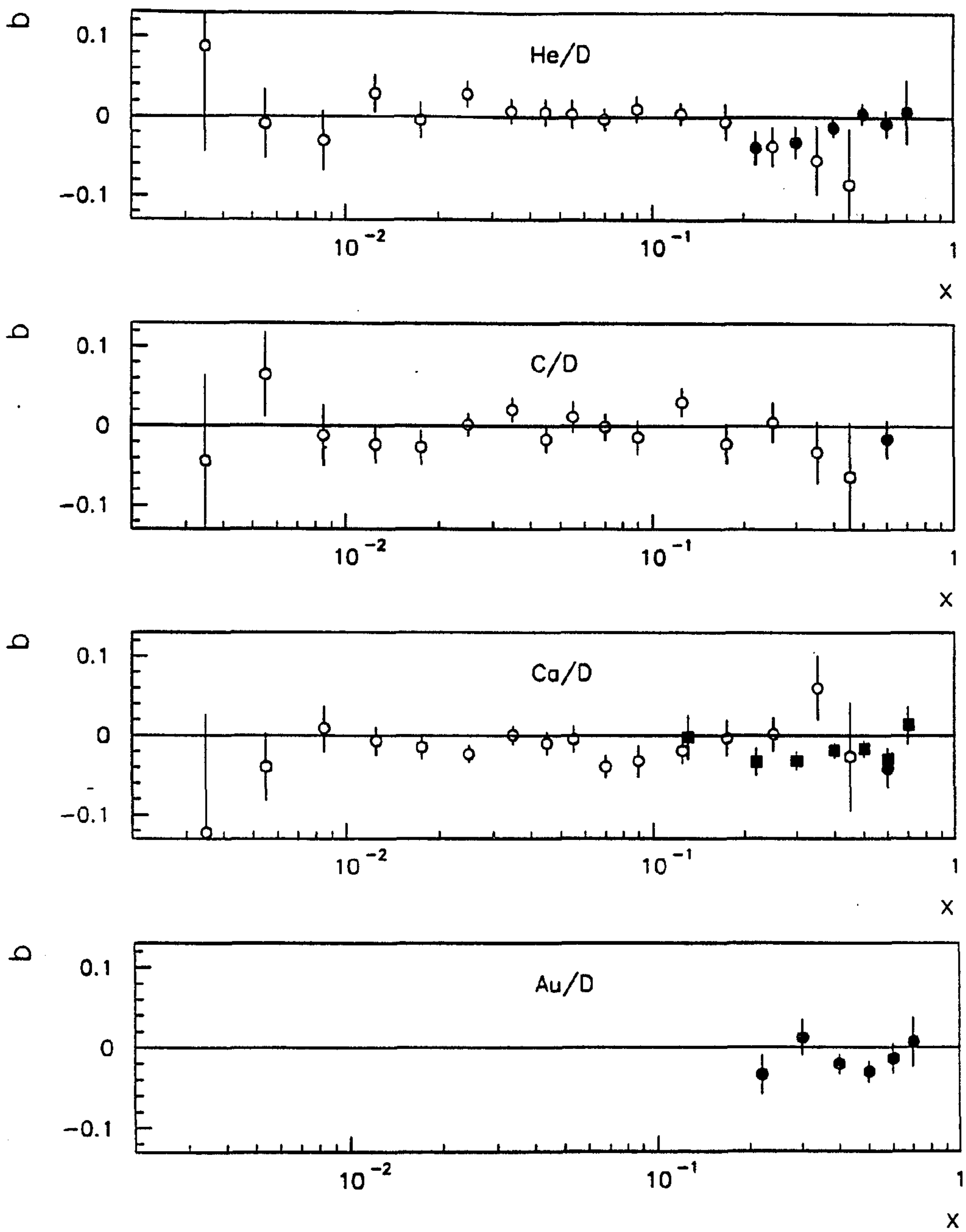

Figure 5.13: The slopes $b = d(\sigma^A/\sigma^D)/d(\ln Q^2)$ as a function of x. Only statistical errors are shown. The open circles are the NMC data of fig. 5.6. The full circles are the results of the SLAC E139 experiment [35]; in the Ca/D figure the full squares are from the Fe/D SLAC data

	x range	$\int\left(\frac{F_2^A}{F_2^D}(x)-1+f_M\right)F_2^D(x)K_2(x)dx$	stat.	syst.
He/D	0.0035 – 0.25	0.6×10^{-3}	0.3×10^{-3}	0.6×10^{-3}
	0.0035 – 0.86	-0.8×10^{-3}	0.4×10^{-3}	2.2×10^{-3}
C/D	0.0035 – 0.25	0.7×10^{-3}	0.3×10^{-3}	0.5×10^{-3}
	0.0035 – 0.78	-1.6×10^{-3}	0.7×10^{-3}	1.4×10^{-3}
Ca/D	0.0035 – 0.25	0.0×10^{-3}	0.3×10^{-3}	0.6×10^{-3}
	0.0035 – 0.78	-3.5×10^{-3}	0.6×10^{-3}	1.4×10^{-3}

Table 5.5: Integrals of the structure function differences $F_2^A - F_2^D$. For an explanation of the symbols and of the integration ranges see text

is actually

$$M_2^A - M_2^D = \int_0^2 \left(\frac{F_2^A}{F_2^D} - 1 + f_M\right) F_2^D K_2(x, Q^2)dx. \tag{5.2}$$

In this formula the constant $f_M = (AM/M_A - 2M/M_D)$ is due to the mass defect of bound nucleons (M_A, M_D are the masses of nucleus A and of deuterium, respectively). In order to account for target mass effects the integration must be carried out over the Nachtmann scaling variable ξ^A [330, 331]. The function $K_2(x, Q^2)$, close to unity, includes the jacobian of the transformation $\xi^A \rightarrow x$.

The NMC data do not cover the whole x range, from $x = 0$ to $x = 2$. In fact their statistical significance, excellent up to $x = 0.25$, rapidly decreases for larger values of x. The integration using the NMC results was therefore carried out up to $x = 0.25$ only. For larger x we used the SLAC E139 [35] data, which extend with small errors up to $x = 0.86$ for He/D and to $x = 0.78$ for C/D and Ca/D. These data do not cover the region $x < 0.1$. Furthermore, the published SLAC E139 results for $x < 0.25$ are underestimated by $\approx 1\%$ [43], as we discussed in 1.2.3. The SLAC and the NMC data are thus complementary and we used them together to extract the integrals over an extended x range, from $x = 3.5 \times 10^{-3}$ to $x = 0.8$.

The Integrals Obtained from the NMC Data Only

Table 5.5 shows the values of the integrals up to $x = 0.25$ obtained by using the NMC data only, with F_2^D evaluated at $Q^2 = 5$ GeV^2. This value is very close to the average Q^2 of both the NMC and the SLAC E139 data. The measured values of F_2^A/F_2^D were used, with no correction for the fact that the average Q^2 in each bin may be different from 5 GeV^2. This is consistent with the fact that no statistically significant Q^2 dependence is visible in this region.

If instead the measured Q^2 slopes of fig. 5.6 are used and the ratios are interpolated – or extrapolated – to 5 GeV^2, the amount by which the results vary is at most of the size of the systematic errors. The statistical errors however then become about twice as large.

The assumption that $R = \sigma_L/\sigma_T$ for target A differs from that for deuterium by 0.05 affects the results of table 5.5 by less than 0.2×10^{-3}.

	x range	$\int \left(\frac{F_2^A}{F_2^D}(x) - 1 + f_M\right) F_2^D(x)dx$	stat.	syst.
C/D	$0.02 - 0.7$	-3.7×10^{-3}	1.8×10^{-3}	2.3×10^{-3}
Cu/D	$0.02 - 0.7$	-0.2×10^{-3}	1.2×10^{-3}	2.3×10^{-3}
Sn/D	$0.02 - 0.7$	-2.5×10^{-3}	2.4×10^{-3}	3.5×10^{-3}

Table 5.6: Integrals of the structure function differences $F_2^A - F_2^D$ for the EMC NA2$'$ data [38] after the binding energy correction

	x range	$\int \left(\frac{F_2^A}{F_2^D}(x) - 1 + f_M\right) F_2^D(x)K_2(x)dx$	stat.	syst.
He/D	$0.02 - 0.7$	-0.5×10^{-3}	0.4×10^{-3}	2.1×10^{-3}
C/D	$0.02 - 0.7$	-0.8×10^{-3}	0.6×10^{-3}	1.3×10^{-3}
Ca/D	$0.02 - 0.7$	-2.4×10^{-3}	0.6×10^{-3}	1.3×10^{-3}

Table 5.7: Integrals of the structure function differences $F_2^A - F_2^D$ (NMC+SLAC data) evaluated over the restricted range $0.02 < x < 0.7$

The Integrals Obtained from the NMC and SLAC Data Together

As we mentioned, the data of the SLAC experiment E139 [35] were used to extend the integration for x larger than 0.25. No correction for the Q^2 dependence of the SLAC data was necessary: the mean value of Q^2 in each x bin is indeed ≈ 5 GeV^2, except for the He/D points at high x, where $Q^2 \approx$ 7-10 GeV^2. In these bins however the measured Q^2 slopes are compatible with zero (cf. fig. 5.13). The systematic errors of the SLAC points were taken from [332]. The results of the integrals thus found are also shown in table 5.5.

In the range covered by the NMC and SLAC results the integrals are negative and appear to decrease with the nuclear mass number A. Only the Ca/D integral however differs from zero by more than one standard deviation.

In a quark-parton model framework these results are thus consistent with a slight decrease of the momentum fraction carried by charged quarks in bound nucleons.

5.4.1 Comparison with EMC NA2$'$

The results presented above can be compared with those of the EMC NA2$'$ experiment [38]. The EMC integrals are for carbon, copper and tin; the integration range is $0.02 < x < 0.7$. The published results do not include the binding energy correction f_M. Furthermore the integrals are carried out over the variable x rather than over ξ^A.

While the effect of the change of variables is rather small, the binding energy correction $f_M \int F_2^D dx$ is substantial. We therefore computed such correction for the EMC data; the corrected results are shown in table 5.6.

We also recomputed the NMC + SLAC results for the restricted range $0.02 < x < 0.7$ in order to allow a direct comparison. The integrals are given in table 5.7.

	x range	$\int \left(\frac{F_2^A}{F_2^D}(x) - 1 + f_M\right) F_2^D(x) K_2(x) dx$	syst.
He/D	$0.0 - 0.0035$	-0.2×10^{-3}	0.1×10^{-3}
C/D	$0.0 - 0.0035$	-0.3×10^{-3}	0.1×10^{-3}
Ca/D	$0.0 - 0.0035$	-0.4×10^{-3}	0.1×10^{-3}

Table 5.8: Contributions to the integrals from the unmeasured region $0 < x < 0.0035$

	x range	$\int \left(\frac{F_2^A}{F_2^D}(x) - 1 + f_M\right) F_2^D(x) K_2(x) dx$	stat.	syst.
He/D	$0.0 - 0.86$	-1.0×10^{-3}	0.4×10^{-3}	2.2×10^{-3}
C/D	$0.0 - 0.78$	-1.9×10^{-3}	0.7×10^{-3}	1.4×10^{-3}
Ca/D	$0.0 - 0.78$	-3.9×10^{-3}	0.6×10^{-3}	1.4×10^{-3}

Table 5.9: Integrals of the structure function differences $F_2^A - F_2^D$ for NMC+SLAC with the inclusion of the small x contribution of table 5.8

A few remarks are in order. The EMC results are negative for all three nuclei but are compatible with zero within rather large errors. The NMC+SLAC results have much smaller errors, by about a factor of two. They are also slightly negative but are still compatible with zero.

The carbon results, the only ones for which a direct comparison is possible, are consistent with each other. The NMC+SLAC integral is however much closer to zero.

5.4.2 Extrapolation to the Unmeasured Region

In order to extend the integrals to $x = 0$ it is necessary to estimate the behavior of the ratio in the unmeasured region. Two limiting cases were considered:

1. The ratio is constant and equal to its value at $x = 0.0035$.

2. The ratio increases linearly from $F_2^A/F_2^D = A^{-1/3}$ at $x = 0$ to the measured value at $x = 0.0035$. The $A^{-1/3}$ behavior corresponds to the case of maximum shadowing, i.e. when only the nucleons on the surface of the nucleus participate to the interaction. The number of the nucleons on the surface is $\approx A^{2/3}$; the cross section per nucleon is thus reduced by the factor $A^{2/3}/A = A^{-1/3}$.

As an estimate of the integrals in the unmeasured region we took the mean value of cases (1.) and (2.). Table 5.8 shows such contribution for the three ratios. The error was taken to be half of the difference between the two limiting cases.

Table 5.9 shows the results for the integrals after the inclusion of the small x contribution.

At large x, from $x \approx 0.8$ up to $x = 2$, the behavior of the structure functions is poorly known. An extension of the integrals up to $x = 2$ was therefore not attempted.

5.5 Comparison with the Theoretical Models

In the following we compare the NMC results on the He, C and Ca to D structure function ratios with some of the models described in chapter 1. We restrict ourselves to the shadowing and to the enhancement regions where our data are the most precise currently available.

A similar comparison was recently carried out [333, 67] using the preliminary version of the NMC data: the conclusion was reached there that none of the existing models gives a quantitative account of the data. We argue that the situation is possibly not as bad.

5.5.1 Generalized Vector Meson Dominance Models

In the model of Schildknecht [165]-[170] off-diagonal transitions are taken into account by an effective vector meson-nucleon cross section $\sigma(M_V) \sim 1/M_V^2$, where M_V is the vector meson mass.

In figure 5.14 we compare our C and Ca to D ratios with the model predictions (continuous curves). The curve superimposed to the carbon data is for $A = 10$. The carbon prediction is for $Q^2 = 14$ GeV^2, while the calcium one is for $Q^2 = 2.8$ GeV^2; they are taken from [170].

The NMC C/D data are at the same Q^2 as the model prediction only for $x = 0.175$, at the upper edge of the enhancement region. Since the model predicts an increase of the ratio with increasing Q^2, the expected values for the C/D ratio in fig. 5.14 should be shifted downward for all $x < 0.175$. Unfortunately in [170] quantitative predictions for the Q^2 dependence are given only for $x = 0.0125$. In this bin the expected Q^2 slope $b = d(F_2^C/F_2^D)/d(\ln Q^2)$ varies from $b \simeq 0.02$ at small Q^2 $(0.75 < Q^2 < 1.36$ GeV$^2)$ to $b \simeq 0.04$ at larger Q^2 $(4.6 < Q^2 < 7.5$ GeV$^2)$, in contradiction with the measured value, $b = -0.02 \pm 0.02$. If the predicted Q^2 slope is anyway used, one finds $F_2^C/F_2^D(x = 0.0125) \simeq 0.86$, much smaller than the experimentally measured value of 0.915 ± 0.009 (stat.) ± 0.007 (syst.).

The Ca/D data have about the same Q^2 as the theoretical curve ($Q^2 = 2.8$ GeV^2) at $x = 0.0175$. Here as well, as in the C/D case, the prediction is lower than the experimentally measured value, as can be seen in fig. 5.14. The expected Q^2 slope at $x = 0.0125$ is $b \simeq 0.05$, again in disagreement with the measured value of $b \simeq -0.01 \pm 0.02$. If we use this slope to obtain the expected value for the ratio in this bin, we find $F_2^{Ca}/F_2^D(x = 0.0125) \simeq 0.83$, lower than the measured value of 0.859 ± 0.007 (stat.) ± 0.008 (syst.).

In order to make the comparison quantitative over a larger x region we deduced Q^2 slopes for this model by comparing the predictions for the EMC NA28 data [40] published in [169] and those – at a different Q^2 – given in [170]. The resulting ratios are plotted in fig. 5.15 as dashed lines. The model does not reproduce the features of the data and systematically underestimates the measurements, except at very small x for Ca.

The comparison between theory and experiment is much easier for the diagonal model of Piller *et al.* [171], since these authors published a comparison [172] between their predictions and the preliminary NMC data on carbon and calcium.

Figure 5.15 compares the model predictions and the experimental data. The agreement is reasonable, although the model tends to slightly underestimate the ratios.

The model also makes explicit predictions for the Q^2 dependence. Shadowing is expected to die out with increasing Q^2, as in all VMD models. For C/D (Ca/D) the slope $b = d(F_2^C/F_2^D)/d(\ln Q^2)$ is predicted to be $b \simeq 0.05$ (0.07) at $x = 0.01$, $b \simeq 0.03$ (0.03) at $x = 0.04$ and $b \simeq 0.02$ (0.02) at $x = 0.06$. The predictions are consistent with the data for carbon. They are somewhat higher than the measurements for calcium.

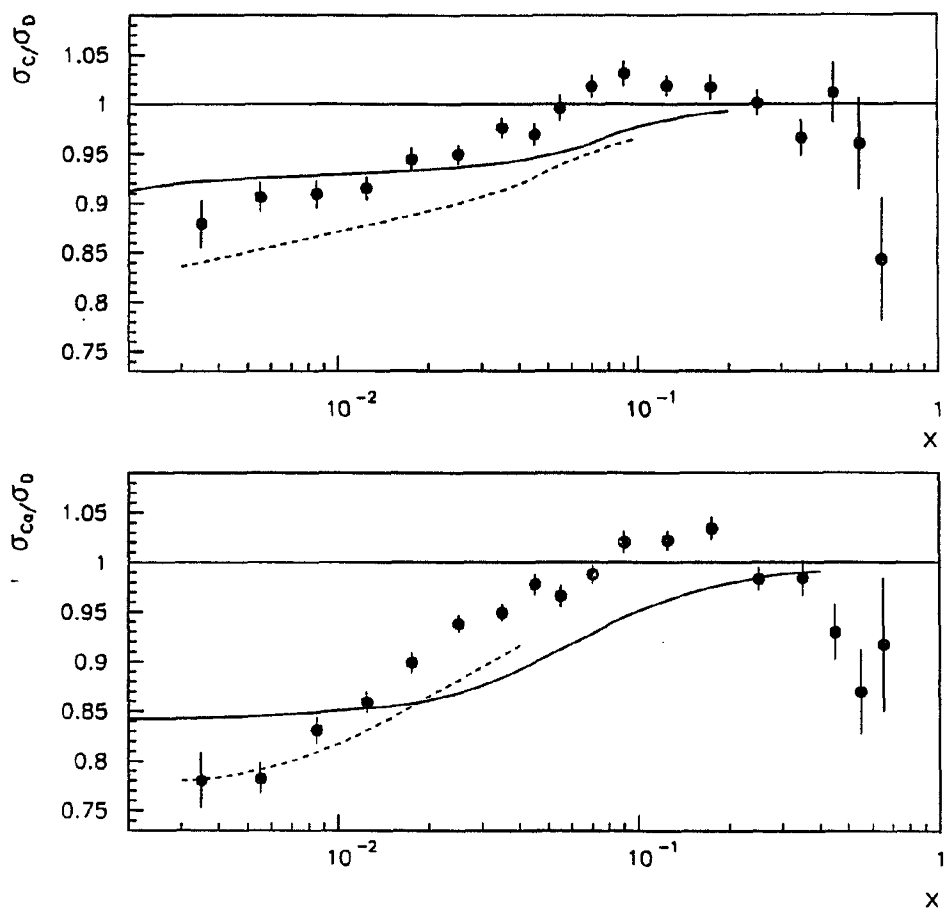

Figure 5.14: The NMC results for carbon and calcium compared with the predictions of the GVMD model of Schildknecht [165]-[170]. The meaning of the different curves is explained in the text. The error bars show the statistical and systematic errors added in quadrature

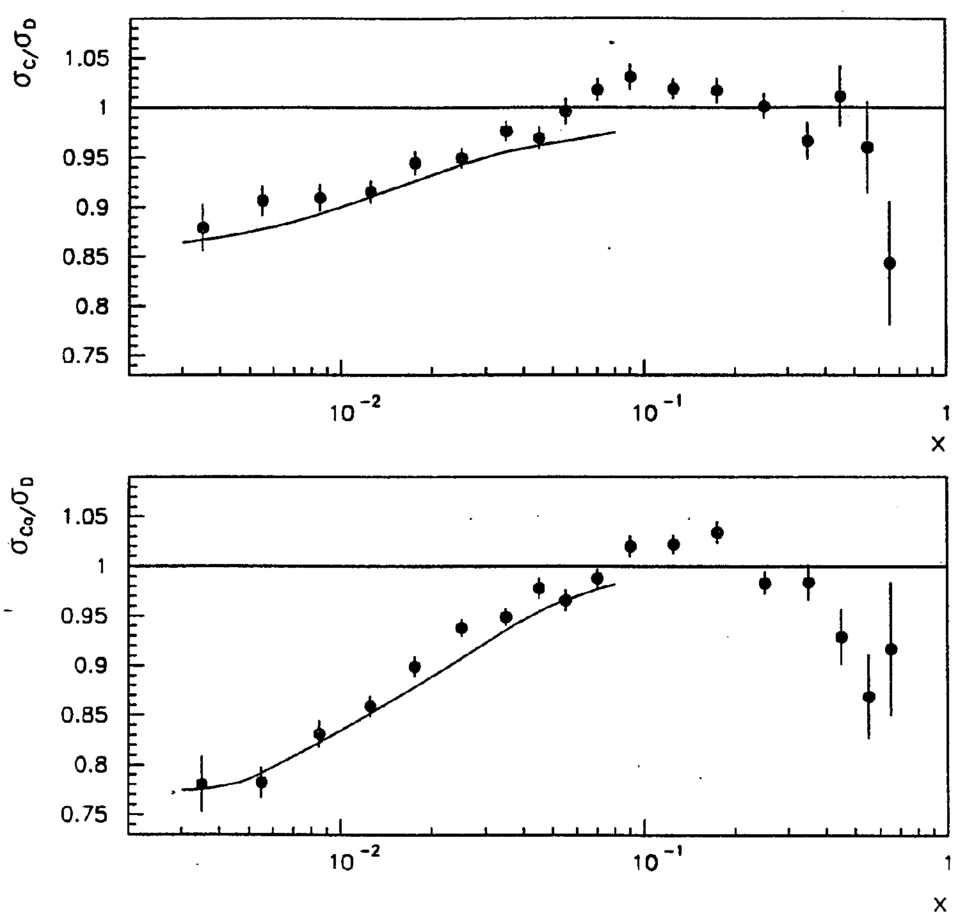

Figure 5.15: The NMC results for carbon and calcium compared with the predictions of the GVMD model of Piller *et al.* [171, 172]. The error bars show the statistical and systematic errors added in quadrature

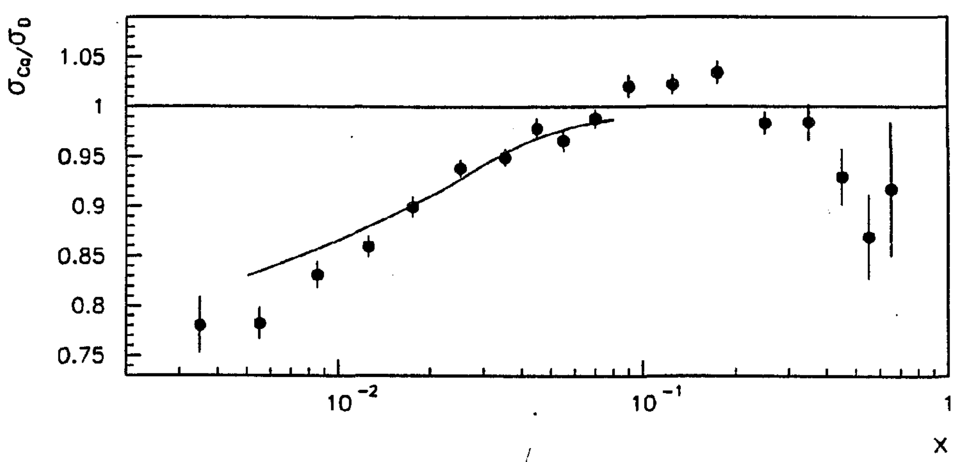

Figure 5.16: The NMC results for calcium compared with the predictions of the GVMD model of Shaw [174]. The error bars show the statistical and systematic errors added in quadrature

Finally we consider the off-diagonal model of Ditsas and Shaw [175, 174]. The predictions for the calcium to deuterium ratio are shown in fig. 5.16, computed at the Q^2 values of the NMC data. The agreement with the experimental data is good for $x > 0.01$; at lower values of x the theoretical expectation is above the data.

5.5.2 Partonic Models

Detailed predictions based on the partonic approaches of Qiu [179], Berger and Qiu [180] and of Close and Roberts [181] were obtained in [333] for the kinematic range covered by the NMC data.

Berger and Qiu [180] do not make explicit predictions on the x dependence of shadowing, but rather restrict themselves to an estimate of the x value where shadowing sets on. These predictions were combined in [333] with the ansatz 1.52 (page 69) proposed by Qiu [179], which gives the amount by which the sea quark distribution in a bound nucleon is suppressed with respect to the free nucleon case. In this equation the quantity x_N (where shadowing should start) is assumed to have the behavior given by expression 1.54 (page 70), while the point where shadowing saturates is taken to vary with A as $x_A = 1/(2MR_A) \approx 0.1A^{-1/3}$ (with R_A the nuclear radius).

In order to obtain a prediction covering the large x domain as well, in [333] both the Q^2 rescaling prescription [103] (equation 1.32, page 46) and the x rescaling one [79] (equation 1.24, page 41) were considered.

Figures 5.17 and 5.18 show the comparison of the model (continuous curves) with the NMC data, for the Q^2 and x rescaling cases, respectively. While the predictions for C/D are in reasonable agreement with the data when Q^2 rescaling is used, in all other cases the model fails to reproduce the experimental results. The predictions for Ca/D change slightly if the values of x_N and x_A in equation 1.52 are replaced by those suggested by Close and Roberts [181] (dashed lines in figs. 5.17 and 5.18), who evaluated x_N using the nucleon-nucleon overlap probabilities of the Q^2 rescaling model [103] and x_A assuming that saturation occurs at $x = 1/(2MR_A)$, where R_A is now the radius of the carbon nucleus, yielding $x_A \approx 0.04$. Also in this case the comparison with the data is rather poor.

Figure 5.19 compares the NMC results for helium, carbon and calcium to the predictions of the model by Zhu and Shen [186]-[188]. We recall from chapter 1 that this model is based on the so-called constituent quarks or valons. At small Q^2 valons coincide with valence quarks. At large Q^2 valons also include a cloud of sea quarks, anti-quarks and gluons. Recombination of these quarks and gluons (belonging to different nucleons) gives rise to shadowing at small x and anti-shadowing at larger x. In the figure the predictions for $Q^2 = 1$, 10 and 40 GeV^2 are given.

The predictions for the three nuclei are in excellent agreement with the measurements. In particular one should remark that the small x points, which have small Q^2 (< 2 GeV^2 for $x < 0.01$) are closest to the prediction for 1 GeV^2. For $x \approx 0.1$, where Q^2 is about 10 GeV^2, the curve for 10 GeV^2 shows the best agreement with the data. The expected Q^2 dependence seems thus to be confirmed. The predicted Q^2 slope for calcium at $x \approx 0.1$, $b \not\approx -0.01$, is consistent with the measured one.

Within the framework of this model, the integrals of the structure function differences were also computed [189]. The predicted values are -0.46×10^{-3}, -1.80×10^{-3} and -3.36×10^{-3} for He/D, C/D and Ca/D, respectively, in good agreement with the results of table 5.9. We recall that the net loss of momentum in bound nucleons occurs in this model because of the $q\bar{q}$ fusion process, which transfers momentum from the quarks to the gluons.

Castorina and Donnachie [193] ascribe shadowing to a suppression of the quark-pomeron coupling in nuclei. The predictions of this model reproduce the NMC data for carbon for $x < 0.01$ but underestimate them for larger values of x (fig. 5.20). The situation is worse for calcium where the expected shadowing signal and the experimental points cross each other at $x \approx 0.15$ but are otherwise in significant disagreement.

In a later paper [194] Castorina and Donnachie adjusted the normalization of the sea quark distribution in order to achieve better agreement with the EMC NA28 [40] and NA2′ [38] data. The new predictions are shown in fig. 5.20 as dashed curves. The agreement with the data is now better, especially for $x > 0.04$. At smaller x the model is however systematically lower than the data, by up to 5-6% in carbon.

The model of Brodsky and Lu [198] is also based on pomeron exchange. In addition the exchange of other Regge trajectories is incorporated in order to account for anti-shadowing. Figure 5.21 compares the data and the model predictions. While the agreement is satisfactory for the carbon to deuterium ratio, it is somewhat worse for calcium. Note however that the prediction is actually for Cu rather than for Ca.

5.5.3 Models which Combine the GVMD and the Partonic Approaches

Figure 5.22 shows the NMC results for the carbon and calcium to deuterium structure function ratios and the predictions of the model by Kwieciński and Badełek [199]. This model ascribes shadowing to the rescattering of low mass vector mesons in the nucleus and to the effects of nuclear screening on the pomeron exchange contribution to the virtual photon-nucleus cross section. The upper and lower continuous curves correspond to $r_0 = 1.5$ and 1.25 fm, respectively, in the formula $R = r_0 A^{1/3}$ for the nuclear radius.

Experimental data and theoretical predictions disagree, especially at high x; the disagreement is more conspicuous in the carbon case. In fig. 5.22 we also show the prediction by

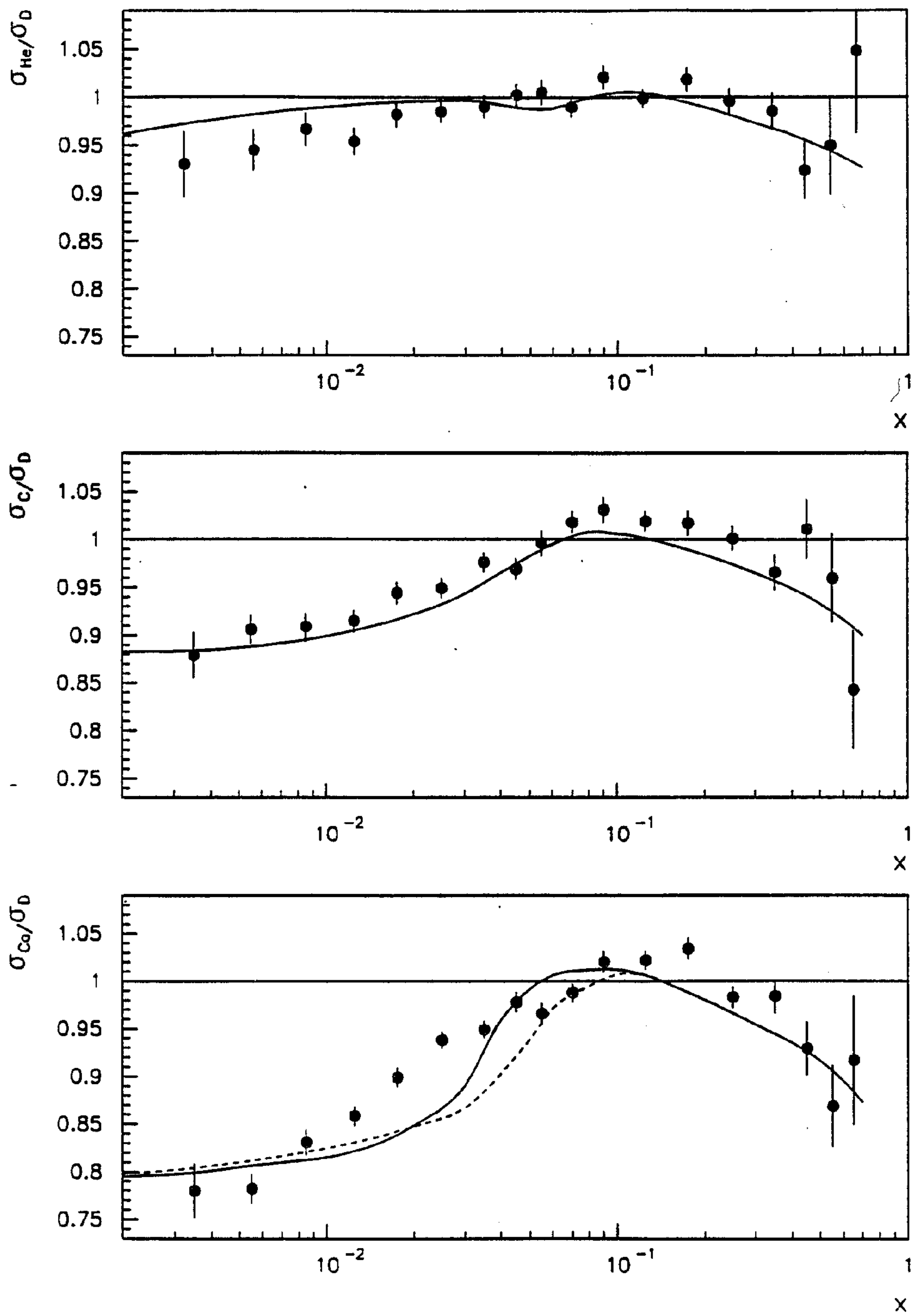

Figure 5.17: The NMC results for helium, carbon and calcium compared with the curves based on the models of Qiu [179], Berger and Qiu [180] (continuous lines) and of Close and Roberts [181] (dashed line) as were obtained in [333]; Q^2 rescaling is used. The error bars show the statistical and systematic errors added in quadrature

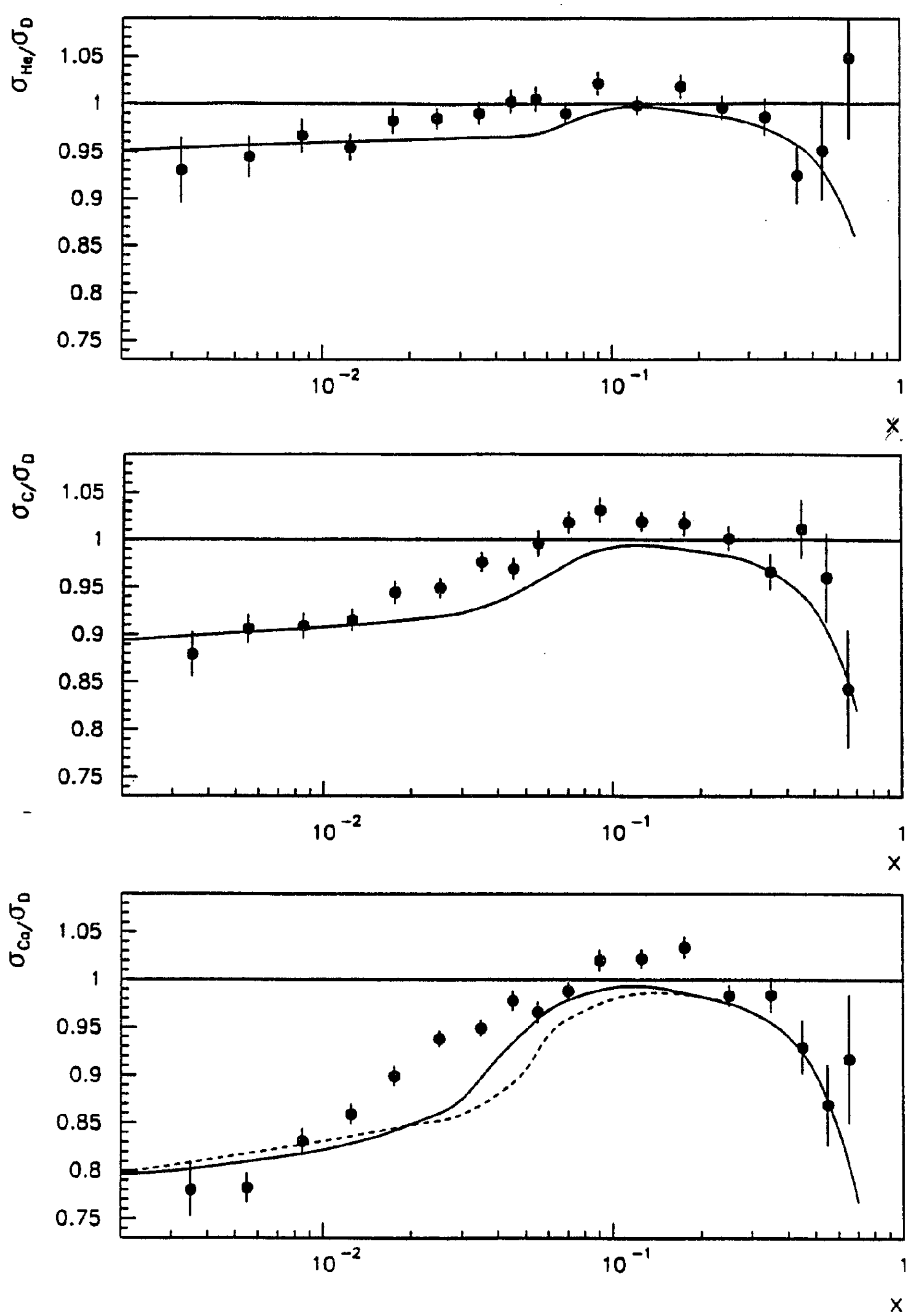

Figure 5.18: The NMC results for helium, carbon and calcium compared with the curves based on the models of Qiu [179], Berger and Qiu [180] (continuous lines) and of Close and Roberts [181] (dashed line) as were obtained in [333]; x rescaling is used. The error bars show the statistical and systematic errors added in quadrature

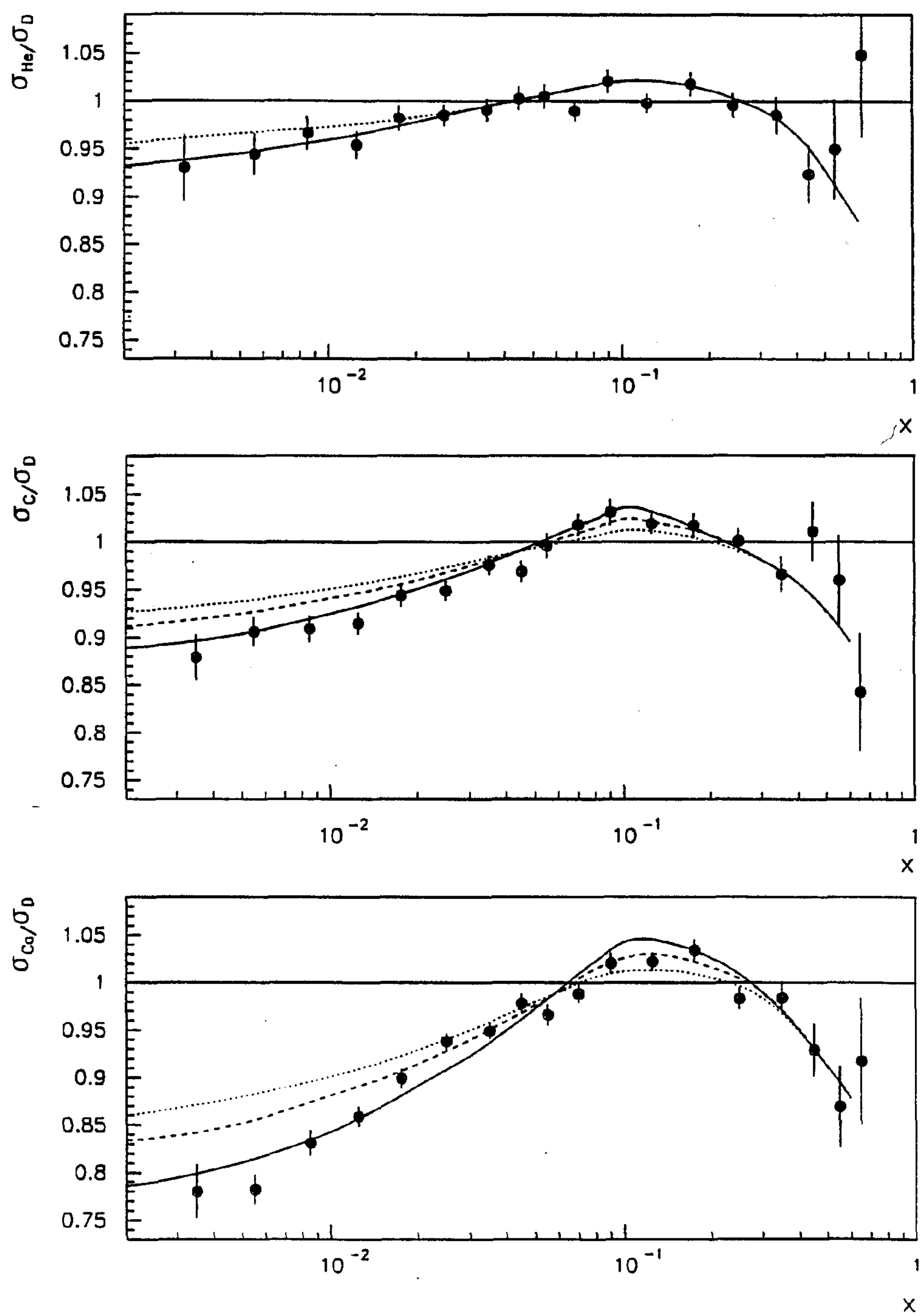

Figure 5.19: The NMC results for helium, carbon and calcium compared with the predictions of the model by Zhu *et al.* [187]. The continuous curve is for $Q^2 = 1$ GeV^2, the dashed one for $Q^2 = 10$ GeV^2 and the dot-dashed one for $Q^2 = 40$ GeV^2 (the curves are from [190] for He/D and from [189] for C/D and Ca/D). The error bars show the statistical and systematic errors added in quadrature

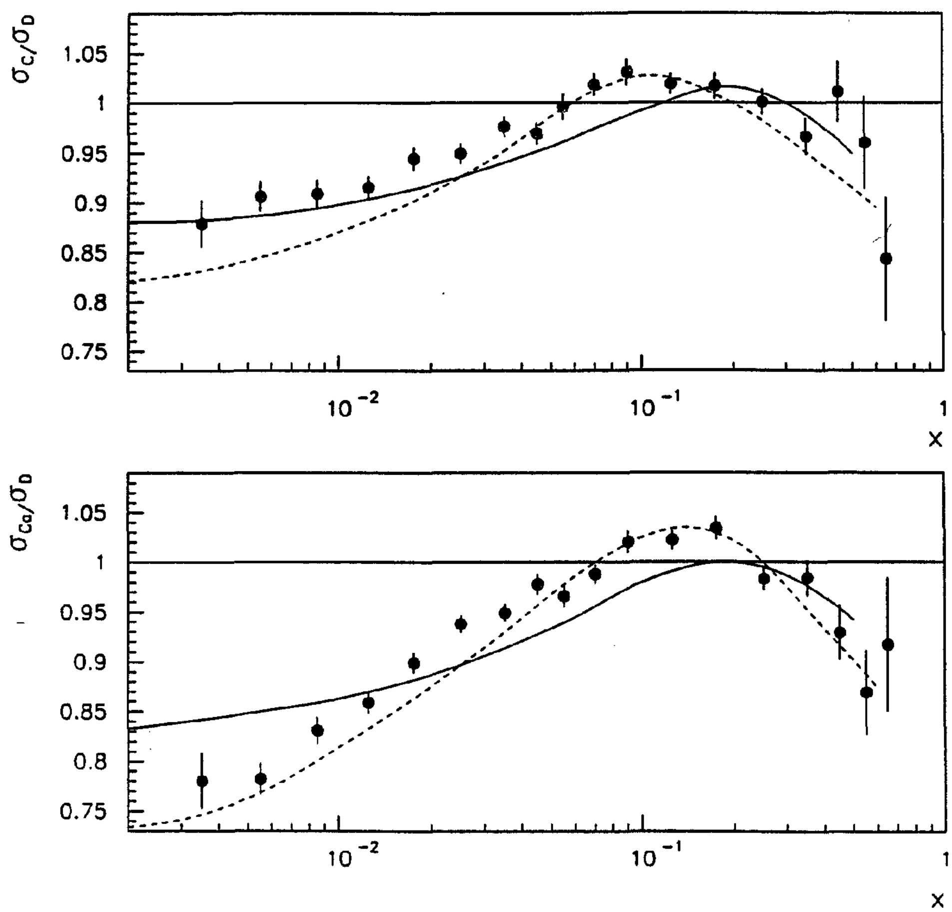

Figure 5.20: The NMC results for carbon and calcium compared with the predictions of the model by Castorina and Donnachie [193]. The dashed lines are the predictions after the adjustment of the sea quark distribution normalization [194]. The error bars show the statistical and systematic errors added in quadrature

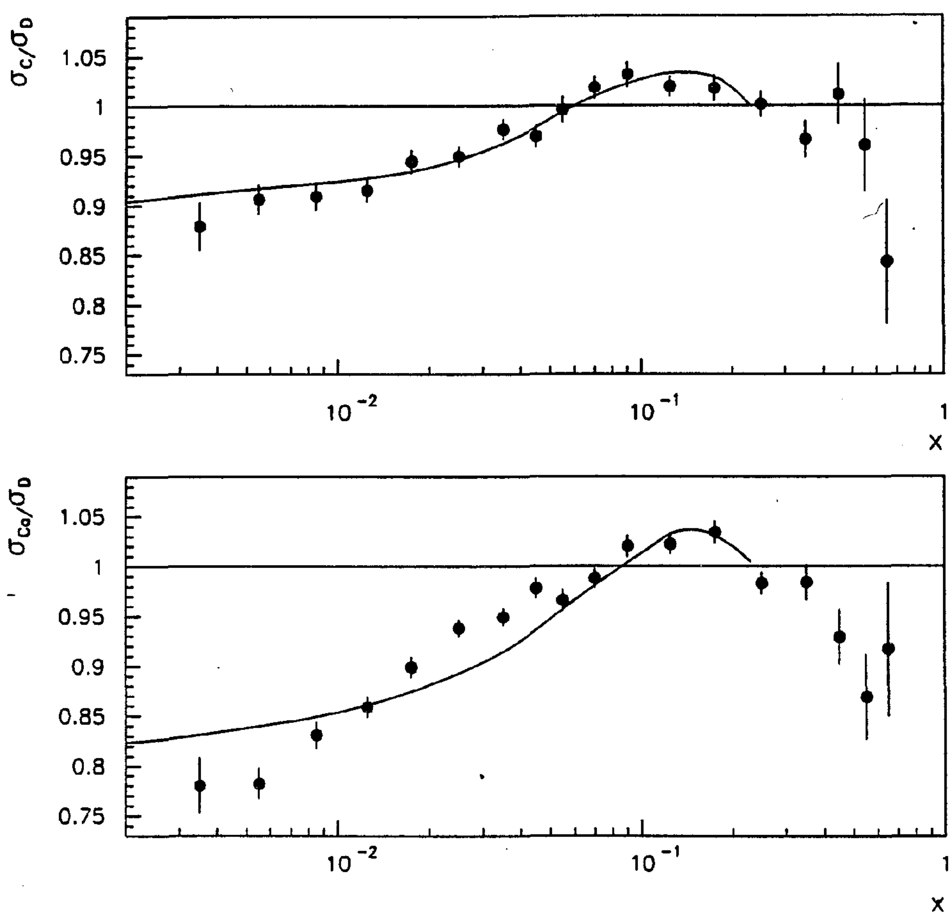

Figure 5.21: The NMC results for carbon and calcium compared with the predictions of the model by Brodsky and Lu [198]. The curve plotted together with the Ca data is for the Cu to D ratio. The error bars show the statistical and systematic errors added in quadrature

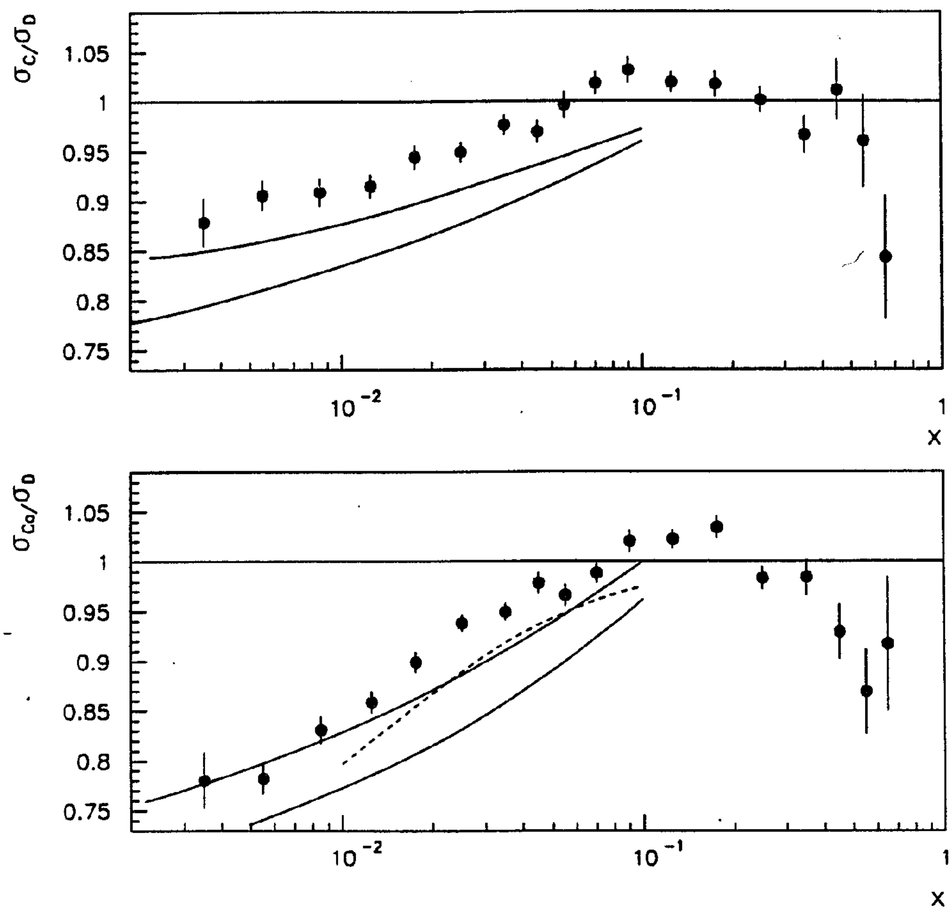

Figure 5.22: The NMC results for carbon and calcium compared with the predictions of the model by Kwieciński and Badełek [199]. The upper and lower continuous curves correspond to $r_0 = 1.5$ and 1.25 fm, respectively, in the formula $R = r_0 A^{1/3}$ for the nuclear radius. The predictions of Kwieciński [200] for iron are also shown (dashed curve). The error bars show the statistical and systematic errors added in quadrature

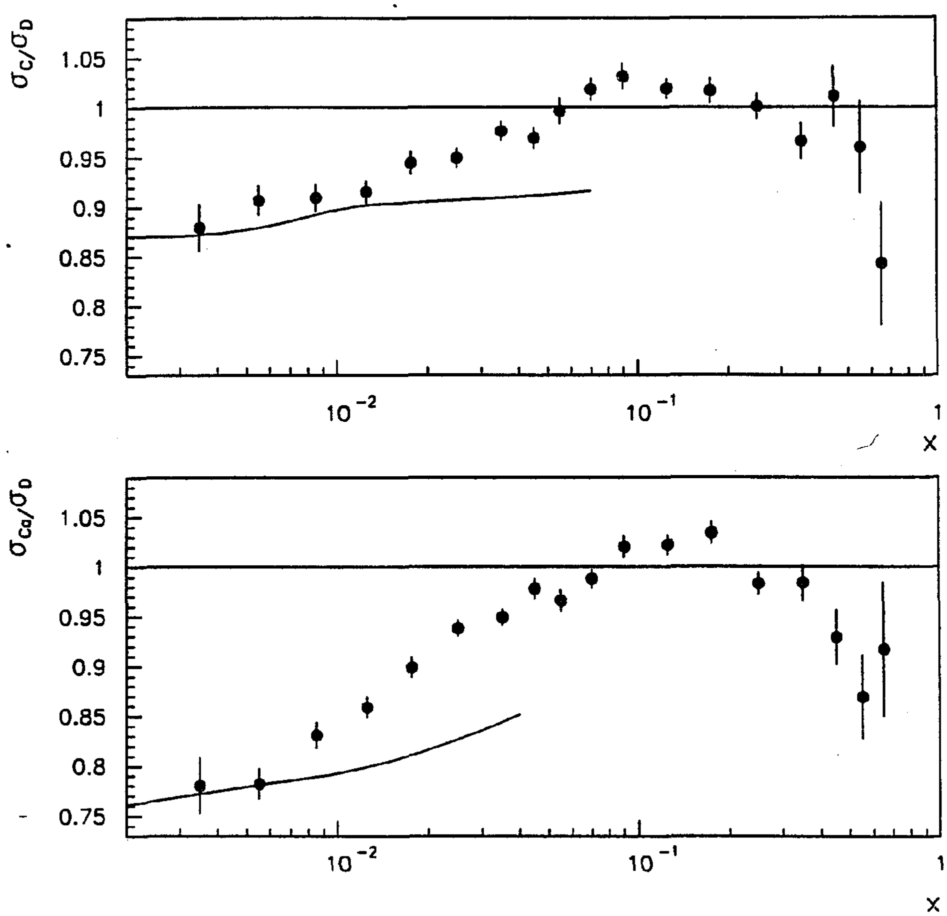

Figure 5.23: The NMC results for carbon and calcium compared with the predictions of the model by Frankfurt and Strikman [202]. The error bars show the statistical and systematic errors added in quadrature

Kwieciński [200] for the iron to deuterium structure functions ratio (dashed line). The curve was computed for $Q^2 = 10$ GeV^2.

A similar trend is visible in fig. 5.23 which shows the predictions of the model of Frankfurt and Strikman [202] in which, as we discussed in chapter 1, GVMD arguments are coupled with considerations on the transverse size of the $q\bar{q}$ pair into which the photon fluctuates. Here as well the model overestimates the size of shadowing, except in the first two x bins, for $x < 0.06$. The theoretical curves are however for the range $0.75 < x < 1.5$ GeV^2 only (in the data $Q^2 > 2$ GeV^2 for $x > 0.01$). The results of the extended model by Frankfurt, Strikman and Liuti [206] are shown in fig. 5.24 for the Ca/D ratio; the curve is for fixed Q^2, $Q^2 = 2$ GeV^2. Except in the anti-shadowing region (where however the Q^2 of the data is larger than 2 GeV^2, $Q^2 \approx$ 10-15 GeV^2), the comparison with the data is rather poor. It would be desirable to have explicit results on the Q^2 dependence in order to make the comparison more conclusive.

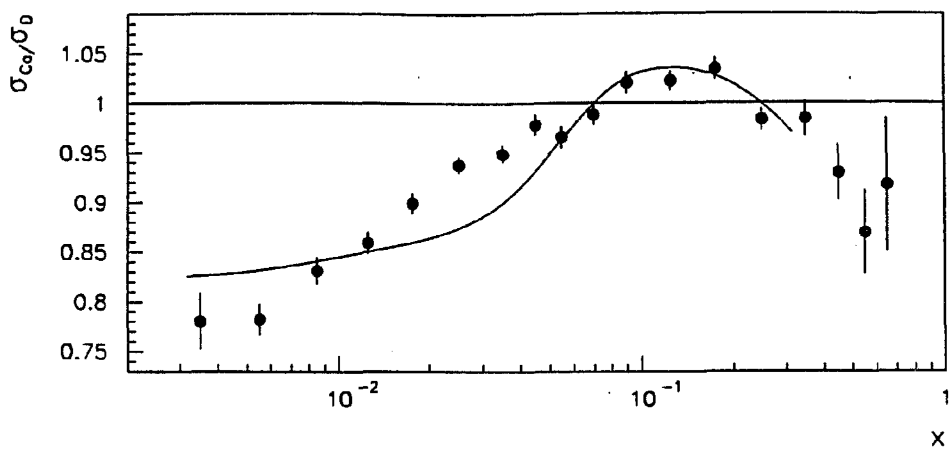

Figure 5.24: The NMC results for calcium compared with the predictions of the model by Frankfurt, Strikman and Liuti [206], computed for $Q^2 = 2$ GeV^2. The error bars show the statistical and systematic errors added in quadrature

Finally, in fig. 5.25 we show the predictions of the model by Nikolaev and Zakharov [207, 208], in which shadowing is discussed in terms of scattering of small transverse momentum $q\bar{q}$ pairs off the nucleons via pomeron exchange. Notably, the pomeron is described perturbatively as a pair of gluons.

The predictions for the helium, carbon and calcium to deuterium structure function ratios lie all significantly below the data. The disagreement becomes more pronounced with decreasing x and reaches the 15-20% level at small x.

The discrepancy was anticipated by the authors and is ascribed to the fact that the model only accounts for shadowing without including other nuclear effects. For example the EMC effect, which determines the depletion of the bound to free nucleon structure function ratios at large x, implies in most models an enhancement of the ratio at small x. Such enhancement may be of the order of $\approx 10\%$. If this is added to the shadowing contribution, one should recover the observed signal. It is clear however that until a unitary description of the small and large x region is found, no quantitative verification of this argument is possible.

5.5.4 Conclusions of the Comparison with the Theoretical Models

The new data allow some discrimination between the models: it is now clear that some of these appeared to describe the EMC NA28 and NA2′ results only because of the large error bars of the data. Among the models which, in their current formulation, do not reproduce the experimental findings we list:

1. the GVMD model of Schildknecht [165]-[170];
2. the partonic models of Berger and Qiu [179]-[180] and of Close and Roberts [181];
3. the partonic model of Castorina and Donnachie [193], also after the readjustment of the sea quark distribution normalization, at least for carbon;
4. the mixed VMD-partonic model of Kwieciński and Badełek [199];

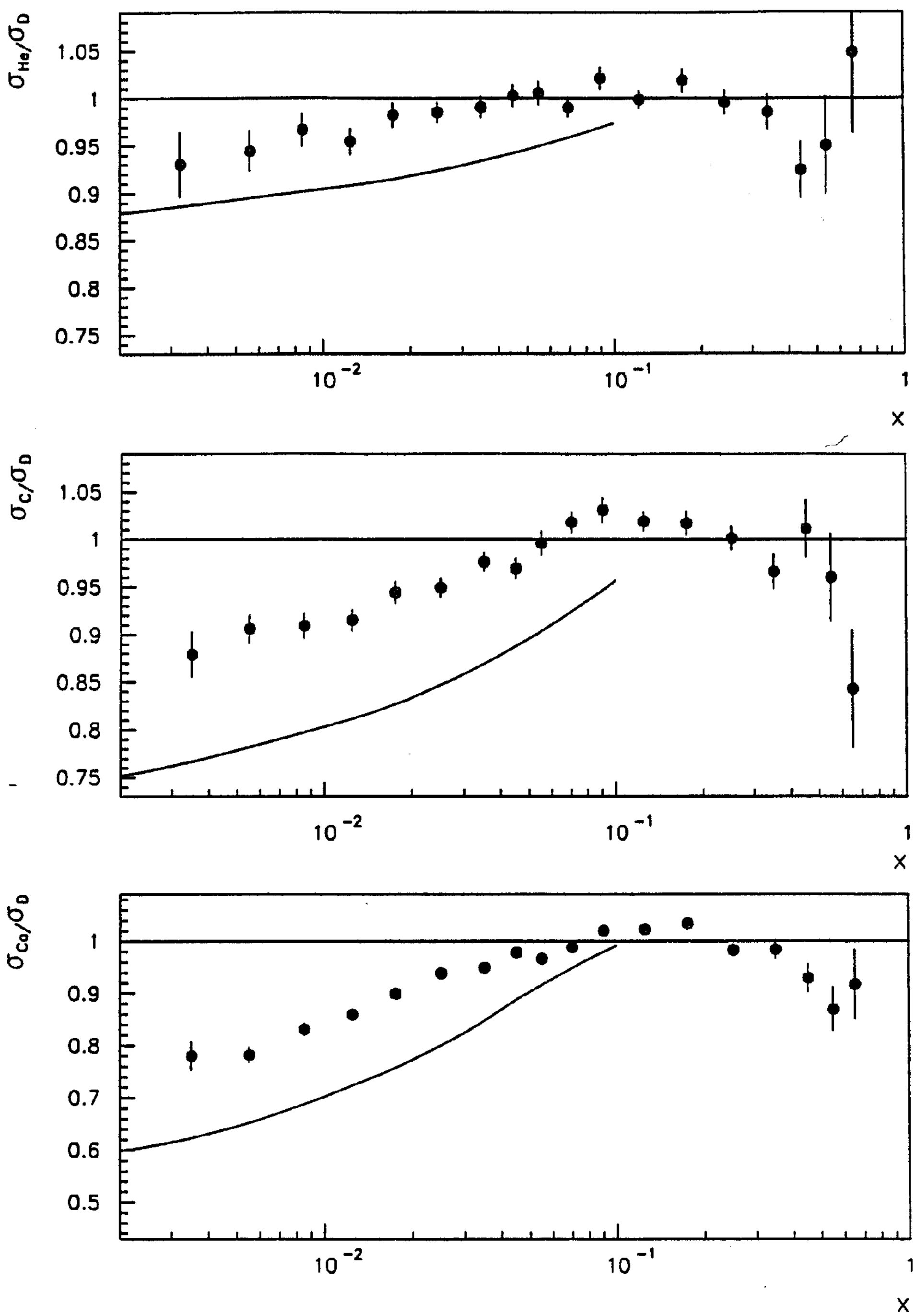

Figure 5.25: The NMC results for helium, carbon and calcium compared with the predictions of the model by Nikolaev and Zakharov [207, 208]. Note the change of scale in the Ca/D plot. The error bars show the statistical and systematic errors added in quadrature

5. the model of Nikolaev and Zakharov [207, 208].

Some are instead in agreement with the NMC results:

- GVMD models
  - Piller *et al.* [171, 172];
  - Shaw ($x > 0.01$) [174].
- Partonic models
  - Brodsky and Lu [198], who reproduce the carbon data but do less well for calcium;
  - Zhu and Shen [186]-[188], who give an excellent description of the helium, carbon and calcium data.

In the case of the model by Frankfurt and Strikman [202, 206], the comparison is not very conclusive because of the lack of explicit predictions on the Q^2 dependence.

A few remarks are in order:

- Generalized vector meson dominance, twenty years after its original formulation, appears to offer still a viable description of shadowing. It is a little disturbing however that different versions of essentially the same model give predictions in disagreement with each other. Part of the problem is in the many adjustable parameters of the model (e.g. the vector meson-nucleon cross section, the spectrum of the high mass vector resonances etc.).
- As it has been emphasized by several authors (see e.g. [65, 180, 207, 208]) a partonic description of shadowing is not necessarily in contradiction with GVMD, but rather expresses the same physical picture in the Breit frame. It is therefore not astonishing that partonic and GVMD models may be both consistent with the data.

  The validity of partonic approaches extends however over a wider kinematic region and includes anti-shadowing. In a formulation based on parton fusion, anti-shadowing is a natural consequence of momentum conservation.
- We remarked elsewhere that the results of the FNAL experiment E772 [61] on Drell-Yan dimuon production also exhibit shadowing. We recall that this experiment is sensitive to the anti-quark distribution only and that its average Q^2 is larger than that of NMC.

  We are not aware of any GVMD prediction for Drell-Yan processes. There are instead detailed predictions within the framework of the quoted partonic approach of Zhu *et al.* [187]. The theoretical expectations are in good agreement with the data and explain the smaller amount of shadowing *and* anti-shadowing visible in the Drell-Yan experiment relative to that in DIS experiments in terms of the different Q^2 ranges covered.

  Frankfurt, Strikman and Liuti also ascribe the smaller amount of shadowing seen by E772 to the higher Q^2 of these data; the explanation offered for the lack of enhancement is instead simply that the sea quark distribution is not expected – in their model – to be enhanced.

- Unfortunately none of the models that we have discussed is really predictive in the sense that it is proven incorrect if it does not describe the experimental data. In most cases the predictions can be "improved" just by careful tuning of the parameters of the model. In a broad sense, for instance, the model by Zhu *et al.* [186]-[188], which gives an accurate description of the data, is a refined version of the one by Close and Roberts [181], which is not proven wrong, strictly speaking, by figs. 5.17 and 5.18; the poor comparisons simply indicate that some of the assumptions (by no means fundamental, e.g. that saturation occurs for nuclei with $A \geq 12$) or of the parametrizations adopted (e.g. the one describing the x dependence of shadowing) need to be revisited.

  Unlike what happens in other branches of particle physics, the role of accurate data seems here that of a guide (sometimes a mere source of parameters) for theory, which for the moment appears to be far from being able to make predictions based on first principles.

We have so far concerned ourselves with the small x region ($x < 0.2$) and have not attempted to compare our data with the theoretical predictions at higher values of x. The reason, as we wrote above, is that the statistical relevance of our data at high x is comparable to or worse than that of previous experiments. Before concluding this section we nonetheless comment on the status of the comparison between theory and experiment in this region.

As we discussed at length in chapter 1, a variety of models is able to describe the EMC effect. Different physical approaches are used in order to make the quark distribution in a bound nucleon softer than that in a free one – which is the essence of the phenomenon. Most approaches give a reasonable description of the results for all the nuclei on which data are available. The x and A dependences of the effect are therefore not sufficient to discriminate among the existing models. If we include in the comparison also the Drell-Yan data [61], then the pion approach (and x rescaling ?) appears to be ruled out, as we discussed in chapter 1. The statement contained in [61] that also other approaches (notably cluster models and Q^2 rescaling) are contradicted by these results has not met significant consensus: there are cluster models which can reproduce these Drell-Yan data (see e.g. [152]); furthermore the fact that Q^2 rescaling does not predict shadowing is well known, but does not automatically rule out the model in the EMC effect region.

Some more definite discrimination between the models of the EMC effect must probably await reliable data in the $x > 1$ region. If nuclear structure functions are proven to be non-zero there, then x and Q^2 rescaling models are ruled out, as well all models based nuclear binding or pions. In none of these models can a quark carry a fraction of the nucleon momentum significantly larger than unity. This is instead possible in a natural way in models based on quark deconfinement or on multi-quark clusters. Note that some attempts [19] made to describe the $x > 1$ region in terms of Fermi motion are in fact based on variants of cluster models.

Quark-cluster models might also offer, at least in principle, the possibility of a unified description of shadowing and the EMC effect. Indeed we observed in chapter 1 that the predictions of some of these models extend to x values well inside the shadowing region. Quark-cluster models in fact overlap to a certain extent with the parton recombination approach for shadowing. As observed in [151] the probability that a quark in a nucleus is part of a cluster may be taken as a crude measure of the amount of recombination. Unfortunately, the predictions of these models are for the moment rather vague in the shadowing region (cf. for example [148, 151] and fig. 1.43) and do not allow a stringent comparison with the data.

The lack of a quantitative and unitary description of both shadowing and the EMC effect suggests some caution in comparing theoretical predictions and experimental results on shadowing. Many models of shadowing neglect the possibility that the mechanisms leading to the EMC effect may be already at work at very small x. However, if this is the case, as suggested for instance in [207, 208], the measured structure function ratios at small x would include both the effects of shadowing and those of the EMC effect. The fact that some shadowing models agree with the data and some do not would become, in this case, largely accidental.

5.6 Concluding Remarks

Experimental Situation

We first summarize the status of the data on the ratio of the bound to free nucleon structure functions. The measurements currently cover the region $5 \times 10^{-5} < x < 0.8$.

- For $5 \times 10^{-5} < x < 10^{-3}$ the only available data are the preliminary ones of the FNAL experiment E665 [42] on the xenon to deuterium ratio. Their statistical accuracy is about $\pm 7\%$; the systematic errors are of similar size.
- In the region $0.0035 < x < 0.35$ the NMC results presented here on He/D, C/D and Ca/D are the most accurate currently available. Statistical and systematic errors are typically 1%. The logarithmic slopes $b = d(F_2^A/F_2^D)/d(\ln Q^2)$ were measured with statistical accuracies $\Delta b \approx \pm 0.02$.
- The best experimental information on the region $0.3 < x < 0.8$ comes from the SLAC E139 data [35] on D, He, Be, C, Al, Ca, Fe, Ag and Au. The statistical errors range from 1 to 3% in each bin, depending on the target nucleus.

The picture that emerges from the data is the following:

1. Shadowing. For values of x smaller than about 0.05 the bound to free nucleon structure function ratios are smaller than unity. The size of the depletion is consistent with being a linear function of $\ln A$ and amounts to 7%, 12% and 22% at $x = 0.0035$ for the He/D, C/D and Ca/D ratios, respectively. In the region $0.0035 < x < 0.05$ the ratios rise approximately linearly with $\ln x$. No significant Q^2 dependence has been observed in this region. At very small x, for $10^{-5} < x < 10^{-3}$ there are indications that the ratios are about constant.

2. Enhancement. In the region 0.05-0.1 $< x < 0.2$ the structure function ratios become larger than unity. The size of the enhancement is approximately 2% for carbon and calcium, possibly less for helium. In this region no Q^2 dependence is observed for the helium and carbon to deuterium ratios. The calcium to deuterium ratio shows instead some evidence of a decrease with increasing Q^2.

3. EMC effect. In the region $0.2 < x < 0.8$ the ratios decrease with increasing x and have a minimum at $x \approx 0.6$. Here as well the size of the depletion is approximately proportional to $\ln A$. There are indications that in this region the ratios decrease with increasing Q^2.

4. For $x > 0.8$ the ratios rise above unity again, a consequence of Fermi motion. The experimental information on this region is however very scarce.

5. The integrals of the structure function differences $F_2^A - F_2^D$, in the range covered by the NMC and by the SLAC E139 data, appear to be negative and to decrease with the nuclear mass number A; yet they are compatible with zero within at most two standard deviations.

Theory

This detailed and extensive experimental information is confronted with a wealth of theoretical models which generally reproduce the qualitative features of the data but fail to be predictive at a quantitative level. It is our hope that the new results presented in this work may stimulate further theoretical analysis, so that a unitary and more quantitative description of the nuclear effects in deep inelastic scattering may be achieved.

At the moment the following theoretical scenario is consistent with the data:

- At small x, the situation can be described in different ways:

  1. In a frame in which the target nucleons are at rest the virtual photon can be seen as fluctuating into a quark-anti-quark pair. The photon thereby acquires hadronic properties and can be effectively treated as a vector meson. The meson interacts strongly with the nucleons on the surface of the nucleus, which thus absorb a significant part of the incoming flux and cast a shadow on the inner nucleons. Of the $q\bar{q}$ pairs into which the photon fluctuates, only those with large transverse size do interact with hadronic cross sections; such pairs are a fraction of the total which decreases with increasing invariant mass of the pair.
  2. In the Breit frame, where the virtual photon has zero energy and the struck quark reverses its three-momentum in the collision, small momentum quarks and gluons, because of the uncertainty principle, spread over a distance comparable to the nucleon-nucleon separation. Quarks and gluons from different nucleons can overlap spatially and fuse, thus increasing the density of high momentum partons at the expense of that of lower momentum ones.

     This point of view is attractive because it accounts, at the same time, for the existence of shadowing and of anti-shadowing. Also it implies that some of the momentum carried by quarks may be transferred to gluons via $q\bar{q} \to g$ processes.

  It is nearly uncontested that sea quarks and gluons are the principal characters of shadowing, the role of valence quarks being negligible at such small values of x. This is also confirmed by the fact that shadowing effects similar to those observed in DIS have been measured in Drell-Yan proton-nucleus dimuon production [61], sensitive to the target anti-quark distribution only.

  The fact that the same Drell-Yan experiment found no evidence of anti-shadowing has instead led to contrasting conclusions. On the one hand, the absence of anti-shadowing in an experiment sensitive to anti-quarks suggests that anti-shadowing has to do with valence quarks (see e.g. [206, 65]). On the other hand, the disappearance of anti-shadowing in Drell-Yan can be a consequence of the measured Q^2 dependence in the enhancement region (cf. [186]-[188]).

- At larger values of x, $0.2 < x < 0.8$, the valence distribution appears to be softer in bound nucleons than in free ones. Many mechanisms have been proposed and most describe the results in a reasonable way. While the pion model appears to be ruled out by the FNAL E772 Drell-Yan data [61], for the others it will probably necessary to wait for good data at $x > 1$ in order to operate a serious selection.

Further Experimental Work

Future theoretical effort should be paralleled by further experimental work with the following goals:

1. An improvement of the statistical and systematic quality of the data for $x < 10^{-3}$. The FNAL experiment E665 should be able to accomplish this, down to $x \approx 5 \times 10^{-5}$, in the next few years.

2. A measurement of the structure function ratios for $x > 1$.

3. A direct measurement of the gluon distribution in nuclei, carried out by studying inelastic J/ψ production, as we discussed in 1.2.3. Data on J/ψ production off hydrogen, deuterium, carbon and tin targets are currently being analyzed by the NMC.

4. High statistics neutrino results. This will help in defining the roles of valence and sea quarks. Another place where neutrino results could make important contributions is deuterium. All measurements with muons or electrons assume that the deuteron is a simple sum of a proton and a neutron, an assumption now being questioned with some insistence. For neutrino scattering $\nu p = \overline{\nu} n$ and hence $\nu D = \nu p + \overline{\nu} n$. No neutrino experiment had so far enough statistics on hydrogen and deuterium to check this relationship.

Appendix A

The Beam Calibration Spectrometer

Introduction

The purpose and the hardware layout of the Beam Calibration Spectrometer (BCS) have already been described in chapter 1. We will concentrate here on the analysis and the results of the BCS calibration runs taken in 1986 and 1987.

The first step in the BCS data analysis was the determination of the MNP26 magnet field map starting from the measured field measurements. The BCS chambers were then aligned by using the data collected with the magnet off.

Calibration runs were at this point analyzed: from the measured track deflection and the knowledge of the magnetic field, the momentum can be computed and compared with that measured by the BMS for the same track. Assuming that the momentum measured by the BCS spectrometer is the "true" one, a straight line is fitted to the BCS versus BMS momentum scatter plot, thus obtaining a calibration line. Such calibration line can be used in the data analysis programs (e.g. those which read the micro-DST's) in order to correct the beam momentum as measured by the BMS on an event by event basis. Alternatively the BCS information can be used instead of the BMS Monte Carlo output file, in order to compute the BMS coefficients (cf. section 2.5) directly.

A.1 The Field Map

The field of the MNP26 magnet was measured in two box-like regions at the upstream and downstream ends of the magnet; each of the regions extended 1.6 m along the beam direction, 0.48 m along y and 0.1 m along z. The measurements, carried out with a NMR probe, were taken at points belonging to a three-dimensional grid with 2 cm pitch; the three components were measured separately. The measurements were repeated for three values of the MNP26 magnet current: 550 A, 960 A, 1800 A.

A field map valid over the whole magnet volume was extracted from the field measurements. A representation was first found for the two regions where the measurements were carried out; such representation was then extrapolated to the unmeasured region. In more detail the procedure was the following:

- Measured region.

It is possible to improve on the accuracy of the measurements by requiring that the field components satisfy Maxwell's equations. In particular, one can demand that $\nabla^2 B_i=0$ ($i = x, y, z$). This is done by imposing [334] that each field component be represented by an harmonic function, i.e. a function with zero laplacian.

The point is that a magnetic field, in a vacuum, is fully determined by its boundary values. If the boundary values are fitted with an appropriate harmonic function (an expansion in trigonometric functions, in this case), the difference between the real and the fitted field is maximum at the boundary. This implies that, if the field is measured at a number of points belonging to a surface Σ and, with equal accuracy, at a point P inside Σ, then the fitted value at P has a smaller statistical error than the measured field at the same point.

Two programs [334] were used:

1. One to compute the coefficients of the expansion, starting from the field measurements. Only the measurements on the outer surfaces of the two boxes were used.
2. A second one to evaluate the field at the required points, thus providing the field map. These points were chosen to be the same as those where the field was measured originally (a three dimensional grid with 2 cm pitch).

- Unmeasured region.

  In order to determine the map in the central magnet region, where no measurements are available, a fit was made, with simple third order polynomials, for each grid line with constant y and z (i.e. for grid lines parallel to the x axis), to the field map values determined with the procedure outlined above. Only the points close to the unmeasured region were used (up to 40 cm away from it). For each grid line of constant y and z, the fit was then extrapolated into the unmeasured region. The field map was obtained by evaluating the fitted functions at equally spaced points (2 cm) along x.

A direct comparison between the actual field measurements and the field map in the two box-like regions where the measurements were carried out was made [335]. The field integrals computed (along lines with constant y and z, inside the two boxes) by means of the original measurements and by means of the field map agree to better than 0.1% in the central magnet region for the 550 A and 960 A currents.

For the 1800 A current however, discrepancies of up to 1% are present in one of the two boxes, the measured field being systematically lower than the map (in absolute value). Using the map thus leads to an overestimate of the momentum. As discussed below, the 1800 A results were therefore not used to determine the calibration lines.

Figure A.1 shows the z component of the field as a function of x for y=0, z=0 at 960 A.

The field integrals, at the three currents, are $\simeq$ 5 Tm, 8.5 Tm and 11.5 Tm, respectively. The field homogeneity is largest at 550 and 960 A.

A.2 Alignment

The BCS chambers were aligned with a procedure very similar to that outlined in section 3.6.1. BCS alignment runs were taken in which the MNP26 magnet was off and beam tracks, deflected by the FSM, traversed five of the six BCS chambers (since chambers 5 and 6 do not overlap in y, a track may hit either of them, not both).

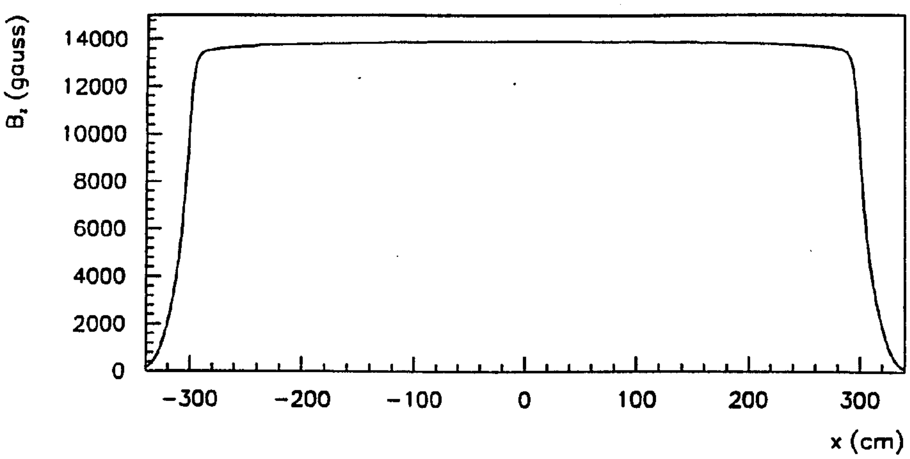

Figure A.1: The z component of the BCS magnetic field as a function of x for y=0, z=0 at 960 A

A modified version of the reconstruction program Phoenix was used, in which tracks are found in the beam hodoscopes and in the chambers P0B, P0C and P0D; such tracks are then extrapolated to P0E and P0A, taking the FSM deflection into account. Hits are looked for in P0E and P0A and a straight line is fitted to them. The line is then extrapolated to P45 and the P45 hits thus found are used to further constrain the fit. The line is finally extrapolated to the BCS chambers. The residuals (i.e. the extrapolation of the P0E, P0A, P45 line minus the coordinate of the found hit) are plotted for each BCS chamber. In principle a chamber is aligned when the mean of the residuals is zero. In practice alignment accuracies better than a few hundred microns cannot be achieved.

A.3 Determination of the Momentum

In order to determine the momentum of a muon passing through the BCS spectrometer one must first reconstruct the track upstream and downstream of the MNP26 magnet. The problem is simple because of the very low hit multiplicities in the BCS chambers: beam calibrations are carried out at intensities of about 10^5-10^6 muons/s, up to 100 times smaller than during normal physics runs.

The incoming track is reconstructed in P0E, P0A and P45 and is extrapolated to the two BCS chambers upstream of the magnet; hits are searched for in these chambers and the track is refitted including the new hits. Only events with multiplicity one in BCS(1) (z plane) and BCS(2) (y plane) are retained.

The outgoing track is defined by the chambers downstream of the magnet. Of these, BCS(3), BCS(5) and BCS(6) detect y deflections, while only BCS(4) is a z plane. The chambers BCS(5) and BCS(6) do not overlap. As the deflection in the z projection is negligible, only the information from the y chambers is used. Hits in BCS(3), BCS(5)+BCS(6) are found by extrapolating the incoming track and by applying a fixed y shift to take the effect of the magnetic field into account. Only events with multiplicity one are selected in BCS(3) and the combined BCS(5)+BCS(6) multiplicity is also required to be unity. No ambiguity is thus left in the downstream pattern recognition.

Once the incoming and the outgoing tracks have been found, the momentum of the muon can be evaluated from the knowledge of the magnetic field. Three different methods were developed to this purpose.

1. Momentum parametrization.

   The principle is to first establish the relationship between the momentum and the track parameters (slope, intercepts) before and after the magnet by means of a Monte Carlo simulation. A few thousand events are generated and tracked through the MNP26 magnet field by using a Runge-Kutta integration procedure. For each one of these events the momentum P is known and so are the incoming and outgoing track parameters. One can then fit an appropriate function to the simulated events. The simplest function is:

   $$\frac{1}{P} = A + B\Delta y', \tag{A.1}$$

   where $\Delta y'$ is the difference between the slopes of the incoming and outgoing lines. Since deflections are small, $\Delta y'$ is nearly the same as the deflection angle $\Delta\theta$.

   The parametrization can be improved by adding a dependence on the point where the track enters the magnet; small inhomogeneities of the field can thus be taken into account:

   $$\frac{1}{P} = A + B\Delta y' + Cy + Dy^2 + Ez + Fz^2, \tag{A.2}$$

   where y and z are the coordinates of the track at the first BCS chamber; A, B, C, D, E are determined by the fit.

   A parametrization of the form A.2 gives a very accurate representation of the momentum: the fitted momentum can be compared with the true, generated one for each event and the r.m.s. deviation is typically $\ll 0.1\%$.

   The NMC Monte Carlo program was used to which the BCS spectrometer simulation had been added. The Runge-Kutta integration in the Monte Carlo is done by the RKPATH routine from the CERN program library [336]. The routine NYSTRK [337] was also tried and shown to give the same results. The fit of the parametrization to the Monte Carlo events is done with the CERN program library package MUDIFI [338].

   Once the parametrization A.2 is found for a given run (i.e. for a given beam energy, sign and MNP26 magnet current) the momentum, for each event, is obtained by feeding the *measured* track slopes and intercepts into the parametrization.

2. Event by event integration.

   Instead of extracting a parametrization which describes, on the average, the beam momentum as a function of the incoming and outgoing track parameters, one can follow the muons through the magnetic field event by event.

   The incoming track is assigned a guessed momentum, e.g. the BMS one; it is then followed à la Runge-Kutta (with the routine RKPATH already mentioned above) through the magnetic field and the slope at the magnet exit is compared with the actually measured slope. Generally the two slopes do not coincide; let δ be the difference between them.

The initial momentum guess is changed by 0.1%: it is increased or decreased depending on the sign of δ. The procedure is iterated until δ changes sign. The final momentum is then the average of the values obtained in the last two iterations. The expected accuracy of the method, on the basis of the iteration, is thus 0.05%. The step size in the Runge-Kutta integration was taken (here and in the previous method) to be 2 cm (this is the same as the pitch of the original field measurements). An explicit check was made that decreasing the step size does not change the results.

3. Circular fit.

Consider the function $Py''(x)$

$$Py''(x) = A(x) = \sqrt{1+y'^2+z'^2}[B_x z' + B_y y' z' - B_z(1+y'^2)]$$

(cf. section 3.2.2) computed along the particle track ($y' = dy/dx$, $z' = dz/dx$, $y'' = d^2y/dx^2$). The integral of $Py''(x)$ is:

$$\int Py''(x)dx = \int A(x)dx \tag{A.3}$$

hence

$$Py' = \int A(x)dx + constant; \tag{A.4}$$

which can be written as:

$$y' = a + \frac{1}{P}\int A(x)dx. \tag{A.5}$$

Expression A.5 can be evaluated at the beginning and at the end of the region where the magnetic field is non-zero. The integration constant a can be eliminated thereby obtaining:

$$\frac{1}{P} = \frac{y'_{end} - y'_{beg}}{\int_{x_{beg}}^{x_{end}} A(x)dx}. \tag{A.6}$$

Both y'_{beg} and y'_{end} are measured quantities. The denominator in formula A.6 depends instead on the trajectory along which the integral is evaluated, since the field is different at different points in the magnet. As there are no chambers in the field region there is no direct experimental information on the path followed by the particle. A circumference is therefore fitted to the incoming and to the outgoing tracks. The result of the fit is used to evaluate the function $A(x)$. There is of course some ambiguity as to where the circumference should join the straight tracks. The homogeneity of the field is however such that the dependence of $\int A(x)dx$ on the trajectory is very weak: moving the points where the circumference joins to the straight line trajectories by 0.6 m (i.e. from inside the magnet to the edge of the fringe field), produces effects on the momentum well below the 0.1% level.

Period	Beam sign, energy
P4A86	−200 GeV
P1C87	+280 GeV
P2A87	+280 GeV
P2B87	+200 GeV
P2D87	−90 GeV

Table A.1: BCS calibration runs

Method 1 is essentially the same as the one used for the BMS and indeed it was initially chosen because of the analogy of the BMS and BCS spectrometers. The preliminary results contained in [339] were obtained with this method.

Method 2 is expected to be the most accurate, because the field integration is carried out event by event. This method was adopted to obtain the results presented here.

Method 3 is in principle the least accurate as it computes the field integral along a circular trajectory which is only an approximation of the actual particle path. As we mentioned before, it can nonetheless be applied to our problem thanks to the large degree of uniformity of the field. This method is interesting as it makes no use of Runge-Kutta integration routines, present in both of the previous methods.

The comparison between the results obtained with the three methods and the implications on the systematic errors will be discussed in sections A.5.3 and A.5.5.

A.4 Results of the BMS Calibration

Several BCS runs were all taken during the years 1986-1989. We report here on the the 1986-1987 ones, all taken with the same experimental set-up. Table A.1 gives a summary of the runs for which results are presented.

All calibrations include a set of four tapes, each with a different current in the MNP26 magnet:

1. $I_{MNP26} = 0$;
2. $I_{MNP26} = 550$ A;
3. $I_{MNP26} = 960$ A;
4. $I_{MNP26} = 1800$ A.

In P2D87 only the I_{MNP26} =0 and I_{MNP26}=960 A runs were taken.

For each of the five sets of calibration runs available, the BCS chambers were aligned by using the I_{MNP26}=0 run. The I_{MNP26}=550 A, 960 A, 1800 A runs were then analyzed separately. The results presented here were obtained with method 2 of section A.3 (event by event integration).

Figure A.2 shows a typical scatter plot of the BCS versus BMS momenta. Most of the events lie in a narrow band, approximately along the diagonal, demostrating the correlation between the momenta measured by the two spectrometers. Events with low probability of belonging to the band can be rejected and a straight line can then be fitted to the remaining ones. The following prescription was adopted:

1. A straight line was fitted to the P_{BCS} versus P_{BMS} plot:

$$P_{FIT} = \alpha + \beta P_{BMS}. \tag{A.7}$$

2. Each event was assigned a χ^2:

$$\chi^2 = (\frac{P_{BCS} - P_{FIT}}{\Delta P})^2, \tag{A.8}$$

   where P_{FIT} is the value obtained from the fitted line and ΔP is set to $\sim 1\% P_{BMS}$; the χ^2 probability $\Pr(\chi^2)$ was calculated and the events with χ^2 probability lower than a given threshold (typically 0.04) were rejected.

3. A straight line was then fitted again to the cleaned distribution.

The procedure was repeated until the results were stable. Usually two iterations were sufficient.

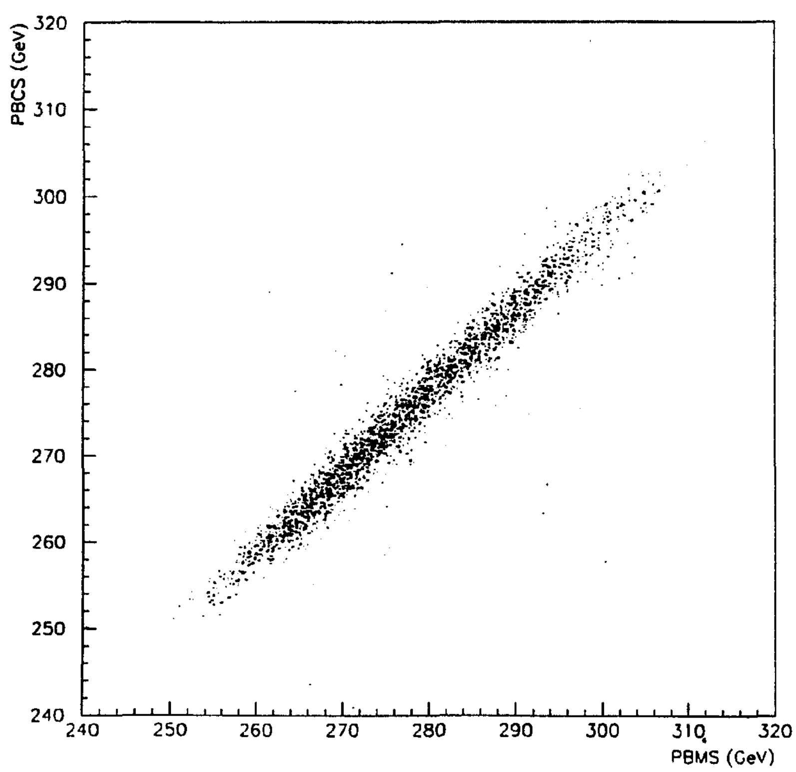

Figure A.2: P_{BCS} as a function of P_{BMS}

The upper part of fig. A.3 shows the ratios of the BCS to BMS average momenta, for each BCS run. The statistical errors on these points are negligible, due to the correlation between

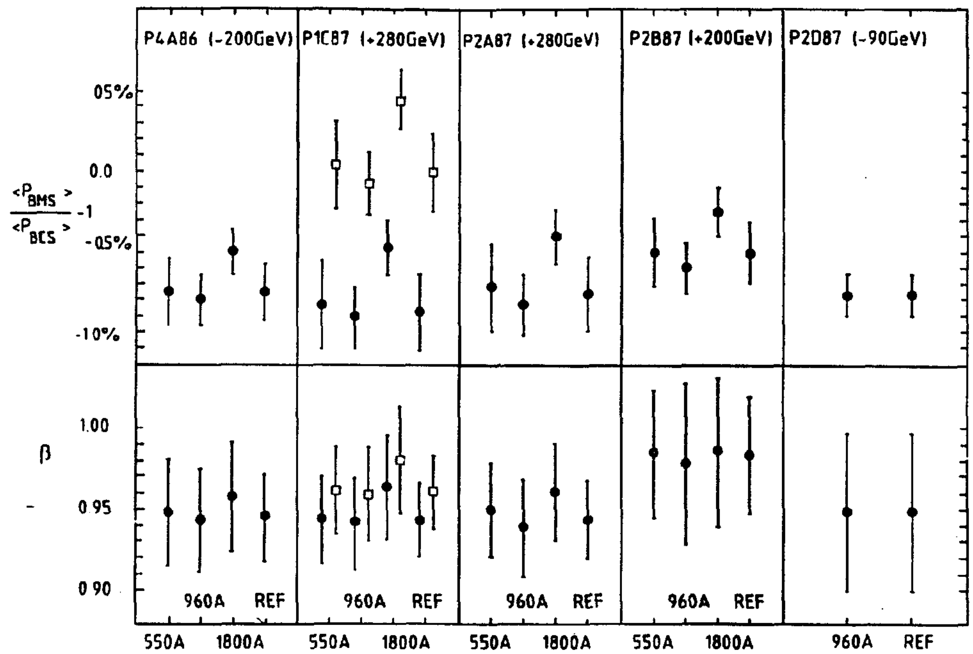

Figure A.3: The ratios of the BCS to BMS average momenta (upper part) and the slopes of the calibration lines (lower part). The points labelled REF are the results of the merged 550, 960 A calibrations

the BMS and BCS momenta. The error bars show an estimate of the systematic errors; their evaluation is discussed in the next section.

The lower part of fig. A.3 shows the slopes β of the calibration lines; the errors are the statistical ones from the fit. As explained in the next section, the systematic contribution to these errors is much smaller than the statistical one.

Two sets of results for the P1C87 calibration (280 GeV) are presented. They were obtained by using different BMS coefficients: the standard ones [340] (full full circles on fig. A.3) and a second set, modified so so as to have the same BMS and BCS average momenta [341] (open squares on fig. A.3).

The general features of the data are the following:

- The average beam momentum as measured by the BCS spectrometer is lower than the BMS one by up to 0.9% (with the exception of the P1C87 results found with the second set of BMS coefficients, where the average BMS momentum is forced to be the same as the BCS one).
- The slope, β, of the calibration line A.7 is smaller than unity: $\beta \simeq 0.95$.

We further remark that:

- In each period the 550 A and 960 A results agree to 0.1% or better (although the 960 A ones are always slightly lower than the 550 A ones) while the 1800 A results are systematically higher by 0.3-0.4%. The discrepancy is to be ascribed to the 1800 A field map, as discussed in section A.1. The 1800 A results should therefore *not* be used for calibration purposes.
- In the 200 GeV, positive beam calibration the BMS and BCS momenta are closer and the slope of the calibration line is consistent with unity.
- The results do not change if events with hits in all four or in only three of the BMS hodoscope planes are selected.

The 550 A and 960 A data were merged for each period. The results for the combined 550 A, 960 A data are shown in fig. A.3. They are also available as FORTRAN FUNCTIONs [342].

The calibration lines can be expressed in the following form:

- P2D87 (−90 GeV)
  - 960 A:
    $P_{BCS} = (1 - 0.76\% \pm 0.13\%)P_{BMS}$ at $P_{BMS} = 89.58$ GeV
    $\beta = 0.949 \pm 0.049$
- P4A86 (−200 GeV)
  - 550 A:
    $P_{BCS} = (1 - 0.75\% \pm 0.21\%)P_{BMS}$ at $P_{BMS} = 200.2$ GeV
    $\beta = 0.948 \pm 0.033$
  - 960 A:
    $P_{BCS} = (1 - 0.80\% \pm 0.16\%)P_{BMS}$ at $P_{BMS} = 200.2$ GeV
    $\beta = 0.943 \pm 0.032$

- 1800 A:
  $P_{BCS} = (1 - 0.50\% \pm 0.14\%)P_{BMS}$ at $P_{BMS} = 200.5$ GeV
  $\beta = 0.958 \pm 0.034$
- Combined 550 A + 960 A results:
  $P_{BCS} = (1 - 0.75\% \pm 0.18\%)P_{BMS}$ at $P_{BMS} = 200.2$ GeV
  $\beta = 0.945 \pm 0.027$

• P2B87 (+200 GeV)

- 550 A:
  $P_{BCS} = (1 - 0.50\% \pm 0.21\%)P_{BMS}$ at $P_{BMS} = 199.5$ GeV
  $\beta = 0.985 \pm 0.040$
- 960 A:
  $P_{BCS} = (1 - 0.60\% \pm 0.16\%)P_{BMS}$ at $P_{BMS} = 200.1$ GeV
  $\beta = 0.979 \pm 0.050$
- 1800 A:
  $P_{BCS} = (1 - 0.25\% \pm 0.15\%)P_{BMS}$ at $P_{BMS} = 200.5$ GeV
  $\beta = 0.986 \pm 0.046$
- Combined 550 A + 960 A results:
  $P_{BCS} = (1 - 0.50\% \pm 0.19\%)P_{BMS}$ at $P_{BMS} = 199.7$ GeV
  $\beta = 0.984 \pm 0.036$

• P1C87 (+280 GeV), BMS coefficients set #1 [340]

- 550 A:
  $P_{BCS} = (1 - 0.83\% \pm 0.27\%)P_{BMS}$ at $P_{BMS} = 276.6$ GeV
  $\beta = 0.944 \pm 0.027$
- 960 A:
  $P_{BCS} = (1 - 0.90\% \pm 0.19\%)P_{BMS}$ at $P_{BMS} = 276.4$ GeV
  $\beta = 0.942 \pm 0.029$
- 1800 A:
  $P_{BCS} = (1 - 0.47\% \pm 0.16\%)P_{BMS}$ at $P_{BMS} = 277.4$ GeV
  $\beta = 0.964 \pm 0.032$
- Combined 550 A + 960 A results:
  $P_{BCS} = (1 - 0.87\% \pm 0.24\%)P_{BMS}$ at $P_{BMS} = 276.5$ GeV
  $\beta = 0.944 \pm 0.023$

• P1C87 (+280 GeV), BMS coefficients set #2 [341]

- 550 A:
  $P_{BCS} = (1 + 0.04\% \pm 0.27\%)P_{BMS}$ at $P_{BMS} = 274.2$ GeV
  $\beta = 0.962 \pm 0.027$

- 960 A:
  $P_{BCS} = (1 - 0.07\% \pm 0.19\%)P_{BMS}$ at $P_{BMS} = 274.0$ GeV
  $\beta = 0.960 \pm 0.029$
- 1800 A:
  $P_{BCS} = (1 + 0.44\% \pm 0.16\%)P_{BMS}$ at $P_{BMS} = 274.9$ GeV
  $\beta = 0.981 \pm 0.033$
- Combined 550 A + 960 A results:
  $P_{BCS} = (1 + 0.00\% \pm 0.24\%)P_{BMS}$ at $P_{BMS} = 274.1$ GeV
  $\beta = 0.961 \pm 0.023$

- P2A87 (+280 GeV)
  - 550 A:
    $P_{BCS} = (1 - 0.72\% \pm 0.27\%)P_{BMS}$ at $P_{BMS} = 276.8$ GeV
    $\beta = 0.950 \pm 0.029$
  - 960 A:
    $P_{BCS} = (1 - 0.83\% \pm 0.19\%)P_{BMS}$ at $P_{BMS} = 276.2$ GeV
    $\beta = 0.939 \pm 0.030$
  - 1800 A:
    $P_{BCS} = (1 - 0.40\% \pm 0.16\%)P_{BMS}$ at $P_{BMS} = 278.0$ GeV
    $\beta = 0.961 \pm 0.030$
  - Combined 550 A + 960 A results:
    $P_{BCS} = (1 - 0.76\% \pm 0.23\%)P_{BMS}$ at $P_{BMS} = 276.5$ GeV
    $\beta = 0.944 \pm 0.024$

A.5 Systematic Studies

A.5.1 Uncertainty on the Field Values

The Field Map

The method used to extract the field map is in principle very accurate and should provide field values with a smaller error than the original measurements. Even taking into account the fact that some of the measured data points are missing (cf. [339]) the estimated error on the field integral does not exceed the 0.1% level. This uncertainty reflects directly on the momentum measurement.

The observed discrepancies between map and measurements at 1800 A indicate a problem in this current – concerning either the measurements or the map extraction procedure – at level of several tenths of a per cent, much larger than the estimate given above. Until the reason for the discrepancy is found, the quoted uncertainty on the field integral should be taken as a lower bound at 1800 A.

	550 A	960 A	1800 A
90 GeV	0.06%	0.03%	0.02%
200 GeV	0.12%	0.07%	0.05%
280 GeV	0.17%	0.10%	0.07%

Table A.2: Sensitivity ($\Delta P/P$) to y misalignments

The Hall Probe

A hall probe, placed well inside the magnet, was used to monitor the field stability: the value of the hall probe in each calibration run can be compared with the one of the original field measurement. Differences between the original value and that in a given run, for a certain magnet current, may indicate hysteresis effects. The map values should in this case be corrected for the ratio of the actual to original hall probe readings.

The hall probe values for all the negative sign beam runs (with "negative" current in the magnet, the same as when the field was originally measured) are very close to those corresponding to the field map measurement, leading to very small corrections (typically $\simeq$ 0.04% and never larger than 0.07%).

For positive beam runs however, the hall probe readings are systematically different from the original ones, leading to sizable corrections: −0.6% (550 A), −0.75% (960 A) and −1.4% (1800 A) (the negative sign indicates that the measured field is smaller than that in the map; the measured momentum should thus be correspondingly decreased).

A test was carried out to establish the reliability of the hall probe for positive currents [343]. A NMR device was placed inside the magnet, close to the center, and a calibration of the hall probe as a function of the absolute value of the field was made at the three currents, for both current signs. It was found that the hall probe was wrongly calibrated for positive currents: the field corresponding to the observed hall probe values for positive currents is in absolute value the same as the the one contained in the map, within 0.05%.

We conclude that:

1. Hall probe corrections should not be applied to the runs with positive currents. This may lead to an uncertainty of ±0.05% on the field (and thus on the momentum) for these runs (P1C87, P2A87 and P2B87).

2. Hysteresis effects in the MNP26 magnet are smaller than 0.1%.

A.5.2 Accuracy of the Alignment

BCS Chambers y Alignment

The BCS chambers alignment in y and z is generally accurate to the level of 100-200 μm: this means that the mean of the residuals (i.e. the extrapolation of the P0E, P0A, P45 line minus the coordinate of the found hit), for each chamber, is less than ± 100-200μm.

The effects on the momentum of a misalignment in y can be easily evaluated. We conservatively assumed a relative misalignment of chambers BCS(3) and BCS(5)+BCS(6) of 300 μm; the resulting error on the slope is then given by (300 μm)/(length of the downstream lever arm). A misalignment of BCS(2) with respect to the NMC forward spectrometer has an effect of similar size on the incoming track slope. By comparing these errors with the actual deflection we obtained the results presented in table A.2. The larger the deflection, the smaller the sensitivity to y misalignments: for fixed energy the dependence on y misalignments decreases with increasing current in the MNP26 magnet. For fixed magnet current the dependence is weakest at the lowest beam energy.

Parallel shifts of the whole downstream set of chambers (BCS(3)-BCS(6)) along y (but also x or z) do not affect the results as the momentum is in essence computed from the difference of the incoming and outgoing track y slopes only.

BCS Chambers x Alignment

The chambers cannot be aligned in x by using the data alone and one has to to rely on the surveyors' measurements. A few considerations on the accuracy of the chambers x alignment are possible.

- As mentioned above only the *relative* x alignment of chambers BCS(3) and BCS(5) + BCS(6) is really relevant: the absolute x position of these chambers is not used to extract the momentum.
- The x position of the chambers BCS(1) and BCS(2) is not very critical, as the beam tracks traverse them always with the same inclination, both in the alignment run and in the calibration runs. The only effect of an x misalignment of these chambers is an error on the point where the track enters the magnet. This is equivalent to a misalignment of the MNP26 magnet, whose effects are discussed below.
- A misalignment of BCS(3) with respect to BCS(5)+BCS(6) in x is in principle detectable by comparing the results obtained from tracks with different slopes dy/dx, e.g. those of the 550 A, 960 A and 1800 A runs. If, for instance, we evaluate the x shift necessary to account for the 0.1% difference between the 550 A and 960 A results, we find that the distance between BCS(3) and BCS(5)+BCS(6) should be decreased by $\sim$ 8 cm, which is a rather substantial amount.
- The chambers downstream of the magnet were moved between the 1986 and 1987 runs and their positions remeasured. The uniformity of the 1986 and 1987 results suggests that if the x alignment is wrong, then it is so for both years in the same way, which is unlikely.

BCS Chambers Tilts

Possible rotations of the BCS chambers in the y-z plane with respect to their nominal position were investigated by plotting the residuals as a function of the coordinate orthogonal to the wire direction.

Tilts larger than 0.4 mm over 8 cm are excluded in the y planes. Tilts larger than 1 mm over 8 cm are excluded in the z planes; the latter were explicitely shown not to have effects on the calibration results.

MNP26 Magnet Alignment along y and z

If the position of the MNP26 magnet is not the one measured by the surveyors, tracks traverse a region of the magnet different from the one assumed in the reconstruction program. The field

	960 A
$y \pm 5$ cm	−0.06%; −0.06%
$y \pm 8$ cm	−0.20%; −0.10%
$y \pm 10$ cm	−0.32%; −0.09%
$z \pm 3$ cm	+0.03%; −0.09%

Table A.3: Sensitivity of $\Delta P/P$ to MNP26 magnet y and z misalignments at 90 GeV

	550 A	960 A	1800 A
$y \pm 5$ cm	−0.11%; −0.11%	0.00%; 0.00%	−0.10%; +0.10%
$y \pm 8$ cm	−0.05%; −0.15%	−0.05%; −0.05%	−0.41%; −0.25%
$y \pm 10$ cm	0.00%; −0.21%	−0.15%; −0.15%	−0.77%; −0.67%
$z \pm 3$ cm	+0.15%; +0.10%	0.00%; −0.05%	+0.20%; 0.00%

Table A.4: Sensitivity of $\Delta P/P$ to MNP26 magnet y and z misalignments at 200 GeV

integral seen by a track is then different from the one used to compute the track momentum, which is therefore systematically wrong.

The dependence of the measured track momentum on the MNP26 magnet position was studied. The magnet position was changed, in the analysis program, by up to ± 10 cm along y and ± 3 cm along z and the momentum recomputed. All combinations of beam energies and magnet currents were considered. Tables A.3, A.4 and A.5 summarize the results on $\Delta P/P$.

The results are quite insensitive (at the 0.1% level) to the z shifts. Shifts along y are also of little consequence to the 550 A and 960 A calibrations: even a ±10 cm shift along the y direction causes changes of the computed momenta typically smaller than 0.2%.

The 1800 A data are on the contrary more sensitive to y shifts of the magnet. This is a consequence of the fact that the field at 1800 is less homogeneous than at the lower currents.

MNP26 Magnet Alignment along x

Misalignments of the MNP26 magnet along the x direction affect the momentum determination because, if the track has a non-zero slope, the y and z coordinates of the point where the particle actually enters the magnet are different from those assumed in the reconstruction program. Once again then the field integral seen by the muon is not the same as the one used to compute

	550 A	960 A	1800 A
$y \pm 5$ cm	−0.11%; −0.26%	+0.14%; +0.07%	−0.08%; −0.08%
$y \pm 8$ cm	−0.19%; −0.26%	+0.11%; +0.07%	−0.40%; −0.51%
$y \pm 10$ cm	−0.11%; −0.26%	−0.03%; −0.08%	−0.58%; −0.92%
$z \pm 3$ cm	+0.07%; +0.03%	+0.03%; +0.07%	+0.03%; −0.08%

Table A.5: Sensitivity of $\Delta P/P$ to MNP26 magnet y and z misalignments at 280 GeV the momentum.

This effect is however very small: a 10 cm misalignment along x causes an error on the y coordinate of the point where the track enters the magnet of about 300 μm (having assumed a typical y slope of the incoming track $y' = 3 \times 10^{-3}$). The error on the z coordinate is about 10 times smaller, since the z slope is $\simeq z' = 4 \times 10^{-4}$.

In view of the discussion presented above on the consequences of y and z misalignments of the MNP26 magnet, the effects of x misalignments are then negligible.

A.5.3 Comparison of the Different Methods to Compute the Momentum

A detailed comparison of the results of the three methods outlined in section A.3 was carried out.

Methods 1 and 2 were both used for all calibration runs. Method 3 was applied to the P4A86, P2B87 (960 A and 1800 A) and P2D87 calibration runs. In all cases the ratios of the mean BCS to BMS momenta computed with the three methods agree within 0.15% or better, with the exception of the P2B87, 1800 A run where method 2 and 3 differ by 0.2%. No systematic trend is apparent.

As we mentioned, method 2 is expected to be the most accurate and was eventually adopted. The fact that the results of methods 1 and 2 agree shows that a parametrization like the one given by equation A.2 is an adequate description of the momentum versus track parameters relationship. It also shows that the Monte Carlo representation of the spectrometer and of the beam phase space is adequate. The agreement of method 3 with the other two in turn proves that the Runge-Kutta field integration is carried out correctly (method 3 makes no use of Runge-Kutta integration routines).

A.5.4 Comparison with Other Calibration Methods

The EMC Result

The EMC Collaboration checked the calibration of the BMS in the years 1979-1981 by comparing the momentum measured by the BMS with that measured the EMC forward spectrometer (and thus the FSM magnet) [344]. The result on $(P_{FSM} - P_{BMS})/P_{BMS}$, obtained by averaging over several runs with different energies, was $-0.3\% \pm 0.4\%$, in marginal agreement with the BCS findings.

Calibration of the BMS by using the FSM

Similarly to what the EMC did, a calibration of the BMS was performed by exploiting the FSM magnet of the forward spectrometer.

The same reconstruction program was used as for the BCS analysis: tracks found in the beam hodoscopes are extrapolated to P0B and P0C; the P0B and P0C hits are then used to build the incoming track. This line is extrapolated to P0E and P0A, taking the FSM deflection approximately into account. Hits are found in P0E and P0A and a line is fitted to them. The line is extrapolated to P45 and hits are found there as well. The momentum can be extracted in several ways:

1. A global straight line fit is made to the P0E, P0A and P45 points, thus defining the outgoing line.

The relationship between the difference of the incoming and outgoing track y slopes, $\Delta y'$, and the momentum is then found by fitting a parametrization of the type A.1 to Monte Carlo events, analogously to what is done in method 1 described in section A.3.

2. Instead of exploiting all the downstream chambers P0E, P0A and P45 just one of them may be used. The difference between the actual hit position on a given plane and the extrapolation of the P0B+P0C line to that plane, without taking the FSM field into account, is inversely proportional to the track momentum. The relationship can again be found by means of Monte Carlo simulation.

3. The hits in P0B, P0C, P0D, P0E and P0A can be passed on to the Geometry program and the momentum can then be extracted by using the quintic spline fit. Two combinations of the downstream chambers may be exploited:

   - P0E and P0A;
   - P0A only.

The FSM versus BMS calibration is intrinsically less accurate than the BCS versus BMS one: the lever arms upstream and downstream of the magnet are smaller, the field integral is smaller and the field itself is less uniform than in the BCS case. Alignment errors and chamber resolutions have thus a larger weight.

We will present below the results obtained with methods 2 and 3 applied to the chambers P0A and P45.

The Comparison of the FSM and BMS Average Momenta

Figure A.4 shows the ratios of the FSM to BMS average momenta for several 1986 and 1987 periods. The BCS to BMS ratios are also indicated for the periods where the BCS calibrations are available and are labelled as "BCS" (for these periods the FSM versus BMS and BCS versus BMS calibration results are shown for the same sample of events, which is, in some cases, smaller than the one used for the results presented in the previous section). The points labelled "P0Ay" and "P45y" were obtained with method 2 applied to the y planes of P0A and P45, respectively. The points labelled "SPL P0A" were obtained with method 3 using only the P0A information downstream of the FSM.

In spite of the large spread of the results obtained with the different methods outlined above, it is clear that the momenta measured by using the FSM are in general lower than those obtained from the BCS spectrometer. This can be interpreted as due to the actual FSM field being different from the one in the field map. A direct measurement of the FSM field map, using a NMR probe, did show that this was the case [314].

It is difficult to extract the size of the correction to the FSM field from the FSM versus BCS comparison presented in fig. A.4 because of the large systematic errors of the FSM measurements. We will limit ourselves to the remark that the FSM versus BCS comparison is in at least qualitative agreement with the corrections derived from the measured J/ψ and K^0 masses [315], also shown – for the periods in which they are available – on fig. A.4 and indicated as "K^0" and "J/ψ ", respectively. Such shifts indicate the amount by which the measured J/ψ and/or K^0 masses differ from their true value. For example the 0.7% mass shift for P1C87 means that the measured mass is 0.7% too small; the momenta as measured by the FSM are therefore also 0.7% too small which in turn implies that the field is overestimated by the same amount.

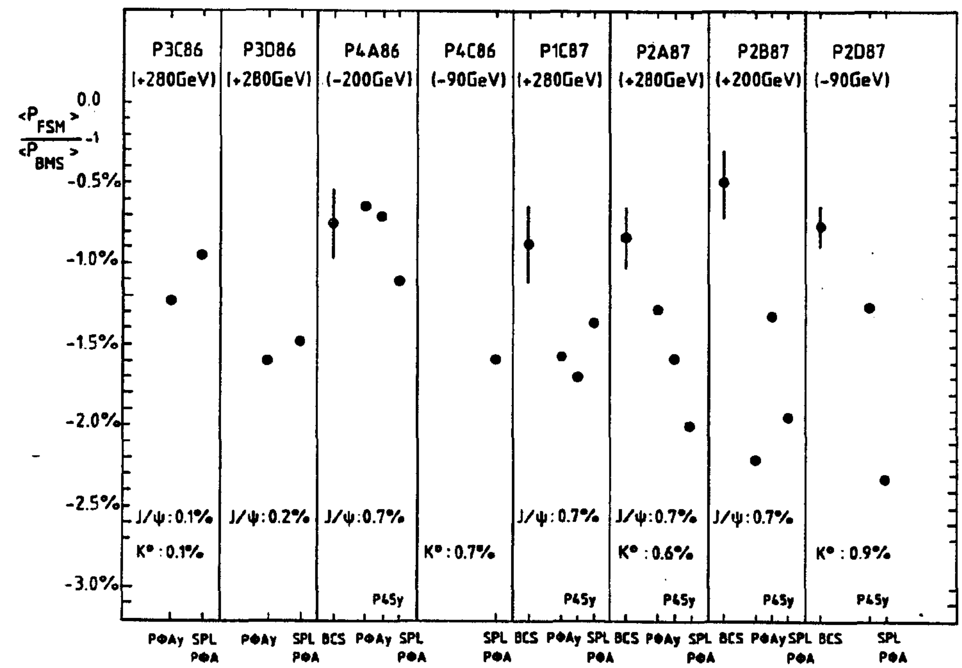

Figure A.4: The ratios of the FSM to BMS average momenta. See text for the explanation of the symbols

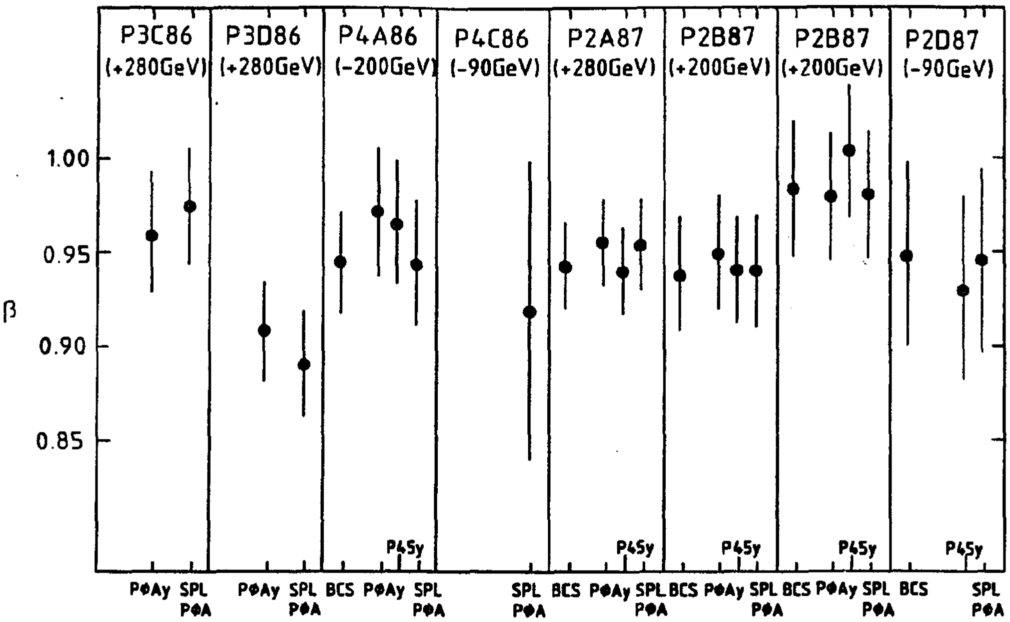

Figure A.5: The slopes of the FSM versus BMS calibration lines. The symbols are the same as for fig. A.4

The Slopes of the FSM/BMS Calibration Lines

Figure A.5 shows the comparison of the FSM versus BMS and BCS versus BMS calibration line slopes β for the same events used for fig. A.4. The error bars show the size of the statistical error from the fits. It can be seen that the BCS results are in general confirmed.

A.5.5 Estimate of the Systematic Errors

The considerations exposed in the previous subsections can be used as a basis for an estimate of the systematic uncertainty of the BCS versus BMS calibration.

As already remarked, the uncertainty on the ratio of BMS to BCS average momenta is dominated by the systematic error, the statistical one being small, due to the correlation between the two measurements. This error allows a shift of the calibration lines parallel to themselves.

On the other hand, the systematic uncertainty on the slopes β of the calibration lines caused by the same sources is small if compared to the statistical error from the fit, and was neglected.

Tables A.6, A.7, A.8 and A.9 give the details of the systematic error calculation. For each beam energy and MNP26 magnet setting, the following contributions were considered:

- uncertainty on the field map;
- uncertainty on the field due to hysteresis effects, only for positive beam sign calibrations, for which, as we saw, the hall probe reading is not reliable (labelled "hall probe");

−90 GeV	960 A
Field map	0.07%
Hall probe	0.00%
Alignment (up)	0.03%
Alignment (dw)	0.03%
Field integration	0.10%
Total −90 GeV	0.13%

Table A.6: Systematic errors at −90 GeV on the ratio of the BCS to BMS average momenta

−200 GeV	550 A	960 A	1800 A
Field map	0.07%	0.07%	0.07%
Hall probe	0.00%	0.00%	0.00%
Alignment (up)	0.12%	0.07%	0.05%
Alignment (dw)	0.12%	0.07%	0.05%
Field integration	0.10%	0.10%	0.10%
Total −200 GeV	0.21%	0.16%	0.14%

Table A.7: Systematic errors at −200 GeV on the ratio of the BCS to BMS average momenta

- error arising from the BCS chambers misalignments;
- uncertainty on the field integration, based on the comparison between the three different methods to obtain the momentum discussed in section A.3.

The systematic errors listed above were treated as independent and summed in quadrature. Two remarks are in order:

1. We mentioned already that the 1800 A field map is probably wrong, at least in some regions. The quoted systematic error for the 1800 A results is thus underestimated by probably a few tenths of a per cent.
2. The uncertainty on the magnet y and z alignment was not included, as it is a priori difficult to assess the error on the magnet position. It should be borne in mind however,

+200 GeV	550 A	960 A	1800 A
Field map	0.07%	0.07%	0.07%
Hall probe	0.05%	0.05%	0.05%
Alignment (up)	0.12%	0.07%	0.05%
Alignment (dw)	0.12%	0.07%	0.05%
Field integration	0.10%	0.10%	0.10%
Total +200 GeV	0.21%	0.16%	0.15%

Table A.8: Systematic errors at +200 GeV on the ratio of the BCS to BMS average momenta

280 GeV	550 A	960 A	1800 A
Field map	0.07%	0.07%	0.07%
Hall probe	0.05%	0.05%	0.05%
Alignment (up)	0.17%	0.10%	0.07%
Alignment (dw)	0.17%	0.10%	0.07%
Field integration	0.10%	0.10%	0.10%
Total 280 GeV	0.27%	0.19%	0.16%

Table A.9: Systematic errors at 280 GeV on the ratio of the BCS to BMS average momenta

that while the 550 A and 960 A results are largely insensitive to this uncertainty, the 1800 A ones are strongly affected by it: if the magnet is misaligned by 5 cm $< \Delta y <$ 8 cm (which cannot be excluded) the results of the 1800 A calibration would decrease by about 0.3%-0.4%. If this were the case the quoted systematic error for the 1800 A results would then be further underestimated.

Appendix B

The Beam Hodoscopes

Introduction

The beam hodoscopes were the only piece of the EMC apparatus which was completely rebuilt by the NMC. The EMC beam hodoscopes [345] consisted originally of 6 planes of 60 channels each. Both BHA and BHB had 3 planes with y, z and ϑ ($+45°$ for BHA, $-45°$ for BHB) orientations, respectively. These planes were supplemented in 1982 by two extra sets of hodoscopes, BHA′ and BHB′, placed immediately downstream of their unprimed omologues and each consisting of 20 y and 20 z strips. In spite of this addition, the performance of the system became rather unsatisfactory, and by 1985 for only about 80% of the triggers was it possible to reconstruct a good beam track. This was a consequence of both the radiation damage suffered by the scintillator and of the deterioration of the glue between scintillator strips and light guides.

The new beam hodoscopes were designed with the purpose of making the system very redundant: the idea was to minimize the degradation of the overall performance in case of a deterioration of the individual counters efficiency, as it had happened for the EMC system, or in case of major failure of some of the planes. In the EMC hodoscopes a beam track was sampled in at most 6 planes (10 after the addition of the BH′ detectors); of these 2 (4) were y, 2 (4) were z, one was ϑ^+ and one was ϑ^-. In the new system a track is seen by up to 16 channels: 4 y, 4 z, 4 ϑ^+ and 4 ϑ^- ones. The track can be fully recostructed even if only half of the counters (e.g. the y, z or the ϑ^+, ϑ^- ones) are working.

The new counters were built in the INFN workshop in Turin between the fall of 1985 and the spring of 1986, including all the mechanical parts and the light guides. The scintillator was cut partly at CERN and partly at the University of Neuchâtel. The old electronics (photomultipliers, bases, discriminators and TDC's) was retained, after a thorough test.

The beam hodoscopes have been working very satisfactorily since 1986. So far no deterioration in the performance of individual channels or of the overall system has been detected.

In this appendix we will complement the information already given in chapters 2 and 3. We will describe details of the mechanical assembly and of the electronics, of the read-out system and of the on-line monitoring and checking programs. The results of a test performed on a prototype plane will also be reported on and a detailed discussion of the off-line recostruction procedure will be presented.

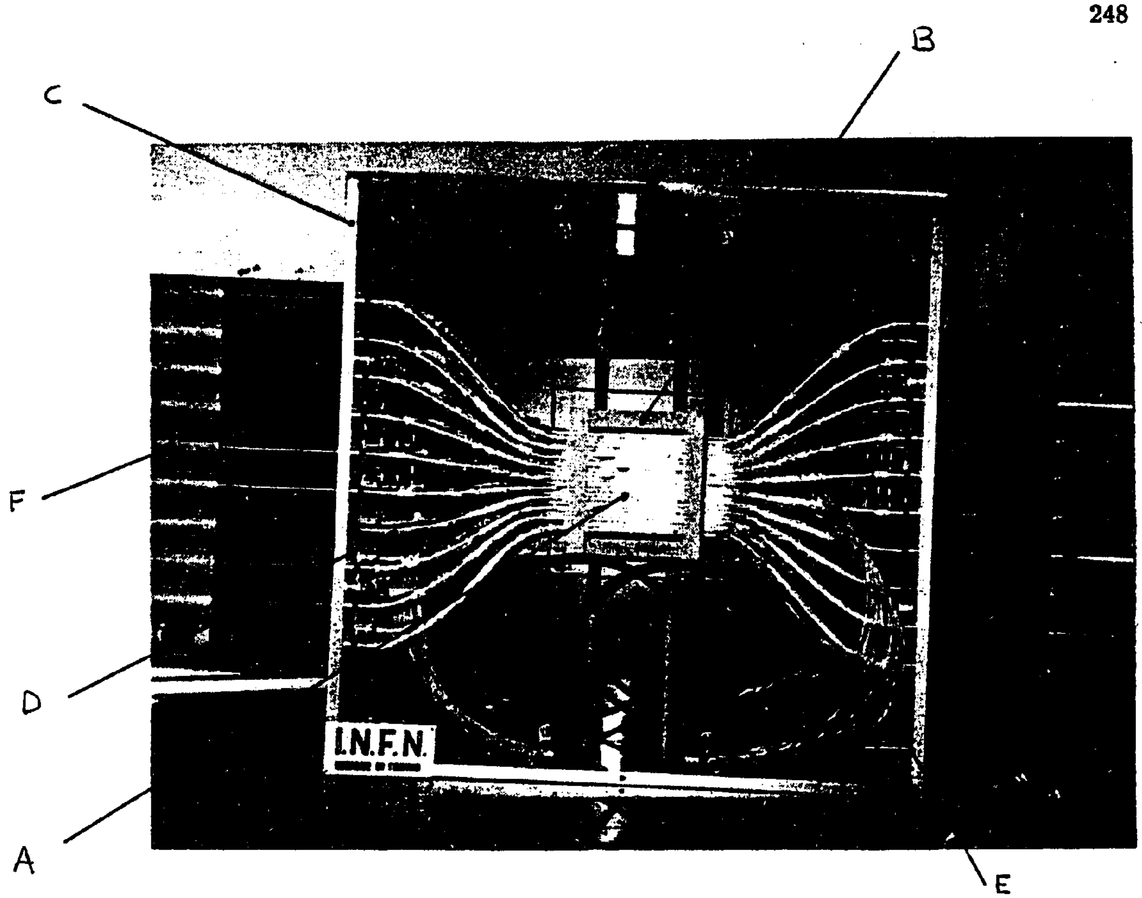

Figure B.1: Photograph of one BH plane

B.1 Mechanical Assembly

The eight BH planes have the same mechanical layout. Figure B.1 shows a photograph of one plane.

The scintillator strips (A in fig. B.1) are inserted into a comblike G-10 frame (B) that insures a relative accuracy of the strip positions better than 0.2 mm. The frame plus scintillator strips system is rigidly attached to a light-tight box, made by an aluminum self-supporting structure (C) closed by two black plexiglass covers (removed in fig. B.1). In the beam region the plexiglass is replaced by a thin PVC window.

Each strip is glued to a plexiglass light guide (D). The surfaces of the scintillator strips to be glued to the light guide were machined so as to make them rough, thereby minimizing light reflection. The scintillating material is NE110. The 4 mm $\times$ 4 mm $\times$ 90 mm strips were cut with a diamond saw from 4 mm thick scintillator plates. Light guides were obtained from cylindrical plexiglass rods of 10 mm diameter, tapered off at one end to a 4 mm $\times$ 4 mm cross section. The machined pieces were polished and then thermally bent to the desired shape (different for each of the 20 strips of a sub-plane, see fig. B.1). Scintillator strips are wrapped into doubly aluminized mylar (0.1 mm thick). Likewise light guides are wrapped into 0.25 mm thick aluminum foil, so as to guarantee the light-tightness of each channel.

An optical fiber (E) is pushed against the scintillator strip end face not glued to the light

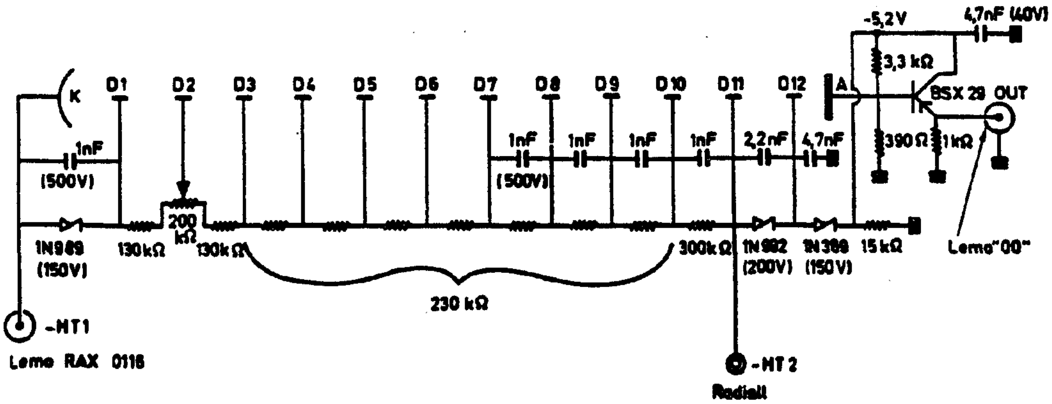

Figure B.2: Scheme of the base (from [345])

guide. The fibers are kept in position by the the G-10 frame mentioned above. The twenty fibers corresponding to one sub-plane can be illuminated by one blue light emitting diode (Siemens SLB 5410, Q68000-A5700) for testing and on-line monitoring purposes.

B.2 Electronics and Read-out

Phototubes and Bases

The photomultiplers used are Thorn-EMI model 9826A. These are 3/4" diameter, 12 stage tubes characterized by high quantum efficiency, high gain, good time resolution and small dimensions. The bialkali photocathodes are particularly sensitive to the blue region of the spectrum; in order to enhance this feature tubes were selected with a Corning Blue (CB) coefficient of at least 8. The CB coefficient is proportional to the photocurrent measured when a half stock Corning CS-5-58 filter is imposed between the light source and the photocathode.

The base circuit diagram is shown in fig. B.2. A standard voltage divider is followed by a current amplifier (a transistor in an emitter-follower configuration) which allows the phototube to operate at lower gain with good time resolution, even at high rates. The low voltage for the current amplifier is supplied independently of the tube high voltage. In order to improve the high-rate performance of the tube, capacitors are inserted between the last seven dynodes and two zener diodes are placed between dynodes 11 and 12 and between dynode 12 and ground. In addition a fixed voltage of 250-300 V ("booster" voltage) can be applied to dynode 11. The overall gain is $\sim 10^8$.

The tubes are mounted in a μ-metal shield, in turn contained in a soft iron cylinder (F in fig. B.1). The latter is screwed onto the aluminum structure C mentioned above. The μ-metal plus soft iron shielding are meant to protect the tube from the fringe field of the last beam line magnets. Fields up to about 100 Gauss can be tolerated.

High Voltage

The high voltage to the tubes is supplied by 6 Le Croy HV4032A units. These are computer controlled via two CAMAC modules Le Croy 2132. Typical high voltage values for the tubes range between 1100 and 1600 V. Generally speaking, tubes with high operating voltages are noisier and less stable in terms of pulse-height than tubes with low operating voltages.

Pulse Shape

Under standard rate conditions ($\approx 2 \times 10^7$ μ/s, corresponding to $\approx 10^6$ μ/s per element) pulse-heights range between 100 mV and 1 V, with typical rise times of about 5 ns.

The response of the tubes is rather sensitive to the rate: the pulse-height increases by a factor ~ 3 if the rate is increased from 1 kHz to 1 MHz. This behavior is not unexpected [346]. For rates larger than 1 MHz the pulse-height starts decreasing; simultaneously the width of the pulses increases. This is the well known "sagging" behavior and is a consequence of the inability of the voltage divider to supply fixed dynode voltages when the current in the tube becomes very large. Sagging can be reduced by applying the booster voltage, but rates larger than ≈ 4 MHz may generally not be tolerated.

Discriminators

The analog signals are fed into the octal discriminators Le Croy 623A. These modules are slightly modified so that one of the three outputs is not a standard NIM pulse, but has a height of -1.2 V. This is done to compensate for the signal attenuation along the 350 ns long cable to the TDC's. The width of the discriminated signals is set to 10 ns. Since the noise of the tubes is negligible, all discriminator thresholds are kept at 40 mV, close to the minimum value of 30 mV.

TDC's

The trigger signal is used as a start of the LeCroy 2228 or 2228A TDC's. A TDC channel receives then a STOP signal, which is the strip's discriminated signal, if there. All TDC's are read out at End-Of-Conversion (the LAM SELECT and Q SELECT switches on the side of the modules are set to EOC) and are used in the 100 ps/count mode. The relative delay of the START and STOP signals is such that for good beam particles the STOP arrives about 25 ns after the START, in the region of maximum linearity of the TDC.

The digitized times are read out by ROMULUS (see chapter 2) and are fed into a CAMAC in-range processor (CERN-EF type 246), programmed to suppress channels with readings larger than 60 ns. The output of the in-range processor is a sequence of words, separate for BHA and BHB, and organized as follows:

$$(ch.\ no.),\ (time); ...(ch.\ no.),\ (time); (marker\ word), (word\ count)$$

where $(ch.\ no.)$ ranges from 1 to 160, $(time)$ may take values between 0 and 600 (units are 0.1 ns), $(marker\ word)$ is a sequence of numbers identifying the piece of apparatus (BHA or BHB) and $(word\ count)$ is the total number of words read out.

B.3 On-line Monitoring and Checking

The program BHMON, originally running on the U1 PDP and now installed on the UXNMCE Micro-VAX, samples events with a given trigger flag and plots the beam profiles and TDC times for the various planes. BHMON makes no use of the standard decoding package (unlike the currently used general purpose monitoring program FASTMON) but decodes directly the BH data as supplied by the in-range processor. It is a powerful debugging tool in case of malfunctioning of the BH's.

Another useful tool, especially in the absence of beam, is the program BHCHK [347]. This program controls the flashing of the diodes mentioned in section B.1 and the subsequent read-out of the hodoscopes. The diodes are connected to the programmable driving units CD-LE 181 [348] (see fig. B.3). These are NIM units that can supply a signal (maximum height 40 V, width 4-5 ns, minimum risetime 1 ns) on one of 6 outputs. Each output is connected to a diode. The selection of the output to be fired and of the intensity can be made manually or via the CAMAC control unit LE 187 [348]. The program BHCHK writes a 16 bit word into the LE 187 module by an appropriate CAMAC instruction; the word is then transferred to the CD-LE 181 unit by means of a serial pulse. A CAMAC output register, upon command from BHCHK, then sends a pulse ("trigger") to the CD-LE 181 module just programmed, thus enabling it to output the signal to the diode. The diode lights up and illuminates the 20 channels of one BH sub-plane. The trigger pulse is also sent, with an appropriate delay, to the START of the BH TDC's; the TDC's are then read out by BHCHK. Dead or inefficient channels can thus be singled out also without beam. In practice each diode is pulsed not just once but twenty times with different intensities. This is because the diode is not seen under the same angle by all the twenty fibers: different diode intensities are thus necessary to provide the same amount of light to each scintillator. All twenty channels are then read out but the pulse height and timing of one only are recorded each time. The BHCHK program can be run automatically at regular time intervals. In order not to interfere with normal data taking, LED's are fired only between spills.

We mention finally the program BHHV, used to interact with the HV units via two CAMAC interface modules Le Croy 2132. Operations on single high voltage channels as well as periodical checks of the high voltage values are possible with BHHV. These functions are now usually done with the program NHVCHK, which controls the high voltages of all the other scintillation counters in the experiment as well.

B.4 Test of the Prototype

All phototubes were tested prior to mounting on the hodoscopes, by measuring the response of the tube to a pulsed light emitting diode. Noisy and inefficient tubes were discarded.

A prototype plane was then brought to SIN/PSI (Villigen, Switzerland) in February 1986 and was tested in a 350 MeV π^+ beam. Two scintillation counters (1.8 cm $\times$ 1.8 cm cross sectional area, 1 mm thickness), one upstream and one downstream of the plane, were used to define the trigger.

Plateau curves were obtained for each tube in order to find the operating voltage: the number of counts recorded by a strip in coincidence with a trigger in a given period of time, normalized to the number of triggers in that period of time, was plotted as a function of the high voltage of the tube, for each tube. Figure B.4 shows a typical example; the arrow indicates the chosen operating voltage.

The efficiency of the hodoscope plane was then measured: the surface of the plane was divided in squares of 1.6 cm $\times$ 1.6 cm area and the efficiency was measured in each of the squares. The efficiency of a sub-plane was found to average around 96%, not far from the value 97.5% expected as a consequence of the 0.2 mm dead space between two neighboring 4 mm strips. No variation in the measured efficiency was detected between regions of the sub-plane close to the photomultipliers and regions far from them. The efficiency of the 2 OR-ed sub-planes was found to be always larger than 99.9%.

The time resolution of the counter was evaluated by measuring the width of the timing

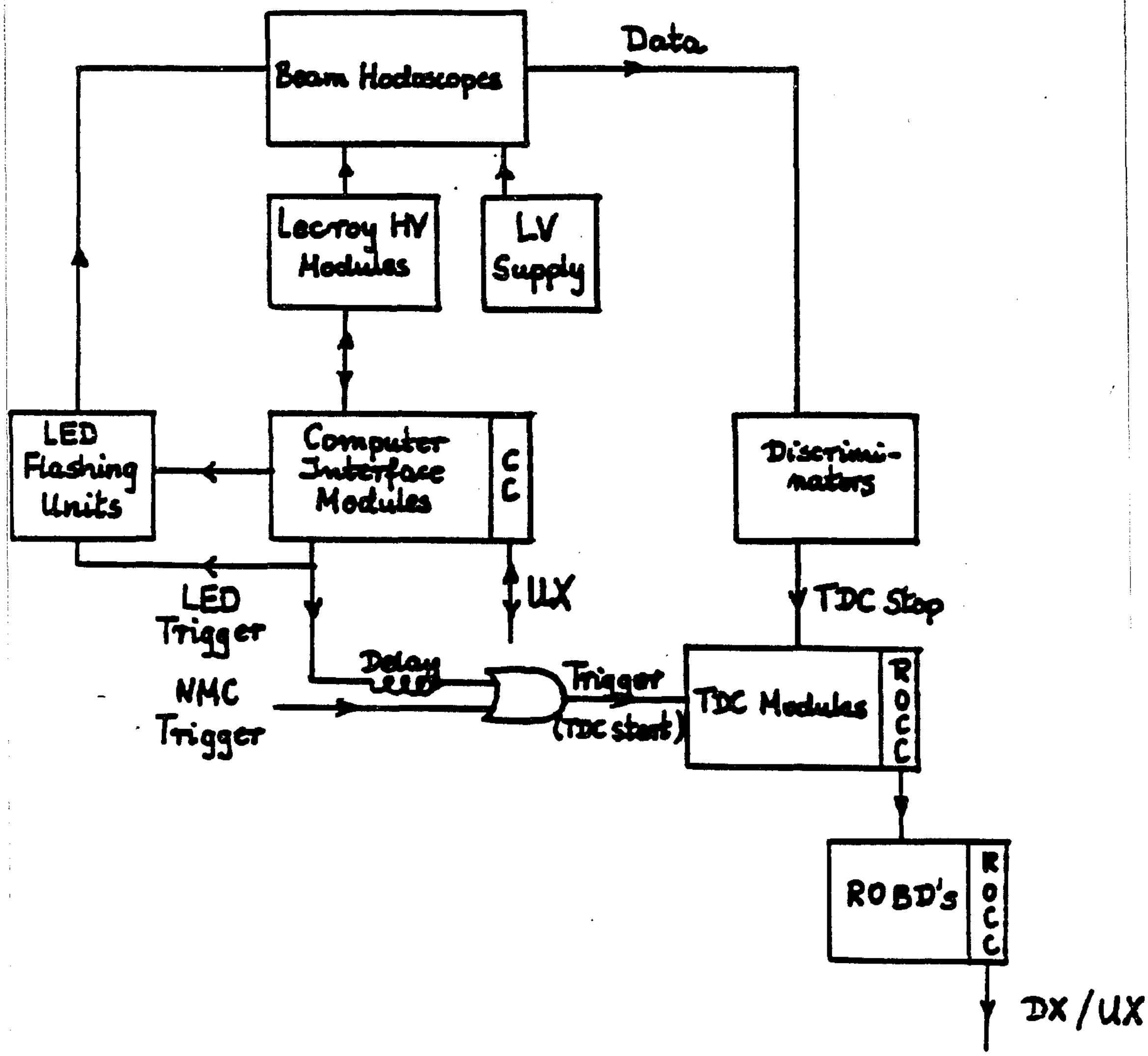

Figure B.3: Layout of the LED flashing system

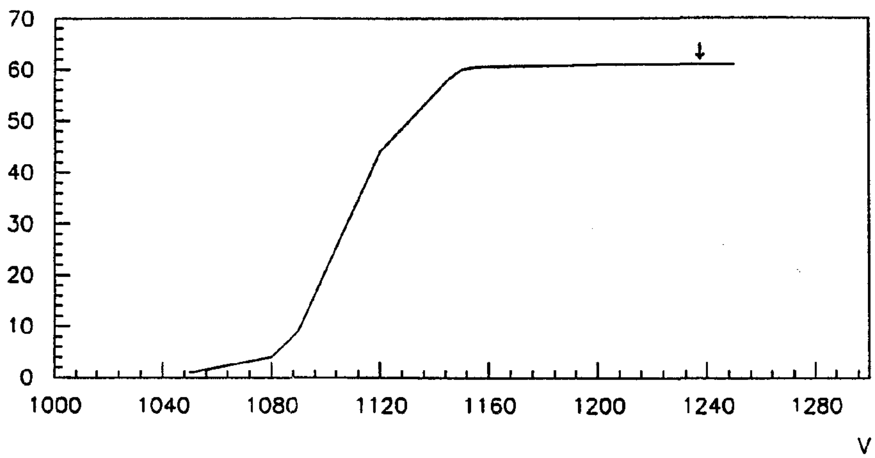

Figure B.4: Example of a plateau curve. The units on the vertical scale are arbitrary. The arrow indicates the chosen operating voltage.

difference between the RF signal from the accelerator and one of the hodoscope strips. The FWHM of the distribution was found to be typically 1.3 ns, corresponding to a time resolution σ of less than 0.6 ns.

During the test the rate per strip was $\approx 3 \times 10^5$ Hz. The stability of the efficiency and time resolution results was checked also for higher rates, up to 2×10^6 Hz.

The full beam hodoscopes system was installed at CERN in the late spring of 1986. In order to define the final operating voltages, the plateau curves of all 320 channels were measured at the standard beam intensities of $\approx 10^7$ muons/s using the hodoscope H5 as a trigger.

B.5 The Off-line Track Reconstruction

The reconstruction of the tracks in the beam hodoscopes is carried out by Phoenix. The relevant routines are contained in the patch BHODO.

Unlike what is done in the hardware, Phoenix treats the BH *sub-planes* (20 channels each) as the fundamental units. In other words the software views the beam hodoscopes as a set of 16, rather than 8, planes. The (sub-)planes are numbered 1-16 in the software: 4 y, 4 z, 4 ϑ^+ and 4 ϑ^-. The y planes, $y_1, ..., y_4$, are in order of increasing x and correspond to the two sub-planes of BHA4 and BHB1. Likewise the four z planes, $z_1, ..., z_4$, correspond to the two sub-planes of BHA3 and BHB2. The ordering of the ϑ^+ and ϑ^- planes is similar.

The philosophy of the beam track reconstruction is the following. The hits in the y and z planes are used to build lines in the y and z projections. The lines found in y and z are then matched using their timing and are associated to hits in the ϑ planes. A three dimensional line fit is finally made to all y, z and ϑ points found for each line. Remaining, unused hits are fed into a similar algorithm, which searches for lines in the ϑ^+ and ϑ^- planes. Lines are matched, associated to hits in y and z and a 3-d fit is performed.

In principle the y, z planes alone or the ϑ^+, ϑ^- ones would be sufficient to reconstruct the beam tracks. The redundancy in the number of measured points per track is one of the major improvements with respect to the old EMC beam hodoscopes: it insures a satisfactory performance also in difficult situations, like at very high beam intensities or in case of malfunctioning of several planes.

We briefly outline the structure of this part of Phoenix. The control routine is BHODO. First the BH information is decoded and TDC cuts are imposed. BHODO then calls the routine BHLINE with argument ITHETA=0. This routine does the line finding in the y and z projections (by calling BHTRAK), matches the y and z lines, looks for hits which may belong to this line on the ϑ planes and finally makes a 3-d fit. All hits used so far are flagged and then BHLINE is called again with argument ITHETA=1. The whole procedure just described is repeated, except that the roles of the y, z and ϑ^+, ϑ^- planes are interchanged.

Line finding in a projection is done by the routine BHTRAK. Let us take a y line as an example. BHTRAK first checks that there are at least 3 hits on different planes (i.e. at least three y planes have been hit, this is the minimum plane requirement). The first and last y planes (along the beam) which have at least one hit are taken as "key-planes". The hits on these planes ("key-plane hits") are used to build a line. Hits on the remaining y planes are then looked for within a given road of this line; if enough hits are found a linear fit is made to them. The contribution of each hit to the global χ^2 is evaluated and if it is larger than a threshold value the hit is discarded. This may cause the line to be rejected, should the minimum plane requirement no longer be satisfied.

The procedure is repeated for all key-plane hits and the combination which gives the lowest χ^2 is taken.

The BHTRAK algorithm is in essence the same as the one used to find lines in most of the other detectors in the experiment (PTRACK). There is however one important difference due to the fact that all beam hodoscopes hits come with timing information, which is used throughout BHTRAK. For instance the relative timing of key-plane hits must fall within a given window; similarly non-key-plane hits must be close to the average time of the key-plane hits. Furthermore, when a χ^2 is computed, it is always a combination of the usual spatial χ^2 and of a "time χ^2 ". The latter is defined as

$$\chi_t^2 = \sum_i (t_i - < t >)^2 / \sigma_t^2,$$

where t_i's are the timings of the individual hits, $< t >$ is their average and σ_t is an appropriate parameter (see next section).

Typical results, for a standard intensity run ($\approx 10^7 \mu/s$) and T1, T2 triggers, are that for about 94-97% of the triggers at least one good beam hodoscope track is successfully reconstructed. This quantity is often referred to as "reconstruction efficiency" and is the fundamental figure of merit for the beam hodoscopes. In the y, z mode (BHLINE(ITHETA=0)) the beam track is found for 80-85% of the triggers; the remaining 10-15% are recovered in the ϑ^+, ϑ^- mode (BHLINE(ITHETA=1)). The quoted value for the reconstruction efficiency does not significantly degrade up to the highest intensities reached of $\approx 5 \times 10^7 \mu$/spill $\approx 3 \times 10^7 \mu/s$.

In order for the BH track to become a good beam track, it must be associated with a good BMS track, recorded within a narrow time window (see parameter BHCUT8(13) below). For normal physics triggers and standard BMS conditions there is at least one BMS+BH correlated track in $\approx 90\%$ of the cases.

B.6 Tuning of the Beam Hodoscopes Reconstruction Parameters

Two sets of parameters need to be tuned for the beam hodoscope reconstruction: the so-called T_0's and the pattern recognition parameters.

T_0 Determination

As we explained in section 3.6.1, the T_0's are the offsets which must be subtracted from the TDC reading of a given channel in order to obtain physically meaningful timings. A perfect timing at the hardware level would in principle be possible, but would require a careful tuning of the lengths of all cables, of the thresholds of all discriminators etc. It is therefore preferrable to have a rough hardware timing (good to, say, 10 or 20 ns) and then do a fine tuning at the software level. This kind of tuning must be repeated at least for every data taking period and everytime the hardware timing is changed (e.g. when a tube is replaced, the length of a cable is changed etc.).

In order to extract the T_0's, Phoenix should be run with the patchy switch BHTIMEALL on a T5 alignment tape. Histograms 2229-2244 show the $(T - T_0)$ distribution for each element of each plane: the point is to adjust the T_0's until the peaks of all channels fall within few nanoseconds. To this purpose the BH and the BMS timings are written out for each channel, for 100 events (patchy switch BHT0). A separate program can be used to compute the new T_0's, which should then be put back in the alignment file (in the section *BHTD). At this point the timing differences between hits of the same track, but belonging to different planes (histogram 2299), should be centered on zero (at least 80% of the events within ± 2 ns and r.m.s. < 2 ns). Finally it should be checked that the results are stable when T1 or T2 events are used.

Pattern Recognition Tuning

Once the T_0's have been determined one should check that the values of the pattern recognition parameters are appropriate. We list these parameters here and for those of them which hardly ever need significant changes, we indicate in brackets their standard values. We also mention the relevant Phoenix histograms which should be considered in the tuning procedure.

1. TDC cut (BHCUT8(1)=150 tenths of ns). See histograms 2261-2276 ($T - T_0$ distributions) and 2205-2212 (multiplicities per plane, before and after the TDC cut).

2. TDC cut for T10 tracks (BHCUT8(1)=600 tenths of ns).

3. BHTRAK key-plane time cut (BHCUT8(3)=50 tenths of ns). See histograms 2300 and 2357 (key-plane hits time differences for all tracks and for good tracks; cf. fig. 3.1, page 134).

4. BHTRAK intermediate plane time cut (BHCUT8(4)=40 tenths of ns). See histograms 2301, 2302 and 2358 (intermediate plane times with respect to the average of the key-plane times for all hits, hits within the roadwidth and hits belonging to good tracks, respectively). This cut is also used to associate ϑ hits to a y, z line and y, z hits to a ϑ line; the relevant time differences are plotted in histogram 2351.

5. BHTRAK spatial roadwidth cut (BHCUT8(5)=0.004 m). See histograms 2304-2307 (distributions of prediction from key-plane line minus coordinate of the actual hit in the intermediate planes).

6. Mean time standard deviation σ_t used to work out χ_t^2 (σ_t =BHCUT8(6)=6.5 tenths of ns). See histogram 2334 (χ_t^2 probability); if σ_t has a sensible value this histogram should be about flat (except for a spike close to zero).

7. Maximum value of χ_t^2 per hit (BHCUT8(7)=8). See histograms 2320, 2330, 2321 and 2331 (χ_t^2 before cuts and after cuts).

8. Maximum time difference between y and z (or ϑ^+, ϑ^-) projections (BHCUT8(8)=20 tenths of ns); these time differences are plotted in histogram 2350.

9. Roadwidth for ϑ hits, when BHLINE is in the y, z mode or for y, z points, when BHLINE is in the ϑ^+, ϑ^- mode (BHCUT8(9)=0.004 m). Histogram 2353 shows the distribution of the residuals (extrapolated minus found hit coordinate). This histogram should be used not only to define BHCUT8(9), but also to verify that the relative spatial alignment of the beam hodoscopes is good. To this purpose one should also check the spatial χ^2 for good tracks (histograms 2340, 2341) and the residuals ofthe final 3-d fit (coordinates of the actual hits minus the extrapolation of the final 3-d fit, histograms 2571-2586).

10. Roadwidths for association of P0B hits to a BH line (BHCUT8(10,11,12)=0.005 m). See histograms 2641-2648 (distances between the reconstructed beam track and the closest hit in each plane of P0B).

11. Minimum number of good ϑ hits (in the y, z mode) or of good y, z hits in the ϑ^+, ϑ^- mode (LHCUT8(1)=0).

12. Maximum difference between the BH and BMS times for a track (BHCUT8(13)=20 tenths of ns). This difference is plotted in histograms 2700-2705 for triggers 1-5 and 10, respectively.

13. Global time shift between BH and BMS (independent of the channel). This quantity may be different for different triggers and reflects timing shifts of the various triggers with respect to each other (BHCUT8(14-19) for triggers 1-5,10, respectively; see again histograms 2700-2705).

14. Global time shift of BH and BMS with respect to the trigger time, as given by H3V and H4', for T1 and T2 respectively (BHODM1, BHODM2). The differences between the BH and BMS times and the trigger time are plotted in histograms 2707 and 2708.

Appendix C

The Input to the Radiative Corrections Program

The evaluation of radiative corrections requires the knowledge of several input parameters; we recall a few of them:

- the structure function F_2 and the ratio $R = \sigma_L/\sigma_T$, for the inelastic tail;
- the nucleon elastic form factors and the so-called quasi-elastic suppression factors, for the quasi-elastic tail;
- the coherent nuclear form factors, for the elastic tail.

For some of these quantities (e.g. form factors, F_2^D, R) parametrizations of the available experimental data were used. For others (e.g. suppression factors) it was necessary to resort to the results of model calculations.

In the following we shall examine in some detail the situation for the most relevant of these quantities. In particular, we will compare the results obtained for radiative corrections when different parametrizations or calculations are used. This will serve as a basis for the determination of the systematic errors on the structure function ratio due to radiative corrections.

C.1 The Inelastic Tail

C.1.1 The Parametrization of F_2^D

For the deuterium absolute structure function we used a fit to the results of deep inelastic scattering experiments and to small W data in the $\Delta(1232)$ resonance region.

The function fitted to the data has the following form:

$$F_2^D(x,Q^2) = \left\{1 - G_E^2\right\} \left\{F^{DIS}(x,Q^2) + F^{res}(x,Q^2) + F^{bkg}(x,Q^2)\right\},$$

where F^{DIS} is a parametrization of F_2 in the deep inelastic region, F^{res} is the resonance region contribution and F^{bkg} parametrizes the background under the resonance. The term $(1 - G_E^2)$, with G_E proportional to the nucleon electric form factor, $G_E = (1 + Q^2/0.71)^{-2}$, suppresses F_2 at small Q^2, where elastic scattering on the nucleon dominates [24].

The explicit form of F^{DIS} reads:

$$F^{DIS}(x,Q^2) = \left[\frac{5}{18}\frac{3}{B(\eta_1,\eta_2+1)}x_W^{\eta_1}(1-x_W)^{\eta_2} + \frac{1}{3}\eta_3(1-x_W)^{\eta_4}\right]\left[1-e^{-a(W-W_{thr})}\right], \quad \text{(C.1)}$$

where

- $x_W = \frac{Q^2+M_A^2}{2M\nu+M_B^2}$ is the so-called Weizmann scaling variable which extends the scaling down to values of Q^2 near 0.1 GeV^2; $M_A^2 = 0.351$ GeV^2, $M_B^2 = 1.5121$ GeV^2 (cf. p. 1495 and table VIII in [263]);
- $\eta_1 = p_1 + p_2\bar{s}$;
- $\eta_2 = p_3 + p_4\bar{s}$;
- $\eta_3 = p_5 + p_6\bar{s}$;
- $\eta_4 = p_7 + p_8\bar{s}$;
- $\bar{s} = \ln\frac{(\ln Q^2+M_A^2)/\Lambda^2}{(\ln Q_0^2+M_A^2)/\Lambda^2}$, with $\Lambda = \Lambda_{QCD} = 0.2$ GeV and $Q_0^2 = 2$ GeV^2;
- $B(z,w) = \frac{\Gamma(z)\Gamma(w)}{\Gamma(z+w)}$ and Γ is Euler's function;
- $a = 4.177$ GeV^{-1};
- $p_1, p_2, ..., p_8$ (as well as p_9, p_{10} mentioned below) are the parameters of the fit.

The first bracket in equation C.1 is the function originally proposed by Buras and Gaemers [262]. The factor $[1-e^{-a(W-W_{thr})}]$ suppresses F^{DIS} in the resonance region, at values of W close to the one pion production threshold, $W_{thr} = M + m_\pi$. The value of a is such that F^{DIS} is suppressed by about a factor two at $W = 2$ GeV. The fit is not very sensitive to the value of a.

The form adopted for the resonance region contribution is

$$F^{res}(x,Q^2) = p_9^2 G_E^{3/2} e^{-(W-M_\Delta)^2/\Gamma^2},$$

in which only the Δ contribution is taken into account and higher mass resonances are neglected. The parameter Γ, defining the effective width of the resonance, has the value Γ=0.0728 GeV^2.

Finally, the background under the resonance region was parametrized as

$$F^{bkg}(x,Q^2) = p_{10}^2 G_E^{1/2} q^* e^{-b(W-W_{thr})^2},$$

where q^* is the pion momentum for single pion production in the π-N center of mass frame

$$q^* = \sqrt{\frac{[(W+W_0)^2+M^2-m_\pi^2]^2}{4(W+W_0)^2} - M^2},$$

	p_1	p_2	p_3	p_4	p_5
standard	0.75966	−0.18202	3.5200	0.46256	0.83691
lower limit	0.74296	−0.20019	3.4819	0.45823	0.79157
upper limit	0.77171	−0.19672	3.5390	0.40757	0.94675
SLAC norm. fixed	0.76533	−0.12523	3.5971	0.46280	0.94008
BCDMS norm. fixed	0.73099	−0.10822	3.5446	0.53400	0.89336
	p_6	p_7	p_8	p_9	p_{10}
standard	0.97906	12.876	−2.9558	0.89456	0.16452
lower limit	0.96662	13.247	−3.5632	0.89456	0.16452
upper limit	1.0889	13.352	−3.9720	0.89456	0.16452
SLAC norm. fixed	1.1679	13.717	−4.3281	0.88181	0.19707
BCDMS norm. fixed	1.1385	14.692	−4.9523	0.86313	0.18792

Table C.1: Results of the F_2 fits

with $W_0 = 0.05$ GeV and $b = 0.5$ GeV^{-1}. The inclusion of the factor q^* insures that the background contribution is zero at the resonance threshold.

The following data sets on deuterium were included in the fit:

1. The results of a global reanalysis [46] of the SLAC experiments E49A,B [263, 264, 265], E61 [24], E87 [263], E89A,B [266, 267], E139 [35] and E140 [43, 45] (electron beams up to 20 GeV). This reanalysis featured a new treatment of radiative corrections, a better estimate of the relative normalization of the data sets and a detailed propagation of systematic errors, including all known correlations.
2. BCDMS [268] (120, 200 and 280 GeV muon beam);
3. EMC NA28 [40] (280 GeV muon beam);
4. FNAL CHIO [219] (147 GeV muon beam);
5. SLAC E89 [267] (electron beam up to 20 GeV, data in the resonance region).

The relative normalization of the various data sets was not adjusted and only the statistical errors of the points were used as weights. Table C.1 shows the results of the fit for the parameters $p_1, ..., p_{10}$. The total χ^2 of the fit is 1975 for 595 degrees of freedom; the poor χ^2 is due to the fact that only the statistical errors of the points were used in the fit. The results of the fit do not change appreciably if the CHIO data [219] are excluded. The function F_2^D obtained from the fit is plotted in fig. C.1.

A lower limit for F_2 was obtained by repeating the fit with data sets 1.-4. simultaneously lowered by their quoted normalization error, which was also included in the weights. Similarly an upper limit was obtained by raising the same data sets by their normalization uncertainty. These limits were taken as an indication of the systematic uncertainty on F_2; the resulting values for the parameters $p_1, ..., p_8$ are given in table C.1; the parameters p_9, p_{10} were kept fixed. The corresponding functions are plotted in fig. C.1.

The fit was also repeated allowing the normalization of the input data sets to vary with respect to one of them, which was kept fixed. Table C.1 shows the results for the following two cases:

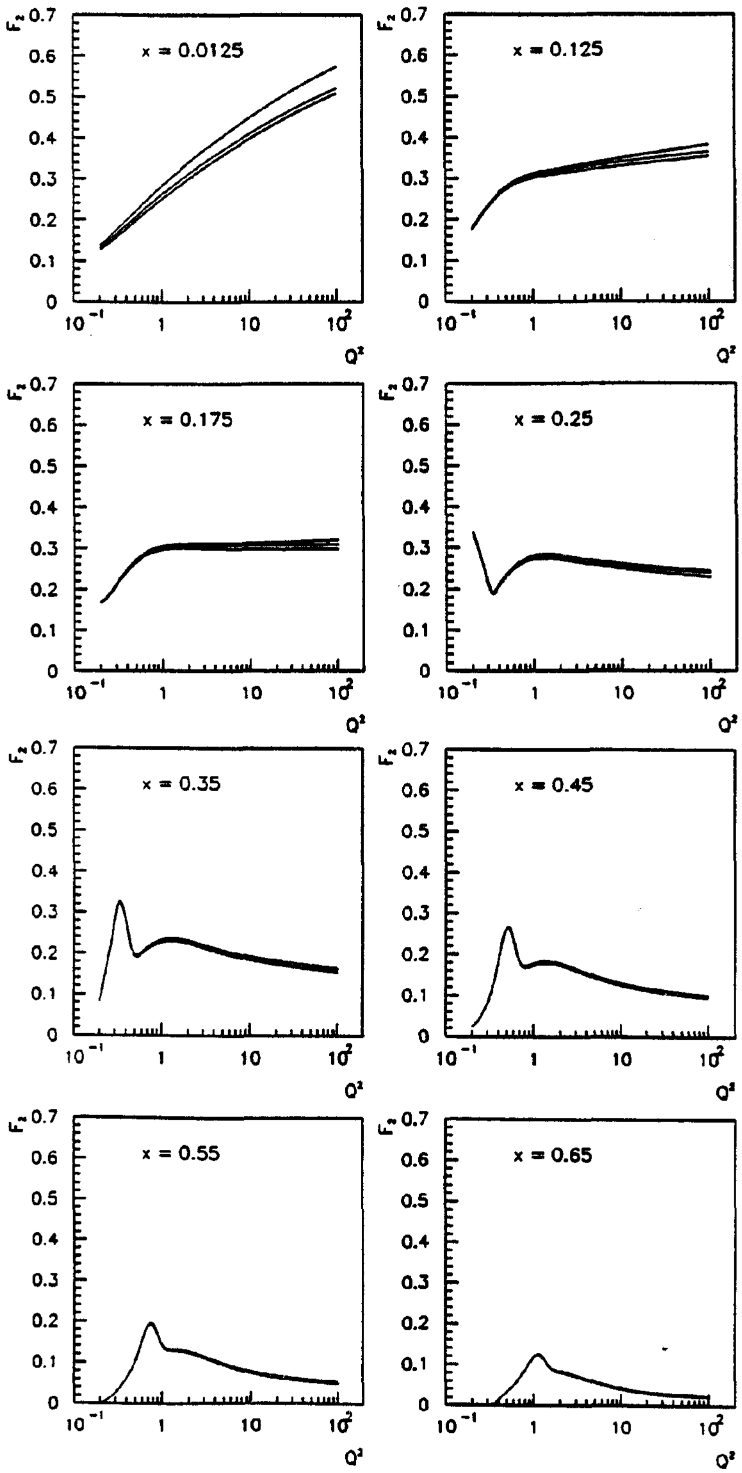

Figure C.1: Fits to F_2^D: the inner line is the fit labelled "standard" in table C.1; the upper and lower lines are the upper and the lower limits described in the text

	SLAC	BCDMS	NA28	CHIO	E89
SLAC norm. fixed	1.0000	0.95164	0.93630	0.96064	1.0841
BCDMS norm. fixed	1.0450	1.00000	0.97464	1.00180	1.1311

Table C.2: Amounts by which the various data set were renormalized

x	He supp. [279] vs [276]	He supp. [281] vs [276]	D supp. [278] vs [276]	F_2^D upper limit vs standard	F_2^D lower limit vs standard	x, Q^2 fit C.4 vs fit C.2
0.0035	−0.012	−0.010	−0.002	0.005	−0.003	−0.004
0.0055	−0.013	−0.009	−0.002	0.004	−0.002	−0.003
0.0085	−0.009	−0.006	−0.002	0.002	−0.001	−0.003
0.0125	−0.006	−0.004	−0.001	0.001	−0.001	−0.003
0.0175	−0.004	−0.003	−0.001	0.001		−0.003
0.025	−0.002	−0.002				−0.003
0.035	−0.001	−0.001				−0.003
0.045	−0.001	−0.001				−0.003
0.055	−0.001					−0.003
0.070						−0.003
0.090						−0.002
0.125						−0.002
0.175						−0.002
0.25						−0.001
0.35						−0.001
0.45						−0.001
0.55						
0.65						

Table C.3: Amount by which σ^{He}/σ^D changes due to modifications of some of the input parameters to the radiative correction program. Changes smaller than 0.001 are not indicated

1. SLAC data fixed;

2. BCDMS data fixed.

The normalization factors for each data set are indicated in table C.2.

The radiative corrections were recomputed for each of the above fits and the largest changes in the results were in fact found for the upper and lower limits defined above. The effect of these changes on the ratio is 0.3-0.5% at low x (see table C.3, fifth and sixth column).

C.1.2 The Parametrization of σ^{He}/σ^D

The parametrization for the EMC effect in helium, used to evaluate the helium structure function $F_2^{He} = F_2^D \times (F_2^{He}/F_2^D)$, was obtained by fitting the following function to the measured ratio σ^{He}/σ^D as a function of x:

$$r(x) = A + Bx + Ce^{Dx} + Ex^F. \tag{C.2}$$

For $x > 0.3$ the SLAC E139 measurements [35] were also included in the fit. The values found for the parameters are given in table C.4. Figure C.2 shows the fit together with the NMC and the SLAC E139 data.

A	B	C	D	E	F
1.0299	−0.15591	−0.09249	−29.423	0.20590	7.2983

Table C.4: Results of the fit of the cross section ratio to the function C.2

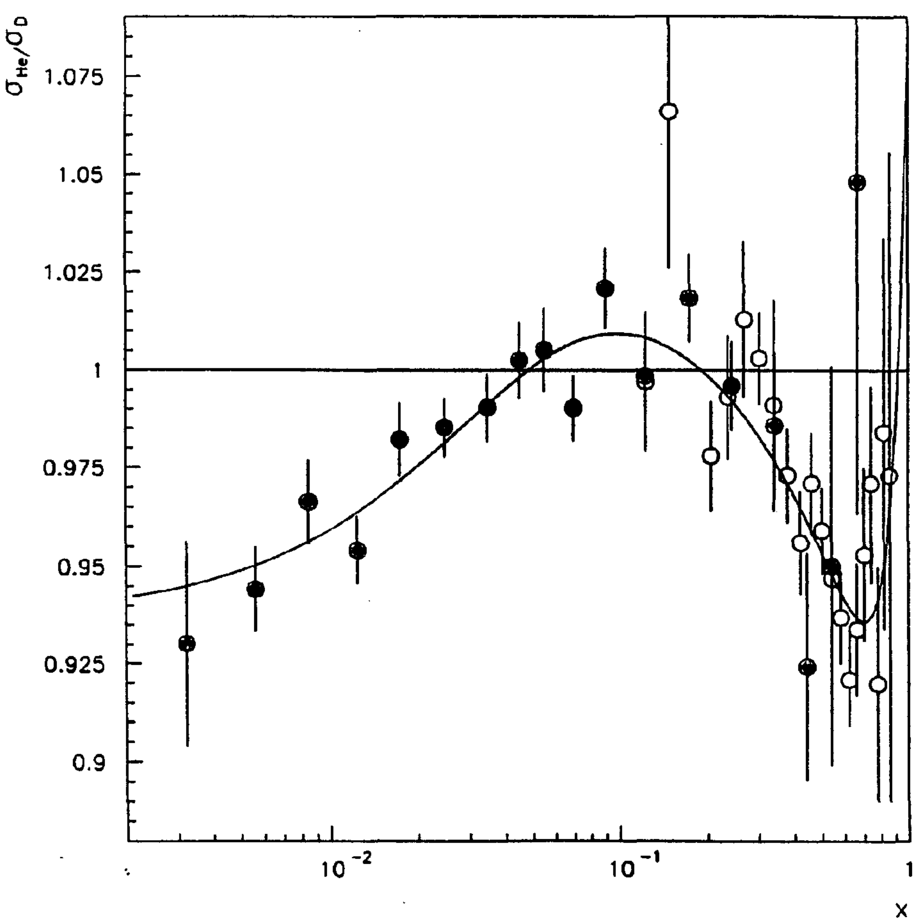

Figure C.2: The cross section ratio σ^{He}/σ^{D}. The present results (full symbols) are shown together with the SLAC E139 ones [35] (open symbols). The continuous line is the result of the fit described in the text

a	b	c	d	α	β	γ
0.75090	−0.68277	0.19090	−0.04227	0.13635	2.3204	−0.10735

Table C.5: Results of the fit to σ^{He}/σ^{D} with the function C.4

Radiative corrections are nearly independent of the behavior of the parametrization at large x. In particular they are hardly sensitive to the inclusion of the SLAC measurements [35] in the fit: if a function of the form

$$r(x) = A + Bx + Ce^{Dx} \tag{C.3}$$

is fitted to the NMC data only – without including the SLAC E139 ones – and is used in the radiative corrections program, the results for the ratio vary by less than 0.1%.

A fit was also made to σ^{He}/σ^{D} with a function depending on both x and Q^2:

$$r(x) = [a + bx + c\exp(dx)]\{1 + [\alpha(1-x)^{\beta} + \gamma]\ln Q^2\}. \tag{C.4}$$

The NMC data only were used. The resulting parameters are given in table C.5. If this fit is used as an input to Ferrad, the radiative corrections for He decrease by 0.2% to 0.3%, nearly independently of x (see table C.3, last column).

C.1.3 The Parametrization of $R = \sigma_L/\sigma_T$

A phenomenological parametrization of R, proposed by Whitlow [46, 47] and known as R^{1990} was used. It is based on fits to the results of several SLAC and CERN experiments. The SLAC experiments are E49A,B [263, 264, 265], E61 [24], E87 [263], E89A,B [266, 267], E139 [35] and E140 [43, 45]. The data from these experiments were globally reanalyzed, as discussed already above for F_2. The fits include also the results of the EMC [8, 29], BCDMS [268] and CDHSW [269] experiments at CERN.

The parametrization R^{1990} is actually the average of three fits to the same data with three functional forms, each with different characteristics outside the measured region; their average is valid over a wide kinematic region, including the resonance region, the $x \to 1$ region and for large Q^2. However it does not apply for $Q^2 < 0.3$ GeV^2. The error on R^{1990}, also given in [46, 47], is estimated as the quadratic sum of three contributions: the uncertainty due to the experimental errors, the uncertainty due to the assumed functional form and the uncertainty due to errors in the radiative corrections.

For the region $Q^2 < 0.35$ GeV^2 we assumed $R = R(Q^2 = 0.35$ GeV$^2)$. Adopting the rather extreme alternative assumptions $R = 0$ or $R = 2R^{1990}$ for $Q^2 < 0.35$ GeV^2 has hardly any effect on the radiative corrections. The resulting changes of the structure function ratio are less than 0.1%. Likewise the variation of R within the estimated error for $Q^2 > 0.35$ GeV^2 affects the structure function ratio by at most 0.1% at small x.

In general the dependence of our results on R is small; going to a simple, QCD inspired parametrization, like [270]

$$R(x) = 0.482\exp(-4.4529x^{0.538}) \tag{C.5}$$

also does not change the results appreciably.

The extreme choice $R = 0$ (consistent with the EMC results [8, 29]) was also tested. Only in this case do the radiative corrections change significantly: the results for the ratio are modified by up to 0.8% at small x.

C.1.4 Effects of $R^{He} - R^D \neq 0$

In this work we assumed that $R^{He} = R^D$; if this is not the case the measured cross section ratio σ^{He}/σ^D does not equal the structure function ratio F_2^{He}/F_2^D (see section 1.2.3). In the iteration procedure one cannot then simply multiply F_2^D by the measured ratio in order to obtain F_2^{He}, but a correction depending on y must also be applied [271]. In order to assess the possible effects of $R^{He} \neq R^D$, we assumed $\Delta R = R^{He} - R^D = \pm 0.05$, about half of the largest fluctuation seen in the $R^A - R^D$ results of the SLAC experiment E140 [46, 47]. We then recomputed the radiative corrections tables; the results thus found for the cross section ratios differ from those obtained under the assumption $R^{He} - R^D = 0$ by at most $\mp 0.2\%$ at small x. The corresponding structure functions ratios differ from the cross section ratios by up to $\pm 1\%$.

C.1.5 The Infrared Cut

The value of the infrared cut Δ normally used is 0.1% of the nominal beam energy, thus corresponding to 200 MeV, in this case. Reducing this cut to 100 MeV does not affect the results.

C.2 The Quasi-elastic Tail

C.2.1 The Nucleon Form Factor

The nucleon form factor parametrization of Gari and Krümpelmann [272] was used. This parametrization has been obtained from a fit of the nucleon form factors $G^{p,n}_{M,E}$ to the available data [273]-[275], which extend up to high values of the transferred momentum squared, $Q^2 \approx 20$ GeV^2 for the proton and $Q^2 \approx 10$ GeV^2 for the neutron. The fitted functions are based on an extended vector meson dominance model, which incorporates quark dynamics at large Q^2 via perturbative QCD.

The radiative corrections are rather insensitive to the details of the parametrizations chosen for the nucleon form factors. Using the results of Höhler *et al.* [273], based on a dispersion analysis of the data on the nucleon form factors available up to 1976, does not cause the results for the ratio to change appreciably.

In both approaches the isoscalar (S) and isovector (V) combinations of the proton (p) and neutron (n) form factors are computed:

$$\begin{aligned} F_i^S &= \frac{1}{2}(F_i^p + F_i^n) \\ F_i^V &= \frac{1}{2}(F_i^p - F_i^n), \end{aligned}$$

where $i = 1, 2$ correspond to the Dirac and Pauli form factors, respectively. From these the standard electric and magnetic form factors can be recovered as:

$$\begin{aligned} G_E &= F_1 - (Q^2/4M^2)F_2 \\ G_M &= F_1 + F_2. \end{aligned}$$

C.2.2 The Deuterium Suppression Factor

We used the results of a calculation by Bernabeu [276] based on the nuclear shell model with spin and isospin correlations between the nucleons built in. The model explicitely assumes that the suppression factors are zero at $Q^2 = 0$ and tend to unity for $Q^2 \to \infty$. The results of the calculation are in good agreement with the existing measurements of A_{QE} for deuterium ($0.06 < Q^2 < 0.179$ GeV^2) [277].

A different approach was adopted by previous experiments (e.g. EMC NA2′ [38, 39, 303]): using the nuclear closure approximation (see for instance the appendix B of [24]) and neglecting all nucleon-nucleon correlations, one obtains

$$\begin{aligned} S_E(Q^2) &= (1 - |F(Q^2)|^2) \\ S_M(Q^2) &= 0, \end{aligned} \tag{C.6}$$

with F the deuterium coherent form factor (eq. C.11, below). This formula expresses the fact that quasi-elastic scattering is unimportant when coherent scattering dominates, and vice versa.

An alternative approach by Arenhövel [278] was also tested. This calculation is based on a non-relativistic treatment of the deuteron electro-disintegration, including effects from meson exchange currents and isobar configurations. The results are valid up to $Q^2 \approx 0.5$ GeV^2.

Figure C.3 compares the three approaches discussed; the discontinuities around $Q^2 = 0.35$ are artefacts of the parametrizations used and are of no consequence on the evaluation of radiative corrections. If the simple expressions C.6 are used in the radiative corrections program instead of the results by Bernabeu, the changes in the structure functions ratio are less than 0.1%. The changes are 0.2% at most if the Arenhövel calculation is adopted (cf. table C.3, fourth column).

C.2.3 The Helium Suppression Factor

Here as well the results of Bernabeu [276] were used. Other calculations, based on a Fermi gas description of the nucleus, are available. The validity of this approach may of course be questioned for small A nuclei like helium. The elastic photon-nucleon cross section is in this case reduced by a Q^2 dependent amount, up to $\sqrt{Q^2} = 2k_F$, where k_F is the Fermi momentum; for helium $k_F = 0.164$ [280]. For momentum transfers larger than $2k_F$ (i.e. when the recoiling nucleon is outside the Fermi sphere) there is no suppression.

Previous experiments (for example EMC NA2′ [38, 39, 303]) used the results of a calculation by deForest and Walecka [279], in which only electric suppression is considered and the finite extent of the nucleus as well as the contribution of meson currents are neglected[1].

[1] In this case the electric suppression factor reads: $S_E(Q^2) = \frac{3}{4}\frac{\sqrt{Q^2}}{k_F} - \frac{1}{16}\left(\frac{\sqrt{Q^2}}{k_F}\right)^3$.

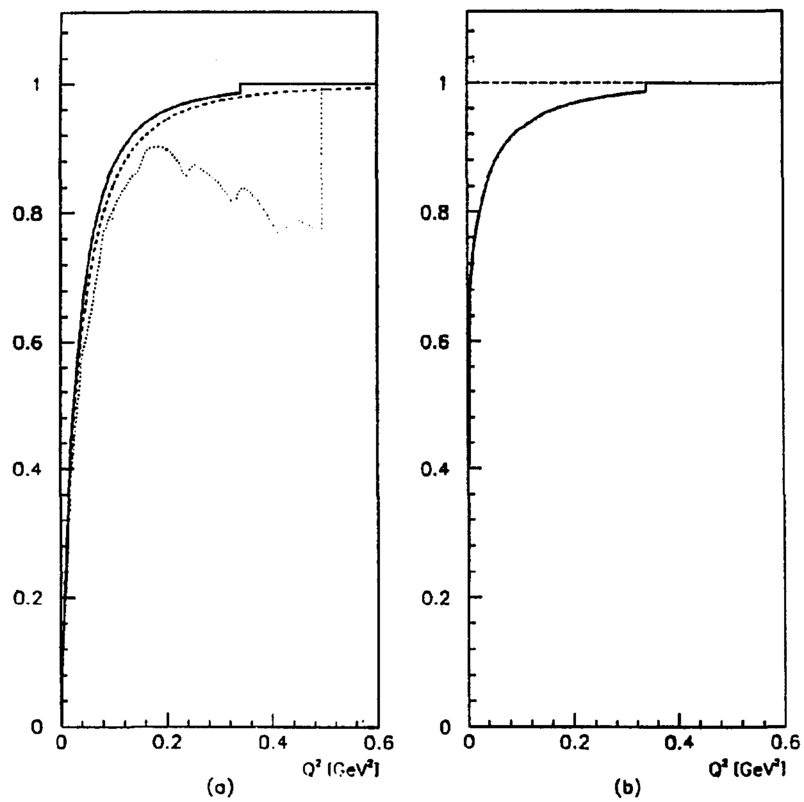

Figure C.3: Quasi-elastic electric (a) and magnetic (b) suppression factors for deuterium: the Bernabeu calculation [276] (continuous curve), and that of Arenhövel [278] (dotted curve) are compared with the approach of formulae C.6 (dashed curve)

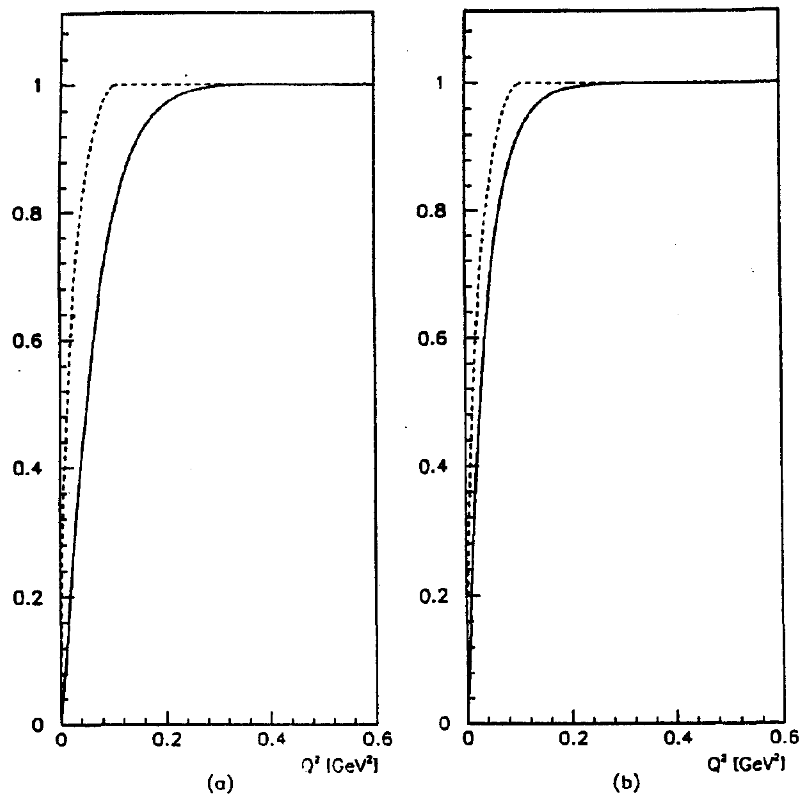

Figure C.4: Quasi-elastic electric (a) and magnetic (b) suppression factors for helium: the result of the calculation by Bernabeu [276] (continuous curve) is compared with the Fermi gas approach of Moniz [281] (dashed curve)

A more refined version of the Fermi gas approach is that of Moniz [281] which gives a full treatment of both electric and magnetic suppression terms.

The results of the two Fermi gas calculations are close, but they differ considerably from the Bernabeu one. These differences cause rather large changes in the radiative corrections. The effect on the structure function ratios amounts to $\approx 1\%$ at small x. It is given as a function of x in the second and third columns of table C.3. Figure C.4 compares the calculation by Bernabeu and that by Moniz as a function of Q^2.

C.3 The Coherent Tail

C.3.1 The Deuterium Coherent Form Factor

We recall the Rosenbluth formula:

$$\frac{d\sigma}{d\Omega} = \left(\frac{d\sigma}{d\Omega}\right)_{Mott} [A(Q^2) + 2B(Q^2)\tan^2\vartheta/2]. \tag{C.7}$$

For coherent scattering off deuterium, the functions $A(Q^2)$ and $B(Q^2)$ can be written as (see e.g. [282, 299]):

$$A(Q^2) = F_{CH}^2(Q^2) + \frac{8}{9}\tau^2 F_Q^2(Q^2) + \frac{2}{3}\tau(1+\tau)F_{MAG}^2(Q^2), \tag{C.8}$$

$$B(Q^2) = \frac{2}{3}\tau(1+\tau)^2 F_{MAG}^2(Q^2), \tag{C.9}$$

with $\tau = Q^2/(4m_D^2)$ and m_D the deuteron mass.

The quantities F_{CH}, F_Q and F_{MAG} are the deuteron electric monopole, electric quadrupole and magnetic form factors, respectively. In the nuclear impulse approximation they are given by the product of the nucleon form factors and the deuteron body form factors:

$$\begin{array}{rcl} F_{CH}(Q^2) & = & 2F_{CH}^S(Q^2)C_E(Q^2) \\ F_Q(Q^2) & = & 2F_{CH}^S(Q^2)C_Q(Q^2) \\ F_{MAG}(Q^2) & = & (m_D/M)[2F_{MAG}^S(Q^2)C_S(Q^2) + F_{CH}^S(Q^2)C_L(Q^2)]. \end{array} \tag{C.10}$$

The electric monopole and quadrupole body form factors of the deuteron are denoted by C_E and C_Q, respectively. The functions C_S and C_L are the deuteron magnetic scalar and longitudinal body form factors. The functions F_{CH}^S and F_{MAG}^S are the isoscalar electric and magnetic form factors of the nucleon and are defined as follows:

$$\begin{array}{rcl} F_{CH}^S(Q^2) & = & F_1^S(Q^2) - \frac{Q^2}{4M^2}F_2^S(Q^2) \\ F_{MAG}^S(Q^2) & = & F_1^S(Q^2) + F_2^S(Q^2), \end{array}$$

where F_1^S and F_2^S are the Dirac and Pauli isoscalar form factors of the nucleon.

For the body form factors of the deuteron we used the parametrization of Locher and Švarc [282], based on a relativistic pole expansion fitted to the available coherent e-D scattering results [283]-[298] and also using the known static properties of the deuteron (e.g. radius, quadrupole moment and binding energy). The data extend up to $Q^2 \approx 2.5$ GeV^2.

Explicit corrections for meson exchange currents are included in the fit. The nucleon form factors were those of Gari and Krümpelmann [272], which we described above.

Locher and Švarc [282] produced in fact two parametrizations, obtained including different data sets in the fit. We used the first of these two parametrizations, in which the Saclay results for $A(Q^2)$ [298] are not used; these data show a $\approx 5\%$ systematic disagreement with the other available ones [283]-[289, 295] at very small Q^2 (< 0.16 GeV^2). The two fits are also available without the meson exchange corrections [299].

The radiative corrections are rather insensitive to which one of the four parametrizations is used; the effects of going from one to any of the others are smaller than 0.1%. Effects of similar magnitude are obtained if an earlier version of the Locher and Švarc fits is used [300].

Small changes are also found if the parametrization

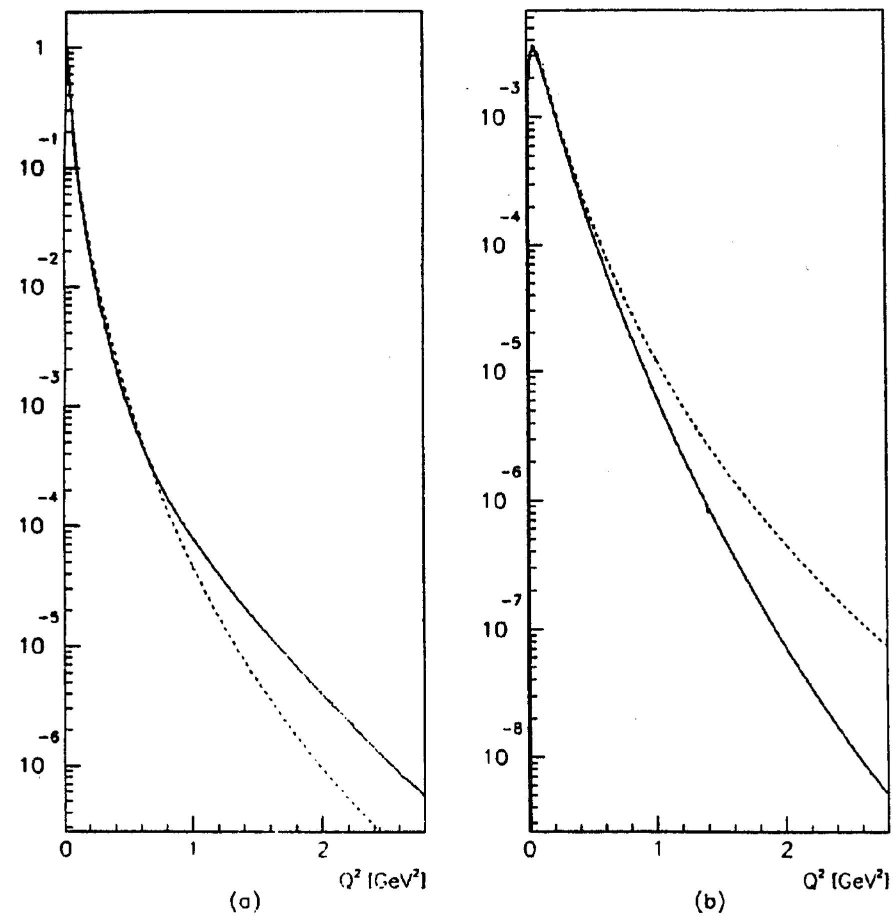

Figure C.5: The functions $A(Q^2)$ (a) and $B(Q^2)$ (b) for elastic scattering from deuterium. The continuous curve is the result of the fit [282], while the dashed curve corresponds to the form factor given in equation C.11 [302]

$$F(q) = \frac{1.580}{q}\left(\arctan\frac{q}{0.930} - 2\arctan\frac{q}{3.19} + \arctan\frac{q}{5.45}\right) \tag{C.11}$$

($q = \sqrt{Q^2}$, in fm^{-1}) is adopted for the body form factor of deuterium. This formula is based on the results of a calculation ([301], [302] equation 2, [24] equations A9-12) which exploits a Hulthén potential for the n-p interaction. It was used, for instance, in the extraction [303, 304] of the EMC NA2′ [38, 39] and NA28 [40] results on structure functions ratios. In this approach the quadrupole terms are neglected, the form factors C_E and C_S are set equal to $F(q)$ and C_L is set to zero.

Some of the parametrizations for $A(Q^2)$ and $B(Q^2)$ are shown in fig. C.5.

C.3.2 The Helium Coherent Form Factor

Several elastic e-^{4}He scattering experiments were made at SLAC and Darmstadt, starting in the 1950's [307]-[313]. Measurements of the helium coherent form factor are available for Q^2 up to 2.4 GeV^2 [313]. The experimental results, in the region where they overlap ($Q^2 < 0.2$ GeV^2), are in good agreement.

We used a sum of gaussians parametrization [305] based on the data [310]-[313], which extend up to $Q^2 = 2.4$ GeV^2. The method used to derive it is of some interest and we briefly summarize it. The essence is to represent the charge density $\rho(r)$ by a sum of gaussians of width γ centered at different radii:

$$\rho(r) \sim \sum_{i=1}^{N} A_i e^{-(r-r_i)^2/\gamma^2}. \tag{C.12}$$

The point is that, due to the rapid decrease of the gaussian tails, the reproduction of local variations of $\rho(r)$ – independent of the behavior of $\rho(r)$ at far away radii – becomes possible. The parametrization is thus rather model independent, in the sense that it does not force on the data features that in fact belong to the functional form of the parametrization. The only assumption is on the width of the narrowest structures: evidently structures narrower than $\sim \gamma$ cannot be reproduced. This is generally not a problem, since structures smaller than the proton diameter are anyway not expected.

In the Born approximation the nuclear form factor can be derived from the charge density $\rho(r)$ through Fourier transformation and can be expressed in the following form:

$$F(Q^2) = \exp\left(-\frac{\gamma^2 Q^2}{4}\right) \sum_{i=1}^{N} \frac{Q_i}{1+\frac{2r_i^2}{\gamma^2}} \left(\cos\sqrt{Q^2}r_i + \frac{2r_i^2}{\gamma^2}\frac{\sin\sqrt{Q^2}r_i}{\sqrt{Q^2}r_i}\right). \tag{C.13}$$

This expression is then fitted to the experimental data.

For helium $N = 11$ and $\gamma^2 = 0.67$ fm^2. The parameters r_i (the centers of the gaussians) range from 0.2 to 4.9 fm. The quantities Q_i fix the relative normalizations of the various gaussians: in helium the largest contributions come from the ones centered at 0.6 fm (43%), 0.9 fm (20%) and 1.4 fm (19%), corresponding to a r.m.s. nuclear radius of 1.676 fm.

The data [310, 312] are also described well by the simple parametrization [312]:

$$F(Q^2) = [1-(a^2Q^2)^6]\exp(-b^2Q^2), \tag{C.14}$$

with a=0.316 fm^{-1} and b=0.675 fm (Q^2 in fm^{-2}). This parametrization however underestimates the large Q^2 data [313] for $Q^2 > 1$ GeV^2.

Finally there exists a fit to the data [310] based on a dispersion relation approach [306]. In this case the form factor is approximated by a sum of poles:

$$F(Q^2) = \frac{1+a\sqrt{Q^2}}{\prod_{i=1}^{N}[1-\frac{\sqrt{Q^2}}{q_p+(i-1)h}]}, \tag{C.15}$$

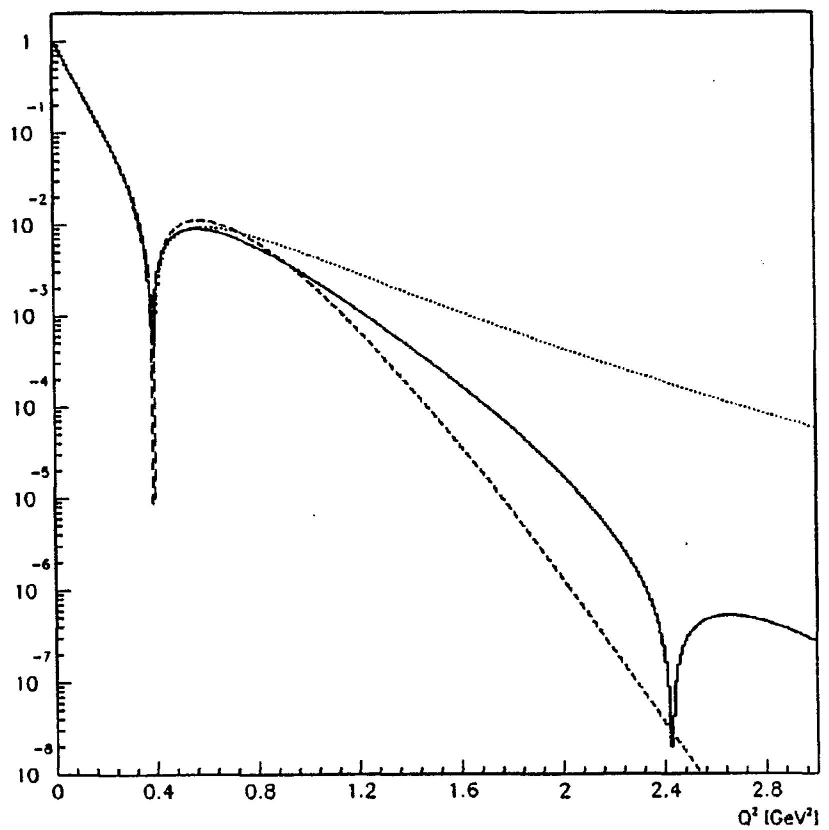

Figure C.6: Helium elastic form factor (the square root of the function $A(Q^2)$ in the Rosenbluth cross section 4.2) as a function of Q^2. The continuous line is the sum of gaussian parametrization C.13. The dashed line and the dotted one correspond to the parametrizations C.14 and C.15, respectively

with $N = 12$, $a = 2.551$ GeV^{-2}, q_p=0.190 GeV^{-2} and $h = 0.489$ GeV^{-2}.
The main difference of this parametrization with respect to those quoted above is in the behavior of the form factor at large momentum transfers: the asymptotic decrease at large Q^2 is slower than the exponential one of C.13 and C.14. This translates into a different shape of the charge density at small radii, which is flat in the center instead of presenting a dip. The data are well reproduced for Q^2 up to $\simeq 1$ GeV^2. For $Q^2 > 1$ GeV^2, the computed values of the form factor are larger than the measured ones [313].

The three parametrizations are shown as a function of Q^2 in fig. C.6.

The radiative corrections were computed in each case and both C.14 and C.15 were tried instead of C.13. All three parametrizations include the data [310] (which extend up to $Q^2 = 0.8$ GeV^2) and differ significantly only at large Q^2; in this region the form factor is anyway very small and its effect on the radiative corrections negligible.

The differences between the results for the structure function ratios obtained in the three cases are always very small, never exceeding 0.1%.

C.4 The Size of the Radiative Correction Tables

As we have explained the radiative corrections tables contain the weights for a number of points in the (x, y) plane. The tables are interpolated in order to determine the value of the correction factor for each event. The larger the number of points on the table, the smaller the interpolation error is expected to be. The grid used contains $n_x \times n_y = 25 \times 19 = 475$ points and is particularly dense in the small x region. Even significant modifications of the grid density do not however have relevant consequences for the results.

Appendix D

The Integrals of $F_2^A - F_2^D$

Introduction

In the following we shall discuss the evaluation of the integrals $\int(F_2^A - F_2^D)dx$ and their extraction from the data. What we want to compute is actually the difference of the second moments (see eq. 1.17, page 9) M_2^A and M_2^D of the structure functions F_2^A and F_2^D.

In section one of this appendix we give a rigorous definition of such moments. In section two we derive an expression for the difference of the moments M_2^A and M_2^D. Finally in section three we explain how the moments have been extracted from the measured struction function ratios.

A comprehensive discussion of the subject can be found in [349], from which what follows has been derived.

D.1 The Moments of the Structure Function F_2

In general, for a nuclear target A, the n'th moment can be written as (cf. equation 13 of [330]; our definition differs by a factor 8/15 from that of [330])

$$M_n^A(Q^2) = \int_0^{\xi^A_{max}} d\xi^A(\nu W_2^A)(\xi^A)^{n-2}\left(1 - \frac{(M_A\xi^A)^4}{Q^4}\right)\left(1 + \frac{Q^2}{\nu^2}\right)(1 + 3\eta_n), \tag{D.1}$$

with

$$\begin{aligned} \xi^A &= \frac{\sqrt{\nu^2 + Q^2} - \nu}{M_A} && \text{(D.2)} \\ &= \frac{Q^2}{M_A}\frac{1}{\sqrt{\nu^2 + Q^2} + \nu} \\ &= \frac{M}{M_A}\frac{2x}{1 + \sqrt{1 + \frac{4M^2x^2}{Q^2}}} && \text{(D.3)} \\ &= \frac{M}{M_A}\xi, && \text{(D.4)} \end{aligned}$$

$$\xi^A_{max} = \frac{2}{1 + \sqrt{1 + \frac{4M_A^2}{Q^2}}}, \tag{D.5}$$

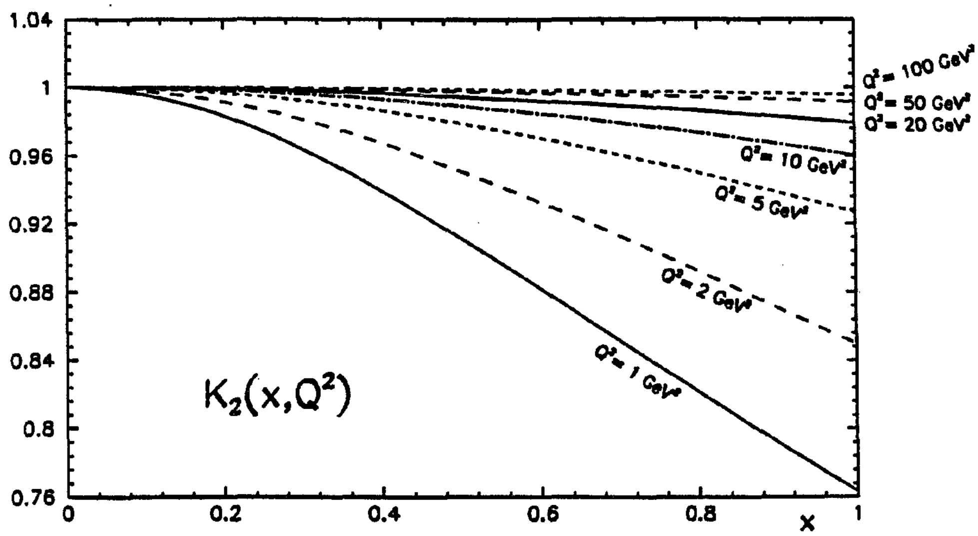

Figure D.1: The correction factor K_2 as a function of x for different values of Q^2 (from [349])

and

$$\eta_n = \frac{-(n+2)Q^2 + (n+1)M_A\nu\xi^A}{(n+2)(n+3)(\nu^2+Q^2)}. \tag{D.6}$$

As discussed in [330], n must be an even number ≥ 2. The variable ξ in formula D.4 is often referred to as the Nachtmann scaling variable.

Expression D.1 can be rewritten as an integral over the usual variable x:

$$M_n^A(Q^2) = \int_0^{M_A/M} dx\, x^{n-2} \left(\frac{M}{M_A}\right)^{n-1} AF_2^A(x,Q^2)K_n(x,Q^2); \tag{D.7}$$

the function $K_n(x,Q^2)$ includes the jacobian of the transformation $\xi^A \to x$.

An expression for K_n can be derived as follows. From the definitions D.2, D.3 we have:

$$d\xi^A = \frac{\nu - \sqrt{\nu^2+Q^2}}{M_A\sqrt{\nu^2+Q^2}}\, d\nu = \frac{\xi^A}{\sqrt{1+\frac{4M^2x^2}{Q^2}}}\frac{dx}{x}. \tag{D.8}$$

By replacing ξ^A with D.3 and $d\xi^A$ with D.8 in equation D.1 and comparing with D.7 we find:

$$K_n(x,Q^2) = \sqrt{1+\frac{4M^2x^2}{Q^2}}\left(\frac{2}{1+\sqrt{1+4M^2x^2/Q^2}}\right)^{n-1}\left(1-\frac{(M_A\xi^A)^4}{Q^4}\right)(1+3\eta_n). \tag{D.9}$$

Note that since $M_A\xi^A$ is independent of A, K_n is also independent of A.

Figure D.1 shows the behavior of K_2 as a function of x for different values of Q^2.

$\left(\frac{AM}{M_A} - \frac{DM}{M_D}\right)$	^{4}He	^{6}Li	^{12}C	^{40}Ca	^{56}Fe	^{118}Sn
	6.35×10^{-3}	4.47×10^{-3}	7.01×10^{-3}	7.49×10^{-3}	8.18×10^{-3}	7.85×10^{-3}

Table D.1: Values of the correction f_M for different nuclei

D.2 The Difference of the Moments M_2^A and M_2^D

For $n = 2$ we now have (using $A \approx M_A/M$)

$$M_2^A(Q^2) = \frac{AM}{M_A} \int_0^A F_2^A(x, Q^2) K_2(x, Q^2) dx. \tag{D.10}$$

We want to compute

$$\begin{aligned} M_2^A - M_2^D &= \frac{AM}{M_A} \int_0^A F_2^A K_2 dx - \frac{DM}{M_D} \int_0^D F_2^D K_2 dx \\ &= \int_0^D \left(F_2^A - F_2^D\right) K_2 dx + \left(\frac{AM}{M_A} - 1\right) \int_0^A F_2^A K_2 dx - \\ &\quad - \left(\frac{DM}{M_D} - 1\right) \int_0^D F_2^D K_2 dx + \frac{AM}{M_A} \int_D^A F_2^A K_2 dx. \end{aligned} \tag{D.11}$$

Here D is the mass number of deuterium, $D = 2$. We may neglect the integral from D to A and replace F_2^A by F_2^D in the second term. Introducing the structure function ratio F_2^A/F_2^D, expression D.11 becomes:

$$M_2^A - M_2^D = \int_0^D \left(\frac{F_2^A}{F_2^D} - 1\right) F_2^D K_2 dx + \left(\frac{AM}{M_A} - \frac{DM}{M_D}\right) \int_0^D F_2^D K_2 dx. \tag{D.12}$$

The factor AM/M_A in front of $\int_0^D F_2^D K_2 dx$ reflects the fact that the x variable that we use, $x = Q^2/2M\nu$, is not the "natural scaling variable" for target A, namely $Q^2/2M_A\nu$. Note that the correction

$$f_M = \left(\frac{AM}{M_A} - \frac{DM}{M_D}\right) \tag{D.13}$$

is non-vanishing due to the difference of the binding energies of nucleus A and of deuterium. Table D.1 gives the values of f_M for different nuclei.

Using the definition of f_M, formula D.11 finally reads:

$$M_2^A - M_2^D = \int_0^D \left(\frac{F_2^A}{F_2^D} - 1 + f_M\right) F_2^D K_2 dx. \tag{D.14}$$

The integration has to be performed at a fixed value of Q^2.

D.3 The Extraction of the Moments from the Measured Ratios

For each x bin the integral

$$I_i = \int_{x_i}^{x_{i+1}} \left(\frac{F_2^A}{F_2^D} - 1 + f_M \right) F_2^D K_2 dx \tag{D.15}$$

was evaluated as

$$I_i = \frac{B_{i+1} + B_i}{2} T_i, \tag{D.16}$$

with

$$B_i(x_i) = (r_i(x_i) - 1 + f_M) F_2^D(x_i) K_2(x_i) \tag{D.17}$$

and

$$r_i = \frac{F_2^A(x_i)}{F_2^D(x_i)}, \qquad T_i = x_{i+1} - x_i, \tag{D.18}$$

in agreement with the prescription of equation D.14. For the deuterium structure function F_2^D the same parametrization was adopted as the one that was used to calculate radiative corrections (cf. section 4.5.3). The parametrization was evaluated at $Q^2 = 5$ GeV^2. As we mentioned in 5.4, the value $Q^2 = 5$ GeV^2 was chosen since it is close to the average Q^2 of both the NMC and the SLAC E139 data used for the integrals. With this parametrization $\int_0^1 F_2^D(x) K_2(x) dx = 0.148$, at $Q^2 = 5$ GeV^2.

The errors were computed as follows:

- Statistical error:

$$\Delta I_i(stat) = \frac{1}{2} \sqrt{[\Delta B_{i+1}(stat)]^2 + [\Delta B_i(stat)]^2} T_i, \tag{D.19}$$

$$\Delta B_i(stat) = \Delta r_i(stat) F_2^D(x_i) K_2(x_i), \tag{D.20}$$

where $\Delta r_i(stat)$ is the statistical error on the structure function ratio r_i.

- Systematic error due to the systematic uncertainty on the ratio:

$$\Delta I_i(syst) = \frac{1}{2} [\Delta B_{i+1}(syst) + \Delta B_i(syst)] T_i, \tag{D.21}$$

$$\Delta B_i(syst) = \Delta r_i(syst) F_2^D(x_i) K_2(x_i), \tag{D.22}$$

where $\Delta r_i(syst)$ is the systematic error on the structure function ratio r_i.

- Systematic error due to the normalization error of the ratio:

$$\Delta I_i(norm) = \frac{1}{2} [\Delta B_{i+1}(norm) + \Delta B_i(norm)] T_i, \tag{D.23}$$

$$\Delta B_i(norm) = \Delta R(norm) F_2^D(x_i) K_2(x_i), \tag{D.24}$$

where $\Delta r_i(norm)$ is the normalization uncertainty on the structure function ratio r_i.

- Systematic error due to the uncertainty on F_2^D, $\Delta I_i(F_2^D)$: it was obtained as the difference between the values of the integrals found using the upper and the lower limits of F_2^D discussed in section 4.5.3.

The integral over the full x range was evaluated as the sum of the individual contributions I_i:

$$I_{tot} = \sum_{i=1}^{N-1} I_i, \tag{D.25}$$

with N the total number of bins.

The systematic error due to the systematic uncertainty on the ratio was obtained by summing the individual contributions $\Delta I_i(syst)$ linearly. The same was done for the systematic errors due to the normalization uncertainty on the ratio and to the uncertainty on F_2^D. These three terms were then summed up quadratically in order to obtain the total systematic error on the integral:

$$\Delta I_{tot}(syst) = \sqrt{\left(\sum_{i=1}^{N-1} \Delta I_i(syst)\right)^2 + \left(\sum_{i=1}^{N-1} \Delta I_i(norm)\right)^2 + \left(\sum_{i=1}^{N-1} \Delta I_i(F_2^D)\right)^2}. \tag{D.26}$$

The statistical errors should not be added in quadrature, since the contributions ΔI_i and ΔI_{i+1} are correlated (they both contain ΔB_{i+1}). Instead one can rewrite equation D.25 as

$$I_{tot} = \frac{1}{2} \sum_{i=1}^{N-1} T_i(B_i + B_{i+1}) = \frac{1}{2} \sum_{i=1}^{N} (T_{i-1} + T_i) B_i, \tag{D.27}$$

where the terms T_0 and T_N are zero.

The total statistical error on the integral is then

$$\Delta I_{tot} = \frac{1}{2} \sqrt{\sum_{i=1}^{N} (T_{i-1} + T_i)^2 (\Delta B_i)^2}. \tag{D.28}$$

Appendix E

The NMC Collaboration

NEW MUON COLLABORATION (NMC)

Bielefeld University[1+], CERN[2], Freiburg University[3+], Max-Planck Institute Heidelberg[4+], Heidelberg University[5+], University of Mainz[6+], Mons University[7], Neuchâtel University[8], NIKHEF-K[9++], Oxford University[10], University of California, Santa Cruz[11], Paul Scherrer Institute[12], Torino University and INFN Torino[13], Uppsala University[14], Institute for Nuclear Studies, Warsaw[15], Warsaw University[16**], Wuppertal University[17+]*

P. Amaudruz[12a)], M. Arneodo[13], A. Arvidson[14], B. Badelek[16], G. Baum[1], J. Beaufays[9b)], I.G. Bird[4], M. Botje[12], C. Broggini[8c)], W. Brückner[4], A. Brüll[3], W.J. Burger[12d)], J. Ciborowski[16], R. van Dantzig[9], H. Döbbeling[4e)], J. Domingo[12f)], J. Drinkard[11], H. Engelien[3], M.I. Ferrero[13], L. Fluri[8], P. Grafstrom[14g)], D. von Harrach[4h)], M. van der Heijden[9], C. Heusch[11], Q. Ingram[12], K. Janson[14], M. de Jong[9], E.M. Kabuß[4h)], R. Kaiser[3], T.J. Ketel[9], F. Klein[6], B. Korzen[17], U. Krüner[17], S. Kullander[14], U. Landgraf[3], F. Lettenström[11], T. Lindqvist[14], G.K. Mallot[6], C. Mariotti[13], G. van Middelkoop[2,9], Y. Mizuno[4i)], J. Nassalski[15], D. Nowotny[4], N. Pavel[17j)], C. Peroni[13], H. Peschel[17k)], B. Povh[4,5], R. Rieger[6], K. Rith[4], K. Röhrich[6l)], E. Rondio[16], L. Ropelewski[16], A. Sandacz[15], C. Scholz[4], R. Schumacher[12m)], U. Sennhauser[12n)], F. Sever[1o)], T.-A. Shibata[5], M. Siebler[1], A. Simon[4], A. Staiano[13], G. Taylor[10p)], M. Treichel[4q)], J.L. Vuilleumier[8], T. Walcher[6], R. Windmolders[7], F. Zetsche[4]

+ Supported by Bundesministerium für Forschung und Technologie.

++ Supported in part by FOM, Vrije Universiteit Amsterdam and NWO.

* Supported by CPBP.01.06.

** Supported by CPBP.01.09.

a) Now at TRIUMF, Vancouver, BC, Canada.

b) Now at Trasys, Brussels, Belgium.

c) Now at INFN, Laboratori Nazionali del Gran Sasso, 67010 Assergi, Italy.

d) Now at Université de Genève, 1211 Genève 4, Switzerland.

e) Now at GSI, 6100 Darmstadt, Germany.

f) Now at CEBAF, Newport News, VA, U.S.A.

g) Now at CERN, 1211 Geneva 23, Switzerland.

h) Now at University of Mainz, 6500 Mainz, Germany.

i) Now at Osaka University, Osaka, Japan.

j) Now at DESY, Hamburg, Germany.

k) Now at Gruner and Jahr AG & CoKG, Itzehoe, Germany.

l) Now at IKP2-KFA, Jülich, Germany.

m) Now at Carnegie Mellon University, Pittsburgh, U.S.A.

n) Now at EMPA, 8600 Dübendorf, Switzerland.

o) On leave from Jozef Stefan Institut, Ljubljana, Yugoslavia, now at DPhN Saclay, 91191 Gif-sur-Yvette, France.

p) Now at University of Melbourne, Parkville, Victoria, Australia.

q) Now at Université de Neuchâtel, 2000 Neuchâtel, Switzerland.

Bibliography

[1] L. Carroll, "Through the Looking-glass", Penguin Books, New York (1960) p. 174

[2] E. Leader and E. Predazzi, "An Introduction to Gauge Theories and the 'New Physics'", Cambridge University Press, Cambridge (1982)

[3] J.D. Bjorken and S.D. Drell, "Relativistic Quantum Mechanics", McGraw-Hill, New York (1964)

[4] F.J. Gilman, Phys. Rev. **167** (1968) 1365

[5] L.N. Hand, Phys. Rev. **129** (1963) 1834

[6] E.D. Bloom *et al.*, Phys. Rev. Lett. **23** (1969) 930;
M. Breidenbrach *et al.*, Phys. Rev. Lett. **23** (1969) 935

[7] W. Albrecht *et al.*, DESY Report 69/46 (1969)

[8] CERN NA2/EMC, J.J. Aubert *et al.*, Nucl. Phys. **B259** (1985) 189

[9] J.D. Bjorken, Phys. Rev. **179** (1969) 1547

[10] R.P. Feynman, "Photon-hadron Interactions", Benjamin, Reading MA (1972)

[11] C. Callan and D. Gross, Phys. Rev. Lett. **22** (1969) 156

[12] CERN NA37/NMC, P. Amaudruz *et al.*, Phys. Rev. Lett. **66** (1991) 2712

[13] T. Sloan *et al.*, Phys. Rep. **162** (1988) 45

[14] CERN NA2/EMC, J.J. Aubert *et al.*, Phys. Lett. **B 123** (1983) 275

[15] A. Bodek and J.L. Ritchie, Phys. Rev. **D 23** (1981) 1070;
A. Bodek and J.L. Ritchie, Phys. Rev. **D 24** (1981) 140

[16] G. Berlad *et al.*, Phys. Rev. **D 22** (1980) 1547

[17] L.L. Frankfurt and M.I. Strikman, Nucl. Phys. **B181** (1981) 22

[18] W.B. Atwood and G.B. West, Phys. Rev. **D 7** (1981) 1080;
W.B. Atwood and G.B. West, Phys. Rev. **D 24** (1981) 1400

[19] K. Saito and T. Uchiyama, Z. Phys. **A 322** (1985) 299

[20] D.O. Caldwell *et al.*, Phys. Rev. **D 7** (1973) 1362

[21] D.O. Caldwell *et al.*, Phys. Rev. Lett. **42** (1979) 553

[22] J. Bailey *et al.*, Nucl. Phys. **B151** (1979) 367

[23] J. Franz *et al.*, Z. Phys. **C 10** (1981) 105 and refereces cited therein

[24] SLAC E61, S. Stein *et al.*, Phys. Rev. **D 12** (1975) 1884

[25] J. Eickmeyer *et al.*, Phys. Rev. Lett. **36** (1976) 289

[26] G. Huber *et al.*, Z. Phys. **C 2** (1979) 279

[27] M.S. Goodman *et al.*, Phys. Rev. Lett. **47** (1981) 293

[28] CERN NA2/EMC, J.J. Aubert *et al.*, Nucl. Phys. **B272** (1986) 158

[29] CERN NA2/EMC, J.J. Aubert *et al.*, Nucl. Phys. **B293** (1987) 740

[30] A. Bodek *et al.*, Phys. Rev. Lett. **50** (1983) 1431

[31] A. Bodek *et al.*, Phys. Rev. Lett. **51** (1983) 534

[32] A. Bodek *et al.*, Phys. Rev. Lett. **30** (1973) 1087

[33] A. Bodek *et al.*, Phys. Lett. **51B** (1974) 417

[34] FNAL BFP, A.R. Clark *et al.*, Phys. Rev. Lett. **51** (1983) 1826

[35] SLAC E139, R.G. Arnold *et al.*, Phys. Rev. Lett. **52** (1984) 727;
R.G. Arnold *et al.*, SLAC Report SLAC-PUB-3257 (1983)

[36] CERN NA4/BCDMS, G.Bari *et al.*, Phys. Lett. **B 163** (1985) 282

[37] CERN NA4/BCDMS, A.C. Benvenuti *et al.*, Phys. Lett. **B 189** (1987) 483

[38] CERN NA2'/EMC, J. Ashman *et al.*, Phys. Lett. **B 202** (1988) 603

[39] CERN NA2'/EMC, L. Ropelewski, talk at the XIXth Symposium on Multiparticle Dynamics, Arles, France, June 13-17 1988

[40] CERN NA28/EMC, M. Arneodo *et al.*, Phys. Lett. **B 211** (1988) 493;
CERN NA28/EMC, M. Arneodo *et al.*, Nucl. Phys. **B333** (1990) 1

[41] FNAL E665, M.R. Adams *et al.* (presented by C. Halliwell), talk at the 25th International Conference on High Energy Physics, Singapore, 2-8 August 1990

[42] FNAL E665, M.R. Adams *et al.* (presented by D.E. Jaffe), talk at the XXVIth Rencontres de Moriond, Les Arcs, Savoie, France, 17-23 March 1991, Proceedings to be published by Editions Frontières, Paris, Editor J. Trân Thanh Vân

[43] SLAC E140, S. Dasu *et al.*, Phys. Rev. Lett. **60** (1988) 2591

[44] S. Dasu, Ph.D. thesis, University of Rochester Report No. UR-1059 (1988)

[45] SLAC E140, S. Dasu *et al.*, Phys. Rev. Lett. **61** (1988) 1061

[46] L.W. Whitlow, Ph.D. thesis, Stanford University (1990), SLAC-Report-357

[47] SLAC E140, L.W. Whitlow *et al.*, Phys. Lett. **B 250** (1990) 193

[48] T. Weiler, Phys. Rev. Lett. **44** (1980) 304

[49] CERN NA2/EMC, J.J. Aubert *et al.*, Phys. Lett. **B 152** (1985) 433

[50] FNAL E691, M.D. Sokoloff *et al.*, Phys. Rev. Lett. **57** (1986) 3003

[51] A.M. Cooper *et al.*, Phys. Lett. **B 141** (1984) 133

[52] M.A. Parker *et al.*, Nucl. Phys. **B232** (1984) 1

[53] CERN CDHS, H. Abramowicz *et al.*, Z. Phys. **C 25** (1984) 29

[54] V.V. Ammosov *et al.*, Pis'ma Zh. Eksp. Teor. Fiz. **39** (1984) 327

[55] FNAL E545, J. Hanlon *et al.*, Phys. Rev. **D 32** (1985) 2441

[56] CERN WA25 and WA59, J. Guy *et al.*, Z. Phys. **C 36** (1987) 337

[57] CERN WA59, P.P. Allport *et al.*, Phys. Lett. **B 232** (1989) 417

[58] J.S. Bell, Phys. Rev. Lett. **13** (1964) 57

[59] FNAL E745, T.Kitagaki *et al.*, Phys. Lett. **B 214** (1988) 281

[60] J. Guy *et al.*, Phys. Lett. **B 229** (1989) 421

[61] FNAL E772, D.M.Alde *et al.*, Phys. Rev. Lett. **64** (1990) 2479

[62] N.N. Nikolaev, private communication (11 January 1990)

[63] E.L. Berger and F. Coester, Ann. Rev. Nucl. Part. Sci. **37** (1987) 463

[64] L.L. Frankfurt and M.I. Strikman, Phys. Rep. **160** (1988) 235

[65] L.L. Frankfurt, M.I. Strikman, University of Illinois at Urbana Champaign preprint ILL-(MAR)-91-#6 (1991), to appear in "Electromagnetic Interactions with Nuclei", Editors B. Frois and I. Sick, World Scientific, Singapore

[66] V. Barone and E. Predazzi, Ann. Phys. (Paris) **12** (1987) 525

[67] R.J.M. Covolan and E. Predazzi, in "Problems of Fundamental Modern Physics", Editors R. Cherubini, P. Dalpiaz and B. Minetti, World Scientific, Singapore (1991) p. 85

[68] T. Uchiyama and K. Saito, Phys. Rev. **C 38** (1988) 2245

[69] B. Badełek and J. Kwieciński, Warsaw University preprint IFD/3/1991 (1991)

[70] C.H. Llewellyn Smith, Phys. Lett. **128B** (1983) 107

[71] M. Ericson and A.W. Thomas, Phys. Lett. **128B** (1983) 112

[72] B.L. Friman *et al.*, Phys. Rev. Lett. **51** (1983) 763

[73] E.L. Berger, F. Coester and R.B. Wiringa, Phys. Rev. **D 29** (1984) 398

[74] E.L. Berger and F. Coester, Phys. Rev. **D 32** (1985) 1071

[75] W-Y.P. Hwang *et al.*, Phys. Rev. **D 38** (1988) 2785

[76] J. Szwed, Phys. Lett. **128B** (1983) 245

[77] J. Kubar, G. Plaut and J. Szwed, Z. Phys. **C 23** (1984) 195

[78] R. Carlitz, Phys. Lett. **58B** (1975) 345;
J. Kaur, Nucl. Phys. **B128** (1977) 219

[79] S.V. Akulinichev, S.A. Kulagin and G.M. Vagradov, preprint of the Academy of Sciences of the USSR, Institute for Nuclear Research, Moscow P-0382 (1984);
S.V. Akulinichev, S.A. Kulagin and G.M. Vagradov, Phys. Lett. **158B** (1985) 485

[80] S.V. Akulinichev *et al.*, Phys. Rev. Lett. **55** (1985) 2239

[81] B.L. Birbrair *et al.*, Phys. Lett. **166B** (1986) 119

[82] C.A. Garcia Canal *et al.*, Phys. Rev. Lett. **53** (1984) 1430

[83] L.L. Frankfurt and M.I. Strikman, Phys. Lett. B **183** (1987) 254

[84] H. Jung and G. Miller, Phys. Lett. **B 200** (1988) 351

[85] P.D. Morley and I. Schmidt, Phys. Rev. **D 34** (1986) 1305;
P.D. Morley and I. Schmidt, Phys. Lett. **B 190** (1987) 35

[86] A. Molinari and G. Vagradov, Z. Phys. **A 332** (1989) 119

[87] G.L. Li, K.F. Liu and G.E. Brown, Phys. Lett. **B 213** (1988) 531

[88] S. Shlomo and G.M. Vagradov, Phys. Lett. **B 232** (1989) 19

[89] G. Chanfray, preprint of the Institut de Physique Nucléaire de Lyon LYCEN/9051 (1990), presented at the "Second European Workshop on Hadronic Physics with Electrons beyond 10 GeV", Dourdan, France, 8-12 October 1990, to be published in Nucl. Phys. A

[90] C. Ciofi degli Atti and S. Liuti, Phys. Lett. **B 225** (1989) 215

[91] C. Ciofi degli Atti and S. Liuti, Phys. Rev. **C 41** (1990) 1100

[92] D. Nowotny, Ph.D. thesis, Heidelberg University (1989), in German

[93] A.N. Antonov *et al.*, JINR Rapid Comm. No.2 41-90 (1990) 14

[94] A.N. Antonov *et al.*, Z. Phys. **A 297** (1980) 257

[95] A.E.L. Dieperink and G.A. Miller, "Nuclear Binding Corrections to Lepton-Nucleus Deep Inelastic Scattering – Use of a Realistic Spectral Function", to appear in Phys. Rev. C

[96] O. Benhar *et al.*, Nucl. Phys. **A505** (1989) 267

[97] M.B. Johnson and J. Speth, Nucl. Phys. **A470** (1987) 488

[98] L. Heller and A.W. Thomas, Phys. Rev. **C 41** (1990) 2756

[99] L.S. Kisslinger and M.B. Johnson, Phys. Lett. **B 259** (1991) 416

[100] G. Preparata and P.G. Ratcliffe, University of Milano preprint MITH 90/9 (1990), submitted to Phys. Rev. Lett.

[101] G. Preparata, Nuovo Cimento **103 A** (1990) 1213

[102] F.E. Close, R.G. Roberts and G.C. Ross, Phys. Lett. **129B** (1983) 346

[103] R.L. Jaffe *et al.*, Phys. Lett. **134B** (1984) 449

[104] F.E. Close *et al.*, Phys. Rev. **D 31** (1985) 1004

[105] R.L. Jaffe, Phys. Rev. Lett. **50** (1983) 228

[106] R.P. Bickerstaff and G.A. Miller, Phys. Rev. **D 34** (1986) 2890

[107] F.E. Close, R.G. Roberts and G.C. Ross, Phys. Lett. **168B** (1986) 400

[108] R.P. Bickerstaff and G.A. Miller, Phys. Lett. **168 B** (1986) 409

[109] R.P. Bickerstaff and A.W. Thomas, Phys. Rev. **D 35** (1987) 108

[110] G.V. Dunne and A.W. Thomas, Nucl. Phys. **A455** (1986) 701

[111] S. Fredriksson, Phys. Rev. Lett. **52** (1984) 724

[112] J. Cleymans and R.L. Thews, Phys. Rev. **D 31** (1985) 1014

[113] A.W. Hendry, D.B. Lichtenberg and E. Predazzi, Phys. Lett. **136B** (1984) 433

[114] A.W. Hendry, D.B. Lichtenberg and E. Predazzi, Nuovo Cimento **92 A** (1986) 427

[115] CERN NA2$'$/EMC, P.R. Norton, contributed paper to the 23rd Intenational Conference on High Energy Physics, Berkeley (1986)

[116] V. Barone and E. Predazzi, Nuovo Cimento **99 A** (1988) 661

[117] J.V. Noble, preprint CERN-TH.4441/86 (1986)

[118] J.V. Noble, Phys. Rev. Lett. **46** (1981) 412

[119] A. Chodos *et al.*, Phys. Rev. **D 9** (1974) 3471;
T. de Grand *et al.*, Phys. Rev. **D 12** (1975) 2060

[120] L.L. Frankfurt and M.I. Strikman, preprint of the Academy of Sciences of the USSR, Leningrad Nuclear Physics Institute, LNPI-886 (1983);
Soviet J. Nucl. Phys. 41 (1985) 1585

[121] G. Chanfray, O. Nachtmann and H.J. Pirner, Phys. Lett. **147 B** (1984) 249

[122] O. Nachtmann and H.J. Pirner, Z. Phys. **C 21** (1984) 277

[123] O. Nachtmann and H.J. Pirner, Ann. Physik 44 (1987) 13

[124] H.J. Pirner, in "Proceedings of the Workshop on Nuclear Chromodynamics", Editors S. Brodsky and E. Moniz, World Scientific, Singapore (1986) p. 272

[125] S. Gupta *et al.*, Z. Phys. **C 28** (1985) 483

[126] A. Krzywicki, Phys. Rev. **D 14** (1976) 152

[127] W. Furmansky and A. Krzywicki, Z. Phys. **C 22** (1984) 391

[128] S. Gupta and K.V.L. Sarma, Z. Phys. **C 29** (1985) 329

[129] J. Cleymans and J. Geris, preprint of the University of Leuven KUL-TF-83/29 and of the University of Bielefeld BI-TP 83/16 (1983)

[130] C. Angelini and R. Pazzi, Phys. Lett. **113B** (1982) 343;
C. Angelini and R. Pazzi, Phys. Lett. **119B** (1982) 231;
C. Angelini and R. Pazzi, Phys. Lett. **135B** (1984) 473

[131] C. Angelini and R. Pazzi, Phys. Lett. **154B** (1985) 328

[132] H.J. Pirner and J.P. Vary, Phys. Rev. Lett. **46** (1981) 1376;
H.J. Pirner and J.P. Vary, Nucl. Phys. **A358** (1981) 413c

[133] M. Sato *et al.*, Phys. Rev. **C 33** (1986) 1062

[134] H.J. Pirner, "Proceedings of the International School of Nuclear Physics", Erice, Progress in Particle and Nuclear Physics **13**, Editor A. Faessler (1984) p. 382

[135] D. Day *et al.*, Phys. Rev. Lett. **43** (1979) 1143

[136] F. Güttner and H.J. Pirner, Nucl. Phys. **A457** (1986) 555

[137] D. Sivers *et al.*, Phys. Rep. **23 C** (1976) 1 and references cited therein

[138] D. Sivers, Annu. Rev. Nucl. Part. Sci. **32** (1982) 149

[139] C.E. Carlson and T.J. Havens, Phys. Rev. Lett. **51** (1983) 261

[140] M. Chemtob and R. Peschanski, J. Phys. **G 10** (1984) 599

[141] H. Faissner and B.R. Kim, Phys. Lett. **130B** (1983) 321

[142] H. Faissner *et al.*, Phys. Rev. **D 30** (1984) 900

[143] H. Faissner *et al.*, Phys. Rev. Lett. **54** (1985) 1902

[144] S. Daté *et al.*, Phys. Rev. Lett. **52** (1984) 2344

[145] L.A. Kondratyuk and M.Zh. Smatikov, DESY internal report DESY L-Trans-293 (1984);
L.A. Kondratyuk and M.Zh. Smatikov, preprint of the Institute of Theoretical and Experimental Physics, Moscow, ITEP-13 (1984)

[146] B.C. Clark *et al.*, Phys. Rev. **D 31** (1985) 617

[147] S. Barshay, Z. Phys. **C 27** (1985) 443

[148] S. Barshay and D. Rein, Z. Phys. **C 46** (1990) 215;
erratum: ibidem 696

[149] P. Hoodboy and R.L. Jaffe, Phys. Rev. **D 35** (1987) 113

[150] K.E. Lassila and U.P. Sukhatme, Phys. Lett. **209B** (1988) 343

[151] U.P. Sukhatme, G. Wilk and K.E. Lassila, preprint of the University of Illinois at Chigago UICHEP-TH/90-10 (1990)

[152] K.E. Lassila and U.P. Suckhatme, "Nuclear and Particle Physics on the Light Cone", Editors M.B. Johnson and L.S. Kisslinger, World Scientific, Singapore (1989) p. 115; K.E. Lassila and U.P. Suckhatme, paper no. 498 presented at the at the 25th International Conference on High Energy Physics, Singapore, 2-8 August 1990

[153] J. Dias de Deus *et al.*, Z. Phys. **C 26** (1984) 109

[154] J. Dias de Deus *et al.*, Phys. Rev. **D 30** (1984) 697

[155] A.I. Titov, Sov. J. Nucl. Phys. **38** (1983) 964

[156] A.V. Efremov and E.A. Bondarchenko, preprint of the Joint Institute for Nuclear Research, Dubna, JINR E2-84-124 (1984)

[157] A.M. Baldín, Nucl. Phys. **A434** (1985) 695c

[158] R.J. Glauber, "Lectures in Theoretical Physics", vol. 1, Editors W.E. Brittin and L.G. Dunham, Interscience, New York (1959) p. 315;
R.J. Glauber, in "Proceedings of the Second International Conference on High Energy Physics and Nuclear Structure", Editor G. Alexander, North Holland, Amsterdam (1967) p. 311;
R.J. Glauber, in "Proceedings of the Third International Conference on High Energy Physics and Nuclear Structure", Editor S. Devons, Plenum Press, New York (1969) p. 207

[159] G. Grammer and J.D. Sullivan, "Nuclear Shadowing of Electromagnetic Processes" in A. Donnachie and D. Shaw, "Electromagnetic Interactions of Hadrons", Vol. 2, Plenum Press, New York (1978) p. 195

[160] A. Donnachie and D. Shaw, "Generalized Vector Dominance" in A. Donnachie and D. Shaw, "Electromagnetic Interactions of Hadrons", Vol. 2, Plenum Press, New York (1978) p. 169

[161] T.H. Bauer *et al.*, Rev. Mod. Phys. **50** (1978) 261;
erratum: **51** (1979) 407

[162] L. Stodolsky, Phys. Rev. Lett. **18** (1967) 135

[163] S.J. Brodsky and J. Pumplin, Phys. Rev. **182** (1969) 1794

[164] S.J. Brodsky *et al.*, Phys. Rev. **D 6** (1972) 177

[165] D. Schildknecht, Nucl. Phys. **B66** (1973) 398

[166] J.J. Sakurai and D. Schildknecht, Phys. Lett. **B 40** (1972) 121

[167] H. Fraas, B.J. Read and D. Schildknecht, Nucl. Phys. **B86** (1975) 346; **B88** (1975) 301

[168] R.C.E. Devenish and D. Schildknecht, Phys. Rev. **D 14** (1976) 93

[169] C.L. Bilchak, D. Schildknecht and J.D. Stroughair, Phys. Lett. **B 214** (1988) 441

[170] C.L. Bilchak, D. Schildknecht and J.D. Stroughair, Phys. Lett. **B 233** (1989) 461

[171] G. Piller *et al.*, University of Regensburg preprint TPR-89-40 (1989)

[172] G. Piller *et al.*, Phys. Rev. **C 42** (1990) R1834

[173] G. Piller and W. Weise, University of Regensburg preprint TPR-91-1 (1989), presented at the "Second European Workshop on Hadronic Physics with Electrons beyond 10 GeV", Dourdan, France, 8-12 October 1990, to be published in Nucl. Phys. A

[174] G. Shaw, Phys. Lett. **B 228** (1989) 125

[175] P. Ditsas *et al.*, Nucl. Phys. **B99** (1975) 85

[176] P. Ditsas and G. Shaw, Nucl. Phys. **B113** (1976) 246

[177] N.N. Nikolaev and V.I. Zakharov, Phys. Lett. **55B** (1975) 397;
V.I. Zakharov and N.N. Nikolaev, Sov. J. Nucl. Phys. **21** (1975) 227

[178] A.H. Müller and J. Qiu, Nucl. Phys. **B268** (1986) 427

[179] J. Qiu, Nucl. Phys. **B291** (1987) 746

[180] E.L. Berger and J. Qiu, Phys. Lett. **B 206** (1988) 141

[181] F.E. Close and R.G. Roberts, Phys. Lett. **B 213** (1988) 91

[182] F.E. Close, J.Qiu and R.G. Roberts, Phys. Rev. **D 40** (1989) 2820

[183] L. Guanglie, C. Zhijun and Z. Chasheng, Institute of High Energy Physics, Chinese Academy of Sciences preprint BIHEP-TH-89-29 (1989)

[184] W. Zhu and J.G. Shen, Phys. Lett. **B 219** (1989) 107

[185] W. Zhu and J.G. Shen, Phys. Lett. **B 235** (1990) 170

[186] W. Zhu and J.G. Shen, Phys. Rev. **C 41** (1990) 1674

[187] W. Zhu and J.G. Shen, Phys. Rev. **C 43** (1991) to be published

[188] W. Zhu and L. Qian, East China Normal University preprint ECNU PPE/91-4 (1991)

[189] W. Zhu, private communication (8 April 1991)

[190] W. Zhu, private communication (29 May 1991)

[191] R.C. Hwa, Phys. Rev. **D 22** (1980) 1593

[192] R.C. Hwa and M.S. Zahir, Phys. Rev. **D 23** (1981) 2593

[193] P. Castorina and A. Donnachie, Phys. Lett. **B 215** (1988) 589

[194] P. Castorina and A. Donnachie, Z. Phys. **C 45** (1989) 141

[195] B. Povh and J. Hüfner, Phys. Rev. Lett. **58** (1987) 1612

[196] J.F. Gunion and D.E. Soper, Phys. Rev. **D 15** (1977) 2617

[197] P.V. Landshoff and O. Nachtmann, Z. Phys. **C 35** (1987) 405

[198] S.J. Brodsky and H.J. Lu, Phys. Rev. Lett. **64** (1990) 1342

[199] J. Kwieciński and B. Badełek, Phys. Lett. **B 208** (1988) 508

[200] J. Kwieciński, Z. Phys. **C 45** (1990) 461

[201] L.L. Frankfurt and M.I. Strikman, Phys. Rep. **160** (1988) 235

[202] L.L. Frankfurt and M.I. Strikman, Nucl. Phys. **B 316** (1989) 340

[203] J.D. Bjorken and J. Kogut, Phys. Rev. **D 8** (1973) 1341

[204] Ch. Scholz, Ph.D. thesis, Heidelberg University (1989), in German

[205] U. Landgraf, plenary talk at the Panic XII Conference on Particles and Nuclei, Cambridge MA, 25-29 June 1990, to be published in Nucl. Phys. A

[206] L.L. Frankfurt, M.I. Strikman and S. Liuti, Phys. Rev. Lett. **65** (1990) 1725

[207] N.N. Nikolaev and B.G. Zakharov, Phys. Lett. **B 260** (1991) 414

[208] N.N. Nikolaev and B.G. Zakharov, Z. Phys. **C 49** (1991) 607

[209] L. Carroll, "Through the Looking-glass", Penguin Books, New York (1960) p. 195

[210] CERN NA37/NMC, D. Allasia *et al.*, CERN/SPSC 85-18 SPSC/P210 (1985)

[211] CERN NA2/EMC, O.C. Allkofer *et al.*, Nucl. Instr. and Meth. **179** (1981) 445

[212] CERN NA2'/EMC, J.P. Albanese *et al.*, Nucl. Instr. and Meth. **212** (1983) 111

[213] for the 1987 data see for instance:
Ch. Scholz, Ph.D. thesis, Heidelberg University (1989), in German;
R. Rieger, Ph.D. thesis, Mainz University (1990), in German;
for the calorimetric target see for instance:
F. Zetsche, Ph.D. thesis, Heidelberg University (1990), in German;
for the J/ψ trigger see for instance:
M. de Jong, Ph.D. thesis, Free University of Amsterdam (1991);
C. Mariotti, Ph.D. thesis, Torino University (in preparation), in Italian

[214] A. Arvidson *et al.*, Nucl. Inst. and Meth. **A 251** (1986) 437;
L. Gustafsson and E.Hagberg, Nucl. Inst. and Meth. **A 265** (1988) 521

[215] CERN NA2'/EMC, J. Ashman *et al.*, Phys. Lett. **B 206** (1988) 364;
CERN NA2'/EMC, J. Ashman *et al.*, Nucl. Phys. **B328** (1989) 1

[216] J. Drees, in "Proceedings of the 1981 International Symposium on Lepton and Photon Interactions at High Energies", Editor W. Pfeil, Physikalisches Institut Universität Bonn, Bonn (1981) p. 474

[217] CERN NA47/SMC, J. Beaufays *et al.*, CERN/SPSC 88-47 SPSC/P242 (1988)

[218] R. Clifft and N. Dobble, CERN/SPSC/74-12 (1974)

[219] FNAL CHIO, A.B. Gordon *et al.*, Phys. Rev. **D 20** (1979) 2645

[220] D. Bollini *et al.*, Nuovo Cim. **63 A** (1981) 441

[221] CERN NA4/BCDMS, A. Argento *et al.*, Phys. Lett. **B 120** (1983) 245

[222] D. Brahy and E. Rossa, Nucl. Instr. and Meth. **158** (1979) 121

[223] G. Dubois *et al.*, CERN-SPS/EPB/77-20 (1977);
A. Placci *et al.*, Nucl. Instr. and Meth. **156** (1978) 115

[224] J.B. Lindsay, Nucl. Instr. and Meth. **156** (1978) 329

[225] R.J. Tapper, "Tables of Vapour Pressure and Molar Volume for Liquid Hydrogen and Deuterium", Rutherford Laboratory, Chilton, Didcot, Great Britain, NIRL/R/95 (1965)

[226] National Bureau of Standards, technical note TN 154 (1962)

[227] Cryogenic Data Center Memorandum M1, Cryogenic Division of NBS, Boulder Co.;
Cryogenic Data Center Memorandum M4, Cryogenic Division of NBS, Boulder Co.

[228] H.J. Hoge and R.D. Arnold, Journal of Research of the National Bureau of Standards **47** (1951) 63

[229] R.A. Erickson and L.D. Roberts, Phys. Rev. **93** (1954) 957

[230] D.B. Chelton and D.B. Mann, Cryogenic Data Book, University of California Radiation Laboratory UCRL-3421 (1956)

[231] R. Berman and C.F. Mate, Phil. Mag. (8) **3** (1958) 461

[232] "A Compendium of the Properties of Materials at Low Temperature" by the National Bureau of Standards, Cryogenic Engineering Laboratory, General Editors R.B. Stewart and V. Johnson; Wright Air Development Division, U.S.A.F., WADD Technical Report 60-56 (1960)

[233] L. Mazzone (SPS-CERN), private communication (1987)

[234] Private communication of J. Zmeskal, SIN/PSI Villigen, to R. Rieger (NMC) (29 January 1990)

[235] R.P. Mount *et al.*, Nucl. Inst. and Meth. **160** (1979) 23

[236] W. Flauger, Nucl. Inst. and Meth. **165** (1979) 113

[237] R.P. Mount, Nucl. Inst. and Meth. **187** (1981) 401

[238] C. Best and A. Osborne, EMC internal report EMC/86/26 (1978)

[239] D.J. White, Rutherford Lab. Report RL-78-023 (1978)

[240] J. Womersley, EMC internal report EMC/85/21 (1985)

[241] J. Gillies, EMC internal report EMC/86/19;
M. Botje, NMC note 90/20 (1990);
M. Botje, NMC note 90/24 (1990)

[242] D. Botterill *et al.*, Nucl. Instr. and Meth. **166** (1979) 541

[243] C. Parkman (Editor), OMNET Manual, CERN DD Division

[244] P.J. Pointing, "A Guide to Romulus/Remus Data Acquisition Systems", CERN-EP Electronic Note 80-01 (1980)

[245] L. Carroll, "Alice's Adventures in Wonderland", Penguin Books, New York (1960) p. 35

[246] H.J. Klein and J. Zoll, "Patchy Reference Manual", CERN Program Library (1988)

[247] R. Brun *et al.*, CERN Program Library, Long Write-up, Q210, CERN DD/EE/85-4 (1985)

[248] R. Brun and D. Lienart, CERN Program Library, Long Write-up, Y250 (1987)

[249] H. Grote and I. McLaren, CERN Program Library, Long Write-up, I101 (1986)

[250] H. Wind, Nucl. Inst. and Meth. **115** (1974) 431

[251] M. van der Heijden, Ph.D. thesis, Free University of Amsterdam (1991)

[252] T. Sjöstrand, M. Bengtsson, JETSET 6.3, CERN Pool Program W5035

[253] H. Brafman *et al.*, "A Fast General Purpose IBM Hardware Emulator", Weizmann Inst., Dept. of Nuclear Physics internal report, January 1983;
H. Brafman *et al.*, in "Three Day In-depth Review on the Impact of Specialized Processors in Elementary Particle Physics", Padova, March 23-25, 1983, edited by I.N.F.N. Padova p. 71;
P.K. Kunz *et al.*, ibidem p. 83;
D. Notz, Nucl. Instr. and Meth. A **235** (1985) 380

[254] see for instance:
M. Düren, EMC internal report 86/3 (1986);
S.J. Wimpenny, Ph.D. thesis, University of Sheffield (1981)

[255] J. Stock, Diplom thesis, Freiburg (BRD) University (1986), in German.

[256] A. Ardvidson, NMC note NMC/89/19 (1989)

[257] L. Carroll, "Through the Looking-glass", Penguin Books, New York (1960) p. 186

[258] G.K. Mallot, NMC note NMC/89/2 (1989)

[259] D.Y. Bardin and N.M. Shumeiko, Sov. J. Nucl. Phys. **29** (1979) 499

[260] Y.S. Tsai, SLAC-PUB-848 (1971)

[261] L.W. Mo and Y.S. Tsai, Rev. Mod. Phys. **41** (1969) 205

[262] A.J. Buras and K.J.F. Gaemers, Nucl. Phys. **B132** (1978) 249

[263] SLAC E49, E87, A. Bodek *et al.*, Phys. Rev. **D 21** (1979) 1471

[264] SLAC E49A, J.S. Poucher *et al.*, Phys. Rev. Lett. **32** (1974) 118

[265] E.M. Riordan, Ph.D. thesis, Massachussets Institute of Technology, MIT-LNS RX-648 (1973)
A. Bodek, Ph.D. thesis, Massachussets Institute of Technology, MIT-LNS COO-3069-116 (1972)

[266] SLAC E89A, W.B. Atwood *et al.*, Phys. Lett. **64B** (1976) 479;
W.B. Atwood, Ph.D. thesis, Stanford University (1975), SLAC-report 185

[267] SLAC E89B, M.D. Mestayer *et al.*, Phys. Rev. **D 27** (1983) 285;
M.D. Mestayer *et al.*, Ph.D. thesis, Stanford University (1978), SLAC-report 214

[268] CERN NA4/BCDMS, A. C. Benvenuti *et al.*, Phys. Lett. **B 237** (1990) 599;
CERN NA4/BCDMS, A. C. Benvenuti *et al.*, Phys. Lett. **B 237** (1990) 592

[269] CERN CDHSW, P. Berge *et al.*, Z. Phys. **C 49** (1991) 187

[270] T. Sloan (CERN), private communication (1987)

[271] Ch. Scholz, NMC note NMC/90/25 (1990)

[272] M. Gari and W. Krümpelmann, Z. Phys. **A 322** (1985) 689

[273] G. Höhler *et al.*, Nucl. Phys. **B114** (1976) 505
and references cited therein (for the experimental data)

[274] G.G. Simon *et al.*, Z. Naturforsch. **35a** (1980) 1

[275] SLAC E133, S. Rock *et al.*, Phys. Rev. Lett. **49** (1982) 1139

[276] J. Bernabeu, Nucl. Phys. **B49** (1972) 186

[277] E.B. Hughes *et al.*, Phys. Rev. **146** (1966) 973

[278] W. Fabian and H. Arenhövel, Nucl. Phys. **A314** (1979) 253;
W. Leidermann and H. Arenhövel, Nucl. Phys. **A381** (1982) 365
H. Arenhövel, private communication (1989)

[279] T. deForest, J.D. Walecka, Adv. in Phys. **15** (1966) 1

[280] R.R. Whitney *et al.*, Phys. Rev. **C 9** (1974) 2230

[281] E.J. Moniz, Phys. Rev. **184** (1969) 1154

[282] A. Švarc and M.P. Locher, Fizika **22** (1990) 549

[283] D.J. Drickey *et al.*, Phys. Rev. Lett. **9** (1962) 521

[284] D. Benaksas *et al.*, Phys. Rev. Lett. **13** (1964) 353;
D. Benaksas *et al.*, Phys. Rev. **148** (1966) 1327

[285] C.D. Buchanan *et al.*, Phys. Rev. Lett. **15** (1965) 303

[286] B. Grossetête *et al.*, Phys. Rev. **141** (1966) 1425

[287] S. Galster *et al.*, Nucl. Phys. **B32** (1971) 221

[288] F. Martin *et al.*, Phys. Rev. Lett. **38** (1977) 1320

[289] J.E. Elias *et al.*, Phys. Rev. **177** (1969) 2075

[290] J. Goldemberg *et al.*, Phys. Rev. Lett. **12** (1964) 298

[291] R.E. Rand *et al.*, Phys. Rev. Lett. **18** (1967) 469

[292] D. Ganichot *et al.*, Nucl. Phys. **A 178** (1972) 545

[293] E.C. Jones *et al.*, Phys. Rev. **C 21** (1980) 1162

[294] G.G. Simon *et al.*, Nucl. Phys. **A 364** (1981) 285

[295] R. Cramer *et al.*, Z. Phys. **C 29** (1985) 513

[296] R.G. Arnold *et al.*, Phys. Rev. Lett. **58** (1987) 1723

[297] S. Auffret *et al.*, Phys. Rev. Lett. **54** (1985) 649

[298] S. Platchkov *et al.*, Nucl. Phys. **A510** (1990) 740

[299] M.P. Locher and A. Švarc, Z. Phys. **A 338** (1991) 89

[300] M.P. Locher and A. Švarc, Z. Phys. **A 316** (1984) 55

[301] M.E. Rose, Phys. Rev. **73** (1948) 279

[302] J.A. McIntyre, Phys. Rev. **103** (1956) 1464

[303] M. Düren, Ph.D. thesis, University of Aachen (1987), in German;
V. Gibson, Ph.D. thesis, Oxford University RAL-T-035 (1986);
F. Lettenström, Ph.D. thesis, Uppsala University, Uppsala Dissertations from the Faculty of Science 23 (1988) ;
A. Staiano, Ph.D. thesis, Heidelberg University (1989)

[304] H. Calén, Ph.D. thesis, Uppsala University, Uppsala Dissertations from the Faculty of Science 98 (1987)

[305] I. Sick, Phys. Lett. **116B** (1982) 212
I. Sick, Nucl. Phys. **A218** (1974) 509
H. De Vries *et al.*, Atomic Data and Nuclear Data Tables, **36** (1987) 495

[306] O. Dumbrajs and M. Staszel, Z. Phys. **A 280** (1977) 249

[307] R.W. McAllister and R. Hofstadter, Phys. Rev. **102** (1956) 851

[308] G.R. Burleson and H.W. Kendall, Nucl. Phys. **19** (1960) 68

[309] R.F. Frosch *et al.*, Phys. Lett. **21** (1966) 598

[310] R.F. Frosch *et al.*, Phys. Rev. **160** (1967) 874

[311] U. Erich *et al.*, Z. Phys. **208** (1968) 209

[312] J.S. McCarthy, I. Sick, R.R. Whitney, Phys. Rev. **C 15** (1977) 1396

[313] R.G. Arnold *et al.*, Phys. Rev. Lett. **40** (1978) 1429

[314] R. Rieger, NMC Note NMC/89/15 (1989)

[315] M. de Jong, C. Mariotti, E. Rondio, private communication (1990)

[316] G. Baum (NMC), private communication (1988)

[317] M. Botje, "Smearing Corrections on F_2^n/F_2^p", talk at the NMC meeting of 21 February 1989

[318] M. Botje, "Bin Centering Corrections on F_2^n/F_2^p", talk at the NMC meeting of 9 November 1988

[319] A.A. Akhundov *et al.*, Sov. J. Nucl. Phys. **44** (1986) 988;
A.A. Akhundov *et al.*, JINR Report E2-86-104 (1986);
A.A. Akhundov *et al.*, Sov. J. Nucl. Phys. **26** (1977) 660

[320] T. Sloan, EMC internal report EMC/87/4 (1987)

[321] C. Lietzke, S.J. Wimpenny, University of California at Riverside report UCR/DIS-89-06 and EMC internal report EMC/89/3 (1989)

[322] CERN NA2/EMC, J.J. Aubert *et al.*, Z. Phys. **C 10** (1981) 101

[323] CERN NA2/EMC, J.J. Aubert *et al.*, Z. Phys. **C 22** (1984) 341

[324] C. Chahine, Phys. Rev. **D 22** (1980) 1062; ibidem 2727;
C. Chahine, Phys. Rev. Lett. **47** (1981) 1374

[325] A. Staiano, Ph.D. thesis, University of Heidelberg (1989)

[326] C. Broggini, Ph.D. thesis, University of Neuchâtel (1989)

[327] R. Rieger, Ph.D. thesis, University of Mainz (1990), in German

[328] A. Bodek, Nucl. Instr. and Meth. **117** (1974) 613

[329] CERN NA37/NMC, P. Amaudruz *et al.*, Z. Phys. C **51** (1991) 387

[330] O. Nachtmann, Nucl. Phys. **B78** (1974) 455

[331] H. Georgi and H.D. Politzer, Phys. Rev. **D 14** (1976) 1829

[332] J. Gomez, Ph.D. thesis, The American University, Washington D.C. (1987)

[333] R.J.M. Covolan and E. Predazzi, Nuovo Cim. **103 A** (1990) 773

[334] H. Wind, Nucl. Instr. and Meth. **84** (1970) 117

[335] D. Allasia (NMC), private communication (1990)

[336] CERN PROGRAM LIBRARY, POOL-X Routines, Routine X1006

[337] CERN PROGRAM LIBRARY, POOL-X Routines, Routine X1010

[338] CERN PROGRAM LIBRARY, POOL-E Routines

[339] D. Allasia *et al.*, NMC note NMC/89/9 (1989)

[340] Alignment file P1C87C10

[341] Alignment file P1C87C13

[342] M. Arneodo, NMC note NMC/90/17 (1990)

[343] C. Mariotti and R. Rieger (NMC), private communication (1988)

[344] T. Sloan, EMC internal report EMC/79/20 (1979);
J. Carr *et al.*, EMC internal report EMC/80/23 (1980);
P. Payre *et al.*, EMC internal report EMC/81/5 (1981)

[345] J.J. Aubert *et al.*, Nucl. Instr. and Meth. **159** (1979) 47

[346] M. De Vincenzi *et al.*, Nucl. Instr. and Meth. **225** (1984) 104

[347] M. Arneodo and A. Sandacz, NMC note NMC/87/12 (1987)

[348] C. Peroni and P.P. Trapani, EMC internal report EMC/81/1 (1981)

[349] D. Nowotny and Ch. Scholz, NMC note NMC/91/2 (1991)